Prototyping the Spectrograph Mechanisms for HARMONI@ELT, and the Drivers of the Main Sequence Positions of 5MUSES Galaxies



Thomas William Foster

Trinity College

University of Oxford

A thesis submitted for the degree of

Doctor of Philosophy

Hilary 2021

for Mom, Dad, and Jim

Prototyping the Spectrograph Mechanisms for HARMONI@ELT, and the Drivers of the Main Sequence Positions of 5MUSES Galaxies

Thomas William Foster

A thesis submitted for the degree of Doctor of Philosophy; Trinity College, University of Oxford

HARMONI (High Angular Resolution Monolithic Optical and Near-infrared Integral field spectrograph) is a planned first light integral field spectrograph (IFS) for the Extremely Large Telescope. Each of the two main mechanical modules within the spectrograph, the Fold Mirror Module (FMM) and the Infrared Grating Module (IGM), used for the folding and dispersion of the beam, respectively, must operate within tight repeatability requirements to ensure that daytime calibration frames (wavelengths and flats) can be taken in the same observational setup following on-sky observations the previous night (to increase the accuracy of the calibration). The first part of this D.Phil thesis involves prototyping and testing the first of the two mirrors of the FMM (the Fold Mirror 1, or FM1) and the entire Infrared Grating Module to ensure they meet the required levels of repeatability. Furthermore, a separate method of achieving the required repeatability is prototyped and tested using detents. This method could be incorporated for use with both the FMM and IGM if their original designs do not meet the required levels of repeatability. A thorough evaluation of the causes of the positional errors is given for each of the three main prototype tests. All tests are conducted at room temperature, as well as initial tests of the detent mechanism and Fold Mirror 1 at 130K, the temperature of the HARMONI cryostat. All three mechanisms achieve warm repeatabilities well within their tolerances.

In the second part of this thesis, data from the Oxford SWIFT Integral Field Spectrograph (IFS) is used to study a statistically significant subset of the 24μm flux-limited 5MUSES galaxies sample. Specifically, the dynamical ratio (rotational velocity V_{rot} divided by the intrinsic disk dispersion σ_0, a diagnostic of the galaxy's evolutionary history) and the Active Galactic Nuclei (AGN) contribution to the Infrared Luminosity (L_{IR}) (AGN fraction, or f_{AGN}) are investigated to help determine whether the high multiplicative offsets from the expected main sequence of star formation (or the offset from the expected level of star formation given a stellar mass and redshift for each galaxy, and later defined as the 'Main Sequence Multiple', or MSM_{IR}) are due to star formation brought on by interactions, or due to luminosity from an AGN. To do this, the SWIFT subset is kinematically modeled to compute the dynamical ratio, and Spectral Energy Distributions (SEDs) of each galaxy are fit with galaxy and AGN templates to determine f_{AGN}, which is then used to correct L_{IR}. It is found that 24% of the SWIFT galaxies are interacting, with 71% isolated, and that galactic interactions are the main cause of the high MSM_{IR} observed, rather than AGN. The SWIFT subset of the 5MUSES galaxies serve as a generic representation of the bulk of star forming, main sequence galaxies, making the conclusions of this work applicable to many galaxies in the universe.

Statement of Originality

I completed the work presented in this thesis under the supervision of Professor Niranjan Thatte, Professor Dimitra Rigopoulou, and Dr. Myriam Rodrigues between October 2016 and April 2020. Everything in this thesis is my own original work, except where stated otherwise. I have not submitted this work for any other degree, diploma, or qualification at any other institution of higher education.

The initial mechanical designs of the detent test mechanism, Fold Mirror 1 prototype, and Infrared Grating Module prototype were completed by Dr. James Lynn. The analysis for determining the repeatability tolerances for each module was carried out by Dr. John Capone.

The copyright of this thesis rests with the author. No quotations from it should be published without the author's prior written consent and information derived from it should be acknowledged.

Thomas William Foster

(Hilary 2021)

Acknowledgements

I would like to thank my supervisors and the larger HARMONI group at Oxford, including Dimitra, Ian, Matthias, Fraser, Miguel, and John. And of course, thank you to Vanessa for always being there to lend a helping hand through it all. Thank you to James Kariuki and Adam Lower for helping with some new designs these past few months.

To my fellow DPhil candidates in HARMONI - Andrea, Alvaro, and Lawrence - thank you three for being great friends and always willing to lend a hand or talk about anything. I wish all three of you the absolute best.

A massive thank you as well to Bob Watkins, Andy Clack, and John Temple for all the help with getting my tests setup - but also for always being great people. It was always a highlight of my day coming by AOPP and chatting with you three.

Thanks to my original professors and mentors at Yale University who first sparked and developed my interest in Astrophysics. Debra Fischer, Louise Edwards, and Tyler McCracken. I wouldn't be here without you three, and your support in college gave me the confidence that I could conduct research at the graduate level. Thank you as well to my high school AP Physics teacher, Dr. Stephen Palfrey, for encouraging me to major in Astrophysics in college.

Outside of my research in astrophysics, I owe so much to my parents and wider family. Your support through thick and thin with everything I attempt is my bedrock. I know that no matter what I try - you will believe in me. This is worth so much, especially when things are exceptionally challenging. Thank you to Upper Thames Rowing Club and all my friends over there - Justin, Clive, and Mark to name a few - for helping to make rowing in Henley the best past time I could ever want. Thanks to all of my friends back home - Alex, Solberg, Matthes, and Matejka to name a few - and all over the world for all of your support these past few years.

Finally, thank you to Jim Lynn. It was an honour to work with you for the short time that I did. You were more than just a colleague - but a true friend. I owe much of the successes in my research to you, and you were always there to lend a hand and help me work through my problems. I will always fondly remember dropping in by your office and talking about rowing, squash, rugby, or football. I do wish that I could have gotten to spend more time with you, and you will be dearly missed.

Contents

Part I: Prototyping the Spectrograph Mechanisms for HARMONI@ELT

Chapter 1: Introduction **23**

1 Spectroscopy . . . 23
2 HARMONI - The ELT's First-Light IFS . . . 26
2.1 HARMONI Spectrograph Operational Concept . . . 30
3 The Challenge of Daytime Calibration . . . 31
4 Challenges of Prototyping and Building Four Spectrographs . . . 40
5 Outline of Part I . . . 41

Chapter 2: Quantifying the Impact of Temperature, and Stability Testing **43**

1 Quantifying the Impact of Temperature . . . 43
1.1 Fluctuations in background temperature . . . 43
1.2 Reduction of heat from the operation of test equipment . . . 47
1.3 Required background temperature stability . . . 49
2 Removing the Drift from Background Temperature . . . 52
3 Stability Tests . . . 54
3.1 Warm . . . 55
3.2 Cold . . . 57
4 Conclusions . . . 58

Chapter 3: A Detent Mechanism For Achieving High Repeatability **61**

1 Design . . . 64
1.1 Detent design . . . 64
1.2 Detent test mechanism design . . . 66
2 Warm Testing . . . 69
2.1 Warm test setup . . . 69
2.2 Warm repeatability test plan . . . 72
2.3 Optimizing the operation of the detent mechanism . . . 72
2.3.1 Solenoid only tests . . . 73
2.3.2 Operational optimization testing . . . 79
2.4 Warm repeatability tests . . . 85
2.4.1 Repeatability about the Y-axis . . . 86
2.4.2 Repeatability about the X/Z-axis. . . . 89

2.4.3 Accelerated lifetime performance . . . 89
2.5 Final warm repeatability performance . . . 90
3 Cold Testing . . . 92
3.1 Cold test setup . . . 92
3.2 Cold repeatability test plan . . . 94
3.3 Cold repeatability test . . . 94
4 Detent Test Mechanism Testing Conclusions . . . 95
4.1 Warm . . . 95
4.2 Cold . . . 96
5 Future Work . . . 96

Chapter 4: Testing of the Fold Mirror 1 Mechanism 99

1 Design . . . 101
1.1 HARMONI FM1 design . . . 101
1.2 FM1 test mechanism design . . . 105
2 Warm Testing . . . 105
2.1 Warm test setup . . . 106
2.2 Warm repeatability test plan . . . 107
2.3 Optimizing the operation of the FM1 . . . 109
2.3.1 Thermal expansion . . . 110
2.3.2 Backlash . . . 110
2.3.3 Stepper motor missing steps . . . 112
2.3.4 Mechanical wear due to constant operation . . . 115
2.3.5 Conclusions from the optimization tests . . . 116
2.4 Warm repeatability tests . . . 116
2.4.1 Repeatability about the X-axis . . . 117
2.4.2 Repeatability about the Y-axis . . . 118
2.4.3 Accelerated lifetime performance . . . 119
2.5 Final warm repeatability performance . . . 119
3 Initial Cold Testing . . . 121
3.1 Cold test setup . . . 121
3.2 Initial cryogenic testing results . . . 123
4 FM1 Testing Conclusions . . . 125
4.1 Warm . . . 125
4.2 Cold . . . 125
5 Future Work . . . 125

Chapter 5: Testing of the Infrared Grating Module 127

1 Design . . . 128

1.1 HARMONI IGM design . . . 128
1.2 IGM test mechanism design . . . 132
2 Warm Testing . . . 132
2.1 Warm test setup . . . 132
2.2 Warm repeatability test plan . . . 137
2.3 Optimizing the operation of the IGM . . . 138
2.3.1 Re-optimization of the FM1 test parameters for the IGM. . . . 138
2.3.2 Sources of errors native to the IGM . . . 141
2.3.3 Conclusions from the optimization tests . . . 145
2.4 Warm repeatability tests . . . 145
2.4.1 Repeatability about the Y-axis. . . . 145
2.4.2 Repeatability about the X/Z-axis . . . 146
2.4.3 Accelerated lifetime performance . . . 146
2.5 Final warm repeatability performance . . . 147
3 Combined HARMONI Spectrograph Repeatability . . . 148
4 Cold Testing Preparations and Future Work . . . 149

Part II: The Drivers of the Main Sequence Positions of 5MUSES Galaxies

Chapter 6: Introduction 155

1 A Brief Introduction to Galaxies . . . 155
2 The Evolution of the Global Star Formation Rate Density and the Star Formation Main Sequence 156
3 Triggers of Star Formation 162
4 Relating Increased Star Formation with Interactions or AGN . . . 167

Chapter 7: Sample and Data Analysis 169

1 Sample Selection - 5MUSES and the SWIFT Subset . . . 169
2 Ancillary Data . . . 172
3 SWIFT Data . . . 173
3.1 Observations . . . 173
3.2 Data reduction . . . 174
3.3 Initial kinematic analysis . . . 176
3.4 GalPak analysis . . . 178
3.5 Extinction correction . . . 183
3.6 Metallicity . . . 184

Chapter 8: Results and Discussion 187

1 The Main Sequence of Star Formation 187
1.1 Calculation of MSM_{IR}, and the AGN/star forming classification 187
1.2 Calculation of f_{AGN} and $MSM_{IR,\,AGN\,Corrected}$ 191
2 Galactic Kinematics and Kinematic Classification 201
3 The Main Sequence Multiple-Dynamical Ratio Relation 208
4 Conclusions 212
5 Future Work 213

Appendix A: SDSS Images and Kinematic Fits for the SWIFT-5MUSES Galaxies 215

Appendix B: SED Template Fits for the SWIFT-5MUSES Galaxies 233

Bibliography 239

List of Figures

1.1 An image of a datacube 25

1.2 Diagrams of lenslet and fibre-based IFS 26

1.3 Diagram of an image slicer based IFS 27

1.4 Block diagram of the end-to-end optical path of HARMONI 32

1.5 Diagram of the three different optical paths between the Fold Mirror Module and the Infrared Grating Module 33

1.6 The HARMONI spectrograph layout and optical path 34

1.7 The difference between repeatability and accuracy 35

2.1 Correlation of moving and reference mirrors while at rest 44

2.2 Correlation of moving and reference mirrors while operational 45

2.3 The impact of the stepper motor heat on the position of the FM1 47

2.4 Warm stability of the detent 50

2.5 Warm laboratory temperature 50

2.6 Repeatability of all mechanisms in a stabilized warm environment 52

2.7 Warm stability of the detent test mechanism 56

2.8 Warm stability of the FM1 57

2.9 Temperature of the cryostat over time 59

2.10 Cold stability of the detent mechanism 59

3.1 The repeatability axes of the detent test mechanism 63

3.2 Drawings of the cantilever and beam detents 65

3.3 Drawing of the spring plunger detent 65

3.4 Images of the detents 66

3.5 An image of the upper rotating wheel 67

3.6 A diagram of the detent test mechanism 68

3.7 Further diagrams of the detent mechanism 68

3.8 Images of the detent test mechanism 69

3.9 Diagram of the detent test mechanism test setup 71

3.10 Image of the detent test mechanism test setup 71

3.11 A diagram of the X/Z-axis equivalency of the detent test mechanism 72

3.12 The warm test plan for the detent test mechanism 73

3.13 Repeatability of one cantilever detent in the solenoid only test 75

3.14 A diagram explaining bearing clearance 75

3.15 A diagram demonstrating the test setup with two detents 76

3.16 Repeatability of two detents in the solenoid only test 77

3.17 Repeatability of three detents in the solenoid only test 78

3.18 The effect of settle time on repeatability 81

3.19 The ‘landing stage’ on the detent test mechanism 82

3.20 A diagram explaining backlash 84

3.21 A plot showing the effect of rotation in different directions 84

3.22 Repeatability of one detent about the Y-axis 87

3.23 Repeatability of two detents about the Y-axis 88

3.24 Repeatability of three detents about the Y-axis 89

3.25 Repeatability of three detents about the X/Z-axis 90

3.26 Histograms of the residuals from all repeatability tests 91

3.27 The detent cold test setup in the AOPP cryostat 93

3.28 A diagram showing the locations of the thermometers 93

4.1 The optical layout of the FM1 and FM2 100

4.2 A CAD model of the Fold Mirror Module showing the defined axes of repeatability for FM1 101

4.3 A CAD model of the Fold Mirror 1 Mechanism 102

4.4 The lead screw assembly 103

4.5 Flex pivots 104

4.6 Images of the FM1 test mechanism 106

4.7 A diagram of the warm test setup 107

4.8 The custom three-sided mirror 108

4.9 An image of the warm test setup 108

4.10 The warm test plan for the FM1 109

4.11 The concept of backlash between the leadscrew and nut 110

4.12 The impact of backlash 111

4.13 The two movement profiles 112

4.14 A plot showing the impact of missed steps 113

4.15 A magnified section of the plot from Figure 3.17 114

4.16 The sheared flex coupling 116

4.17 A plot showing the X-axis repeatability of FM1 118

4.18 A plot showing the Y-axis repeatability of FM1 119

4.19 A histogram of the residuals of all the warm repeatability tests 120

4.20 The FM1 mounted in the cryostat 122

4.21 The thermometer and heater locations 122

4.22 The FM1 mounted inside the radiation shield 123

5.1 A CAD model of the Infrared Grating Module defining the repeatability axes 128

5.2 CAD models of the IGM 129

5.3 An image of the worm gear assembly 130

5.4 A CAD drawing of the bearing housing 131

5.5 Images of the IGM test mechanism 133

5.6 A diagram of the warm test setup 134

5.7 A diagram of the X/Z-axis equivalency of the IGM 134

5.8 Diagram demonstrating the updated IGM repeatabilities 135

5.9 Image of the IGM test setup in the laboratory 137

5.10 The warm test plan for the IGM 138

5.11 A diagram demonstrating the two movement profiles 140

5.12 A plot showing the impact of the flex coupling slipping 143

5.13 A plot showing repeatability about the Y-axis 147

5.14 A plot showing repeatability about the X/Z-axis 147

5.15 A histogram of the Y-axis residuals of all the warm repeatability tests 150

5.16 A histogram of the X/Z-axis residuals of all the warm repeatability tests 151

6.1 The evolution of the global star formation rate 162

6.2 The $SFR - M_*$ (star formation main sequence) relation 163

7.1 L_{IR} vs redshift for the 5MUSES sample and SWIFT subset 170

7.2 $Log(SFR_{IR})$ vs $Log(M_*)$ for the 5MUSES sample and SWIFT subset 171

7.3 Fitted spectra for M036 177

7.4 Flux, and line-of-sight velocity and dispersion maps for M202 180

7.5 Output flux, velocity, and dispersion maps for M202 182

7.6 De-projected observed and model rotation and dispersion maps for M202 182

8.1 The redshift evolution of $sSFR$ 189

8.2 MSM_{IR} vs $EW_{PAH6.2\mu m}$ 191

8.3 $EW_{PAH6.2\mu m}$ vs $f_{AGN,\,Magdis\,2013}$. 193

8.4 The best SED fits for M005 and M310 196

8.5 The far-infrared SED for M188 197

8.6 $EW_{PAH6.2\mu m}$ vs $f_{AGN,\,Foster}$ 198

8.7 $f_{AGN,\,Magdis}$ vs $f_{AGN,\,Foster}$ 200

8.8 V_{max}/σ_0 vs σ_0 203

8.9 MSM_{IR} vs V_{max}/σ_0 209

8.10 AGN-corrected MSM_{IR} vs V_{max}/σ_0 210

A.1 SDSS continuum image for M005. 215

A.2 SDSS continuum image for M012. 215

A.3 SDSS continuum image for M013. 216

A.4 [$H\alpha$]6562Å flux, velocity, and dispersion maps, GalPak fits, and curves for M018, along with the SDSS continuum image. 216

A.5 [$H\alpha$]6562Å flux, velocity, and dispersion maps, GalPak fits, and curves for M019, along with the SDSS continuum image. 217

A.6 SDSS continuum image for M020. 217

A.7 [$H\alpha$]6562Å flux, velocity, and dispersion maps, GalPak fits, and curves for M022, along with the SDSS continuum image. 218

A.8 [$H\alpha$]6562Å flux, velocity, and dispersion maps, GalPak fits, and curves for M028, along with the SDSS continuum image. 218

A.9 [$H\alpha$]6562Å flux, velocity, and dispersion maps, GalPak fits, and curves for M035, along with the SDSS continuum image. 219

A.10 [$H\alpha$]6562Å flux, velocity, and dispersion maps, GalPak fits, and curves for M036, along with the SDSS continuum image. 219

A.11 [$H\alpha$]6562Å flux, velocity, and dispersion maps, GalPak fits, and curves for M037, along with the SDSS continuum image. 220

A.12 SDSS continuum image for M039. 220

A.13 SDSS continuum image for M041. 221

A.14 [$H\alpha$]6562Å flux, velocity, and dispersion maps, GalPak fits, and curves for M050, along with the SDSS continuum image. 221

A.15 [$H\alpha$]6562Å flux, velocity, and dispersion maps, GalPak fits, and curves for M055, along with the SDSS continuum image. 222

A.16 SDSS continuum image for M057. 222

A.17 SDSS continuum image for M061. 223

A.18 SDSS continuum image for M062. 223

A.19 [$H\alpha$]6562Å flux, velocity, and dispersion maps, GalPak fits, and curves for M066, along with the SDSS continuum image. 224

A.20 [$H\alpha$]6562Å flux, velocity, and dispersion maps, GalPak fits, and curves for M069, along with the SDSS continuum image. 224

A.21 SDSS continuum image for M070. 225

A.22 [$H\alpha$]6562Å flux, velocity, and dispersion maps, GalPak fits, and curves for M073, along with the SDSS continuum image. 225

A.23 SDSS continuum image for M075. 226

A.24 [$H\alpha$]6562Å flux, velocity, and dispersion maps, GalPak fits, and curves for M086, along with the SDSS continuum image. 226

A.25 [$H\alpha$]6562Å flux, velocity, and dispersion maps, GalPak fits, and curves for M107, along with the SDSS continuum image. 227

A.26 [$H\alpha$]6562Å flux, velocity, and dispersion maps, GalPak fits, and curves for M185, along with the SDSS continuum image. 227

A.27 [$H\alpha$]6562Å flux, velocity, and dispersion maps, GalPak fits, and curves for M188, along with the SDSS continuum image. 228

A.28 [$H\alpha$]6562Å flux, velocity, and dispersion maps, GalPak fits, and curves for M202, along with the SDSS continuum image. 228

A.29 SDSS continuum image for M294. 229

A.30 [$H\alpha$]6562Å flux, velocity, and dispersion maps, GalPak fits, and curves for M297, along with the SDSS continuum image. 229

A.31 [$H\alpha$]6562Å flux, velocity, and dispersion maps, GalPak fits, and curves for M299, along with the SDSS continuum image. 230

A.32 [$H\alpha$]6562Å flux, velocity, and dispersion maps, GalPak fits, and curves for M310, along with the SDSS continuum image. 230

A.33 [$H\alpha$]6562Å flux, velocity, and dispersion maps, GalPak fits, and curves for M315, along with the SDSS continuum image. 231

A.34 [$H\alpha$]6562Å flux, velocity, and dispersion maps, GalPak fits, and curves for M317, along with the SDSS continuum image. 231

B.1 SED template fits for M005 and M012 233

B.2 SED template fits for M013 and M018 233

B.3 SED template fits for M019 and M020 234

B.4 SED template fits for M022 and M028 234

B.5 SED template fits for M035 and M036 234

B.6 SED template fits for M037 and M039 235

B.7 SED template fits for M041 and M050 235

B.8 SED template fits for M055 and M057 235

B.9 SED template fits for M061 and M062 236

B.10 SED template fits for M066 and M069 236

B.11 SED template fits for M070 and M073 236

B.12 SED template fits for M075 and M086 237

B.13 SED template fits for M107 and M185 237

B.14 SED template fits for M188 and M202 237

B.15 SED template fits for M294 and M297 238

B.16 SED template fits for M299 and M310 238

B.17 SED template fits for M315 and M317 238

List of Tables

1.1 The HARMONI system parameters 28

1.2 HARMONI wavelength calibration error and stability error budgets 37

1.3 First order estimates for the repeatability and stability tolerances 39

2.1 RMS stability tolerances for the detent mechanism, FM1, and IGM 56

2.2 Stability results and Chapter 2 conclusions 60

3.1 The RMS repeatability tolerances for the detent test mechanism 62

3.2 Conclusions from the solenoid only testing 79

3.3 A summary of the sources of error and their mitigations 86

3.4 A summary of the detent test mechanism warm repeatabilities 91

4.1 The RMS repeatability tolerances for the FM1 100

4.2 A summary of the sources of error and their mitigations 117

4.3 A summary of the FM1 test mechanism warm repeatabilities 120

5.1 The RMS repeatability tolerances for the IGM 128

5.2 The updated RMS repeatability tolerances for the IGM 136

5.3 The test parameters for the IGM 139

5.4 A summary of the sources of error and their mitigations 145

5.5 A summary of the IGM test mechanism warm repeatabilities 148

7.1 Ancillary data used 174

7.2 The SWIFT system parameters 175

7.3 SWIFT subset galactic locations, observation date, seeing, and redshifts 176

7.4 $SFR_{H\alpha}$, $log(SFR_{H\alpha}/SFR_{IR})$, A_V, and $12 + log(O/H)$ from Pettini and Tacconi . . . 186

8.1 MSM_{IR}, f_{AGN}, $MSM_{IR,\,AGN\,corrected}$, and AGN/Star Forming classifications 202

8.2 V_{max}, σ_o, V_{max}/σ_0 and kinematic classifications 205

8.3 Position angle, inclination, radius, and dynamic mass 206

Part I

Prototyping the Spectrograph Mechanisms for HARMONI@ELT

Chapter 1

Introduction

This part of the thesis focuses on the prototyping work done for the spectrograph sub-system of HARMONI, the first-light integral field spectrograph for the Extremely Large Telescope. This part begins with an introduction to integral field spectroscopy and the HARMONI instrument, followed by a discussion of the method of calibrating ELT spectroscopic data and how it drives strict tolerances on repeatability with the HARMONI spectrograph's mechanical modules. The designing, prototyping, and testing of three mechanical prototypes is then presented.

1. Spectroscopy

The analysis of spectra has been fundamental to many major advancements in astronomy for centuries. The intensity and wavelength of absorption and emission lines allow astronomers to measure properties that could not otherwise be measured, such as galactic chemical compositions, star formation rates, and rotation curves.

Traditionally, spectra were obtained by dispersing a beam from a long slit illuminated by light from a telescope, and then focusing the dispersed beam onto a detector. The slit would be aligned over part of an object (such as a galaxy), with a spectrum returned for only the area covered by the slit. This inherently limits the science that can be done, as spectra are not returned for the full spatial extent of the object, preventing accurate measurements of integrated line fluxes and 2D maps of rotational velocity (among other science goals). Ideally, the entire object

would be covered by the spectrograph, simultaneously returning a spectrum for each spatial element of the science target, outputting a 3D image with two spatial axes and one spectral axis.

To obtain 3D data on the object with only a long-slit spectrograph, the slit can be scanned spatially across the object, with observations after each re-positioning of the slit over the object. This method is subject to two main difficulties. First, the cumulative integration time required for all exposures to have enough signal-to-noise would be long (depending on exposure time, up to tens or even hundreds of hours) (Bacon & Monnet, 2017). Second, atmospheric distortion in seeing-limited observations, such as fluctuations in temperature and air density (which would impact the point spread function full width half maximum and change the size of the maximum resolvable element), between the observations would change, having a significant and negative impact on the spatial resolution and making calibration observations difficult.

An alternative to a long-slit spectrograph is a Fabry-Perot spectrometer, which has an optical cavity that only allows light of a specific wavelength to pass through. The distance between the two optical elements in the cavity can be changed, varying the resonance wavelength. To obtain 3D data, a Fabry-Perot can thus be scanned spectrally over an object rather than spatially. However, this method is also limited as hundreds of exposures are needed to spectrally cover the whole object. Similarly, an imaging Michelson interferometer produces fringes by first splitting an input beam, with the output beams then striking either a fixed mirror or movable mirror. These two beams are then recombined and amplified using the superposition principle to create an interference pattern. As such, an imaging Michelson interferometer could be used as an alternative to a Fabry-Perot spectrometer, but would be limited by the same factors in obtaining 3D data, as it would also have to scan over the object spectrally.

The integral field spectrograph (IFS) overcomes the limitations in retrieving 3D data from both scanning 2D spectrographs and multi-object spectrographs by putting three dimensions of information (two spatial, and one spectral) simultaneously onto a two dimensional detector, with no spatial or spectral scanning required. The IFS samples a 2D field of view and retrieves spectra for each spatial pixel in a single exposure. The output is a ‘datacube’ with intensity along 3 axes, in x, y, and λ (Figure 1.1). Each pixel in the spatial axes x and y contains a spectrum in the spectral axis λ, and is referred to as a spaxel (SPAtial piXEL).

There are three main methods of sampling the 2D field. The simplest involves a series of lenslets where each transforms a discrete part of the focal plane into a micro-pupil, with each

micro-pupil then dispersed by a spectrograph. However, a significant area on the detector is unused due to the input light not being arranged into a single long slit, with the spectrum from each micro-pupil mapped directly onto the detector. As such, the spacing between the micro-pupils is wasted in detector space.

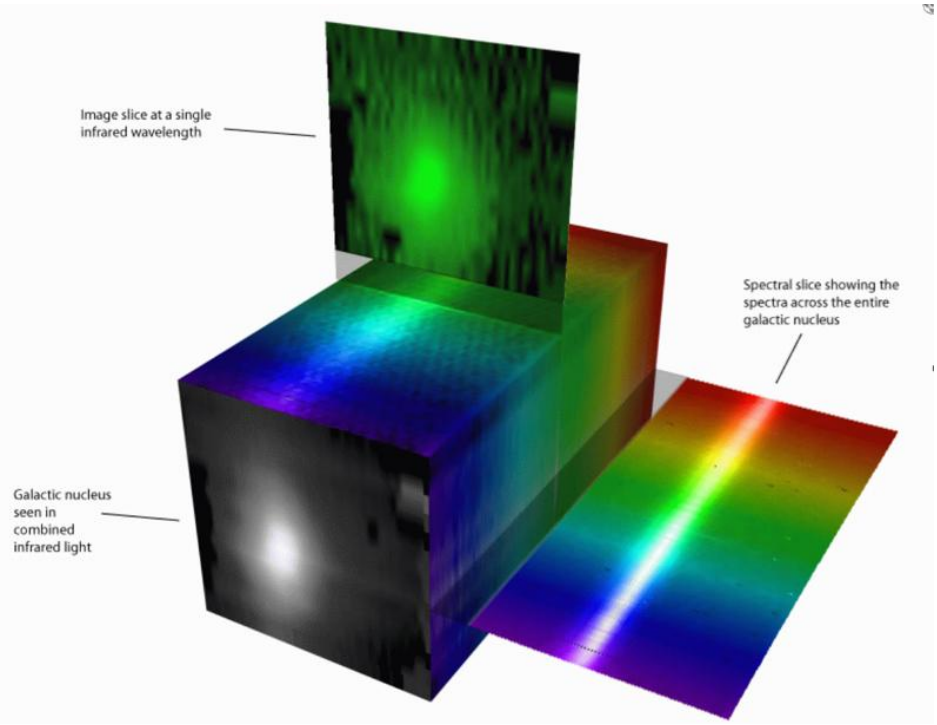


Figure 1.1: An image of a datacube, which can be thought of as a series of images of an object at different wavelengths, or a series of pixels each containing a spectrum. Credit: Stephen Todd and Douglas Pierce-Price.

To overcome this, the second method involves sending the focused light from each lenslet into a fibre. The fibres are then rearranged to form a long slit at the entrance of the spectrograph, which is then dispersed and focused onto a detector. While this method makes better use of detector pixels than lenslets (however, there is still some wasted detector space due to the spacing of the circular fibres), the use of fibres causes significant throughput losses of up to 35% (Bacon & Monnet, 2017). Both of these concepts are outlined in Figure 1.2 (Credit: Mark Westmoquette, adapted by the author for this thesis).

The third IFS technique involves using an image slicer to sample the 2D field. A stack of mirrors all arranged at slightly different angles with respect to the input light splits the field into several slices which are then realigned by a second set of mirrors into a pseudo long-slit, which

is then dispersed by a spectrograph (Figure 1.3). Slicer-based IFS make extremely efficient use of detector pixels, with almost no loss of light due to the high fill factor in the focal plane of the image slicing mirror. However, the optical systems (such as the image slicer) are often large and complicated and can be difficult and expensive to manufacture.

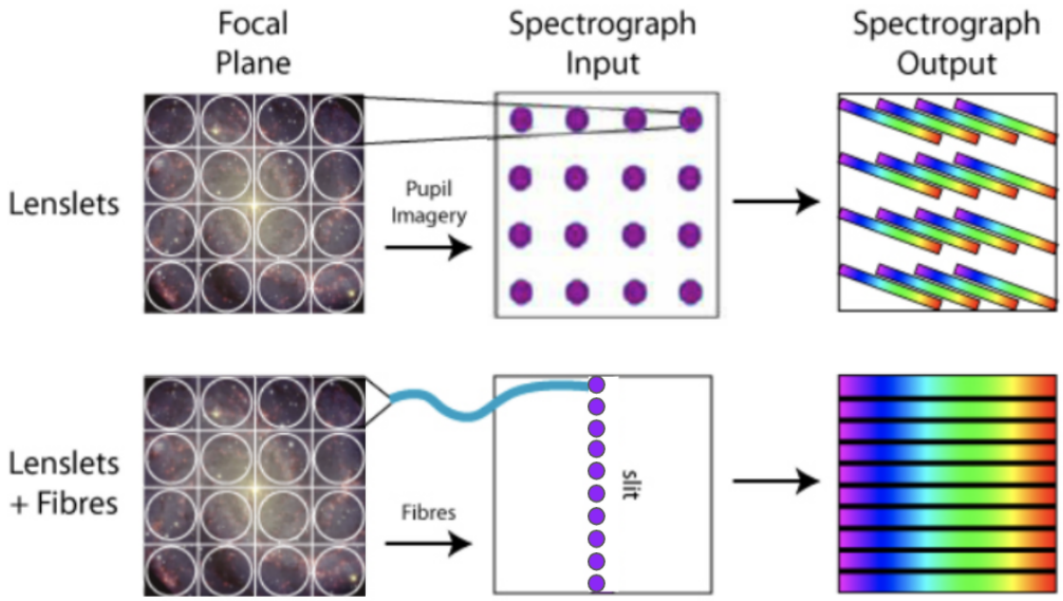


Figure 1.2: (Top) Diagrams explaining the concept of the lenslet-based IFS. Light from the focal plane of the telescope is focused and dispersed by a spectrograph. (Bottom) Diagrams explaining the fibre-based IFS. (Credit: Mark Westmoquette, adapted by the author for this thesis).

2. HARMONI - The ELT's First-Light IFS

The Extremely Large Telescope (ELT) (Tamai et al., 2018) is a 39-metre optical and near infrared (NIR) telescope currently being built by the European Southern Observatory (ESO) at Cerro Armazones, Chile. Ground was broken in 2014, with construction set to be complete by 2025. With a 39m primary mirror, it will have a greater light gathering capability than almost all of the current optical/NIR telescopes in the world, combined (credit: ESO).

HARMONI (Thatte et al., 2014) is an image-slicer based IFS designed to be the first-light 'workhorse' IFS for the ELT. The University of Oxford heads the HARMONI consortium jointly with the UKATC. The HARMONI consortium is tasked with designing, prototyping, and

building the instrument. Set to be completed in 2025, HARMONI passed its preliminary design review in 2018 and is now headed towards completion of the Final Design Review in 2020.

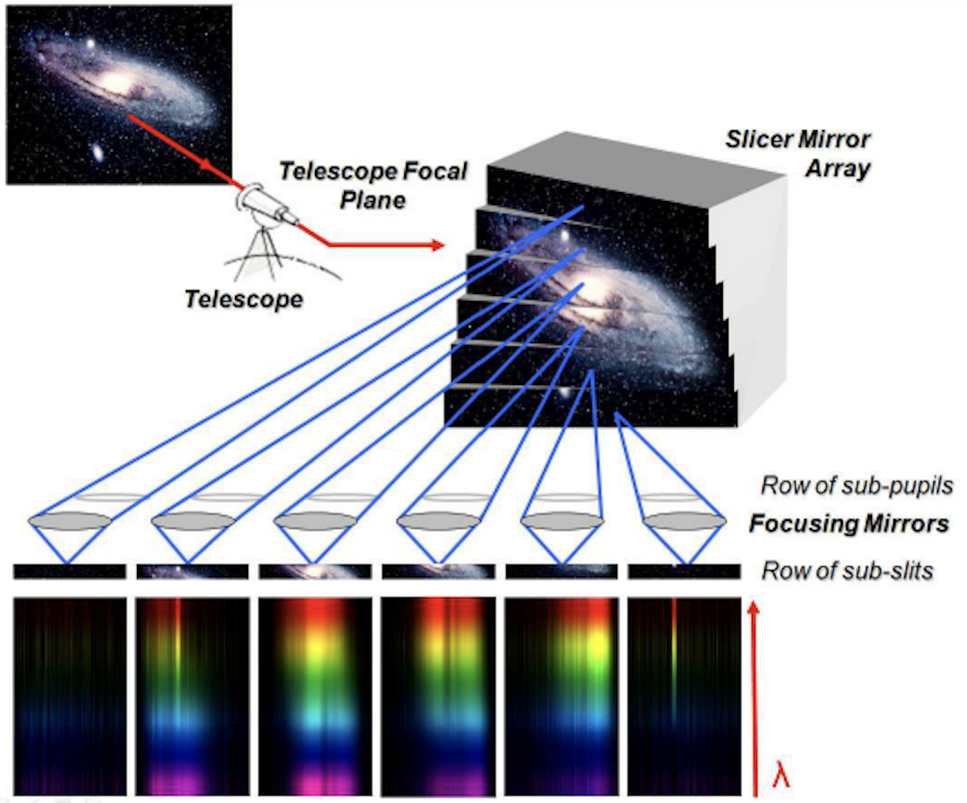


Figure 1.3: A diagram outlining the principle of an image slicer based IFS. Credit: Vivès & Prieto, 2006.

HARMONI will provide spectra over a continuous field measuring 206×152 spaxels in size, with four different spaxel scales. The field of view will range from $0.82" \times 0.61"$ to $9.1" \times 6.2"$, consisting of ~31300 spaxels. Eleven different grating settings are provided in all spatial scales and cover different parts of the wavelength range of $0.47 - 2.45$ micrometres at three different spectral resolving powers (Clarke et al., 2017). Ten of these gratings are available in the infrared and mounted on a rotating wheel to allow for their selection depending on the observational requirements. The HARMONI system parameters are shown in Table 1.1.

Wavelength range	0.47 - 2.45μm
Spatial scales (FoV)	4 mas (0.82" × 0.61"), 10 mas (2.06" × 1.52")
	20 mas (4.12" × 3.04"), 30 × 60 mas (6.2" × 9.12")
Resolving Power	3000 (*V+R*, *H+K, I+z+J*)
	7000 *(K, H, J, I+z)*
	18000 (Half of each NIR band)
Temperature	130K cryostat
	40K NIR detectors, 130K VIS detectors
Detectors	Teledyne HgCdTe 4k × 4k for NIR, ×8
	4k × 4k CCD for VIS, ×4

Table 1.1: The HARMONI system parameters.

The gratings used are volume phase holographic gratings (VPHG). As opposed to regular transmission gratings which diffract light through a periodic structure, VPHGs diffract light through periodic fringes with varying refractive indices within the grating. To maximise efficiency by causing constructive interference between the input and output light, VPHGs must satisfy the Bragg condition whereby the diffraction angle and incidence angle for the central wavelength are equal relative to the angle of the fringes. The classical grating equation is shown in equation 1.1, with Bragg's law for VPHGs (with unslanted fringes relative to normal of the grating surface) shown in equation 1.2:

$$a[sin(\theta_m) - sin(\theta_i)] = m\lambda \tag{1.1}$$

$$2sin(\theta_i)a = m\lambda \tag{1.2}$$

where a is the spacing between the grooves, θ_i is the input angle (relative to normal) of light with wavelength λ, and θ_m is the output angle of the dispersed light of order m.

Therefore, given a fixed resolving power and central wavelength λ, the Bragg condition defines the angles of incidence and diffraction (θ_i and θ_m), as well as the groove spacing a. As such, three different resolving powers corresponds to three different angles of incidence, with each of the 10 gratings having a different central wavelength λ and groove spacing a to satisfy the Bragg condition.

The telescope focus is first relayed to the IFS by the focal plane relay sub-system (FPRS), and is then fed through the IFS, consisting of a pre-optics sub-system, integral field unit (IFU) sub-system, and four spectrograph sub-systems. A block diagram of HARMONI can be seen in Figure 1.4 (Clarke et al., 2019).

HARMONI's pre-optics, IFU, and spectrograph sub-systems will be housed in a large cryostat with a 3-tonne cold mass, cooled using a cryocooler to an operating temperature of 130 Kelvin to reduce thermal noise on the detector (as HARMONI is an infrared instrument, background thermal radiation would add significant noise). The pre-optics sub-system reformats and conditions the relayed telescope focus for input to the IFU sub-system by setting the spaxel scale and allowing for use of filters, focal plane and cold pupil masks (to limit the size of the field and the angles from which the rays come, respectively), and a shutter (which allows for shorter exposures than the minimum read time of the detectors) (Cagigas et al., 2018). The alignment of the instrument and telescope pupil can also be checked (misalignment would cause loss of light and excess background noise). The integral field unit splits the field into four quadrants and then uses four separate pairs of image slicers to create four 540mm pseudo long-slits (Kosmalski et al., 2016). The light from each pseudo long-slit is then dispersed by one of four identical spectrographs mounted vertically within the cryostat.

Each spectrograph sub-system consists of a Collimator Module with a 1500mm focal length that collimates the beam from the slit, a Fold Mirror Module (FMM) with two moving mirrors to preserve optical path length (Fold Mirror 1 and Fold Mirror 2, each with three positions corresponding to different angles of incidence to satisfy the Bragg condition and maximise efficiency for the low, medium, and high resolution gratings, as described in equations 1.1 and 1.2 and shown in Figure 1.5) (Rodrigues et al., 2019) to fold the collimated beam onto the grating (located at the pupil to ensure the gratings can be as small as possible and the same region of the grating is illuminated for all points along the slit), an Infrared Grating Module (IGM) for grating selection, an Infrared Camera Module to focus the dispersed beam, and an Infrared Science Detector Module. The spectrographs also have a Visible Grating Module, Visible Camera Module, and Visible Science Detector Module. The complete optical layout of the spectrograph can be seen in Figure 1.6 (Rodrigues et al., 2019). The University of Oxford is responsible for the design, prototyping, assembly, integration, and testing for the entire spectrograph sub-system.

2.1 HARMONI Spectrograph Operational Concept

Assuming normal observational operation, the full HARMONI system lifetime is 15,000 movements (10 movements per night of observations, with 150 observing nights per year, over a 10 year lifetime) (Clarke et al., 2020). Each of the 10 observational setups per night will have a corresponding calibration setup in the morning in the same operational configuration, leading to 20 total movements over 24hrs during normal operation. However, at system-level, the HARMONI system lifetime requirement is still defined as 15,000 movements (Clarke et al., 2020).

Ahead of operating the instrument during initial night-time observations, HARMONI must first be configured and calibrated, with all templates and operational configurations being tested rapidly. This will involve constantly changing the configuration of the spectrograph and measuring the performance with which the moving mechanisms operate, effectively replicating a whole night of observations (equivalent to 20 movements) in 2 hours (Clarke et al., 2020), resulting in operation of the mechanisms a maximum of once per 6 minutes. This frequency of movements will be conducted over a 10 hour period. As such, this is the minimum frequency requirement and duration over which the mechanisms must be able to continuously operate without losses in performance. As discussed in Chapter 2, constant operation of the mechanisms adds large thermal fluctuations in the cryostat, which has a noticeable negative impact on the performance of the mechanisms.

The system-level HARMONI system requirement (R-INS-920) states that the full spectrograph must be able to fully change configurations and be ready to start science integration within 3 minutes. Of this overall budget, 2 minutes are allocated to the spectrograph sub-system's moving mechanisms (FMM and IGM), and 1 minute to both the initialisation and acquisition of the wavefront sensors (Clarke et al., 2020). The 2 minute budget allocated to the movements of the mechanisms assumes they operate in parallel (rather than sequentially), and is a constant budget regardless of which AO system is being used. As described later in this thesis (see for example Chapter 3, Section 2.3.2), each of the mechanical mechanisms also has a minimum 'settle time' that is required following each movement for the mechanism to mechanically stabilize, which is required ahead of each observation. As such, the 2 minute budget can be further broken down into a 'movement time' budget, and a 'settle time' budget.

This budget is slightly altered in practice for each mechanism, as each has a different movement time and settling time, but is typically 90 seconds for movement and 30 seconds for settling. A broader description of the operational concept can be found in the HARMONI Operational Concept document (HRM-00114, Clarke et al. 2020).

3. The Challenge of Daytime Calibration

To maximize the time on-sky each night, calibration frames (wavelength and flats) will be taken the following morning. Each set of calibration frames must be taken in the same exact operational configuration as was used for the corresponding observations. If HARMONI returns to a slightly different observational setup when taking calibration frames, spectra on the detector will be shifted relative to the observations, and the calibration frames will be inaccurate. Changes about the spectral axis of the detector will cause errors in wavelength calibration, and shifts about the spatial axis (and spectral axis) will cause errors in the flat calibration. The flat calibration frames are used to determine the response of each detector pixel to a uniform light source, so shifts of the beam about the detector in either axis will impact the accuracy of the flat field calibration frames. Having decreased repeatability in both the wavelength and flat field calibrations will have a significant negative impact on the quality of the science that can be done with the data, as both the measured spatial and spectral values will be inaccurate.

As such, high repeatability of the beam about each axis of the grating is needed when returning to an observational configuration in the morning for calibration. High stability of the beam is also needed about each axis of the grating during observations, as any shifts in the spectral and spatial directions will cause direct errors in the raw data that cannot be calibrated out (as the spectral and spatial position of the dispersed beam on the detector will move over the course of an exposure, effectively broadening the instrumental line spread function and reducing the spectral resolving power), having a significant negative impact on image quality and spectral resolution. A high stability requirement is also driven by the need to take sky frames immediately following object frames, as subtraction of bright NIR skylines will leave large residuals if the wavelengths of the sky frame and object frame do not align properly.

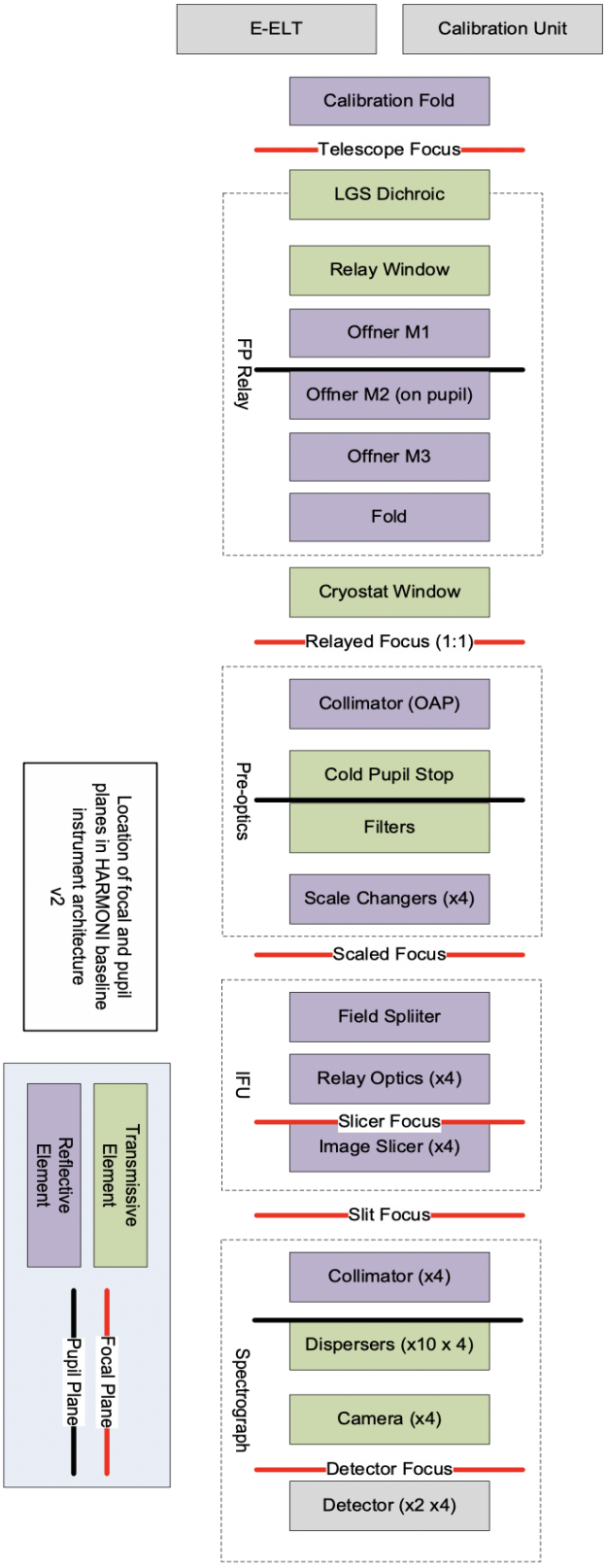
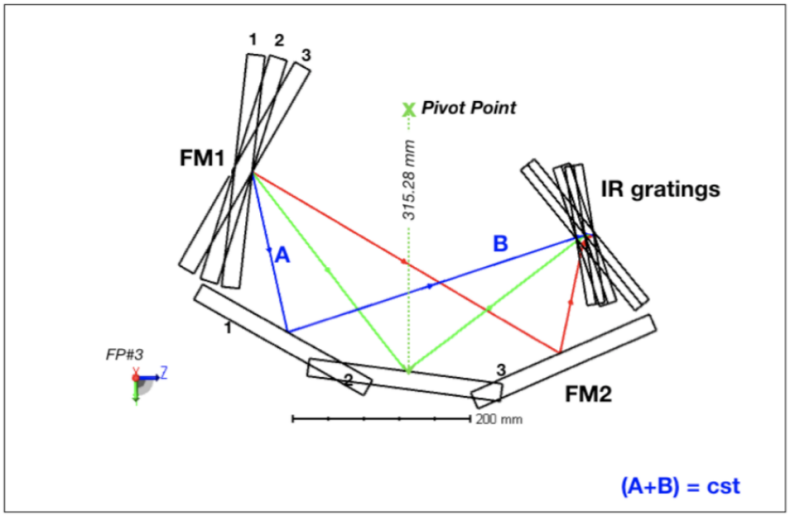


Figure 1.4: A block diagram of HARMONI.



Configuration	FM1		FM2
	Position	*Angle*	*Position*
IR Low Resolution	3	29.77	1
IR Med Resolution	2	17.19	2
IR High Resolution	1	6.26	3

Figure 1.5: A diagram of the three different optical paths that ensure the beam enters the grating at the appropriate angle of incidence. There are three separate angles of incidence corresponding to the low, medium, and high resolution gratings. Credit: Rodrigues et al., 2019.

Repeatability is the degree of precision to which a movement can be made relative to a previous movement. Repeatability is not the same as accuracy - accuracy is the degree of precision to which a movement can be made. The requirements on accuracy for HARMONI are far less tight than on repeatability, as the accuracy only needs to be good enough to ensure the beam is in an appropriate position on the grating (defined at system level as $\pm$1.0mm). As such, assuming a constant optical path length of 530mm between the Fold Mirror 1 and the grating, the total tolerance on accuracy can be calculated using the small angle approximation as ~6.5 arcminutes (accounting for back-reflection of the mirrors will double this tolerance). As such, the accuracy tolerances are significantly larger and trivial when compared to the repeatability tolerances. A more detailed analysis of the accuracy tolerances has been completed by John Capone. The concept of accuracy vs repeatability is outlined in Figure 1.7 (Credit: Parker Hannafin).

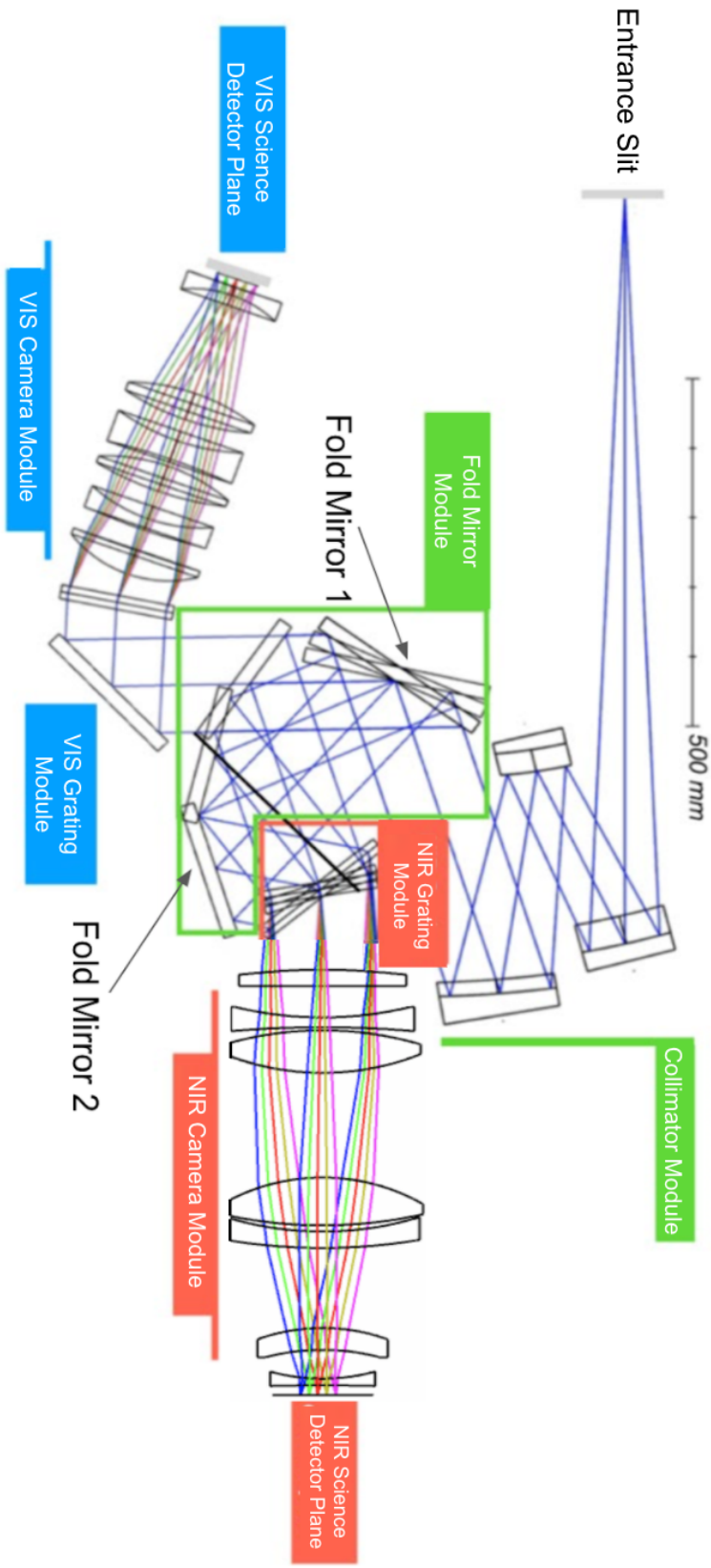


Figure 1.6: The optical layout of the HARMONI spectrograph. Credit: Rodrigues et al., 2019.



Figure 1.7: An image demonstrating the difference between accuracy and repeatability. Credit: Parker Hannafin.

Repeatability (and stability) is defined at system level as the root-mean-square (RMS) error of the movements relative to the mean of the distribution. Assuming the movement errors (such as low-level random vibrations, random inaccuracies in the step size of the stepper motors used to drive the mechanisms, and variations due to play in the mechanisms) are Gaussian, this translates to one standard deviation (1σ), meaning 68% of the movements have to be within the repeatability tolerance. The 32% of movements that are not within tolerance can be remedied by using skylines to improve the wavelength calibration (this 32% applies to the repeatability of all sources of movement, including the moving mechanisms, slit drift, and lens flexures). This will significantly bring down the fraction of calibrations dependent purely on the positioning of the beam on the grating, likely to ~5% (this being the percentage of observations with poor repeatability that also are too short to have skylines, or are in the 4mas scale where the sky is faint because the solid angle of each pixel is very small). The average error of the repeatability (measured by comparing the level of correction applied to the wavelength solution from the skylines, when used) could then be used as an uncertainty level on the exposures that do not have sky lines. For these few remaining observations where the calibration must be known to be highly accurate, calibration frames could be taken at night (this is normally not done to maximize on-sky time at night). Repeatability could also have been calculated as peak to valley, which would be a factor of ~2 tighter assuming a Gaussian distribution of errors, but was not used as the system level definition was RMS.

The system-level HARMONI wavelength calibration accuracy requirement (R-HRM-148) states that 'The reconstructed data cube shall be calibrated to ≤ 0.1 RMS of a spectral resolution element when using standard calibrations obtained the following morning.' A

spectral resolution element is equivalent to 2 pixels on the detector (to ensure Nyquist sampling), and as such this wavelength calibration accuracy requirement can be translated to a ≤ 0.2 pixel requirement over 24 hours. This is interpreted as 0.2 pixels RMS at system level (Clarke et al., 2020). Furthermore, the stability of the beam on the detector must be better than 0.075 pixels RMS on timescales of 1 hour (Clarke et al., 2020).

This top-level wavelength calibration accuracy budget is split up into two main components: error due to the goodness of fit of the wavelength solution applied when calibrating, and error due to the inherent repeatability of the beam on the detector when switching back to the observational configurations during calibration the following morning.

The calibration error is estimated based on the contribution of three main components: the interpolation error of the polynomial fit, the measurement error on the detector, and the error in the knowledge of the actual arc line wavelengths (Clarke et al., 2020). Based on experience with other instruments such as the Multi Unit Spectroscopic Explorer (MUSE) (Bacon et al., 2010), a total calibration error of ~0.026 pixels is achievable in HARMONI's lower resolution settings, but higher resolution errors may be larger due to a higher arc line density. As such, the total calibration error budget is doubled and set conservatively at 0.05 pixels RMS.

The remainder of the error budget is allocated to the repeatability of the beam on the detector as impacted by the mechanical mechanisms in the spectrograph (the FMM and IGM), which is the focus of this thesis. The repeatability requirement is therefore set at 0.15 pixels RMS.

A further possible source of error is due to temperature fluctuations internal to the HARMONI cryostat, as well as those from the simultaneous operation of all the mechanisms. As discussed in Chapter 2, temperature fluctuations directly impact the repeatability and stability of the mechanisms, and so this error is effectively included in the repeatability and stability budgets of 0.15 and 0.075 pixels RMS, respectively. However, as discussed in Chapter 2, this likely won't have a significant effect as the mechanisms are separated within the cryostat, and the operation of each mechanism individually currently adds minimal heat load in the cryostat. Furthermore, the HARMONI cryostat itself provides a temperature stabilized environment.

However, there are other potential sources of error, such as drift of the spectrograph relative to the IFU slit, or movement of the lens flexures. The drift of the spectrograph relative to the IFU slit will likely be minimal as the entire cryostat will be temperature controlled (Clarke et

al., 2020), but this will still need to be verified when commissioning the instrument. A similar argument can be made for the lens flexures, and these are currently being developed and tested by other members of the HARMONI consortium and are unlikely to add any significant errors (Clarke et al., 2020). These two sources are allocated 0.01 pixels RMS in the overall error budget (the total overall budget at system level is still treated as 0.2 pixels RMS, despite the sum of these three individual budgets being 0.21 pixels RMS).

Another source of error could come from vibrations induced by the cryocooler used on the HARMONI cryostat. However, as the vibrations are on significantly faster timescales than the exposure times, they will not affect repeatability, but only stability (they effectively 'blur' the image during an exposure) (Clarke et al., 2020). There is a small budget for vibrations in the overall stability tolerance of 0.075 pixels RMS, and a model is currently being developed by the HARMONI consortium to determine how vibrations will translate into image motion. However, as discussed in Chapter 2, Section 3.2, stability tests were conducted in a cryostat cooled with a cryocooler, and no significant impact was measured on stability. A table showing the wavelength calibration budgets can be seen in Table 1.2.

Contribution	**Allocation (pixels RMS)**
Calibration Error	≤0.05
Repeatability Error (incl. temperature)	≤0.15
Slit Drift / Lens Flexures	≤0.01
Stability Error (incl. vibrations)	≤0.075

Table 1.2: Wavelength calibration error and stability error budgets.

Spectra must be repeatable to within 0.15 pixels RMS on the detector (in both the spectral and spatial axes) over 20 movements **(**Clarke et al., 2020). The spectra must be stable to better than 0.075 pixels RMS on timescales of 1 hour. Each pixel is 15 micrometres in size, leading to a required repeatability of within 2.25 micrometres RMS (over 20 movements), and stability of within 1.13 micrometres RMS (over one hour). The total repeatability can be calculated to first order using equation 1.3 below:

$$\theta_i = \frac{d}{f} \times \frac{180}{\pi} \times 3600 \quad (1.3)$$

where θ_i is the total angular shift of the beam about the grating in arcseconds that will cause shift on the detector d (2.25 micrometres RMS) and f is the focal length of the camera (350mm). Accounting for back-reflection from the mirrors will double these tolerances.

However, these values are the total repeatability and stability tolerances for the spectra on the detector. The three mechanical modules (FM1, FM2, and the IGM) will all contribute to this about multiple axes, and the individual repeatability and stability tolerances per module will be more strict. Repeatability tolerances about the axes of rotation of the individual mechanical modules are as tight as 1 arcsecond RMS due in part to the large system architecture and long optical path lengths which magnify angular errors. The total arcsecond repeatability budget and arcsecond stability budget are the only ones that matter, however. Therefore, if certain mechanisms provide better repeatabilities and stabilities, other mechanisms can provide worse repeatabilities and stabilities.

All three mechanisms will contribute to error about the spectral axis of the detector. The FM1 and FM2 shift the beam about this axis due to their normal operational motion (see Chapter 4, Section 1). The co-axial ‘wobble’ of the IGM will also shift the beam about the spectral axis (see Chapter 5, Section 2.1). To calculate the tolerances first order, the total arcsecond tolerance is evenly divided linearly among these three mechanisms to allow for tolerances for shifts of the beam about the spectral axis for each mechanism. However, in reality, as the FM1 articulates about its own axis, its repeatability tolerances are the most stringent. FM2 traces out an ellipse about a focal point a distance of 315mm from its mirror, and so has mechanical tolerances that are far less tight (on the order of multiple arcseconds).

On the other hand, the FM1 and FM2 are fixed about the spatial axis of the detector, and so it is assumed they will add negligible amounts to the repeatability of the beam in that axis. This is confirmed for the FM1 in Chapter 4, Section 2.5. As only the IGM shifts the beam about the spatial direction, the IGM initially gets most of the error budget when calculating the tolerances about the spatial axis of the detector to first order. In reality, due to the behavior of the grating and the dispersed beam, the repeatability required for the IGM about the spatial axis of the detector is not as stringent (on the order of 5 arcseconds) (HRM-00418).

Similar estimations can be made for the stability tolerances, with the FM1, FM2, and IGM splitting the total arcsecond stability tolerance budgets about both axes as described above. A summary table of the first order repeatability estimates can be found in Table 1.3.

Mechanism	**Spectral Axis Repeatability / Stability Tolerances (arcseconds RMS)**	**Spatial Axis Repeatability / Stability Tolerances (arcseconds RMS)**
FM1	1.0 / 0.5	0.5 / 0.25
FM2	1.0 / 0.5	0.5 / 0.25
IGM	1.0 / 0.5	2.0 / 1.0

Table 1.3: A table summarizing the first order estimates for the repeatability and stability tolerances.

The calculations of the true repeatability and stability tolerances of the individual mechanisms were carried out in Zemax by John Capone, and are outside the scope of this thesis, but are very similar to the values shown in Table 1.3. The true stability tolerances can be found in Table 2.1. The true repeatability tolerances for the FM1 can be found in Table 4.1, and the true repeatability tolerances for the IGM can be found in Table 5.1. As these are very tight tolerances, especially in the spectral direction, it is possible the tolerances will be made looser at system level in the future to allow for larger mechanical errors in movements.

It is therefore necessary to test each mechanical module individually to determine its repeatability and stability. It is noted that to determine the actual repeatability of the HARMONI mechanisms - and the repeatability of the position of the beam on the detector, which is ultimately all that matters - the full instrument will need to be tested with all mechanisms operating simultaneously. As of the writing of this thesis that is not yet possible, as the optics have not been built and there is no final design for FM2. However, once these are available, a full-scale engineering model of the spectrograph will be built and tested in its proper orientation inside a large cryostat. This will allow for the true repeatability of the beam on the detector to be measured, along with the true impact of temperature from all mechanisms operating simultaneously.

Tests must be carried out over the full HARMONI system lifetime of 15,000 movements (10 movements per night, 150 nights per year, 10 year lifetime), both in warm for initial verification, and then at the HARMONI cryostat temperature of 130K. The tolerances need to be met over groups of 20 movements at a time (10 observational setups per night, 10 corresponding calibration setups in the morning), or over 24hrs (whichever is worse) for the 15,000 movement lifetime. As described in Section 2.1 of this chapter, the tolerances also need to be met with the mechanisms operating at least once per 6 minutes, and with a total operational time of less than 2 minutes (including both 'movement time' and 'settling time').

A summary of the achieved warm repeatabilities for both the FM1 and IGM, and the resulting total shift of the beam on the detector about both the spectral and spatial axes, can be found in Chapter 5, Section 3.

4. Challenges of Prototyping and Building Four Spectrographs

There are two main challenges associated with prototyping and building the mechanical modules of the four HARMONI spectrographs: achieving sub-arcsecond repeatability, and measuring and testing sub-arcsecond repeatability.

Achieving sub-arcsecond repeatability

The biggest challenge of prototyping the HARMONI mechanical modules is achieving sub-arcsecond repeatability. State of the art instruments, such as KMOS (Sharples et al., 2013), HAWK-I (Pirard et al., 2004), and CRIRES (Kaufl et al., 2004), contain similar moving mechanisms that achieve repeatability of tens of arcseconds, rather than sub-arcsecond. Furthermore, the FMM and IGM are large and heavy (for example, the IGM weighs over 80kg and is 1.3 metres in diameter), making it more difficult to reach these levels of repeatability.

Achieving sub-arcsecond repeatability at cryogenic temperatures presents many further challenges. The most significant is due to different rates of contraction of materials with different coefficients of thermal contraction (CTE) as they are cooled. HARMONI is not manufactured from a single material, so each part of the instrument will contract at a different rate during cooldown. This presents many problems with maintaining repeatability of mechanisms at

temperature, as moving parts can become too tight to move or even cold weld together. As such, different materials (specifically designed for cryogenic use) may be needed for testing in the cold versus at room temperature, which may not provide as high levels of repeatability and wear at faster rates. Furthermore, a vacuum (of ~$5 \times 10^{-6} mbar$) is required in the cryostat to achieve and maintain the low temperature, therefore introducing the need for all objects within the chamber to outgas minimally and operate while completely clean of dust, lubricants, and grease. A lack of lubricant may prevent the mechanism from proper operation (especially when compounded with thermal contraction), and also increase the rate of wear on the moving parts, decreasing the repeatability over time.

Measuring and testing sub-arcsecond repeatability

Measuring sub-arcsecond repeatability presents another challenge. If this high level of repeatability cannot be measured, there will be no way to confirm that the mechanisms are operating within their tolerances.

However, many optical instruments exist which are able to measure movements of optical elements (that can be mounted on the mechanisms) with high precision, such as interferometers and autocollimators. The Oxford HARMONI team has access to both a precision interferometer and autocollimator which are able to measure sub-arcsecond repeatability.

Assuming the mechanisms are able to operate within their repeatability tolerances in cryogenic environments and sub-arcsecond movements are able to be measured, designing a formal test of repeatability is still a challenge. Laboratory space for testing is limited, as is experimental volume within cryostats. The tests need to optimize use of space, and modifications of the mechanisms specifically for testing need to be made (such as the manufacturing of mounting units for the entire modules).

5. Outline of Part I

Part I of this thesis will be structured as follows:

- Chapter 2 will discuss the impact of temperature on all three mechanisms, as well as all stability testing.

- Chapter 3 will discuss warm and initial cold testing and development of a detent-based mechanism for achieving high repeatability.

- Chapter 4 will discuss prototyping, warm testing, and initial cold testing of the Fold Mirror 1 mechanism.

- Chapter 5 will discuss prototyping and warm testing the moving mechanism of the Infrared Grating Module, as well as preparations for cold testing.

Chapter 2

Quantifying the Impact of Temperature, and Stability Testing

1. Quantifying the Impact of Temperature

The first objective of the prototyping tests was to determine and quantify the impact of fluctuations in temperature on the positions of the mechanisms. There were two sources of temperature changes - the background temperature in the laboratory or cryostat (depending on if the test was a warm or a cold test), and increases in temperature from the operation of the mechanism (such as from the stepper motors).

This chapter is dedicated to proving (using the data available) that long-term positional drifts in the mechanisms are due to temperature, and that they can be accounted for through the fitting of a linear polynomial. The majority of the repeatability testing was not conducted concurrently with either a reference mirror or thermometer or in a temperature stabilized environment, and it was not possible for the testing to be repeated.

1.1 Fluctuations in temperature

The detent test mechanism was the first prototype available for testing. To determine if there was a long term drift due to fluctuations in temperature (either radiative from background heat, or

from both radiative and conductive heat from operation of the mechanism), two mirrors were mounted on the mechanism. The first was located on the rotating part of the mechanism (the 'test' mirror), and the second was mounted on the lower, fixed part of the mechanism (the 'reference' mirror). The mounting of the two mirrors is discussed further in Chapter 3, Section 1.2.

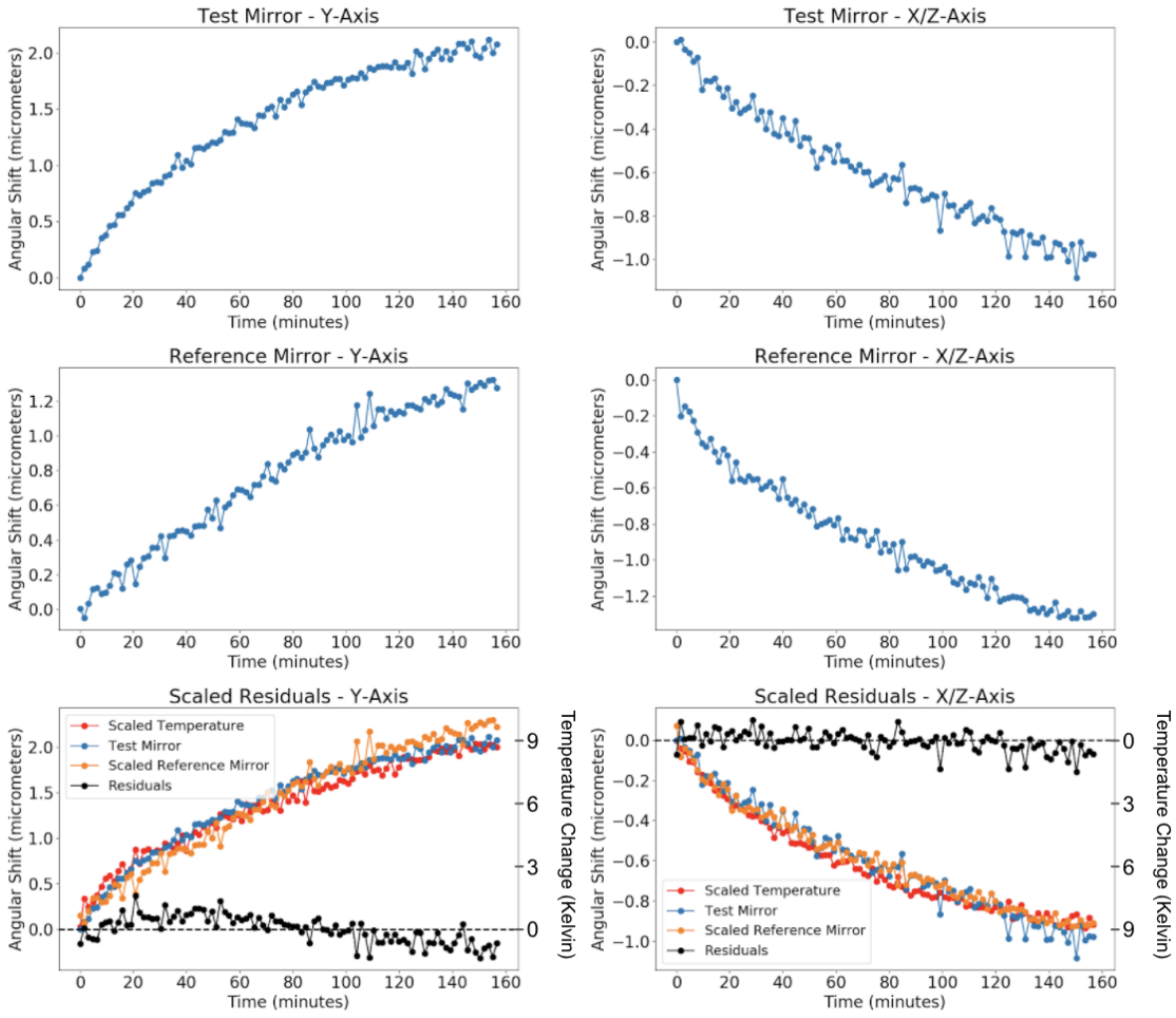


Figure 2.1: Plots of the angular shift vs time of the test mirror and reference mirror of the detent mechanism while the system was at rest (the motor was off). The two bottom plots show the residuals of the position of the test mirror and reference mirror, with the absolute position of the reference mirror scaled to match that of the test mirror and the temperature changes of the stepper motor at the time of each measurement (the thermometer was internal to the motor, see Figure 3.28).

As the test mirror was free to move and the reference mirror was fixed, the drift of the reference mirror could be subtracted from the test mirror, as its movements would be inherent to

the entire system, rather than just the moving part of the mechanism (which is what the repeatability would be need to be measured from). Furthermore, a thermometer internal to the stepper motor was used to measure the temperature concurrently with the positional measurements of the test and reference mirrors (see Figure 3.28).

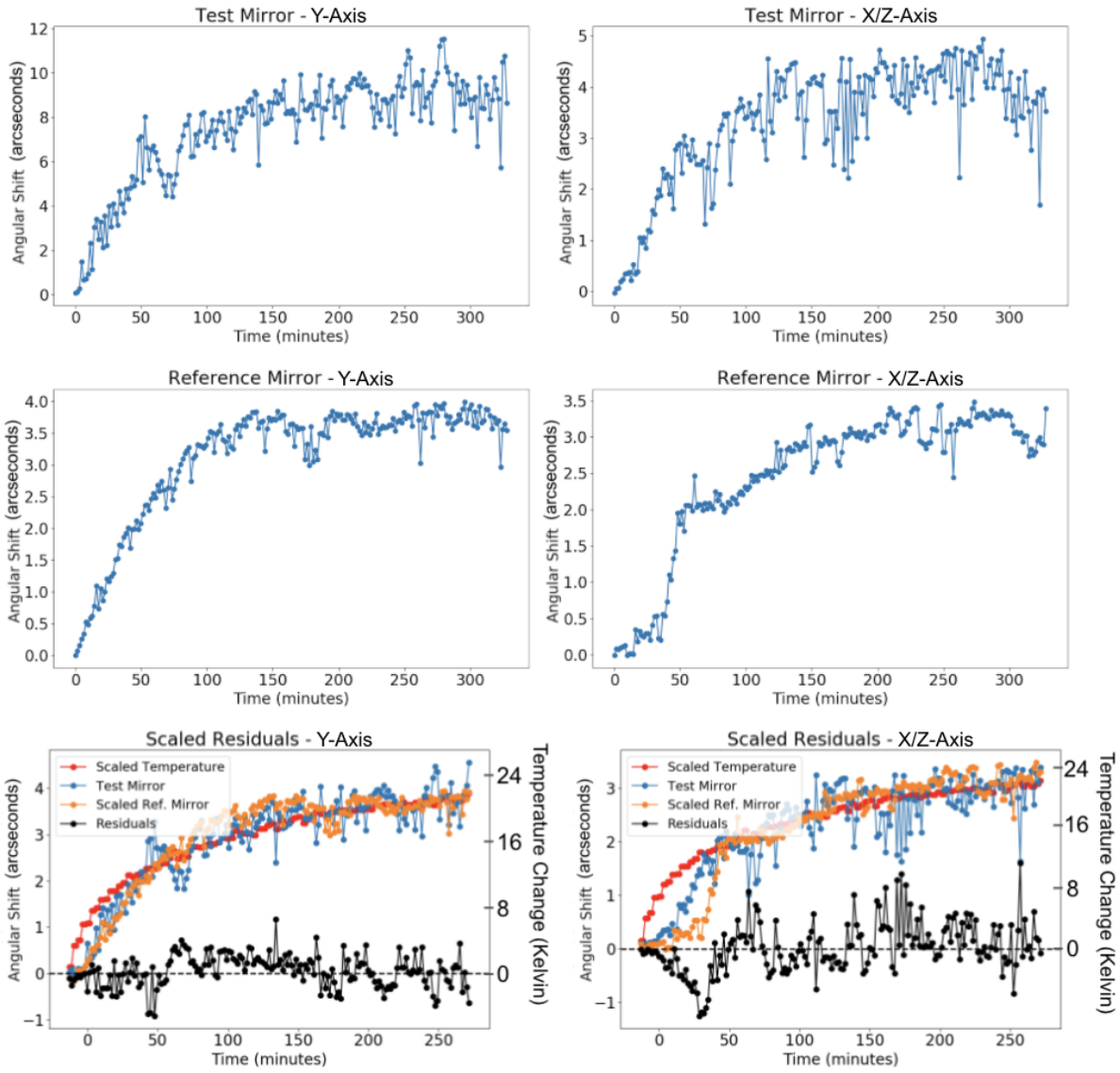


Figure 2.2: Plots of the angular shift vs time of the test mirror and reference mirror of the detent mechanism (an early test with three cantilever detents and solenoids, see Chapter 3 Section 1.1) from a repeatability test in a non-temperature stabilized warm environment. The two bottom plots show the residuals of the position of the test mirror and reference mirror, with the absolute position of the reference mirror scaled to match that of the test mirror and the temperature changes of the solenoids at the time of each measurement (the thermometer was placed on the solenoid, see Figure 3.28).

Measurements while the system was at rest in a non-temperature stabilized warm environment (and the stepper motor off) showed the drift of the reference mirror was highly correlated to the drift of the test mirror and the change in temperature (Figure 2.1), which implied the drift was not due to the detents or the test mechanism, but the entire system, and was likely due to the changes in the background temperature (which were high as the HVAC and temperature control system in the laboratory were not properly functioning). The absolute distance of the drift, however, was not always the same. This was due to the mounts and positions of both mirrors being different and at different radii.

To confirm that any observed drifts during a repeatability test in a non-temperature stabilized warm environment would also be due to temperature, the detent mechanism was tested with a reference mirror while operational. Solenoids were used (unlike with the test in Figure 2.1, as the detent mechanism was operational here), and a thermometer placed on one of the solenoids (see Figure 3.28).

The results are shown in Figure 2.2, and the drift between the test and reference mirrors and temperature is again highly correlated. However, as both the motors and solenoids were in operation, the temperature rose higher and more quickly than in Figure 2.1. The mechanism was running for about 25 seconds every 90 seconds, which caused the solenoids and the stepper motor to get hot (to about 40-45 degrees Celsius). This caused expansion in the components of the system, which can be seen in the asymptotic drift as the tests started. This rate of drift was high at first as the motor (and solenoids) heated up, but then lowered as the units reached their equilibrium temperature. This drift was separate to the drift due to the changing temperature of the laboratory (proven by the larger absolute value of the initial drift in arcseconds, when compared to Figure 2.1).

In both tests, some of the drift could have been due to the test setups moving over time with respect to the measuring equipment, but this is unlikely as similar drifts were also observed in tests where the instruments were mounted on the same optical table. Furthermore, there was no long-term drift during the cold testing where the instruments were mounted on different tables (inside and outside of the cryostat), as seen in Figure 2.10.

These two tests confirmed that temperature fluctuations could cause direct positional movements of the mechanisms. The profile was always asymptotic, and in the same direction. This same profile was seen during the operation of all three mechanisms. A representative plot

from the FM1 can be seen in Figure 2.3 (but also in the profile of Figure 2.2), where the mechanism was constantly moving. Once the temperature has stabilized, there is minimal drift.

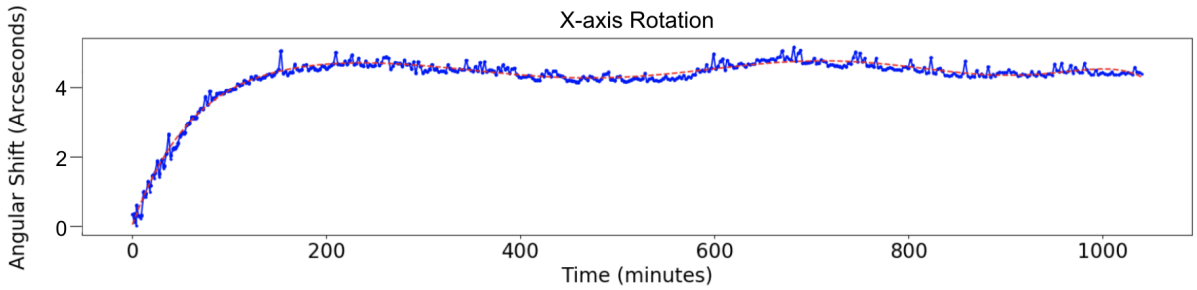


Figure 2.3: Angular rotation about the X-axis vs time for the FM1, demonstrating the impact of the motor getting hot during operation. The red dotted line is a 3rd order polynomial fit to the profile.

Furthermore, as seen in Figure 2.2, there is a noticeable 'lag' between the temperature and the position of the mechanism, as the mechanism shifts in position as it equilibrates in temperature with the background temperature. In this case, it is constantly behind the changes in background temperature, as these changes are too large and too fast, and the mechanism is never in equilibrium with the background temperature. However, when the background temperature changes at a slow enough rate, the 'lag' disappears as the mechanism temperature is effectively at constant equilibrium with the background temperature, as can be seen in Figure 2.3 after ~200 minutes (also see Figures 2.4-2.6). This defines a requirement for a maximum ΔT over a given timeframe that will not result in drift of the mechanism due to fluctuations in temperature (this was later determined to be a maximum ΔT of ~1K per hour - see Section 1.3 of this chapter, as well as Figure 2.9).

1.2 Reduction of heat from the operation of test equipment

All final repeatability tests discussed in the remainder of this thesis were conducted with 5 minutes in between movements (within the 6 minute tolerance, as discussed in Chapter 1, Section 2.1) and the motor turned completely off while not in use, allowing the motor (and solenoids in the case of the detent) to cool down (and not get initially hot enough to cause positional drifts in the mechanisms). This removed the asymptotic trend due to thermal

expansion, as well as the corresponding heat loads (which would impact temperature stability in the cryostat), leaving a drift only due to fluctuations in the background temperature (either of the lab or cryostat). The stepper motors were operated at 1A and 27V for less than one minute at ~100RPM. and the heat loads became minimal. This corresponded to the motors heating up internally <1K over the duty cycle, which added a negligible instantaneous heat load on the mechanism (<<0.1K), and did not impact the temperature stability (as can be seen in the warm testing in a temperature-stabilized environment in Figure 2.5, as there is no long term drift measured).

The solenoids were in use for ~3 seconds per movement and operated at 2A and 7.5V. They also heated up <1K over their duty cycle, introducing a further negligible instantaneous heat load in the cryostat (<<0.1K). (This duty cycle of the solenoids was only for later testing of the detent. Initially, the solenoids had much longer duty cycles and the heat was significant. This is discussed in Chapter 3, Section 2.3.2).

Even if all three main moving mechanisms in the HARMONI spectrograph (FM1, FM2, and IGM) are operated simultaneously (as they will in reality), assuming the Phytron motors are used with at least 5 minutes in between movements (the highest frequency of operation, i.e. during configuration or troubleshooting, is one movement per 6 minutes, as described in Chapter 1 Section 2.1), there will be no significant instantaneous heat load introduced in the HARMONI cryostat. This has been verified individually for the detent mechanism, FM1, and IGM (as there was no drift due to heat from their individual operation, assuming the tests were conducted 5 minutes apart, as described in Chapters 3-5). As the FM2 will likely use the same drive system as FM1, it will produce similar and negligible amounts of heat during operation. Furthermore, the HARMONI cryostat has a 3-tonne cold mass, and these small heat loads will not have a significant impact on a unit of this size.

The IGM has the longest theoretical mechanical operation time (at most 90 seconds), with the FM1 the shortest (at most 45 seconds), indicating that the maximum possible time all three systems could be operating together is 45 seconds. Given that the FM1 and IGM motors are nearly one metre apart, this will not introduce significant heat load to impact the positions of the neighboring mechanisms. However, as discussed in Chapter 1, all three mechanisms have not yet been tested simultaneously, and this has not been formally investigated. This simultaneous

testing of all moving mechanisms will be done with the engineering model, ahead of building and testing the four real HARMONI spectrographs.

There will also be further heat load introduced from other modules within HARMONI cryostat (such as the integral field unit), as all will operate in parallel to the spectrograph mechanisms. Thermal testing for these units is being carried out at other member institutions in the HARMONI consortium, but these mechanisms will generate a few 10s of Watts for less than one minute. This will add further minimal heat load on the 3-tonne cold mass, and they are also separated spatially from the spectrograph.

1.3 Required background temperature stability

The HARMONI requirement for absolute temperature stability is ±2K (HRM R4100-020). This was a system level tolerance, and was chosen based on the large size of the HARMONI cryostat and its assumed temperature stability and time constant being >24 hours, as well as a sufficient reduction of thermal background (with an implied maximum temperature of 132K). It is noted the HARMONI temperature requirement is absolute, and not defined over a specific timescale (Clarke et al., 2020).

However, as can be seen in Figure 2.1, there was noticeable drift on timescales of 1 hour even when the temperature was still within a ±2K range. This is because the temperature was changing at a significantly faster rate than shown in the stabilized environment of Figures 2.5 and 2.9, and the temperature of the mechanism was not able to reach equilibrium with the background temperature (thus the position of the mechanism was constantly changing). The positional drift of the mechanisms is far more sensitive to the rate of change of temperature than 'absolute' temperature, and this leads to an additional (and more important) requirement that the background temperature not move by more than ~1K per hour to be considered stabilized. ~1K per hour was the fastest measured rate of change that would allow the temperature of the mechanism to reach equilibrium synonymously with fluctuations in the background temperature, as seen in Figure 2.9, and therefore not have any noticeable changes in position. Faster rates of temperature change will cause greater positional shifts than lower rates of temperature change as

they will bring the system further out of thermal equilibrium, causing greater instantaneous and non-uniform thermal expansion in the system and greater positional drift.

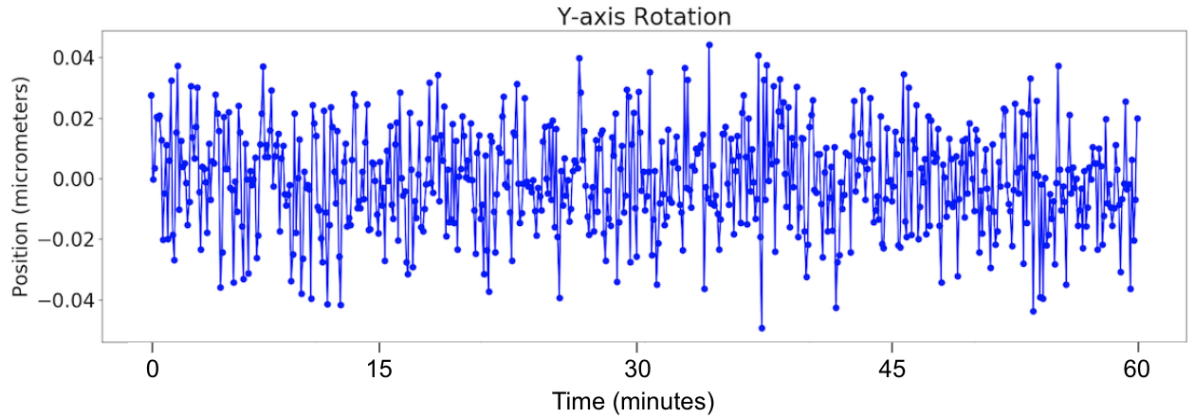


Figure 2.4: (Top) Angular rotation about the Y-axis vs time for the detent mechanism in the temperature-stabilized warm environment from Figure 2.5 while the system was at rest. Micrometers were 1:1 with arcseconds. Stability was ~0.02 micrometers. There is minimal long-term drift.

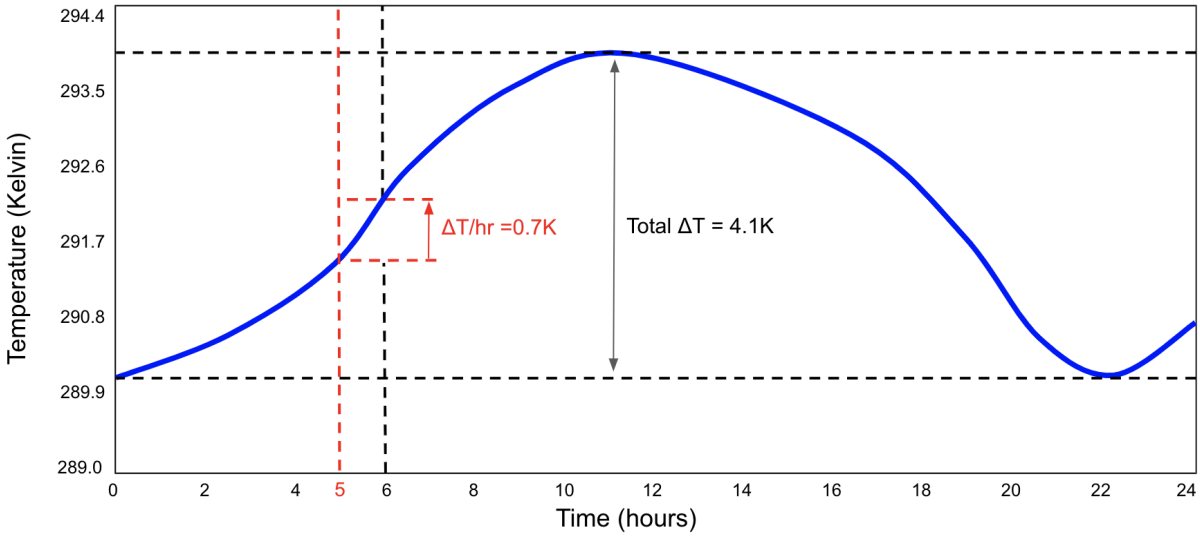


Figure 2.5: A plot of the stabilized temperature in the HRDLS (Dials et al., 1998) laboratory, which was stabilized to ±2K, with ΔT~ 0.7K per hour at most.

It is likely this requirement is less stringent than ~1K per hour in reality, but the exact relationship was not investigated further as a rate of change of ~1K per hour was achievable in the lab (and will be achievable in the HARMONI cryostat, as it has a time constant >24 hours)

(Clarke et al., 2020), and caused minimal positional drifts in the mechanisms (as seen in Figure 2.10). A 1 hour timescale was chosen as this was the time over which stability tolerances had to be met. However, further work should be done to determine what the maximum rate of temperature change can be before the mechanical performance doesn't meet tolerances, and this was not possible at the time of the writing of this thesis.

While there is currently no system-level HARMONI requirement for the rate of change of temperature in the cryostat, it is unlikely the background temperature in the HARMONI cryostat will have a faster rate of temperature change even while all three mechanisms are operating simultaneously (as operation of the individual mechanisms heated up the test cryostats <<0.1K, and separately the HARMONI cryostat has a time constant of >24 hours). As described above, it is also unlikely that other modules within the HARMONI cryostat will also add enough further heat load to cause the temperature to change at a rate greater than 1K per hour.

As such, for the rest of this thesis, a 'temperature stabilized' environment assumes a rate of change in temperature of <1K per hour within an absolute $\pm$2K range. Further testing within the HARMONI cryostat will need to be done to ensure good thermal coupling, which will ensure that the actual rates of change of temperature at each mechanism are as low as possible. It is, however, recommended that there be a HARMONI requirement for the maximum rate of change of temperature in the cryostat of <1K per hour within an absolute $\pm$2K range.

This <1K per hour and $\pm$2K absolute tolerance was confirmed when stability testing in a temperature stabilized environment, as negligible drift was measured in the raw position of the mechanism (in this case the detent mechanism) (Figure 2.4) on timescales of 1 hour. This means that any drifts on timescales of 1 hour seen during tests in temperature stabilized environments would be instrumental, and indicative of real positional changes. This was further confirmed when repeatability was tested in the same stabilized warm environment and negligible long-term drifts were observed. This held for all three mechanisms, as seen in Figure 2.6, helping to confirm that long-term positional drifts are due to temperature.

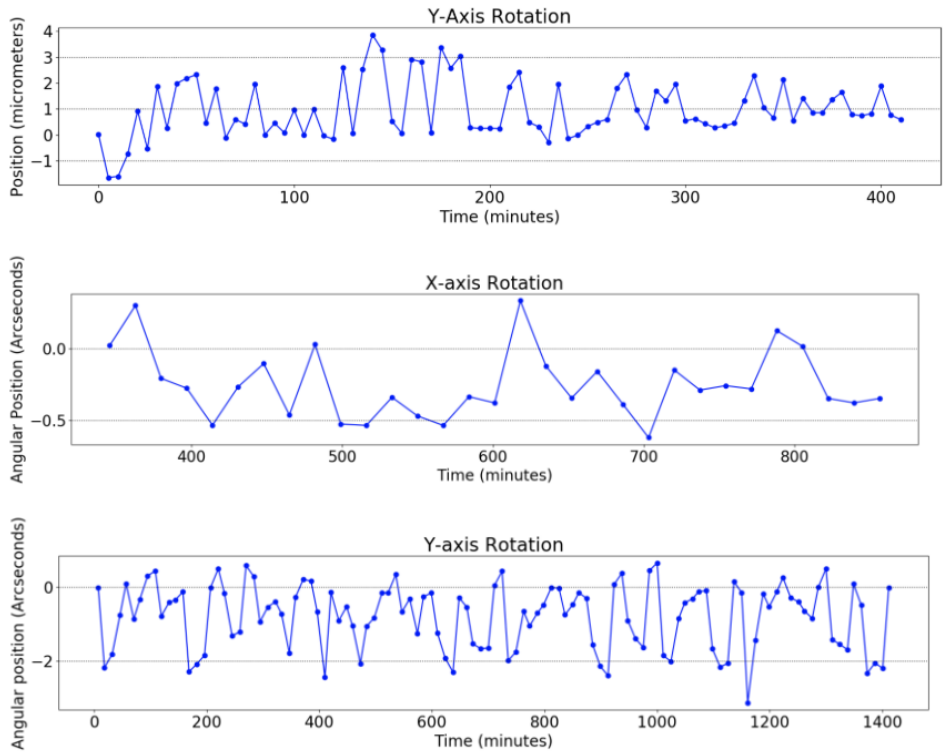


Figure 2.6: Plots of position vs time for warm repeatability tests of the detent test mechanism (top), FM1 (middle), and IGM (bottom) when the lab was temperature stabilized to ±2K (the same temperature-stabilized warm environment as Figure 2.5) and ΔT~ 0.7K per hour. Micrometers are 1:1 with arcseconds for the detent mechanism. There is minimal long-term drift.

2. Removing the Drift from Background Temperature

Ideally, during each test in a non-temperature stabilized environment, a thermometer would record the background temperature in the room, and a polynomial would be fit to that profile. That polynomial would then be scaled from temperature to arcseconds, and then fit directly to the profile of the position of the mechanism. The residuals of that forced fit would be used to calculate the true repeatability of the mechanism, ensuring that the fit was only removing effects due to temperature (i.e. as done in Figures 2.1 and 2.2). The reference mirror served a similar purpose in the some testing of the detents, but was not used for further testing as a reference mirror could not be used with the other larger mechanisms and the autocollimator (which could only fit one mirror simultaneously in its field of view, and the software did not allow for absolute measurement of two mirrors). It was also preventatively difficult to mount it in a stable position

on the lower disk of the detent mechanism, as the disk was not originally designed to accommodate a mirror (Chapter 3, Section 1.2). Ideally, however, a reference mirror (and additionally a thermometer) would have been used concurrently during all testing. Unfortunately, most of the repeatability testing was not conducted concurrently with either a reference mirror or thermometer or in a temperature stabilized environment, and it was not possible for the testing to be repeated.

As a workaround, following testing in a non-temperature stabilized environment, a linear polynomial was fit to the movement profiles and removed (effectively removing the drift due to temperature to first order), with the stability or repeatability calculated as the RMS of the residuals. Fits were only applied in non-temperature stabilized warm environments. A linear fit was chosen to ensure an extremely conservative calculation of repeatability, despite the drift due to temperature often being not linear (see Figures 2.1, 2.2, and 2.5). There was, however, no way to formalize fitting a higher order polynomial with no reference mirror or thermometer simultaneously in use.

The linear fit was applied to stability tests in non-temperature stabilized warm environments on timescales of at least one hour. For the repeatability tests in non-stabilized warm environments, the fit would be applied assuming the test was over at least one hour and the mechanism moved at least 20 times, or whichever came second (for example, if during a repeatability test the mechanism only moved twice over an hour, a fit could clearly not be applied to the two data points). An hour was chosen as the minimum time required for fitting because the stability requirement was on timescales of one hour, and there was always a measurable drift over this timescale (in non-stabilized warm environments) as seen in Figures 2.1 and 2.2. For fits applied to the repeatability tests, a minimum of 20 movements were also required because the repeatability tolerance was over this many movements.

Fits were not applied to repeatability tests conducted in a temperature stabilized warm environment, because, as shown in Figure 2.6, there was no long-term drift due to temperature observed in the stability of the mechanisms. If there was an observed drift in repeatability measurements, it would be inherent to the mechanism rather than changes in temperature, and could not be removed.

This implied that any long term drift even during repeatability tests in non-temperature stabilized warm environments would be due to temperature. However, if a long-term drift was

observed in repeatability tests in a non-stabilized warm environment, there would be no way to know if it was due to the mechanism or due to temperature (without a reference mirror or thermometer).

It is not certain if this is true for the FM1 and IGM as this type of data was not taken. However, given all of the above evidence, it is believed beyond a reasonable doubt that the same would hold for these two mechanisms as well, and linear fits could be applied to repeatability measurements in non-temperature stabilized warm environments. Furthermore, later warm testing of the FM1 and IGM was conducted in a temperature-stabilized environment, and fits were not needed anyway.

In a temperature-stabilized cold environment certain fits could still be applied. The cryostat would be temperature stabilized to $\pm$2K with fluctuations in temperature of <1K per hour, and as with HARMONI, instrumental drifts due to small temperature fluctuations within the cryostat would not be able to be removed. However, the testing equipment (autocollimator, optical table, and etc.) would still be in the warm and subject to separate temperature variations. Drift inherent to temperature fluctuations in the warm (that impacted only the measurement equipment) would still need to be removed. As such, for the cold testing of the FM1 and IGM, thermometry will be used to monitor the temperature of the cold mechanisms as well as the autocollimator (which is in the warm). The two profiles could then be compared with the movement of the mechanism, with the change due to only the warm temperature variations removed if it existed. Despite the temperature being stabilized in the laboratory, monitoring the temperature of the warm measurement equipment was still performed in case the laboratory's temperature control failed to perform normally.

For the stability and repeatability tests presented throughout the remainder of this thesis (in non-temperature stabilized environments), the output values and figures are shown assuming a linear fit with stability and repeatability calculated from the residuals of this fit. However, to ensure full transparency, the absolute stabilities and repeatabilities are also presented (i.e. with no fit) and are often still well within tolerance. Furthermore, stabilities and repeatabilities assuming a second order polynomial fit are also shown to demonstrate an upside case.

3. Stability Tests

To characterize the stability of each of the three test setups, measurements of each mechanism were taken (in non-temperature stabilized environments) while stationary to determine their stability on both short (<1 hour) and long (>24 hours) timescales. The stability requirements for each of the three mechanisms are listed below in Table 2.1, and were for timescales of 1 hour. As discussed in Chapter 3, the tolerances from the Fold Mirror 1 were used as the goal tolerances for the detents, as they were the most stringent amongst the moving mechanisms. X/Z-axis stability for the detent is equivalent to Y-axis stability for the FM1 due to their respective axes of rotation.

3.1 Warm

Figure 2.7 shows a standard example of a stability test for the detent mechanism with one cantilever detent in use (the type and number of detents are discussed in Chapter 3, Section 1.2) in a non-temperature stabilized warm environment. There was clear evidence of absolute drift of $\sim 0.4''$, which was due to temperature and removed with a linear polynomial fit, as discussed in Section 1.1 and Section 2 of this chapter. The RMS error of the residuals from the linear polynomial fit was $0.036''$(this is of the same order as those recorded in the temperature stabilized warm environment in Figure 2.4, providing further evidence that the fitting and removal of a linear polynomial is allowed). The residuals represent the upper limit on the stability of the system, and are indicative of the measurement error of the interferometer (which was used for all warm testing of the detent), as anything below this level could not be resolved. It is noted that the stability on timescales of 1 hour with no linear fit (i.e. absolute stability) was $0.13''$ in Figure 2.7, and $0.02''$ in Figure 2.8. This demonstrates that even with no correction for temperature changes, the stabilities are still well within tolerance. An upside case, assuming a second order polynomial fit to Figures 2.7 and 2.8, returns stabilities of $0.035''$ and $0.012''$, respectively.

This value was observed for both types of detents, and was irrespective of how many detents were used. As such, an upper limit of $0.036''$ is used for stability tests taken with the interferometer. Another source of error came from the residuals of the fitting of the plane (via a Monte Carlo) to the phase map produced by the interferogram to obtain the angular shifts of the mirror. These were 1/1000th of an arcsecond (assuming a constant variance in the

interferometer's pixel values, and assuming 10,000 Monte Carlo iterations). Given the target stability tolerances were at worst 0.25", these errors were too small to be meaningful and were disregarded.

Stability Tolerances (RMS)	*Spectral*	*Spatial*
Detent	0.5"	0.25"
FM1	0.5"	0.25"
IGM	0.5"	1.0"

Table 2.1: RMS (1σ) stability tolerances for the detent mechanism, FM1, and IGM about the axes of the detector. The stability tolerances were on timescales of up to 1 hour with no movement.

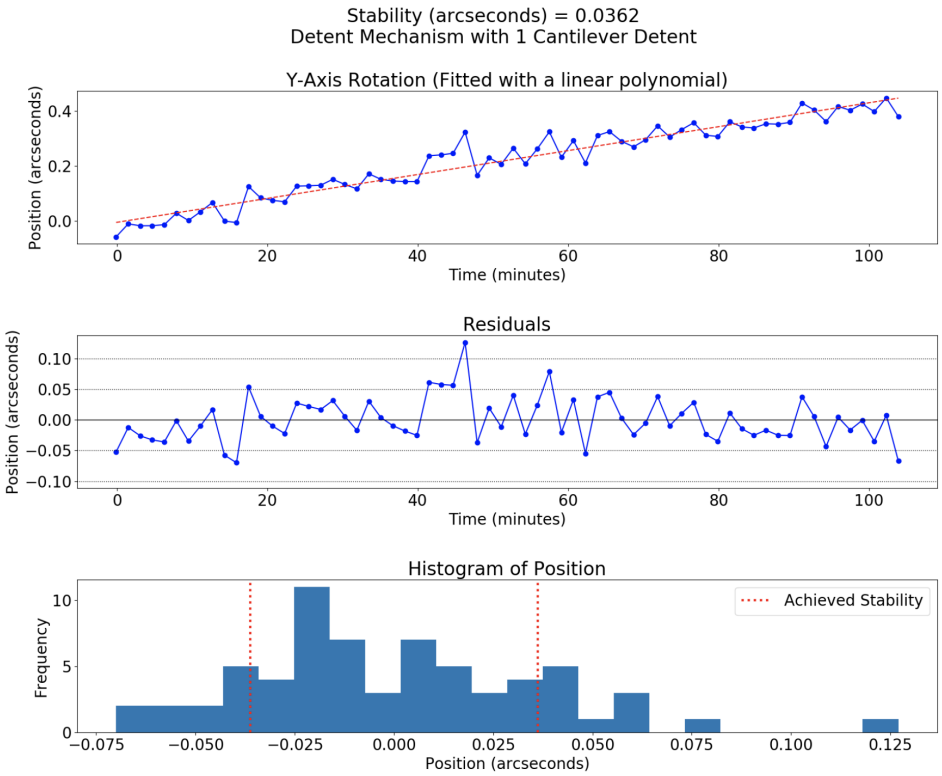


Figure 2.7: (Top) Angular rotation about the Y-axis vs time for the detent mechanism with one cantilever detent in a non-temperature stabilized warm environment, with a linear polynomial fit to the trend. (Middle) The residuals of the fit, plotted against time. (Bottom) A histogram of the residuals.

For all testing of the FM1 and IGM, as well as cold testing of the detent, an autocollimator was used instead of an interferometer. The measured stability was better than with the interferometer, at $0.013''$, and also represent an upper bound on the stability of these mechanisms. A plot of a standard exposure during a warm stability test for the FM1 with the autocollimator can be seen in Figure 2.8. The same values were also found during stability testing with the IGM, and about all axes for each mechanism. As such, an error of $0.013''$ is considered as an upper limit on stability with all further measurements taken with the autocollimator.

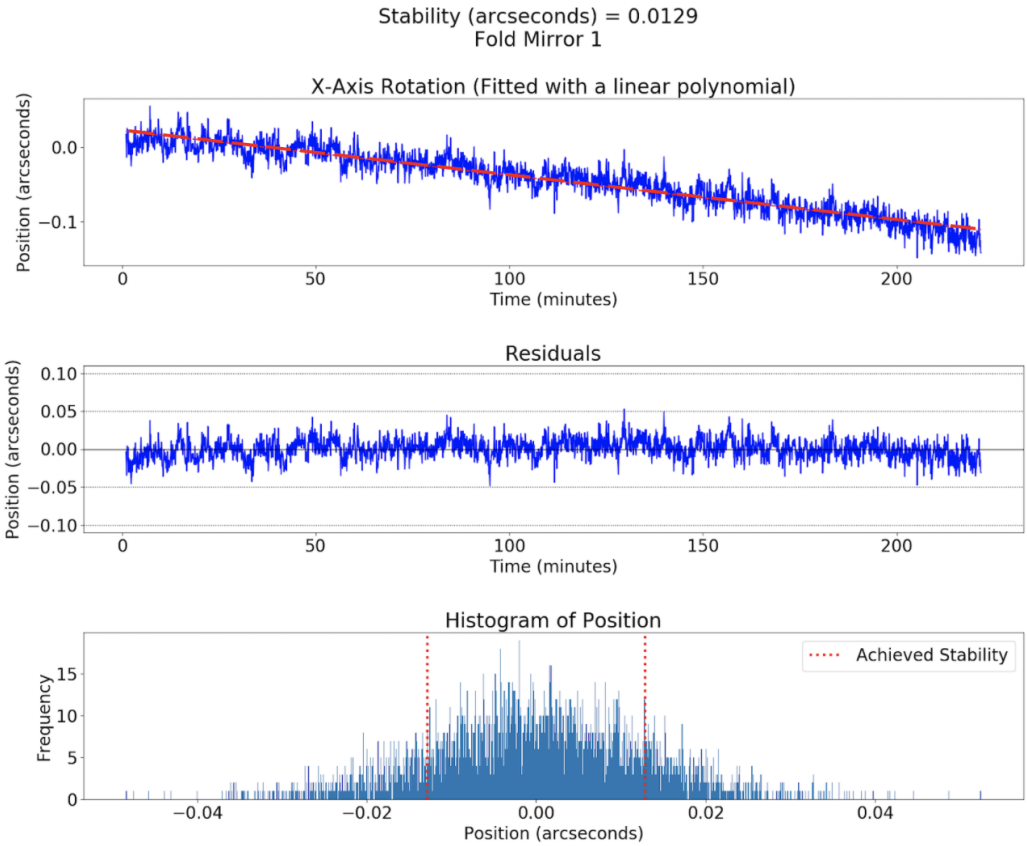


Figure 2.8: (Top) Angular rotation about the X-axis vs time for the FM1 in a non-temperature stabilized warm environment, with a linear polynomial fit to the trend. (Middle) The residuals of the fit, plotted against time. (Bottom) A histogram of the residuals. This data was taken with the autocollimator.

3.2 Cold

As can be seen in Figures 2.9 and 2.10 with the detent mechanism, stability in a temperature stabilized (±2K and fluctuations of <1K on timescales of 1 hour) cold environment was also well within tolerance. A plot of the temperature in the chamber can be seen in Figure 2.9. However, as shown in Figure 2.8, the error with the autocollimator was $0.013''$, whereas the measured stability in Figure 2.10 is worse, at $0.037''$, which indicates that the cold environment may have a negative impact on the stability of the detent mechanism (the warm stability was $0.036''$, but measurements were taken with the interferometer). This could possibly be due to added vibrations from the operation of the cryostat (this cold test was conducted in a chamber cooled using a cryocooler). It is noted, however, that even with the vibrations from the cryocooler, the stability is within tolerance, and so it is likely the HARMONI cryocooler will not add further significant vibrations to take these stabilities and repeatabilities out of tolerance. The cold stability of the FM1 was also well within tolerance, at $0.025''$. There was, again, no long-term drift observed.

4. Conclusions

This chapter first concludes that the long-term positional drift seen is due to temperature, and can be removed by fitting a linear polynomial, through the following evidence:

1) Direct relationship between the position of the test mirror, reference mirror, and motor temperature while mechanism at rest in a non-temperature stabilized warm environment (Figure 2.1)
2) Direct relationship between the position of the test mirror, reference mirror, and solenoid temperature while mechanism operational in a non-temperature stabilized warm environment (Figure 2.2)
3) Significant asymptotic positional drift of the mechanisms due to temperature from the constant operation (movements every ~25 seconds) of the motors and solenoids (Figures 2.2 and 2.3)
4) No long-term positional drift in a temperature stabilized warm environment (±2K and fluctuations of <1K on timescales of 1 hour) while the mechanisms were at rest or moving (Figures 2.4-2.6)

5) No long-term positional drift in a temperature stabilized cold environment (±2K and fluctuations of <1K on timescales of 1 hour) while the mechanisms were at rest (Figures 2.9 and 2.10)

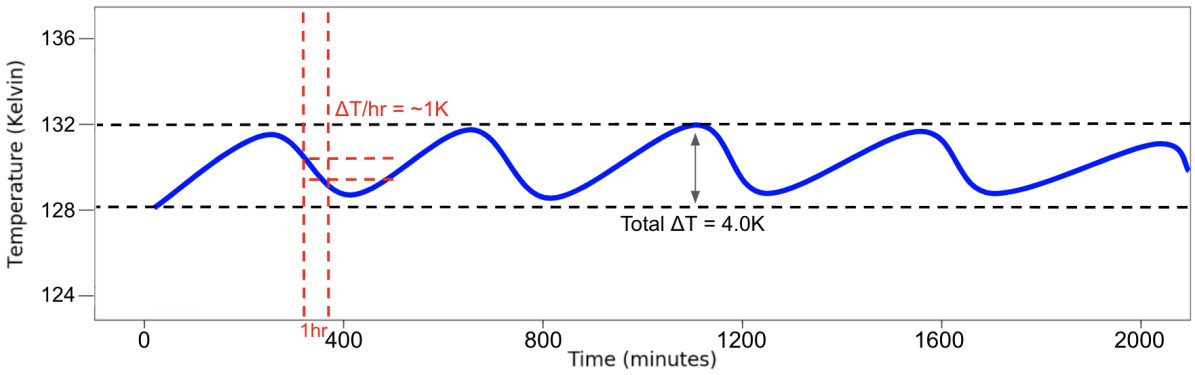


Figure 2.9: A plot of the stabilized temperature in the cryostat over time (the thermometer was mounted on the baseplate, see Figure 3.28), demonstrating how the temperature fluctuated at most ~1K per hour with absolute changes of ±2K.

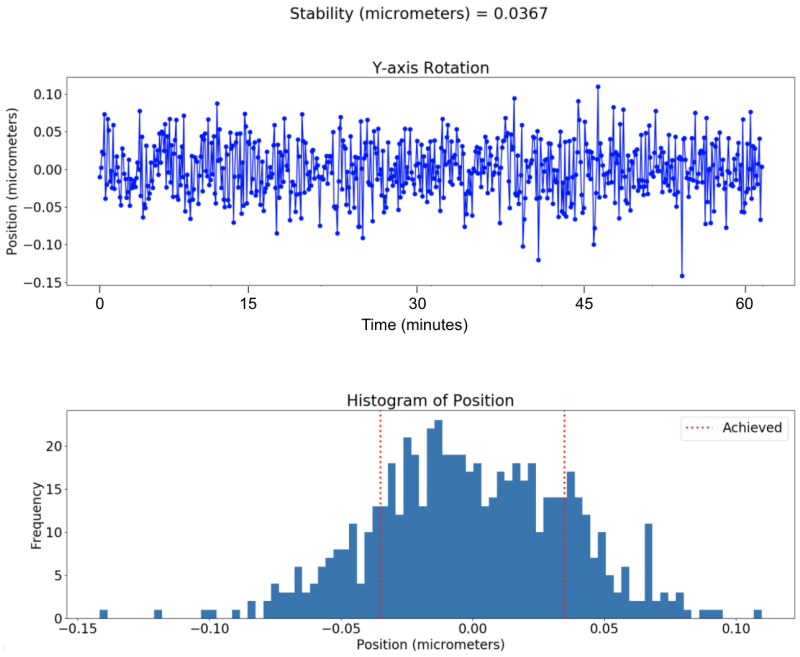


Figure 2.10: (Top) Angular rotation about the Y-axis vs time. (Bottom) A histogram of the measurements. This is a plot of the background stability in a temperature stabilized cold environment in a cryocooler-cooled cryostat (with corresponding vibrations) for the detent mechanism with one cantilever detent. Micrometers are 1:1 with arcseconds for the detent mechanism. There is minimal long-term drift.

Furthermore, in this chapter it is concluded that the stability for all three mechanisms was well within tolerance and trivial in both warm and cold environments, and about all axes. This also held for absolute stability in non-temperature stabilized warm environments, with stability still well within tolerance. It is also likely the actual stabilities are even better, as the observed stabilities are limited by the measuring equipment. The remainder of this part of the thesis will concern the repeatability testing of the detent mechanism, FM1, and IGM. The repeatability for each mechanism was calculated as the RMS (1σ) of the residuals from a linear polynomial fit (assuming at least a 1 hour-long test and at least 20 movements) to the data, as the long term positional drift is due to temperature. If the test was longer than 1 hour and had more than 20 movements, the repeatability was calculated as the average of all the individual 1 hour / 20 movement segments. For example, if the test was 2 hours long with 40 movements, the repeatability was calculated as the average of the repeatability of the two 1 hour / 20 movement segments. The main conclusions from this chapter are summarized in Table 2.2.

Removal of Drift Due to Temperature - Stability Testing	
1) Testing in a non-stabilized warm environment	
2) Linear fit to data, no higher order polynomials. Stability calculated as the RMS of the residuals from the fit	
3) Test duration of at least 1 hour	
Removal of Drift Due to Temperature - Repeatability Testing	
1) Testing in a non-stabilized warm environment	
2) Linear fit to data, no higher order polynomials. Repeatability calculated as the RMS of the residuals from the fit	
3) Test duration of at least 1 hour	
4) Test consisting of at least 20 movements	
Temperature Stabilized Environment Definition (in which removing any drift due to temperature is not allowed)	
± 2K (with changes of <1K per hour)	
Tightest Stability Tolerance (RMS)	**0.25"**
Warm Stability Upper Limit - Detent (Interferometer)	0.036"
Warm Stability Upper Limit - FM1/IGM (Autocollimator)	0.013"
Cold Stability Upper Limit - Detent (Autocollimator)	0.037"
Cold Stability Upper Limit - FM1 (Autocollimator)	0.025"

Table 2.2: A summary of the main conclusions from Chapter 2.

Chapter 3

A Detent Mechanism For Achieving High Repeatability

As some of the mechanical modules within the HARMONI spectrograph sub-system will have to operate with extremely tight repeatability tolerances, multiple methods of meeting the requirements were investigated. In all tests, repeatability was defined as the RMS error of the movements (1σ, assuming a Gaussian distribution). If one module were to fail to meet the requirements, the mechanism could incorporate another design that had already been tested. One method of achieving high repeatability involved locking the mechanism in place using a series of detents. A detent is a unit that kinematically locks within a fitted hemispherical socket, with an external return force ensuring the detent is properly seated within its position. While a detent is in place and with a high enough return force, the system is unable to move and its position is constrained based on the location of the detent, resulting in high levels of repeatability. The return force is the linear force applied to the detent while it is in its socket, and a higher return force was believed to provide a better and more secure seating of the detent within its socket, and therefore higher repeatability. However, the return force couldn't be too high otherwise the detent would not be able to be easily removed from its position (unless the return force could be 'released' prior to movement). The constraint is in only two axes when one detent is used, and is dependent upon bearing play. As such, to constrain a system about three axes multiple detents would be needed.

If successful, the detents designed could be used with any of the HARMONI mechanical modules. As such, the tolerances from the Fold Mirror 1 were used as the goal tolerances for the

detents, as they were the most stringent amongst the moving mechanisms. The true repeatabilities were calculated by John Capone, and are outside the scope of this thesis, but first order repeatability estimates are discussed in Chapter 1, Section 3. The testing of Fold Mirror 1 is discussed in Chapter 4.

The repeatability tolerances need to be met over groups of 20 movements at a time (10 observational setups per night, 10 corresponding calibration setups in the morning), or over 24 hours (whichever is worse), over a 15,000 movement lifetime. As described in Chapter 1, Section 2.1, the tolerances also need to be met with the mechanism operating at least once per 6 minutes, and with a total operational time of less than 2 minutes (including both 'movement time' and 'settling time'). All must be met at the cryogenic temperature of 130K$\pm$2K. The goal repeatabilities for the detent mechanism are shown in Table 3.1. It is noted that, as described in Section 2.1 of this chapter, arcseconds are 1:1 with micrometres for the detent mechanism, given its geometry.

	X	Y	Z
Repeatability (RMS)	0.5"	1.0"	N/A

Table 3.1: A table showing the RMS repeatability tolerances for the detents, at the position of the detent, with the axes defined in white in Figure 3.1. The tolerances from the Fold Mirror 1 were used as the goal tolerances for the detents, as they were the most stringent amongst the moving mechanisms. Further discussion of the calculation of the repeatabilities can be found in Chapter 1, Section 3.

The repeatability axes of the detents are defined in this chapter with reference to the axes of rotation of the mechanism (as will be done in with the FM1 and IGM in Chapters 4 and 5). Repeatability of the detents due to rotation of the mechanism about its X-axis is equivalent to tip at the position of the detent (up/down, and hereafter defined as repeatability about the X-axis), and repeatability of the detents due to rotation of the mechanism about its Y-axis is equivalent to a side-to-side tilt at the position of the detent (translation, and hereafter defined as repeatability about the Y-axis). Repeatability of the detents due to rotation of the mechanism about its Z-axis is equivalent to a rotation of the detent within its socket, and as such has no tolerance. The axes of rotation of the mechanism, and the resulting repeatability axes at the position of the detent, are

shown in Figure 3.1.

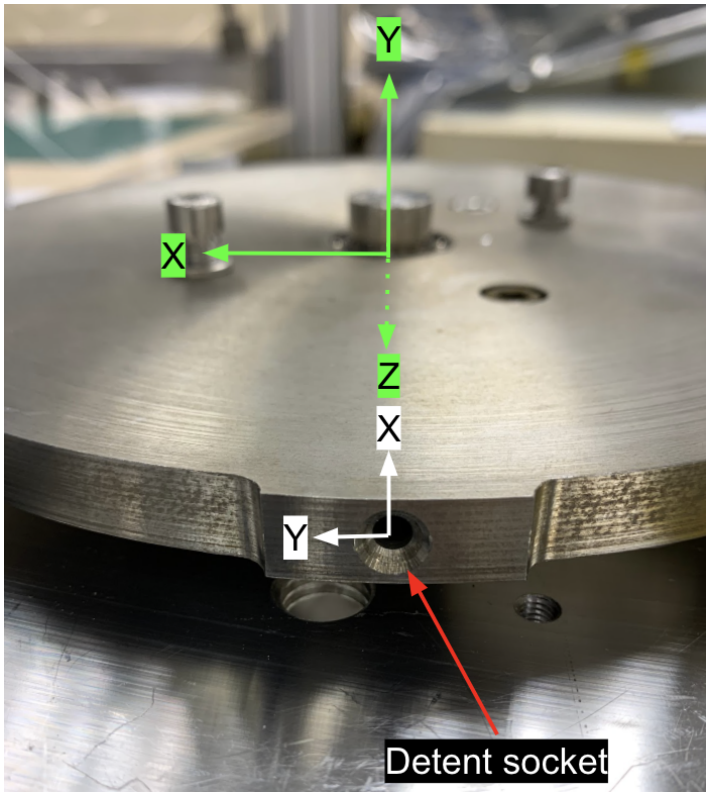


Figure 3.1: An image demonstrating the axes of rotation of the mechanism (green), and the resulting movement axes at the position of the detents (white).

Many other state of the art astronomical systems and instruments use detents to achieve high levels of repeatability, such as for the K1 deployable tertiary mirror for the Keck I telescope (Prochaska et al., 2016), and for a detent-based filter wheel in HAWK-I (Pirard et al., 2004) on the VLT. Both of these mechanisms returned ~12" repeatability about the axis of rotation despite having completely different sizes and masses. This is most likely due to the K1 tertiary mirror detent having a return force of 1200N, compared to that of 20N for the much smaller HAWK-I filter wheel. Our system is a similar size to the HAWK-I detent mechanism, and the detents will provide significantly higher return forces (~40N), potentially translating to higher repeatabilities. A higher return force will produce a stronger ‘lock’ on the system, which would lead to a higher repeatability. The upper limit on the return force would be defined by not being able to remove the detent from its position (and the associated heat load with operation). The HAWK-I system uses solenoids to act as linear actuators, pulling the detents out from their socket. This design was adopted for the test mechanism discussed in Section 1.2.

Achieving sub-arcsecond repeatability with detents is a significant challenge due to the mechanism only being constrained by a physical locking mechanism. The rest of this chapter will discuss the design of the detents used as well as a prototype mechanism built to test their performance. The detents were then tested at both warm and cryogenic temperatures.

1. Design

1.1 Detent design

Three different types of detents were designed by James Lynn and tested by the author, as outlined below. Images of all three detents in use on the test mechanism can be seen in Figure 3.4.

Cantilever

This type of detent consists of a rectangular strip of steel, 1mm in thickness, and 70mm in length. These dimensions were chosen as they were similar to the HAWK-I dimensions, but slightly thicker to provide a higher return force. When the detent is pulled out of position, the metal cantilever provides a return force of 40N. The cantilever pulls the detent out along an arc, and as such the return force is perpendicular to the tangent of the arc. It has a built-in pre-load so that it does not permanently deform when it is in use, and always provides a return force (discussed further in Section 2.3.2). It is mounted with a custom-designed aluminum mount. A CAD drawing of the cantilever detent can be seen in Figure 3.2 (left).

Beam

This type of detent is similar in concept to the cantilever, although it extends to either side of the detent position and is fixed with a mount at each end. It is also made out of steel, and is 130mm in length, with a thickness of 1mm. It can provide a return force of 100N, and also has a built-in pre-load. The beam detent pulls the detent out in a straight line, and as such the return force is applied always at a direct 90 degree angle. A CAD drawing of the beam detent can be seen in Figure 3.2 (right).

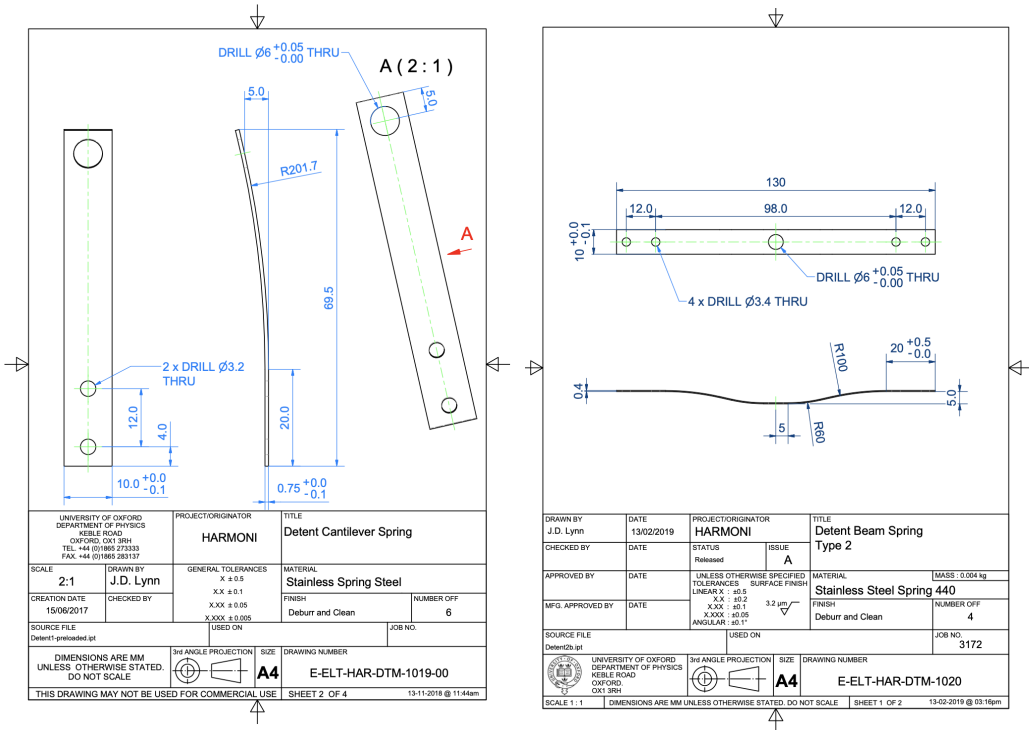


Figure 3.2: CAD drawings of the cantilever (left) and beam (right) detents. The detent ball is screwed in to the end of the cantilever detent, or the center of the beam detent. Credit: James Lynn.

Spring plunger

The spring plunger is a 1cm-diameter threaded screw with a spring-loaded detent ball at the end. It is screwed into a custom mount. It can provide a return force of 20N. However, due to play between the screw threads and the mount, and the inability to use a linear actuator to remove it from position, the spring plunger was deemed early on to not be a suitable detent, and was not considered during further testing. A drawing of the spring plunger can be seen in Figure 3.3 (credit: RS).

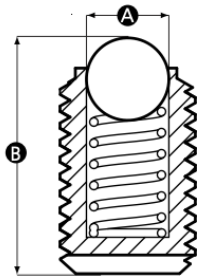


Figure 3.3: A drawing of the spring plunger detent. For the spring plunger tested, dimension A was 8mm, and dimension B was 25mm. Credit: RS.

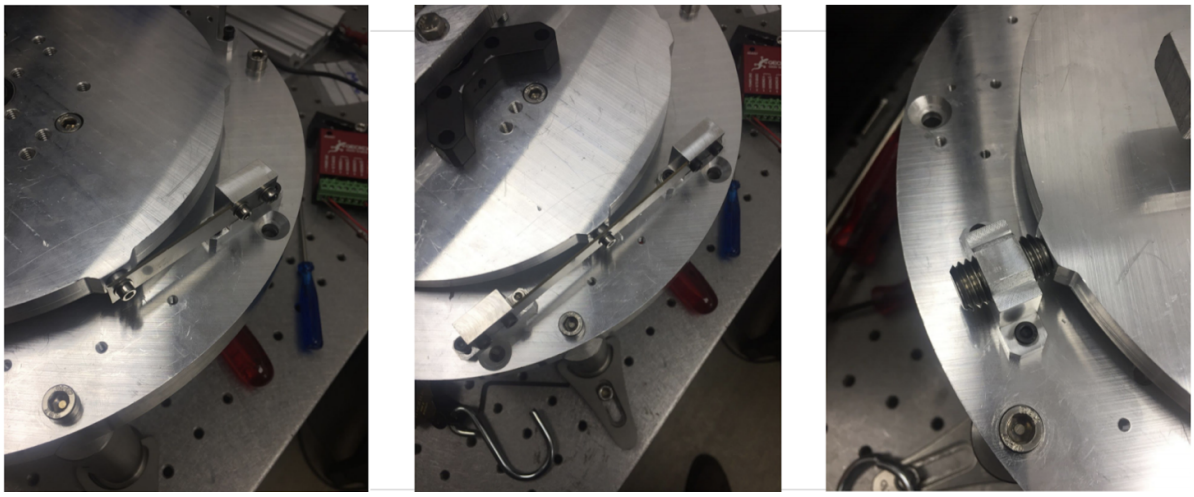


Figure 3.4: Left to right: cantilever detent, beam detent, and the spring plunger detent.

1.2 Detent test mechanism design

The test mechanism consists of two discs mounted on one another. The upper disk (Figure 3.5) is made out of steel and has a 100mm radius, and is free to rotate. Steel was used as opposed to aluminum to prevent wear in the detent sockets over time. It is fixed to the lower disk via a shaft with two radial ball bearings. The upper disk has multiple 5mm sunk hemispherical positions so up to three detents (spaced at 120°) can be used simultaneously, and wear and deformation is not a concern as both the detents and wheel are made out of steel.

With three detents in place, the third detent eliminates motion perpendicular to the axis of rotation. The accuracy of the placement of the sockets/detents within the 120° alignment was not important, as deviation from 120° alignment would not impact repeatability. This is because the bearing clearance would still be constant between movements (this was ensured by releasing the detents in a set order each time in later testing. See Section 2.3.2). However, any deviation of the sockets/detents from exactly 120° would cause an unbalanced force on the bearing. This would only lead to wear in the races over time, but not impact repeatability as the clearance on the bearing would be constant. The impact of this wear would then be measured by an accelerated lifetime test. As such, as long as the system was constrained on all axes, the accuracy of the placement of the detents was not important (and this was later proven by the mechanism passing the accelerated lifetime test. See Section 2.4.3).

The detent springs are mounted directly to the aluminium lower disk, and each is connected to a solenoid (Figure 3.6). The solenoids act as linear actuators with a 1cm stroke, and pull the detents out of position when activated. With the solenoids activated, the detents are not in contact with the wheel, allowing it to rotate freely. When the solenoids are deactivated, the return force of the detent spring combined with a return spring inside the solenoid (Section 2.3.2), ensures that each detent is pushed firmly back into position. The solenoids were an important part of the mechanism, and were adapted from the HAWK-I design. The mechanism was first designed and tested without them, where the wheel would rotate and the detents would be forced out of position and slide along the wheel until they fell into another position. However, this caused significant wear on the wheel and noise due to vibrations, so it was decided that a linear actuator would be needed to pull the detents out of position before the wheel would rotate.

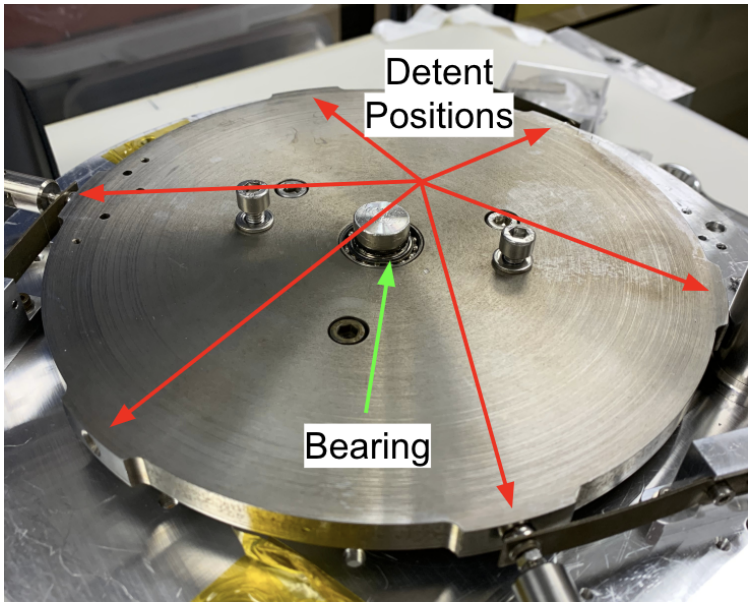


Figure 3.5: An image of the upper rotating wheel. The six detent sockets are labelled. Up to three detents could be used at any time, spaced at intervals of 120°.

The rotating wheel is connected to a stepper motor via a 245:1 worm gear (Figure 3.7). The worm gear interfaces with a 3.5:1 spur gear below the rotating wheel. Together, these provide enough torque (>1500N-cm) so that the mechanism can still move even if a solenoid fails (by 'pushing' that detent out of its position). As such, the stepper motor is responsible for rotating the wheel back to the detent, which then locks and defines the position. The repeatability

is not determined by the motor, and there is ~2° of play built into the system between the worm gear and the spur gear to ensure that it is the detent that always defines the return position (this corresponds to half the size of the detent socket). This high level of play is used to ensure that even if the detent is not released directly over the center of a socket, the return force of the detent can still 'rotate' the wheel by the necessary amount of play to ensure a proper lock. Images of the test mechanism in the laboratory can be seen in Figure 3.8.

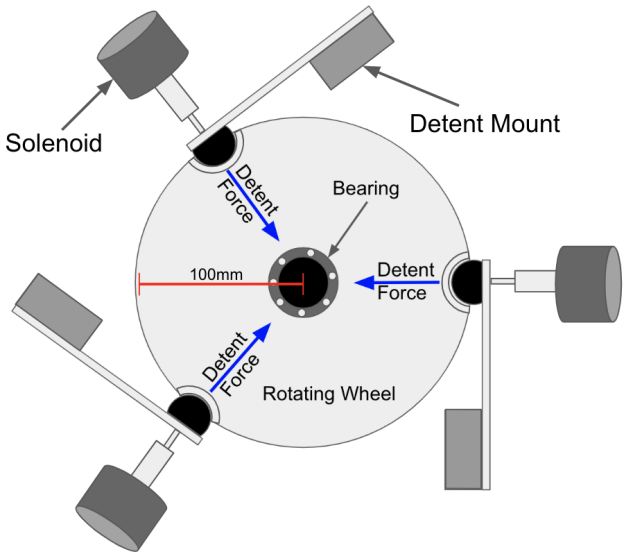


Figure 3.6: A diagram of the detent test mechanism, shown from above (detents not to scale). The fixed disk is not shown.

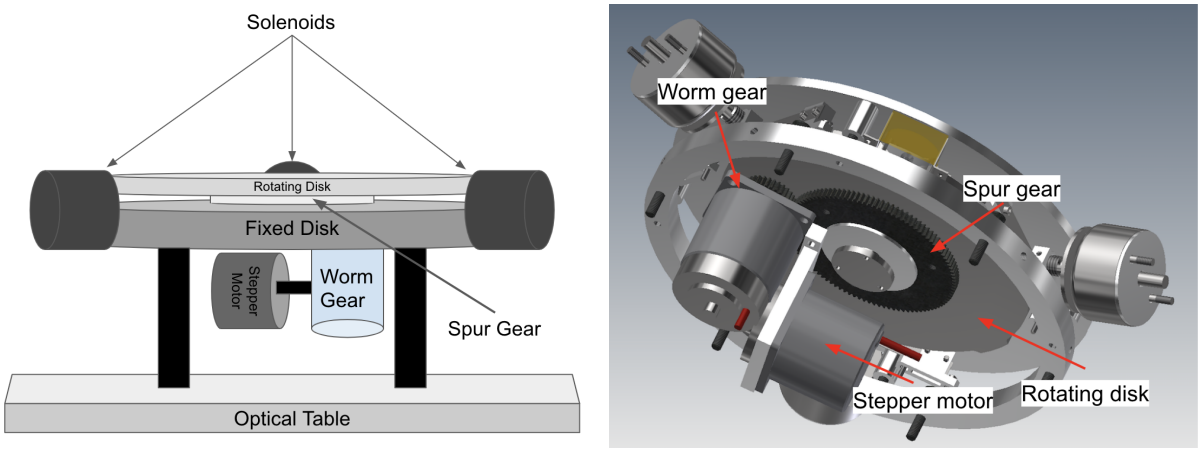


Figure 3.7: (Left) A side view of the detent test mechanism, showing the stepper motor connected to a 245:1 worm gear beneath the two disks. (Right) A CAD image of the bottom of the detent test mechanism, showing how the worm gear interfaces with the spur gear. The fixed disk is not shown. Credit: James Lynn.

2. Warm Testing

The objective of the warm testing was to optimize the mechanical design and method of operation (such as the order of releasing the detents) so the highest level of repeatability could be consistently achieved. Significant effort would be spent identifying sources of error. What was learned could then be directly applied to the cold testing, saving significant amounts of time. If parts of the mechanism didn't work in the warm, there would be little chance of them working in the cold.

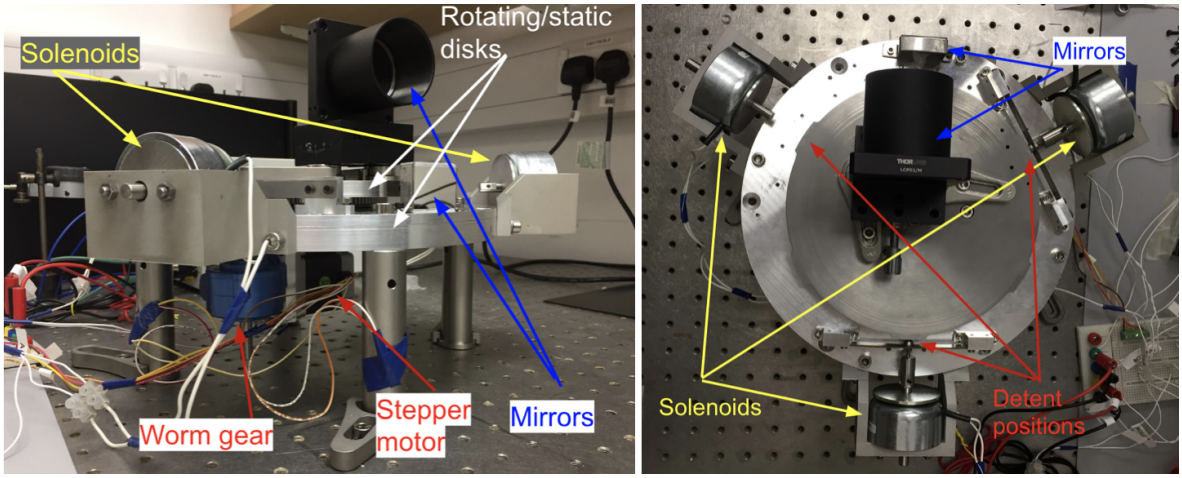


Figure 3.8: Images showing the detent test mechanism from different angles. The worm gear and stepper motor can be seen underneath the two main disks, with the three solenoids placed at 120° intervals.

To determine how various components of the mechanism (such as the number and type of detents used) impacted repeatability, two separate rounds of testing were conducted. The first would be to optimize the mechanism design (i.e. number of detents used, type of detent, etc), with the second round being the final repeatability tests. The knowledge gained from the optimization tests was then incorporated into the design of the detent test mechanism, as well as how it was operated.

2.1 Warm test setup

Ahead of testing, two mirrors were mounted on the mechanism. The first, a 1" square mirror, was fixed to the static disk with a bracket, so that it was completely stationary (referred to as the reference mirror). The second was a 2-inch circular mirror, mounted to a goniometric stage that was fixed to the rotating disk (referred to as the test mirror). The warm testing of the mechanism involved the use of an interferometer with a 6" beam to simultaneously measure the angular positions in arcseconds of the two mirrors (the autocollimator would have been preferable for testing, but it was not yet available for use at this point). The angular positions were then converted to micrometres at the position of the detent. At a radius of 100 mm, the conversion is ~1:1. Use of a high-precision angular encoder or resolver to confirm the positions was considered, but was deemed unnecessary as the precision of the interferometer was 0.9nm for a 2" mirror, and there was visual confirmation that the detents were at the correct position.

The stepper motor, a McLennan 23HSX-206, and solenoids were controlled by a Windows Desktop via an Arduino and Geckodrive stepper motor driver, while the interferometer was controlled directly via the Windows Desktop. Multiple power supplies were used, and the entire test was automated. A diagram of the test setup can be seen in Figure 3.9 and an image of the test setup in the laboratory can be seen in Figure 3.10.

For all testing of the detent mechanism, rotation about the X-axis of the mechanism (tip) was equated to rotation about the Z-axis (clock), as a rotation about the X-axis for one detent would be the same as rotation about the Z-axis for a perpendicular detent. These concepts are outlined in Figure 3.11.

To complete a movement, the solenoids would activate, and the wheel would then rotate away from its 'home' position and then back again. The solenoids would then deactivate and the detents would engage. Early tests involved the solenoids deactivating at the same time, but in later testing they were deactivated in a set order. This is discussed further in Section 2.3.2. Before and after movements of the mechanism, the interferometer would take a simultaneous exposure of the moving and reference mirrors every 90 seconds.

This was the minimum time between exposures for the warm testing, as it took 90 seconds for the Windows Desktop to save the phase maps of the two mirrors. The angular shift of the moving mirror between measurements could be used to determine the repeatability of the system, with the angular shift of the reference mirror used to determine if there was a background shift common to the entire mechanism that could be removed. After the exposures

had completed, the mechanism would move again, using the recent measurement as the reference measurement for the next movement. This process would repeat for an extended period of time, usually a full work day. Overnight tests were not possible due to health and safety regulations with using the interferometer.

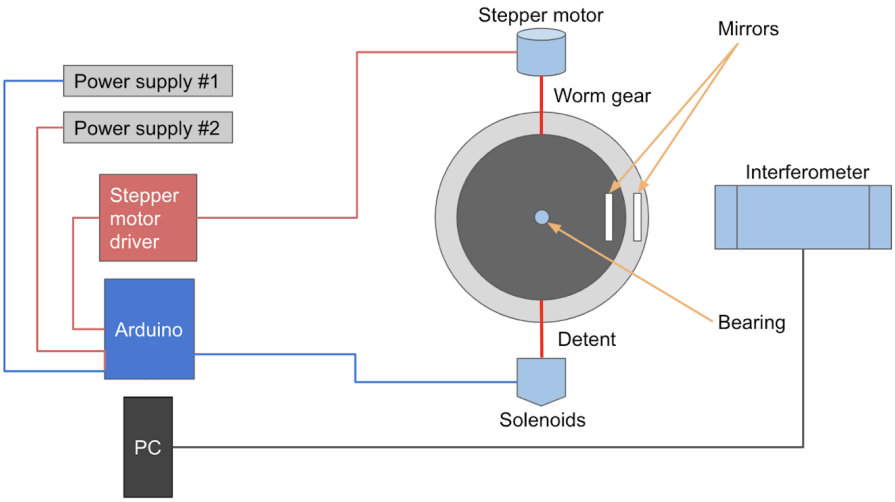


Figure 3.9: A diagram of the test setup for the detent mechanism. The stepper motor was driven by an Arduino via a Geckodrive stepper motor driver. The solenoids were controlled by the same Arduino. Two test mirrors were aligned to an interferometer which was connected to a Windows PC.

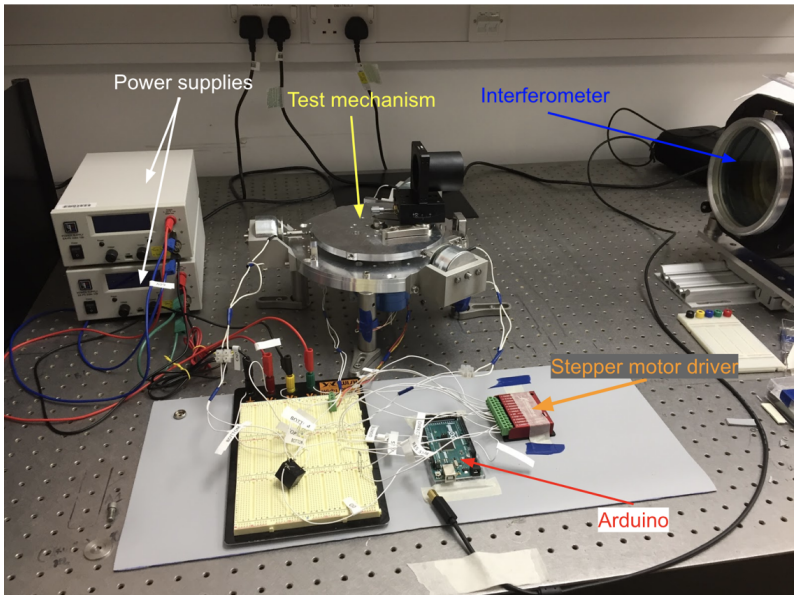


Figure 3.10: An image of the test setup for the detent mechanism. The power supplies, arduino, stepper motor driver, interferometer, and test mechanism are all labeled. The Windows PC is not in frame.

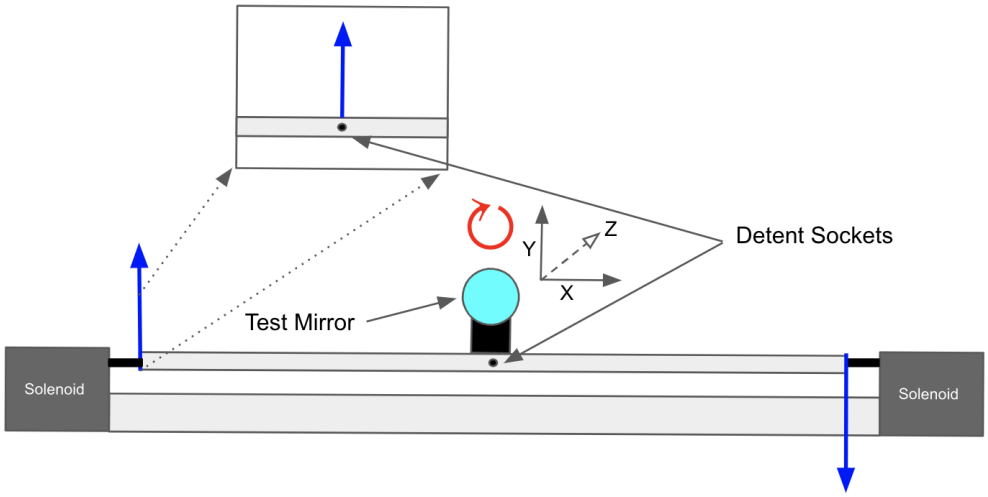


Figure 3.11: A diagram showing, from the reference frame of the interferometer, how a rotation about the Z-axis of the mechanism (shown in red) would be equivalent to rotation about the X-axis of the mechanism for a perpendicular detent. Therefore, the rotation of the mechanism about its X-axis was treated as equivalent to rotation about the Z-axis.

2.2 Warm repeatability test plan

Both types of detent (cantilever and beam) were tested in the warm to determine which provided better repeatability. Each type of detent was tested with one, two, and three detents in place to determine which number was optimal and if the system became overconstrained. Tests were first to characterize the background stability, performance while only activating the solenoid, and then while fully operational. Sources of error would be identified at this stage, as well as defining methods of mitigation. Finally, final repeatability tests were conducted with the motor rotating the wheel a random distance while all the identified sources of error were being mitigated (assuming these mitigations could be used in the final instrument). Finally, the system underwent an accelerated lifetime test of 15,000 movements. A summary of the warm test plan is shown in Figure 3.12. The same test plan was followed with the cold testing.

2.3 Optimizing the operation of the detent mechanism

The objective of the optimization tests was to determine the highest level of repeatability the detent test mechanism could achieve while in functional operation. Early optimization tests were

run at a high frequency of movements (ranging from every 25 seconds to every 3 minutes). Final repeatability tests were run for 10 hours, with movements every 5 minutes (as discussed in Chapter 1, Section 2.1, the mechanism had to function properly with movements with a minimum movement frequency of once every 6 minutes). This constant operation would put the mechanism under higher levels of stress than in HARMONI, where moving mechanisms would only move ~20 times per day (or 10 times per hour during configuration or troubleshooting, as discussed in Chapter 1, Section 2.1) (Clarke et al., 2020). Two types of optimization testing were conducted, with the first involving the use of only the solenoid, and the second with the mechanism fully operational.

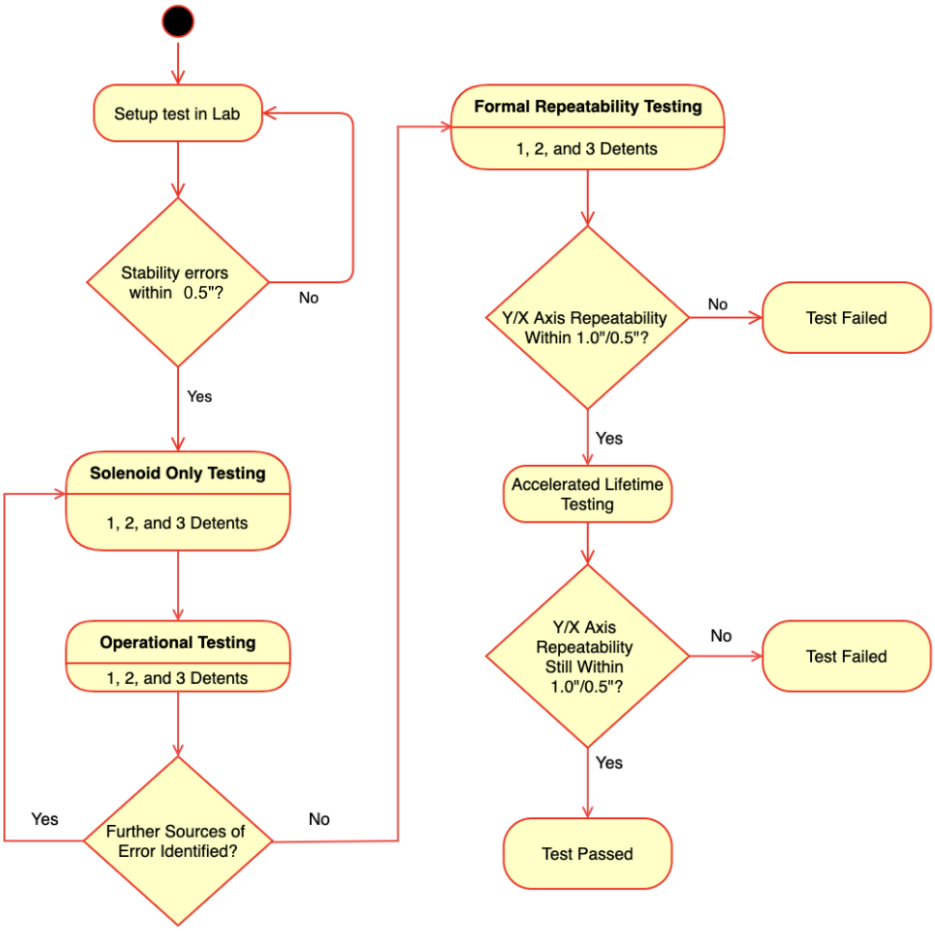


Figure 3.12: The warm repeatability test plan for the detent mechanism.

2.3.1 Solenoid only tests

This test was used as the first real test of the repeatability of the system. It was similar to the stability tests, except that the solenoids would activate in between exposures. They would hold the detents for two seconds, and then release them back into position.

The main goal behind the solenoid testing was to see what the theoretical 'ideal' repeatability of the system would look like, and if there was an impact of the type of detent and number of detents on system repeatability. As this test involved minimal moving parts, and the motor's operation would not add further potential error, it provided the best-case scenario for the system.

Type of detent

The cantilever was determined to be the optimal detent type, and was used for all further testing. It provided repeatabilities twice as better (on average) than the beam detent. This is because the beam detent required twice as many mounting points to the mechanism, which doubled the potential for noise and movement of the mounts, and overconstrained the position of the detent ball itself. If the mounts moved at all due to imperfect fastening to the lower plate, the repeatability would be drastically lowered, as the 'home' position would change each movement. This is discussed further in Section 2.3.2. Even after the mounts were modified to be more stable, the repeatability provided by the beam detents was still worse than with the cantilever detent by a factor of two (likely due to the overconstrained position of the detent ball). Any residual noise added by the mounts (even once minimized) would still impact the beam detents twice as much.

Furthermore, with a return force of 100N, the bearing and detent ball wore at a significantly higher rate than with the cantilever detent. The solenoids also required 5A to operate (as opposed to 2A for the cantilevers), which added more heat load on the system than with the cantilever detents.

Repeatability of 1 detent

The solenoid test with one cantilever detent provided results well within tolerance, and much better than was expected. Representative data can be seen in Figure 3.13. This test produced repeatability about the Y-axis of 0.14 micrometres (0.32 micrometers absolute, and 0.13 micrometers with a 2nd order polynomial fit). As discussed in Section 2 of Chapter 2, the data is fit with a linear polynomial, with the repeatability calculated from the residuals. The linear

polynomial is fit to remove the drift due to fluctuations in background temperature. The background temperature was not recorded simultaneously (the absolute drift on timescales of 1hr was ~0.5 micrometers, and tests were being run once every ~2 minutes at this stage, leading to increased background temperature from operation of the solenoids).

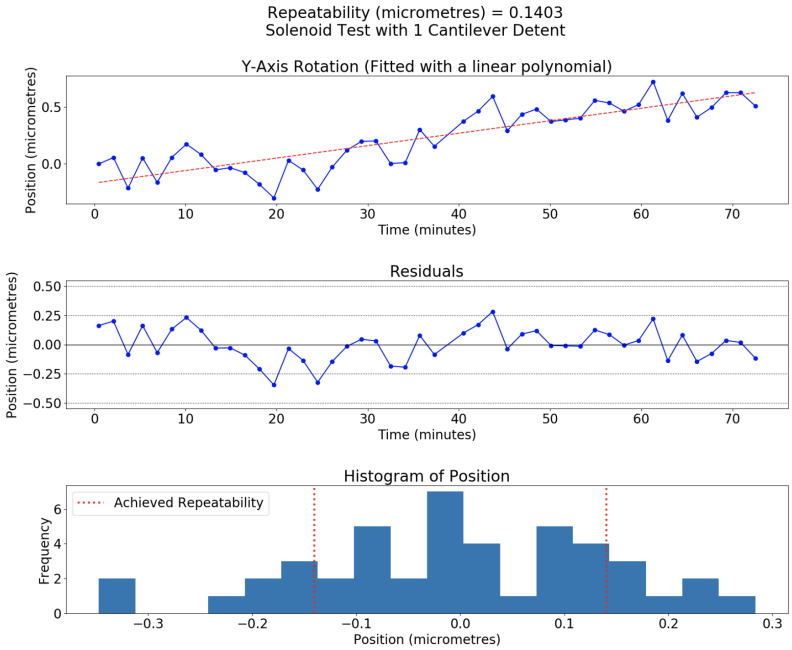


Figure 3.13: (Top) Angular rotation about the Y-axis vs time, with a polynomial fit to the trend. (Middle) The residuals of the fit, plotted against time. (Bottom) A histogram of the residuals. This is a representative plot of a solenoid only test with one cantilever detent.

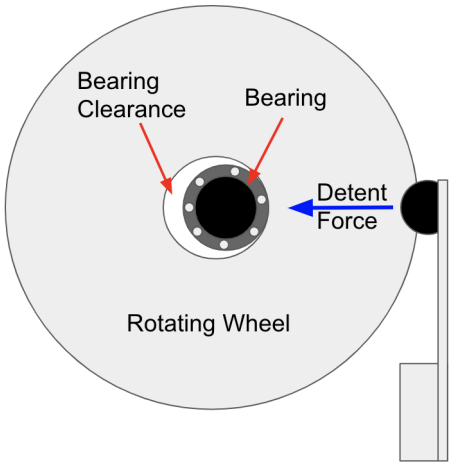


Figure 3.14: A diagram demonstrating how the bearing clearance would remain constant during the solenoid only tests with one detent. The bearing clearance is not to scale.

The reason for the high repeatability of this test had to do with the clearance of the bearing. Since there was only one detent being used, the entire force applied to the system when the detent was in position was in one direction. Therefore, the clearance on the bearing was always in the same location. When the detent came out of position, this clearance didn't change at all. The detent then went back into position, and applied the same force to the system, but didn't change the position of the wheel relative to the bearing. This concept is outlined in Figure 3.14.

Repeatability of 2 detents

The two detents were chosen such that the net force applied was perpendicular to the face of the mirror. That way the detents would just push the mirror away from the interferometer, and the repeatability about the Y-axis would theoretically not be impacted (Figure 3.15).

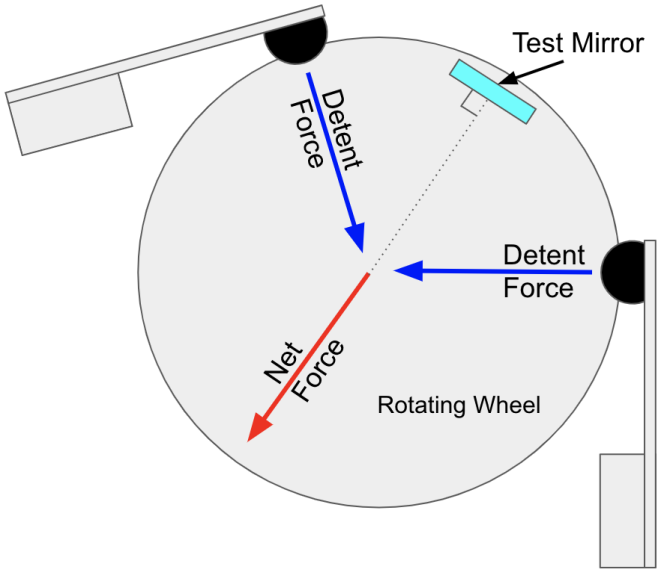


Figure 3.15: A diagram showing the test setup with two detents.

However, the repeatability of the tests while only activating the solenoids was significantly worse with 2 detents than with only one, returning values around 6 micrometres. A representative plot can be seen in Figure 3.16. As can be seen, the position was fairly random, but seemed to oscillate between two points. This was exactly what was expected, as the position

of the rotating wheel was dependent on the position of the clearance of the bearing. In this case, the clearance of the bearing was solely determined by which of the two detents was dominating at that point, or which detent engaged first. Even though the detents were released at the same time, on small timescales the two would still engage at slightly different times. Releasing the detents in a set order significantly improved the repeatability, and is discussed in Section 2.3.2. It is noted that the absolute drift in Figure 3.16 is larger than that in Figure 3.13 (~1 micrometre per hour). However, as discussed in Chapter 2, this is likely due to a combination of temperature and the use of two detents (the changing direction of the non-uniform force likely impacted the 'home' position of the mechanism over time, as opposed to when 1 or 3 detents was in use), but was not investigated further as the repeatability was already worse than required and two detents would not be viable for use in HARMONI. The purpose of Figure 3.16 is purely to demonstrate the 'bi-positional' impact of having two detents, with the position defined by whichever one engaged first.

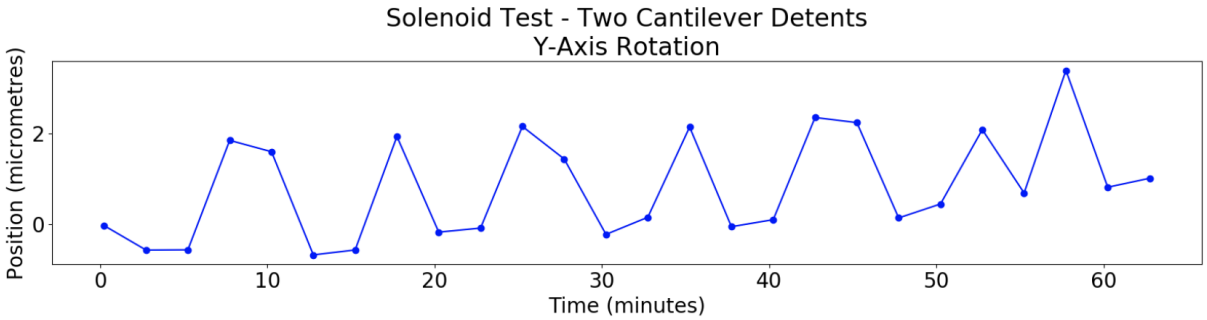


Figure 3.16: Angular rotation about the Y-axis vs time for a solenoid test with two cantilever detents.

Repeatability of 3 detents

Repeatability for three detents in the solenoid only test was better than with only two detents, but also worse than with only one. This test worked similarly at a physical level to that with two detents, except there was the final detent which provided a direct force in the opposite direction (still perpendicular to the face of the mirror). With the third detent acting as a final constraint, the clearance of the bearing was less random. As the clearance of the bearing was fully constrained, it was believed the addition of movement in between detents engaging would not negatively impact repeatability. A representative plot can be seen in Figure 3.17. While the profile appears to be sinusoidal, this was believed to be a random error and was not seen in any other tests, and

was not investigated further. The repeatability about the Y-axis was 1.16 micrometres (2.35 micrometers absolute, 1.12 micrometers with a 2nd order polynomial fit). The larger absolute drift on timescales of 1hr (~2.5 micrometres) is due to increased temperature from the operation of the three solenoids simultaneously and in quick succession (tests were once every 25 seconds at this early stage of testing), as described in Chapter 2 Section 1.2). It is noted that at this point the detents were also still being released at the same time, rather than in a set order. As described in the next section, releasing the detents in a set order significantly improved the repeatability.

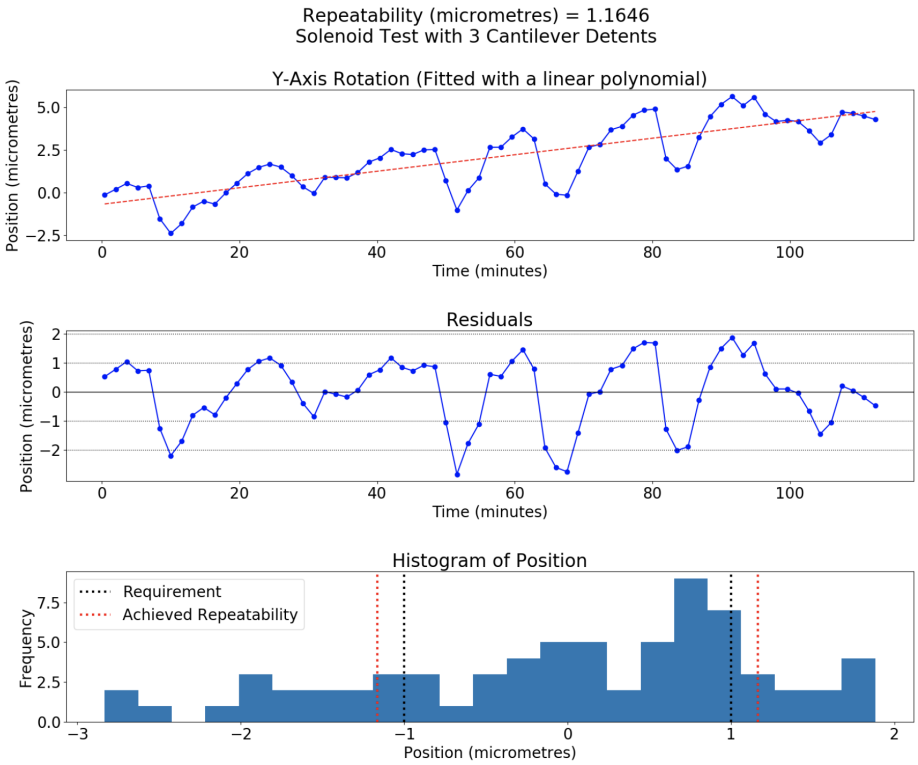


Figure 3.17: (Top) Angular rotation about the Y-axis vs time, with a polynomial fit to the trend. (Middle) The residuals of the fit, plotted against time. (Bottom) A histogram of the residuals. This is a representative plot of a solenoid only test with three cantilever detents.

Conclusions from solenoid only testing

The testing while using only the solenoids was encouraging given the results for the single detent. However, it was believed that the results from the tests with three detents, with repeatability at 1.16 micrometres, would be similar to the repeatability achieved with three detents while the mechanism was fully operational. The cantilever detent was determined to be

the optimal detent type, as it provided better repeatability than the beam detent. A summary of the solenoid only testing is shown in Table 3.2.

Solenoid Only Testing	
Optimal Detent Type	Cantilever
Test Type	**Repeatability (micrometres) (RMS)**
1 Detent	0.14
2 Detents	~6.0
3 Detents	1.16

Table 3.2: A table showing the results for the solenoid only testing.

2.3.2 Operational optimization testing

The operational optimization testing involved using the mechanism as intended with the motor and solenoids in use. It was found that error was due to seven primary sources: the detent mounts moving in position, the detent settling time, the method of releasing the detents, the order in which the detents were released, thermal expansion of the system, the direction of rotation, and the return force of the detents.

Detent mounts

The first major source of error came from the poor stability of the detent mounts. These were the aluminum units that connected the detent spring to the static disc. If these moved by a certain distance, then the position of the detent also moved accordingly - and the repeatability of the system could not be higher than that distance.

A Mitutoyo digital dial indicator was used to test how much the mounts were moving during a measurement. This device had precision levels of one micrometre. The dial indicator was positioned alongside the detent mount, with the initial position recorded as ‘home’. The mechanism was then run. During the activation and deactivation of the solenoids, large fluctuations on the order of several micrometres were noticed in the positioning of the mount. These were permanent - the mount would not return to the original ‘home’ position; a new ‘home’ position had been defined.

To reduce this large source of error, the mounts were modified so that they were fixed with both dowels and screws, constraining the movement of the mount completely in both axes. The tests were re-run with the dial indicator, and the movement was found to have been removed, with remaining position errors on the order of 1/100th of a micrometre. This improved the repeatability by ~1 micrometres.

Detent settling time

The settling time was defined as the time it took for the detent to relax into a position and become static and stable. Determining the settling time required for the detent was important in reducing error in the measurements, as measurements taken before the settling time had elapsed would be meaningless. From initial tests, it was known that this time was greater than 5 seconds and shorter than 30 seconds, but the exact time needed to be determined. That way, measurements (which would be taken after this settling time had elapsed) reflected the actual position of the system when it was in equilibrium.

To find the settling time, a test was run where the time at which exposures were taken varied by 0.5 seconds each time. The first exposure was taken x seconds after the movement of the system completed, the second was taken $x - 0.5$ seconds after, the third after $x - 1$ seconds, and so on. The test was long enough to accommodate two sets of measurements. A plot of the tilt of the moving mirror can be seen in Figure 3.18. As the measurements approached the movement, the values and positional error increased significantly. From this plot, it was determined that the settling time was roughly 15 seconds. With settling times longer than this, as seen in Figure 3.18 with movements to the left of the vertical dotted lines, the movements were within ~3 micrometres. To be safe, at least 30 seconds were always allowed before measurements were taken in all subsequent tests. While this did not directly improve the repeatability of the mechanism, taking measurements within the settling time could increase errors by up to 30 micrometres, depending on when the measurement was taken.

According to HARMONI system requirement R-INS-920, the maximum time allowed for a change in observational setups is two minutes (as described further in Chapter 1, Section 2.1). Early tests demonstrated that one full rotation took 60 seconds for the detent mechanism.

Assuming a 30 second settle time, this allows 90 seconds for a complete rotation of the detent mechanism, putting the operation of the detent mechanism within the 2 minute tolerance.

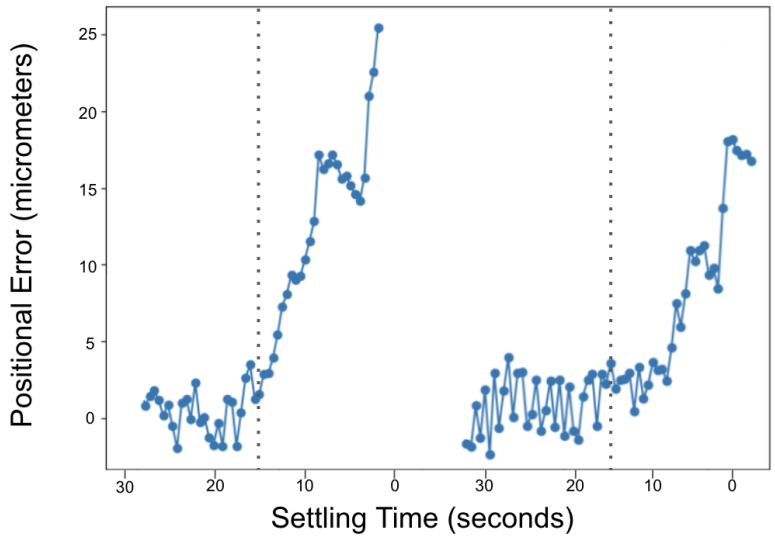


Figure 3.18: A plot of positional error about the Y-axis vs settling time during testing. This test was conducted to determine the optimal settling time for the detents (two tests are shown in the plot). As the time between the end of a movement and the measurement was decreased to zero (see X-axis labels), the measured positional error at a given settling time would increase significantly. The 15 second settling time cutoff is shown by the black dotted lines, with the measurements being relatively uniform after settling times longer than this cutoff.

Detent release method

Two main ways of returning the detents to their positions were identified before testing began. The first was to release the detents when they were directly over their position. The second involved releasing the detents while they were over the 'landing stage' as seen in Figure 3.19. As the wheel continued to rotate, the detents would slide into their position.

It was assumed the second method would be preferable, as the distance the detents had to travel to reach the landing stage was lower, and so there would not be a strong shock to the system as the detents slammed into place. They would fall more gently onto the landing stage, and then just slide into position.

However, after significant testing, it was found that the first method, the 'direct release' method, was far more preferable. The detents sliding along the landing stage as the wheel continued to rotate added in significant positional error. When the detents were in contact with

the moving wheel, they put a lot of stress not only on the detent mount, but also the connection between the detent and the detent spring. This would introduce high levels of noise that were not present when using the 'direct release' method. Using the 'direct release' method improved repeatability by ~3.0 micrometres compared to the 'landing stage' method.

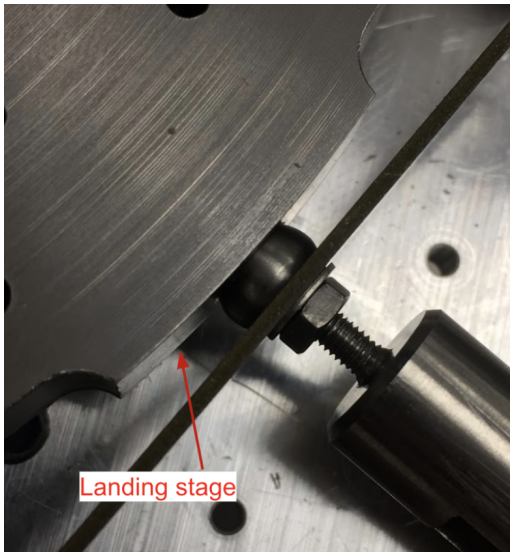


Figure 3.19: 'Landing stage' on the edge of the detent platform. The 'landing stage' was a raised platform with respect to the rest of the rotating steel wheel.

Detent release order

Another variable identified was in the way in which the detents were released. The first method involved releasing all of the detents at once, which would immediately snap the system back to position. However, this introduced significant amounts of error in the system because the return order of the detents was random. Different detents would be engaging first and defining the position with each measurement.

To remove this source of error, the detents were released individually in a set order every time. This ensured that the same detent defined the initial position (and the position of the bearing) every time. This release method increased the repeatability by ~5.0 micrometres.

Thermal expansion

As discussed in Chapter 2, Section 1.2, changes in the temperature of the system (from fluctuations in the background temperature, or heat dissipated from the motors/solenoids due to constant use) would increase the positional errors of the mechanism. Two solutions mitigated this issue. The first was completely turning off the stepper motor in-between movements, as it had previously been idling causing excess heat. The second was to increase the rest time in between movements to 5 minutes (still within the 6 minute requirement), letting the motor and solenoids cool. While this rest time could be shorter, it was not needed, as the actual system in HARMONI will be run far less frequently (20 movements per night of observations), making this method of mitigation viable for use within the actual instrument. These two solutions together improved repeatability by ~5.0 micrometres, as the mechanism was sufficiently cooled between movements.

Direction of rotation

A further source of error was due to the direction of the movement. While the angular distance had no impact on the repeatability, the direction did have an impact. This was due to the backlash between the stepper motor and the moving wheel arising from the clearance in the gears (Figure 3.20), which was about 2°, or roughly 1/2 the size of the detent position (~2.5mm).

These two separate directions translate to different repeatability positions due to the play in the system. The profile was bimodal, but with each distribution still having a high level of repeatability. An example of this can be seen in Figure 3.21. There are two clearly defined positions that the mechanism was returning to. The asymptotic drift is again due to the operation of the motor and solenoids, as discussed in Chapter 2, Section 1.2, but the only purpose of Figure 3.21 is to demonstrate the bimodal distribution of positions.

Theoretically the direction of rotation and backlash should have no effect on a detent-based system, as the detents would always define the position irrespective of backlash. In this case, the distance of the play (~2.5mm - half of the detent socket) was large enough that when returning from the opposite direction, the detent would release while over the edge of the detent position. When returning from the initial direction, it would release directly over the center of the position. It is likely that when the detent is released over the edge of its position it would not engage perfectly, and define a slightly different position with worse repeatability, as

seen in the right distribution in Figure 3.21. As such, if rotation in both directions is needed, the play in the system must be less than half of the size detent position. Results from additional testing showed that the maximum amount of play must be less than one quarter of the size of the detent position to ensure the detent seats accurately.

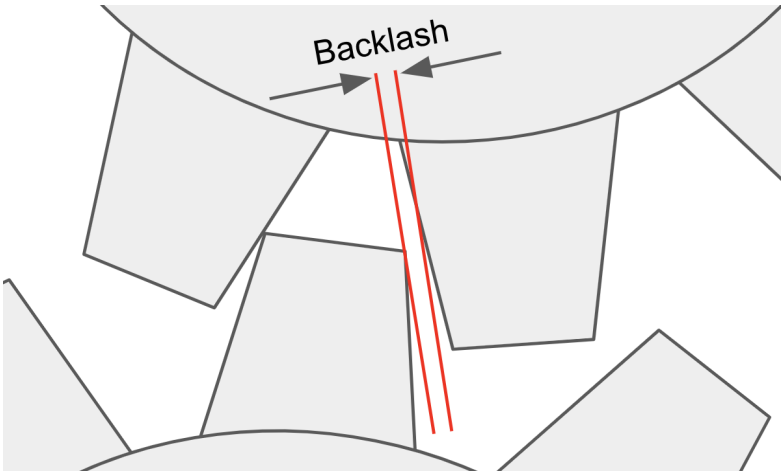


Figure 3.20: A diagram demonstrating the concept of backlash due to clearance in between the gears. The backlash caused sources of error when driving in two directions.

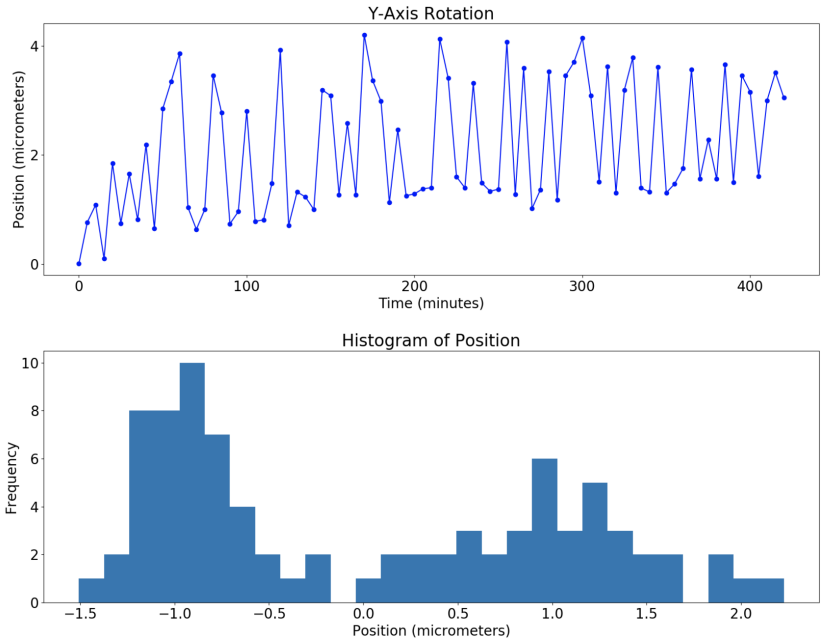


Figure 3.21: (Top) Angular rotation about the Y-axis vs time. (Bottom) A histogram of the normalized positions.

Further testing was done with each test only moving in one direction at a time. As long as both directions weren't tested simultaneously, the direction would not impact repeatability. When testing with both directions, the repeatability worsened by ~1.0 micrometre.

Detent return force

With early cantilever and beam detents, the stroke of the solenoid was long enough to cause permanent deformations in the detent springs after just a few movements. The detent springs alone would then not be able to apply a significant enough return force to effectively seat the detent in position. The wheel would be slightly free to move even when the detents were released, completely compromising the repeatability.

Two solutions were formulated to overcome this issue. The first involved placing a return coil spring within the housing of the solenoid. This ensured that a linear return force was applied even when the solenoid was not in operation, applying a further return force, pushing the detent back into place along with the return force from the detent spring. The second solution involved putting a pre-load on the detent itself, so that it would not deform when being pulled out of position. Both of these solutions mitigated this issue, improving repeatability by ~25 micrometres (the level achieved when the detents were loosely seated).

Conclusions from the operational optimization tests

A summary of the problems that impacted the repeatability, along with the methods for removing them from the operational optimization test, is shown in Table 3.3. The dominant problems were the settling time and return force. Once these were removed, the remaining problems were 'additive' - in that each mitigation directly improved the repeatability by the shown amount.

2.4 Warm repeatability tests

All warm repeatability tests were conducted with the mitigations listed above in a non-temperature stabilized environment. The tests began with the interferometer taking a reference measurement of both mirrors. Then, after a 150 second delay, the solenoids were activated, pulling the detents out of position. The stepper motor then rotated the wheel a random distance (up to a full rotation) in one direction, and then back again to its original position

(taking between 20-30 seconds in total). The solenoids deactivated in a specific order, such that the detents always engaged in the same way. There was a half-second delay between each solenoid deactivating. The system then sat idle for ~120 seconds while the detents relaxed into position. A fan was used to keep the solenoids cool, and they were turned off during movements while the detent was not over a 'landing stage', with the detents relaxed and not in contact with the wheel.

Problem	Mitigation	Improvement (micrometres)
Detent mounts moving in position	Mounts fixed in two axes	~1.0
Detent settling time	Exposures taken 50 seconds after movement	Up to 30
Method of releasing detents	Release detents directly over position	~3.0
Order of releasing detents	Release detents individually in a set order	~5.0
Thermal expansion	1) Turn off the stepper motor in between movements 2) Turn off solenoids during movements 3) Increase rest time in between movements to 10 minutes	~5.0
Direction of rotation	Rotate in one direction per test	~1.0
Return force of detents	1) Add return spring in solenoid 2) Pre-load detents	Up to 25

Table 3.3: This table shows all of the main problems encountered with the optimization testing of the detent mechanism, along with how they were mitigated, and by how much the mitigations improved the repeatability.

Tests were run for extended periods of time to put the entire system under stress, and see the highest level of repeatability that could be achieved. The main goal was to determine the optimal operational setup, and whether the movement of the motor had an impact on the repeatability. Repeatability was tested about both the Y-axis and X/Z-axis of the test mirror.

2.4.1 Repeatability about the Y-axis

Repeatability with 1 detent

Despite the strong success of the solenoid only testing with one detent, this test performed significantly worse when the system was moving. A representative plot can be seen in Figure 3.22. The repeatability achieved was ~5.5 micrometres.

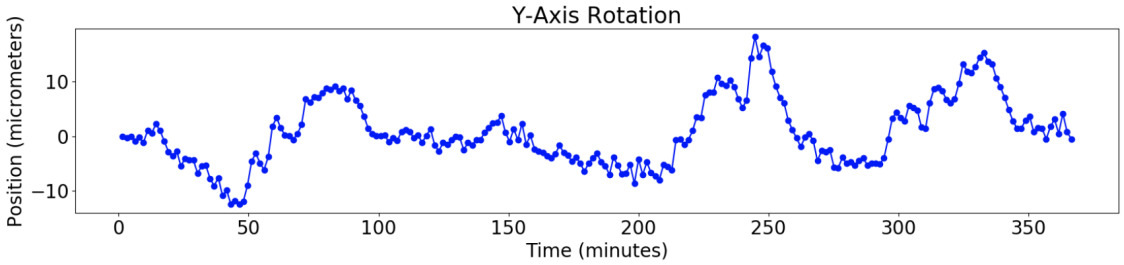


Figure 3.22: A plot of angular rotation about the Y-axis vs time. This is a representative plot of a moving test with 1 detent.

In the solenoid only test, the clearance of the bearing never changed. The force was always being applied in the same direction, so theoretically the system was completely stationary, with the detent just coming in and out of position. However, once rotation over a random distance was introduced, the clearance of the bearing was no longer perfectly constant (theoretically it would not change, but in practice it could never return to *exactly* the same position when the system was rotating). Every rotation changed this value, and the positioning of the system was then defined by this distance, rather than the detent.

This is demonstrated in the plot above. There are regions where the repeatability was high and the random error was low. However, these are flanked by noisy regions of high error and low repeatability. It was completely random which state the system was in, and as such, one detent was not a viable option assuming a bearing was used.

Repeatability with 2 detents

The moving test with two detents performed significantly better than with two detents in the solenoid only test due to the detents releasing in a set order. It also provided higher levels of repeatability than with one detent. A representative plot can be seen in Figure 3.23. The repeatability achieved was ~3.5 micrometres.

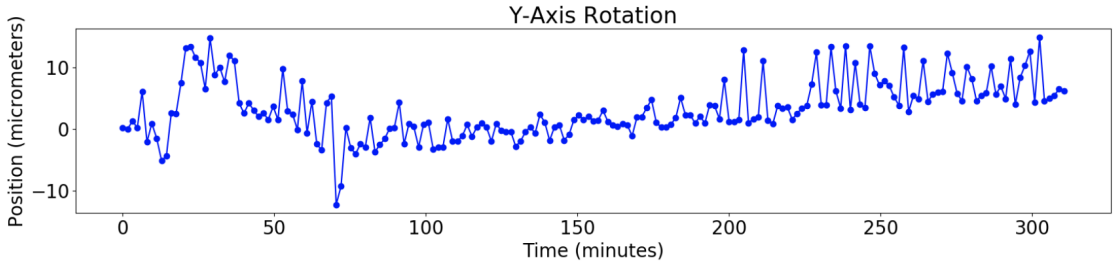


Figure 3.23: A plot of angular rotation about the Y-axis vs time. This is a representative plot of a moving test with 2 detents.

Comparing this result to the moving test with one detent, which only had a single constraint, it was expected that a second constraint would improve the repeatability by a factor of about two. This is what was seen - the repeatability improved from ~5.5 micrometres to ~3.5 micrometres.

Repeatability with 3 detents

The repeatability test with three detents yielded the best results. Given that the moving test with two detents provided repeatability of ~3.5 micrometres, it was predicted that adding in a third detent, which would reduce the net force on the bearing while stationary to zero, would improve repeatability significantly to around 1.0 micrometre.

A plot of a representative test can be seen in Figure 3.24. This test produced repeatability about the Y-axis of 0.93 micrometres (1.01 micrometers absolute, 0.91 micrometers with a 2nd order polynomial fit), and absolute drift on timescales of 1hr was due to temperature and low at ~0.4 micrometers. This was worse than with the solenoid only testing with one detent, but was well within tolerance, and better than current state-of-the-art systems due to the high return forces on the detent and all the mitigations of sources of error. While higher return forces would likely improve repeatability further, the increased heat load required to remove them from their positions would limit the cryogenic viability of the mechanism. The RMS repeatability over all final repeatability tests was 0.95 micrometres.

The repeatability test with three detents was similar theoretically to the solenoid only test with one detent, and the similar levels of repeatability reflect that. When the three detents moved

back into position (in a set order), the net force on the bearing was zero, with the position defined fully by the detents.

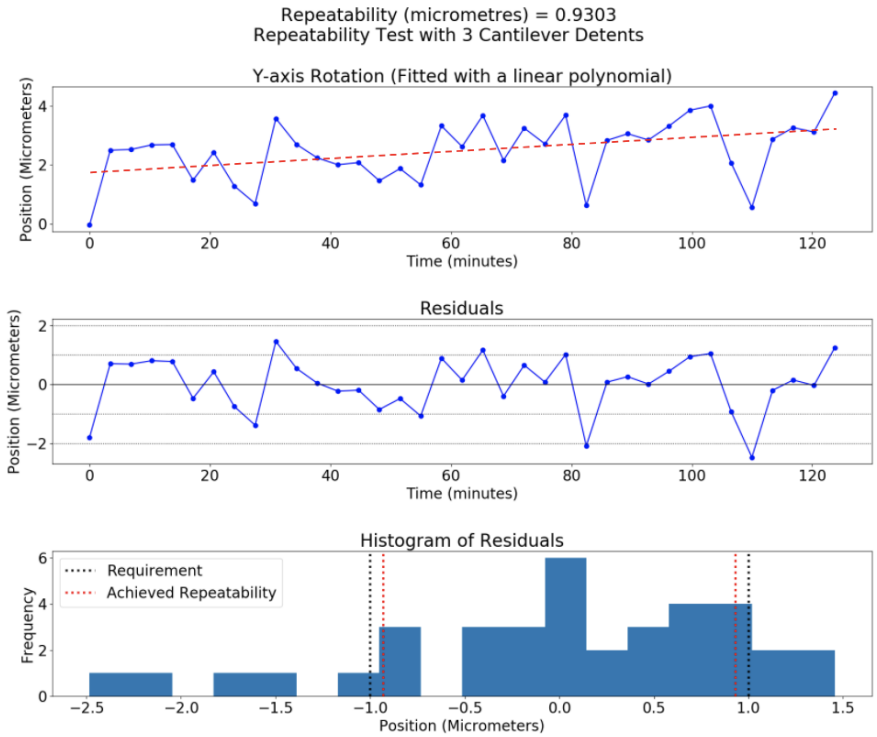


Figure 3.24: (Top) Angular rotation about the Y-axis vs time, with a polynomial fit to the trend. (Middle) The residuals of the fit, plotted against time. (Bottom) A histogram of the residuals. This is a plot of the repeatability achieved with three cantilever detents in a repeatability test.

2.4.2 Repeatability about the X/Z-axis

As seen below in Figure 3.25, repeatability about the X/Z-axis was on the order of that seen in the stability tests (0.048 micrometres with a linear polynomial fit, 0.18 micrometers absolute, and 0.047 micrometers with a 2nd order polynomial fit). This indicated that the bearings were not subject to any axial runout during operation. Axial runout in the bearings would cause an up and down ‘wobble’ in the bearings which would translate to worse repeatability about the X/Z axis. Repeatability was within the target of 0.5 micrometres, and absolute drift on timescales of 1hr was due to temperature and low at ~0.2 micrometers.

2.4.3 Accelerated lifetime performance

Over the course of all of the testing, the detent test mechanism was subjected to multiple lifetimes of movements. No degradation to any parts of the system were noticed. The best repeatability achieved was at the end of the final warm repeatability testing, which was the last testing conducted. As such, it was concluded that the detent test mechanism passed its accelerated lifetime performance test in the warm.

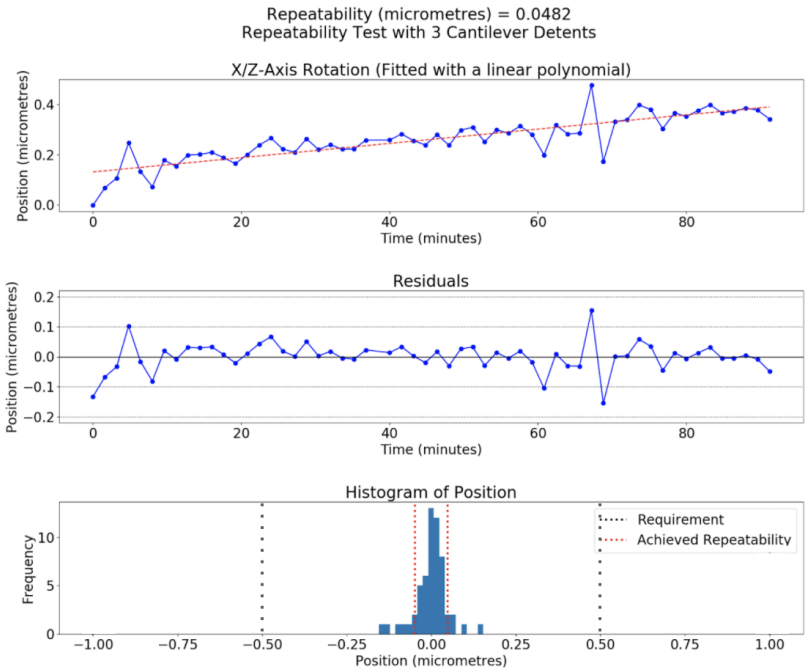


Figure 3.25: (Top) Angular rotation about the X/Z-axis vs time, with a polynomial fit to the trend. (Middle) The residuals of the fit, plotted against time. (Bottom) A histogram of the residuals.

2.5 Final warm repeatability performance

The moving test with one and two detents provided predictable results given the solenoid only testing and the initial hypothesis on system repeatability. However, with three detents, the moving test provided repeatability of about the Y-axis of 0.95 micrometres RMS (out to ~1. 1σ, repeatability is less than 1.0 micrometre, indicating that ~73% of movements will be within tolerance). Repeatability about the Y-axis assuming no linear polynomial fit (i.e. absolute repeatability) was 1.19 micrometers, and was 0.91 micrometers when fitting a 2nd order polynomial fit. Repeatability about the X/Z-axis was on the level of stability measurements at 0.048 micrometres (0.16 micrometers absolute, and 0.047 micrometers with a 2nd order

polynomial fit). The remaining errors are likely due to small misalignments of the detents with each movement, or micro-wear on the detents themselves. Figure 3.26 shows a histogram of all tests with three detents combined. The stability on timescales of 1 hour was also within tolerance (Chapter 2, Section 3.1). Over the course of all of the testing, the mechanism was run over multiple lifetimes of 15,000 movements, and it showed no signs of wear or degradation in repeatability. A summary of the warm repeatability can be found in Table 3.4.

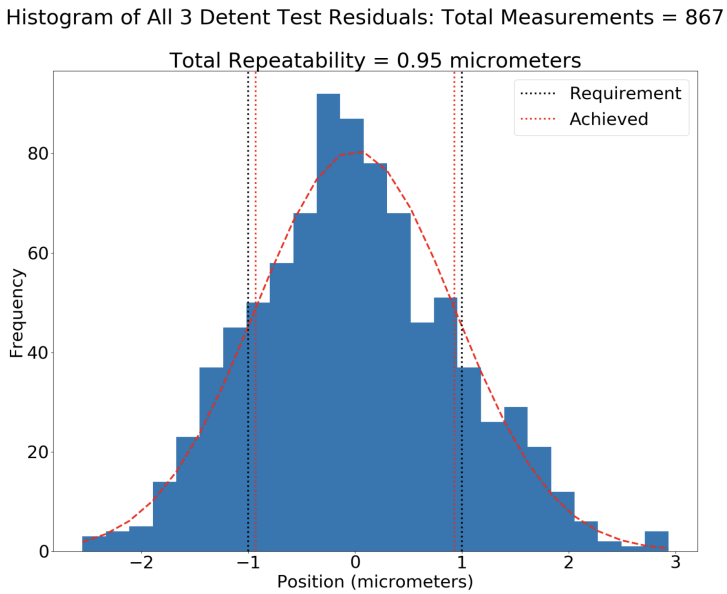


Figure 3.26: A histogram of the residuals of rotation about the Y-axis from all repeatability tests with the motor moving and three detents used. A Gaussian is fitted to the distribution, shown in red. The overall repeatability was 0.95 micrometres over 867 measurements.

Y-axis Repeatability Tolerance (micrometers) (RMS)	**1.0**
X/Z-axis Repeatability Tolerance (micrometers) (RMS)	**0.5**
Test Type	**Repeatability (micrometres) (RMS)**
Y-axis (1 detent)	~5.5
Y-axis (2 detents)	~3.5
Y-axis (3 detents)	0.95
X/Z-Axis (3 detents)	~0.05

Table 3.4: A table showing the repeatability tolerances about the rotation axes, along with the repeatability achieved for tests with 1, 2, and 3 detents. The overall repeatability in both axes is within tolerances.

3. Cold Testing

The purpose of the cold testing was to define and characterize the system's performance in a cold environment of 130K: the HARMONI operational temperature. Significant effort would be given to monitoring the performance and operation of the solenoids while in a cold environment, as it was theorized they would present the biggest operational challenge.

3.1 Cold test setup

The cold test was conducted in the AOPP 1-metre chamber at 130K and $5 \times 10^{-6} mbar$, which had a window placed on the side flange. After being completely dismantled and thoroughly cleaned (so as to prevent grease and debris in the cryostat, which would outgas and make pumping down more difficult), the entire mechanism was mounted to a baseplate on aluminium optical posts and covered in MLI blankets for insulation. The solenoids were rated for cryogenic use, but were still loosely applied to the mechanism so they were flexible and able to move slightly during cooldown.

Grease was applied to these optical posts to ensure a thorough thermal contact with the cold baseplate. A cryogenic Phytron VSS UHVC 57.200.2.5 stepper motor replaced the McLennan 23HSX-206 stepper motor used for warm testing. An autocollimator replaced the interferometer to take measurements, and this unit was aligned to the test mirror. Custom cryogenic electronic feedthroughs were made to control the mechanism from outside the chamber. Those wires were soldered to 24-pin d-sub connectors. A 24 hour period was given for both cooling down/pumping down and warming up. An image of the test setup in the cold chamber can be seen in Figure 3.27.

A series of five thermometers connected to a LakeShore temperature monitor were used to measure temperatures. Multiple thermometers were used so the temperature across the entire setup could be tracked. The LakeShore automatically recorded temperature data to a PC via a LabView Virtual Instrument (VI). Four of the thermometers were placed inside rectangular copper sheaths and taped to the mechanism with Kapton tape. This ensured maximum thermal contact. As the upper wheel would rotate, thermometers were not placed on it, as the wire would become tangled. The thermometers were located as shown below in Figure 3.28. To control the

temperature, heaters internal to the AOPP 1-metre chamber were used to raise the temperature to and maintain it at 130K±2K.

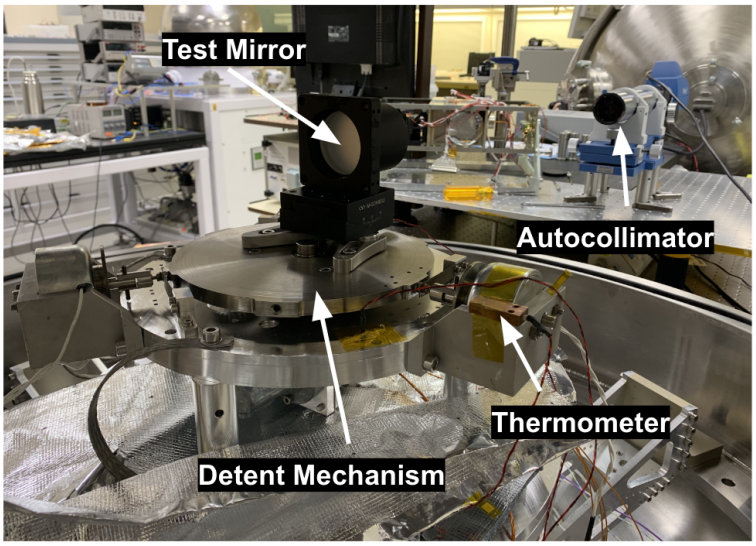


Figure 3.27: An image showing the detent cold repeatability test setup in the AOPP 1-metre chamber. The mechanism was covered in MLI blankets for insulation, and aligned to the autocollimator.

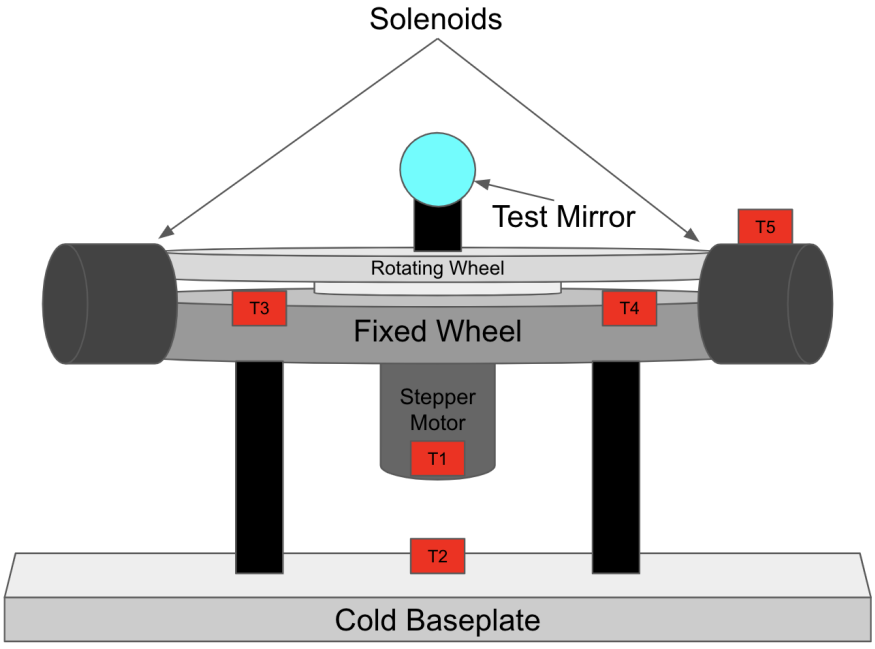


Figure 3.28: A diagram showing the locations of the five thermometers, indicated by red boxes. Thermometer 1 was internal to the Phytron stepper motor, thermometer 2 was on the cold baseplate, thermometer 3 was on the left side of the fixed wheel, thermometer 4 was on the right side of the fixed wheel, and thermometer 5 was on a solenoid mount.

3.2 Cold repeatability test plan

Three cantilever detents were used for the cold testing, along with all methods of mitigation from Table 3.3. Tests would be first to measure the background stability. Then, the performance while only activating the solenoid and not running the motor would be tested. Finally, tests with the motor fully operational would be conducted with the motor rotating the wheel a random distance. The system would then undergo an accelerated lifetime test of 15,000 movements. The cold test plan was the same as shown in Figure 3.12.

3.3 Cold repeatability tests

The solenoid and moving repeatability tests will be discussed together as both were unsuccessful due to two effects from the cold environment.

When solenoids were activated there was only a ~10% chance that each one would successfully operate. This was due to cold welding between the detent and the socket, as well as differential thermal expansion between various parts of the mechanism, putting further stress on the detents and solenoids. The moving shaft of the solenoid could also easily catch on the inside of the outer solenoid ring, preventing movement. This was made worse by the return force of the cantilever detent spring being not at a direct 90 degree angle, pushing the moving shaft into the inside of the outer solenoid ring. Together, these effects made it extremely difficult for all solenoids to simultaneously disengage the detents, despite the solenoids being cryo-rated. Often, one or two would work, but it was rare that all three would simultaneously work. Using the beam detent would provide a linear force, but as discussed in Section 2.3.1, it did not provide nearly as high levels of repeatability as the cantilever detent, even once the dowels were added to the mounts, as the position of the detent ball was overconstrained.

While the solenoids would occasionally catch during warm operation, once the return spring was added this stopped happening. It was not foreseen that this would change in the cold because the combined return force of the spring and detent was nearly 70N. The issue in the cold was the combined effects of the cleaned metallic surfaces (which are very likely to catch, even in the warm), as well as the thermal expansion while cooling. The solenoids were likely only cryo-rated for perfectly linear use.

Once the chamber was at temperature there was no way to access the mechanism, and so the only option was to warm up and manually adjust the solenoids. Loosening their mounts further was attempted. This decreased the contact between the detent and socket, but also lowered the return force. This helped, but only marginally, and not enough for the system to work in a cryogenic environment.

However, the test was run without the solenoids, and the mechanism did rotate, meaning the gears and motor did operate properly at cryogenic temperatures. It is likely that implementing some of the mitigations mentioned in Section 5 of this chapter would have allowed the mechanism to operate properly in the cold. However, by this point the FM1 was returning very low levels of repeatability, and the detents were decided to not be needed. It was decided at group level that full efforts needed to be applied to testing the FM1 and IGM, which halted progress on the cold testing of the detents.

4. Detent Test Mechanism Testing Conclusions

4.1 Warm

With three detents, the moving test provided repeatability about the Y-axis of 0.95 micrometres RMS which was below the goal repeatability of ≤1.0 micrometre. Repeatability about the X/Z-axis was on the level of stability measurements at 0.048 micrometres. It is noted that absolute repeatability (assuming no correction at all for drifts due to temperature) was not within tolerance at 1.19 micrometers. However, this is still close to the goal repeatability, and as discussed in Chapter 2, it is unlikely that there was no drift due to temperature as the majority of these tests were conducted in a non-temperature stabilized warm environment.

Over the course of all of the testing, the mechanism was run for multiple lifetimes, and it showed no signs of wear or degradation in repeatability. The <1hr stability requirements were also met. In the warm, the detent mechanism provided high levels of repeatability, and this system could be easily adapted for use with many other mechanisms and instruments. Despite the cold testing not yet showing promising results, it is believed this is still a positive outcome as this technology provides high levels of repeatability in warm environments, for low cost. Furthermore, the repeatability measured was in micrometres at the position of the detent.

Therefore, at larger radii the angular repeatabilities would be even better. The HARMONI repeatability tolerances are angular, so this makes the detents even more viable for instrumental use, specifically with the IGM (a very similar mechanism, discussed in Chapter 5).

4.2 Cold

Due to differential thermal contraction and cold welding, the solenoids were unable to consistently activate and disengage the detents. The detent mechanism did not provide the required repeatability in the cold. The accelerated lifetime test was not attempted. The <1hr stability requirements, however, were met.

5. Future Work

To overcome the issues found with the cold testing, multiple options are being investigated, each of which is listed here.

Boring out the solenoids

There was very little clearance between the moving shaft of the solenoid and the outer ring. If there was any deviation in angle between the two, the shaft would catch on the ring and be unable to move. This was exacerbated at low temperature, with effects of differential thermal expansion and cold welding making it even harder for the solenoid to operate. To combat this, the inside of the ring could be bored out slightly, adding a small amount of clearance which would allow for easier operation. The inner shaft could also be replaced with a cryo-rated plastic, such as Vespel or Torlon, which would provide a smoother operation.

Lubrication

To combat the same issue with the solenoid shaft catching on the ring, a cryogenically-rated dry lubricant could also be used internally to the solenoid. This was not done for the cold testing initially because the solenoids were loosely mounted on the mechanism, which was thought to give them enough flexibility to operate properly and not catch. Furthermore, lubricant could not

be applied before the solenoids were bored out, as operating the solenoids would have immediately removed the lubricant.

Cam-based linear actuator

This solution involves a redesign of the mechanism to not use solenoids, but rather a rotating cam that would act as a linear actuator. This could be connected to a gear which would rotate the cam during movement, moving the detent out of its position. However, this would require three motors (one for each detent), which could decrease the viability of the mechanism in a cold environment depending on the heat load from the motors that would be used. The design for this is still being worked on by the HARMONI mechanical engineer, James Kariuki.

Fixed-clearance bush

Replacing the central ball bearing with a fixed clearance bush would not help to solve the problems introduced by the cold testing, but could increase repeatability even further, as there would be a fixed clearance between it and the drive shaft. This would lower the random noise introduced by the clearance of the bearing. The design for this is still being worked on by the HARMONI mechanical engineer, James Kariuki.

However, as described in the next chapters, the FM1 and IGM test mechanisms returned results well within tolerances (and are far less complex, and more reliable, than the detent mechanism), and so a system involving detents will likely not be needed in HARMONI. As such, the designing and testing of these modifications is on hold until after the testing of the FMM and IGM is completed.

Chapter 4

Testing of the Fold Mirror 1 Mechanism

The purpose of the Fold Mirror 1 (FM1) is to appropriately fold the collimated beam onto the Fold Mirror 2 (FM2). The FM1 must provide highly repeatable rotation of its mirror to three positions, each according to one of three different positions of FM2, and corresponding to gratings of different resolutions. To ensure the pupil is maintained at the position of the grating, the optical path length must be preserved between the collimator and the grating regardless of position. This results in the FM1 articulating about its own axis, and the FM2 tracing out an elliptical track approximated by a circle with an offset, with its foci at the centre point of FM1 and the grating. The optical path is shown in Figure 4.1 (credit: Clarke et al., 2019). In all tests, repeatability was defined as the RMS error of the movements (1σ, assuming a Gaussian distribution). Articulation of the FM1 translates to a shift of the beam about the spectral direction of the detector. A working design utilizing a stepper motor driven lead screw has been fully developed by James Lynn to meet these mechanical requirements, and a prototype has been built by the Oxford Physics mechanical workshop.

The design features a mirror that articulates about its own axis, which leads to strict tolerances of the repeatability of the three positions, as articulation about its own axis causes 1:1 changes of its angle with respect to the beam (unlike with an off-axis design like Fold Mirror 2). The axes of repeatability are defined in Figure 4.2, and the goal repeatabilities of the FM1 are shown in Table 4.1.

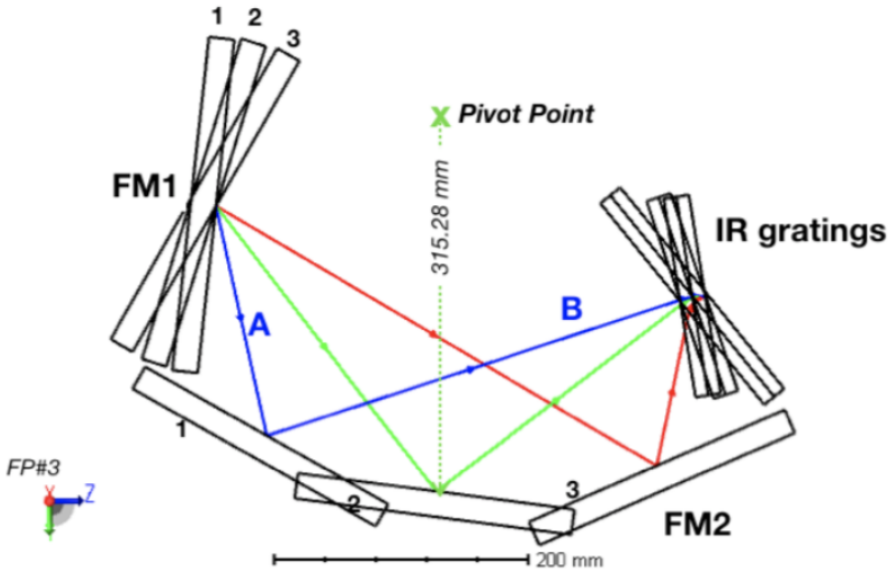


Figure 4.1: The optical layout of the Fold Mirror 1 and Fold Mirror 2. Three positions are needed corresponding to low, medium, and high resolution gratings. 'A' is the distance from FM1 to FM2, and 'B' is the distance from FM2 to the IR gratings. In all three setups, A+B is constant, and the optical path length to the grating is preserved. Credit: Clarke et al., 2019.

Many other state of the art astronomical systems and instruments use lead screws to achieve high levels of repeatability, such as the CRIRES (Kaufl et al., 2004) grating unit, the EMIR (Garzon et al., 2016) detector translation unit, and the UIST (Howat et al., 2004) fold mirror mechanism. Achieved repeatabilities are in the 5-10" range, due to no use of actuator arms (rotation being directly off the lead screw), and lead screws with coarser pitches.

The rest of this chapter will discuss the design of the FM1 and of the FM1 prototype. The prototype was then tested at warm temperatures, followed by initial testing at cryogenic temperatures.

	X	*Y*	*Z*
Repeatability (RMS)	1. 0"	0. 5"	N/A

Table 4.1: A table showing the RMS repeatability tolerances for the FM1 about the axes defined in Figure 4.2.

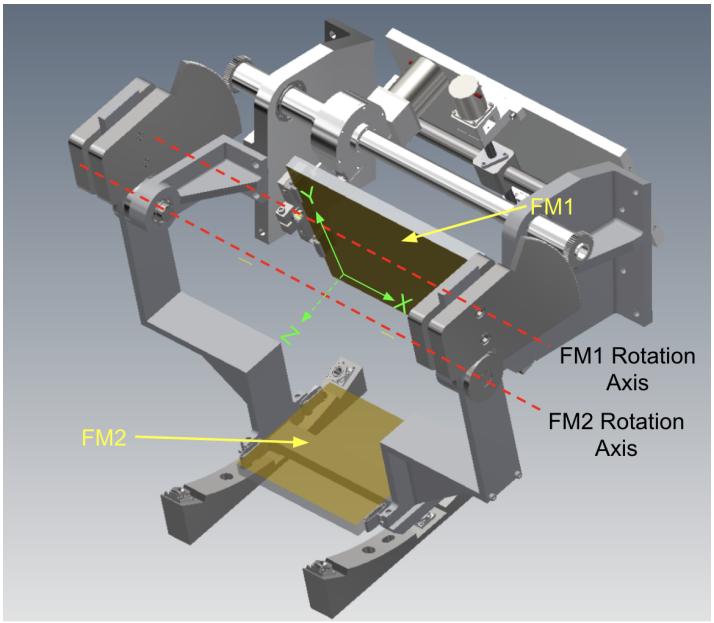


Figure 4.2: A CAD model of the Fold Mirror Module, showing the rotation axes of both the FM1 and FM2. The repeatability axes of FM1 are highlighted in green. The tolerances about each axis are shown in Table 4.1.

1. Design

1.1 HARMONI FM1 design

The FM1 (Figure 4.3) has three mirror positions, relative to its central mirror position (for mid-resolution gratings): +12.23° / 0° / -12.09° (hereafter P1, P2, P3), and consists of a stepper motor driven lead screw that moves a nut attached to a transverse bar (Figure 4.4). This bar then pushes/pulls on the actuator arms of the mirror, causing a tilt of the mirror about its own axis. The mirror is mounted with flex pivots attached to the actuator arms, and the whole mechanism weighs ~25kg, and the dimensions of the mirror are 344mm×258mm. It takes 45 seconds for the FM1 to move between P1 and P3 - the longest possible operational time. A settle time of five seconds was used for all tests, leading to a 50 second maximum operational time, which is within the 2 minute movement tolerance (as discussed in Chapter 1, Section 2.1). If detents are used, a 30 second settling time will be required, leading to a total 80 second operational time, which is still within the 2 minute tolerance.

The stepper motor is connected to the lead screw via a flex coupling which compensates for inconsistencies in the alignment of the lead screw and motor drive shaft. The flex coupling is tightened down using grub screws so it does not slip during operation. The detent torque of the stepper motor prevents the lead screw rotating freely.

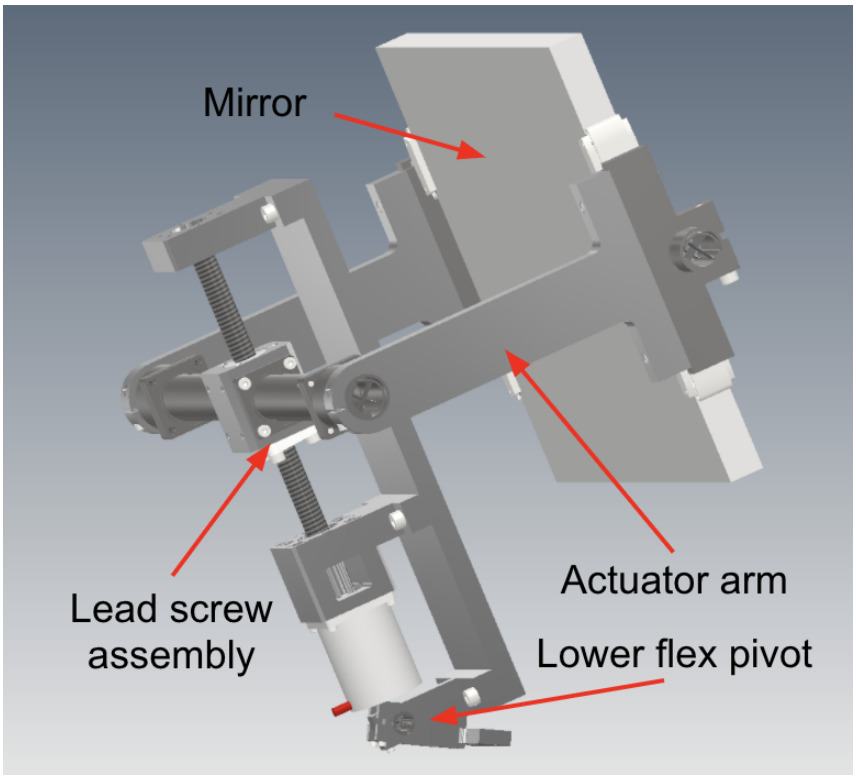


Figure 4.3: A CAD model of the FM1. The lead screw assembly, actuator arm, and main mirror can be seen. The mechanism drives the main mirror to one of three positions.

The nut moves up and down along the lead screw as it rotates, and there is a spring preload applied inside the nut to reduce play between it and the lead screw. There are two nuts: one made out of Acetal for warm operation, and the other made out of Torlon for cryogenic operation. The differing CTE's of each material make them only viable for one range of temperatures. At cryogenic temperatures, the Acetal nut would shrink and prevent any motion (see Section 3.2 of this chapter) with the lead screw. The Torlon nut, on the other hand, depends on thermal contraction while at cryogenic temperatures to be the appropriate size, and it would not work in warm temperatures as it would be too loose.

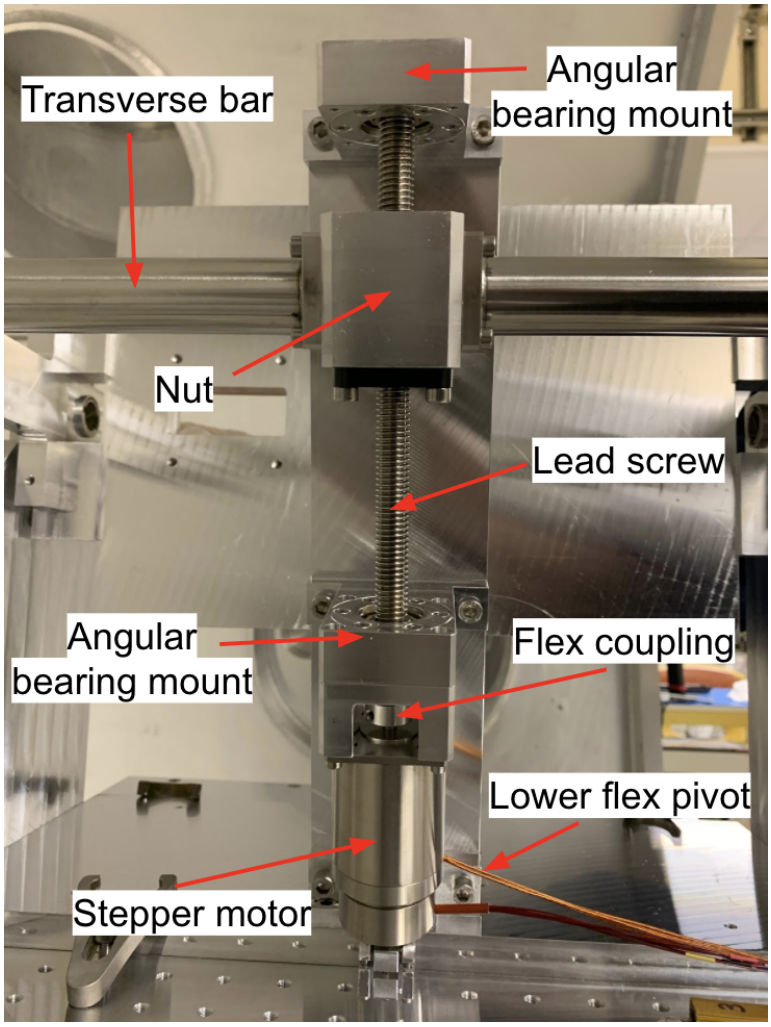


Figure 4.4: An image of the lead screw assembly on the FM1 prototype (discussed in Section 1.2). The stepper motor drives the lead screw, which moves a nut attached to a transverse bar, which rotates the mirror.

To reduce play in the lead screw itself, angular contact bearings are used at each end which apply opposing forces along the lead screw, eliminating play. These angular contact bearings are pushed into their mounts with spring washers (in cryogenic temperatures, this would be maintained as the spring washers would still apply force, but would need to be loosened ahead of cooling down). If the nut is mistakenly driven further than the outer mirror positions, the nut will come into contact with these bearing mounts and the mechanism will stop moving without causing any damage.

The mechanism uses flex pivots (Figure 4.5) at each end of the mirror actuator arms (four in total). These allow for smooth rotation of the mirror, and also account for the slight rotational motion of the transverse bar as it moves, which sweeps out an arc. These offer many benefits

over ball bearings for this type of mechanism in a cryogenic environment. First, flex pivots are frictionless (there are still minor energy losses due to the flexing), as the inner rotating section is not in contact with the fixed tube. They also have no moving parts, and as such do not require lubrication or regular maintenance. The main drawback of flex pivots is their limited range of motion. However, this is not an issue for the FM1 as the full range of motion must only be 24.31°.

As the nut and transverse bar sweep out an arc, the lead screw and nut assembly is free to pivot off its bottom mount, which has a further flex pivot (as shown in Figures 4.3 and 4.4). This allows a degree of freedom in its movement, and prevents tension building up as the nut moves up and down the lead screw. If the transverse bar was detached from the lead screw assembly, the lead screw assembly would be free to swing to/from the mirror.

The HARMONI design will theoretically provide better repeatability than other comparable mechanisms due to the rotation being directly off the axis of the lead screw with longer actuator arms (so rotation of the lead screw translates 1:1 to a rotation of the mirror based on the length of the actuator arms), and a finer pitch used in the lead screw (reducing the angular rotation per step of the motor). This improves repeatability as lead screws, when compared to worm drives, are easier to maintain and take up a smaller space, but do not allow a large range of motion.

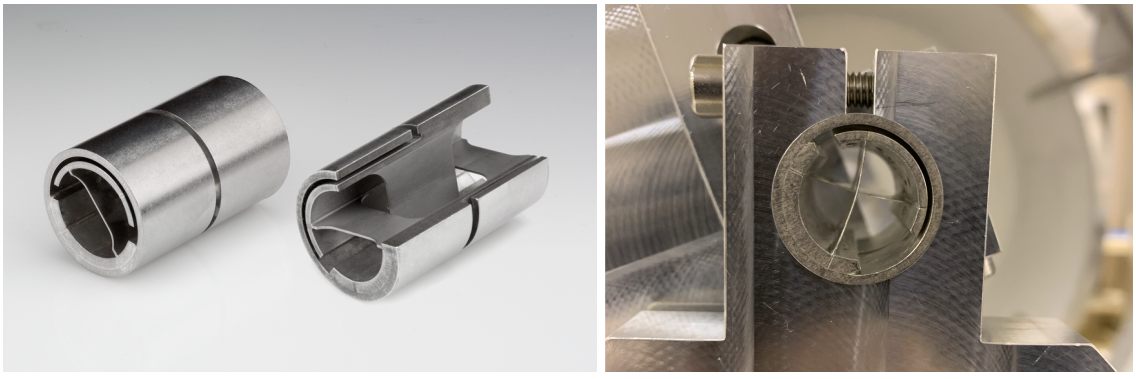


Figure 4.5: (L) External and internal view of a flex pivot. (Source: www.wikipedia.com) (R) Image of a flex pivot used on the FM1. Flex pivots offered many advantages over traditional ball bearings, such as being frictionless and not needing lubrication.

The repeatability of the FM1 is entirely dependent on the movement of the stepper motor. No detents or locks are used. The length of the actuator arms and pitch of the lead screw define

the angular rotation of the mirror per step of the motor. The lead screw has a 2mm pitch, with each step of the motor (200 steps/revolution) corresponding to a $10.3''$ rotation of the mirror (with the actuator arms having a length of 200mm). Assuming a 10% error within a step (the stepper motors used had a quoted inherent positioning accuracy within a step of 5%, or 0.27°, which is doubled to be safe. This value is also in-line with stepper motor error assumptions used in industry with similar stepper motors) (credit: LTN Engineering, 2020), this gives a theoretical $1.03''$ repeatability. Backlash would worsen the repeatability, but this issue was mitigated after both the lead screw and nut were spring-loaded, removing backlash from the system (Section 2.3.2). Increasing the length of the actuator arms is not possible due to size constraints within the spectrograph, and lead screws of this size are not available with a finer pitch.

1.2 FM1 test mechanism design

The FM1 test mechanism is a full-scale 1:1 model of the HARMONI FM1. Unlike the detent mechanism, which was made to purely test a method of repeatability, this allowed testing of a fully completed prototype of the FMM module.

The prototype is shown in Figure 4.6. An aluminium plate is used in place of a mirror, and is bolted directly to the transverse bar rather than mounted in flexures. Testing to quantify the impact of the flexures on the position of the mirror is being conducted separately, and is outside the scope of this thesis. Fully assembled, the unit weighs ~25kg, and is made entirely out of aluminium but with a steel lead screw and flex pivots (the thermal analysis of the design and effects of differing CTE's was done by James Lynn, and is outside the scope of this thesis). The stepper motor is intended to have a resolver attached to help confirm the position of the FM1.

2. Warm Testing

The objective of the warm testing was to optimize the mechanical design and operation of the FM1 prototype so the highest level of repeatability could be consistently achieved ahead of testing in a cold environment. The same testing methodology was followed as with the detent. Tests would first be to characterize the stability of the test setup and identify sources of error

while the mechanism was operational. Formal repeatability tests would then be conducted while mitigating the sources of error identified.

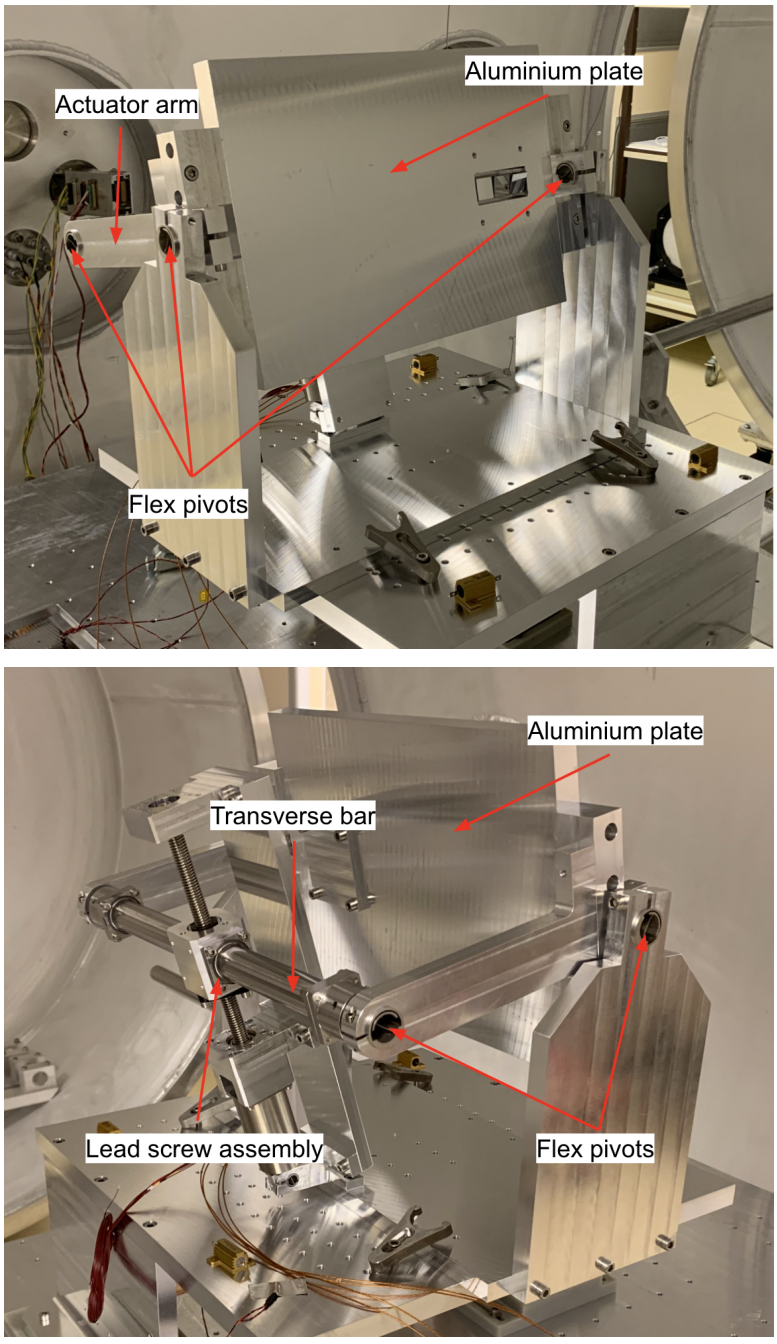


Figure 4.6: (Top) Image of the front of the FM1 test mechanism. The aluminum plate, as well as multiple flex couplings can be seen. The mounting structure was also aluminium. (Bottom) View of the FM1 test mechanism from behind. The lead screw assembly, as well as the transverse bar that rotates the main plate, can be seen.

2.1 Warm test setup

To conduct the warm test of FM1, the mechanism was placed on an optical table and the test mirror aligned to an autocollimator with a 2-inch beam, which would take constant exposures of the angular position of the test mirror in both the X and Y axes. Exposures were once per second. Simultaneously, the stepper motor (a McLennan 23HSX-206 controlled by a Beckhoff PLC) drove FM1 out from its 'home' position to another position, waited, and then returned to the 'home' position. The angular shift of the 'home' mirror before and after the movements could then be compared. The stepper motor was always driven to full steps, as it had to be turned off in between movements to reduce heat load. If the motor was driven to microsteps, it would relax to the nearest position when turned off, negatively impacting repeatability. A diagram showing the warm test setup can be seen in Figure 4.7.

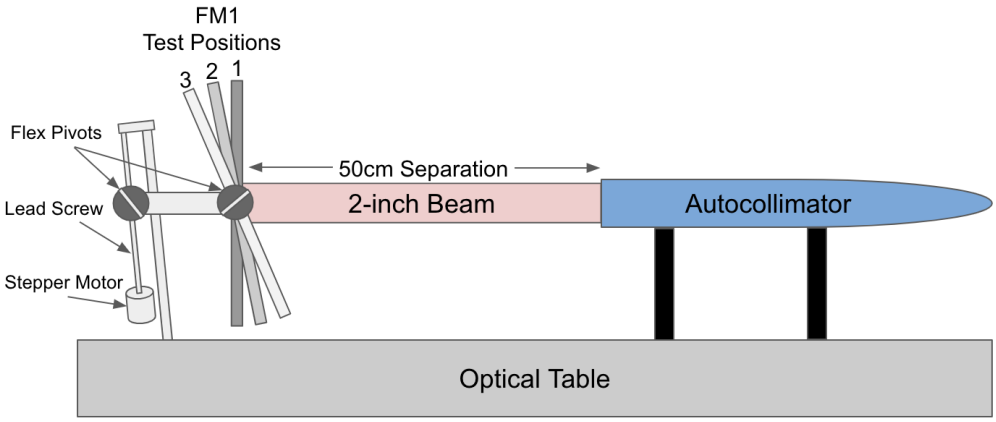


Figure 4.7: Diagram showing the warm test setup of the FM1, as well as the three main positions tested.

All testing discussed below was conducted with a custom three-sided mirror that allowed testing of all three positions of FM1 (Figure 4.8). The final warm test set-up in the lab is shown in Figure 4.9.

2.2 Warm repeatability test plan

The warm testing began with characterization of stability and measurement of background noise, followed by fully operational tests to identify sources of error, and define methods of mitigation. Final repeatability tests were then conducted with the motor moving the system between all combinations of movements between the three positions. Once each of these had passed, the

system underwent an accelerated lifetime test of 15,000 movements. A summary of the warm test plan is shown in Figure 4.10.

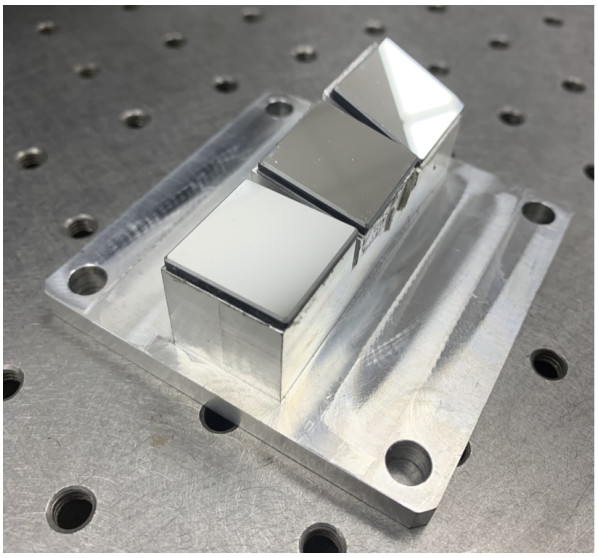


Figure 4.8: The custom three-sided mirror that allowed for testing of all three positions of the FM1.

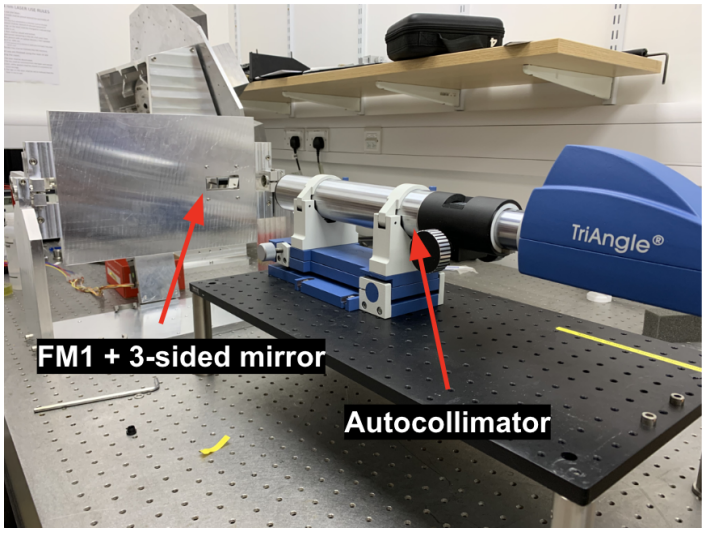


Figure 4.9: Image of the warm FM1 test setup in the lab, with the custom three-sided mirror in place.

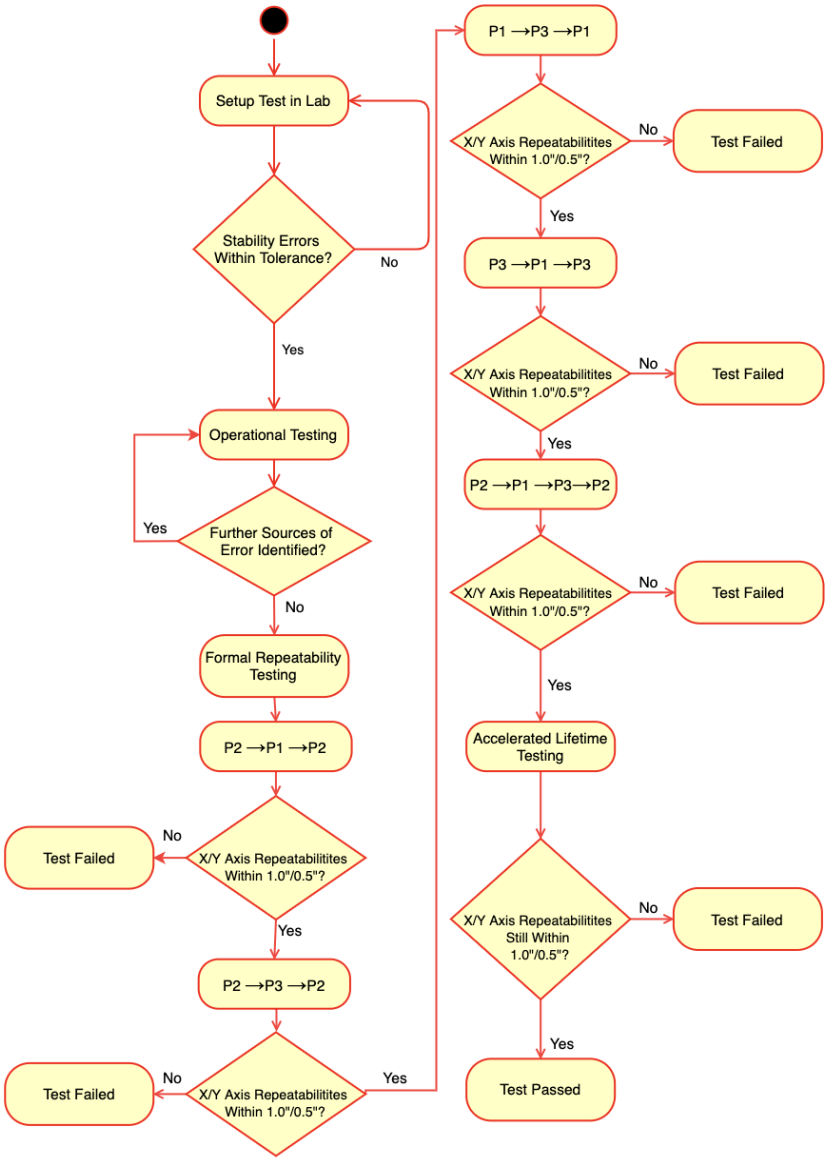


Figure 4.10: The warm test plan of the FM1.

2.3 Optimizing the operation of the FM1

The objective of the moving tests was to determine the highest level of repeatability the FM1 could achieve while in functional operation. Tests were run over extended periods of time (10-72hrs), with movements every 5 minutes (as with the detent mechanism, and within the 6 minute tolerance).

It was found that error was due to four primary sources: thermal expansion due to the stepper motor temperature (Section 2.3.1), backlash (Section 2.3.2), the stepper motor missing

steps (Section 2.3.3), and mechanical wear due to constant operation (Section 2.3.4). The results of these initial tests will be discussed in regards to how they helped identification and removal of sources of error.

2.3.1 Thermal expansion

As discussed in Chapter 2, Section 1.2, this was accounted for by increasing the time in between movements to 5 minutes, which prevented the motor from becoming hot during operation, and improved repeatability by up to 10".

2.3.2 Backlash

Backlash due to the separation between the nut and the lead screw (Figure 4.11), as well as between the lead screw and its mounts at either end, caused significant errors in the repeatability of the FM1. This was noticed when operating the mechanism in multiple directions, as the measurements would be off by the distance of the backlash.

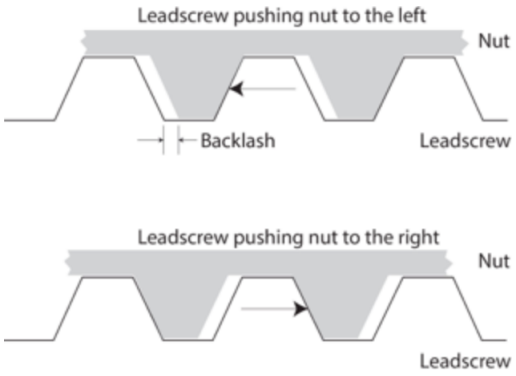


Figure 4.11: The backlash for the FM1 was due to the play in between the lead screw and nut as shown above, and caused significant errors in repeatability. Credit: CNC in the workshop (http://www.cncintheworkshop.com/Backlash.html).

Backlash was most prominent when changing the direction of rotation of the stepper motor. The first few steps of rotation in the new direction would take up the ‘slack’ caused by the play but not actually translate to rotation. The final position of the motor would short by the same amount of steps as the ‘slack’.

As with the detent testing, there was a bi-modal distribution when testing in two directions, as seen in Figure 4.12. The distance between the peaks of these two distributions is the angular separation caused by the backlash.

Two methods were identified that could help mitigate the errors caused by backlash: active compensation by the Beckhoff system, and eliminating the mechanical play in the mechanism.

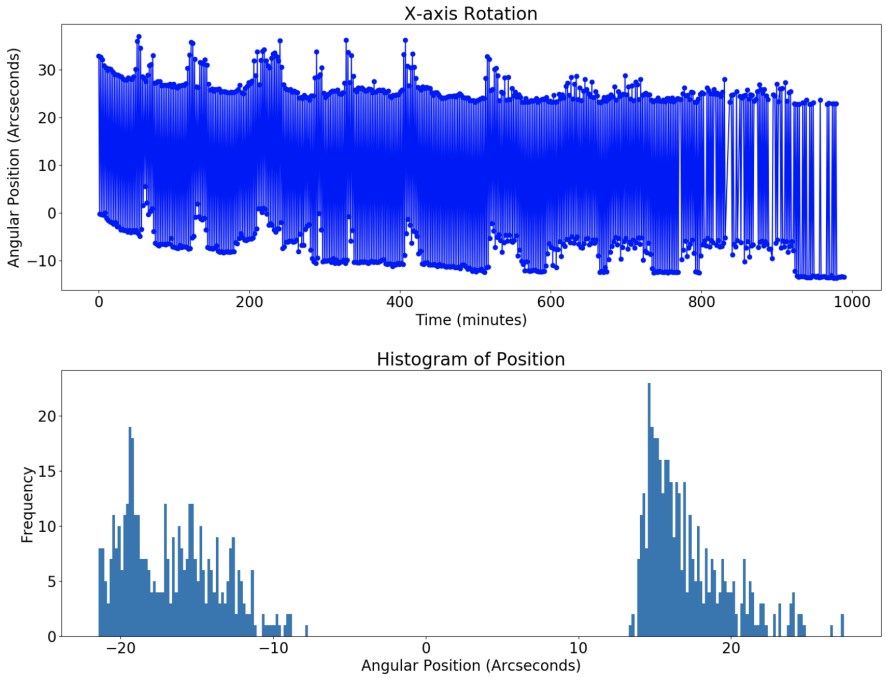


Figure 4.12: (Top) Plot of rotation about the X-axis vs time. (Bottom) Histogram of the measurements. The repeatabilities of each distribution are low and are skewed, but this is disregarded as the purpose of this figure is only to demonstrate the effect of backlash, and the test was not conducted with mitigation of sources of error.

Active compensation for backlash

To eliminate negative effects due to backlash, the Beckhoff system allowed for active compensation (see Figure 4.13 for the movement profile). This was not used in warm testing as there was no resolver to confirm the absolute starting position (regardless of motor steps) of the FM1 ahead of any of the three positions, making the operation useless.

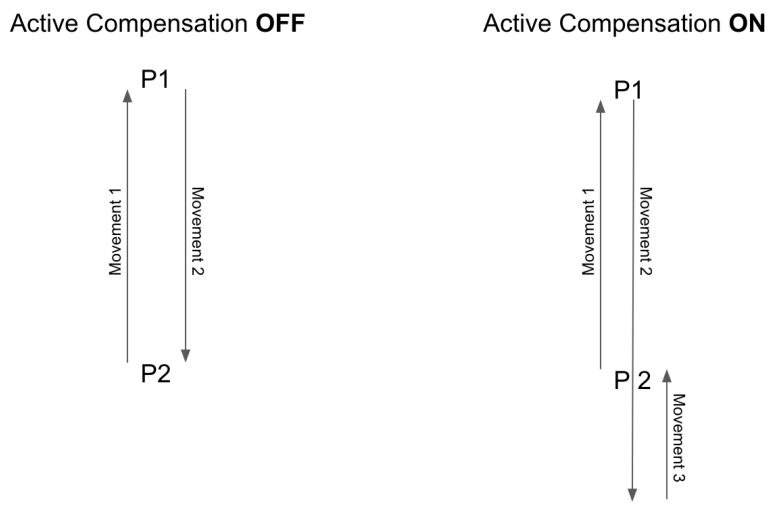


Figure 4.13: The two movement profiles tested. With the active compensation off (L), the motor simply drove away from the home position and then back again. With the active compensation turned on (R), the motor would drive past the starting position by a distance larger than the play in the system, and then drive back.

Play in the lead screw and within the nut

While building the system, there was not a strict tolerance on the preload of the lead screw (applied by opposing angular bearings at each end of the lead screw). This preload prevented the lead screw from moving in position relative to its mounts. When the FM1 was first assembled, the angular bearings were not applying enough force to the lead screw, which caused significant amounts of play and led to significant errors. Furthermore, within the nut itself, there was initially no spring to provide a return force on the lead screw, leading to further backlash.

To remove the play, the preload on the angular contact bearings was increased. The backlash between the lead screw and the nut was also similarly mitigated by ensuring a spring-loaded nut was used. Both of these methods of mitigations were viable for cryogenic use, as the backlash was being removed only by pre-loads from angular contact bearings and springs which were designed to maintain the preload at cryogenic temperatures (they would need to be loosened before cryogenic operation). These removed the errors due to backlash, improving repeatability by over 30" when testing in multiple directions.

2.3.3 Stepper motor missing steps

The biggest source of error was due to missed and skipped steps. Initially, it was not known if these were due to the motor, the Beckhoff control system, or some part of the mechanism itself causing excess resistance. Each missed step is roughly ~10", which is in agreement with the calculated value of 10. 3" in Section 1.1.

An example of missed steps can be seen in Figure 4.14. At points, complete steps are missed, but then over time the motor goes back to its original position. The return to the home position is also quantized, as highlighted in Figure 4.15. It takes multiple movements for the motor to return to its initial position, and it returns by fractions of a step. The cause of this is not known.

Five potential sources of the missed steps were investigated: the motor rotation being in fractions of steps, turning the motor off after movements, the motor's acceleration and deceleration, the motor's maximum rotational velocity, and the tightness of the flex pivots.

Moving in increments of 1.8° (full steps) at the motor

The motor had 200 steps per revolution, and the Beckhoff system defined rotation in degrees of rotation at the motor. If the movement specified in degrees wasn't a common factor, the final position would be at a fraction of a step. As such, the motor was always driven to a full step (1.8° per step).

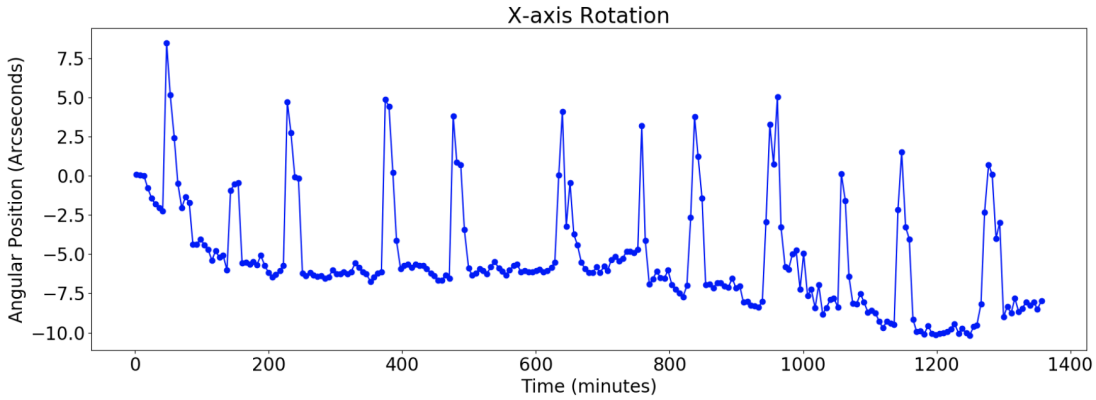


Figure 4.14: A plot of rotation about the X-axis vs time. Each missed step is roughly ~10", which is in agreement with the calculated value of 10. 3" in Section 1.1.

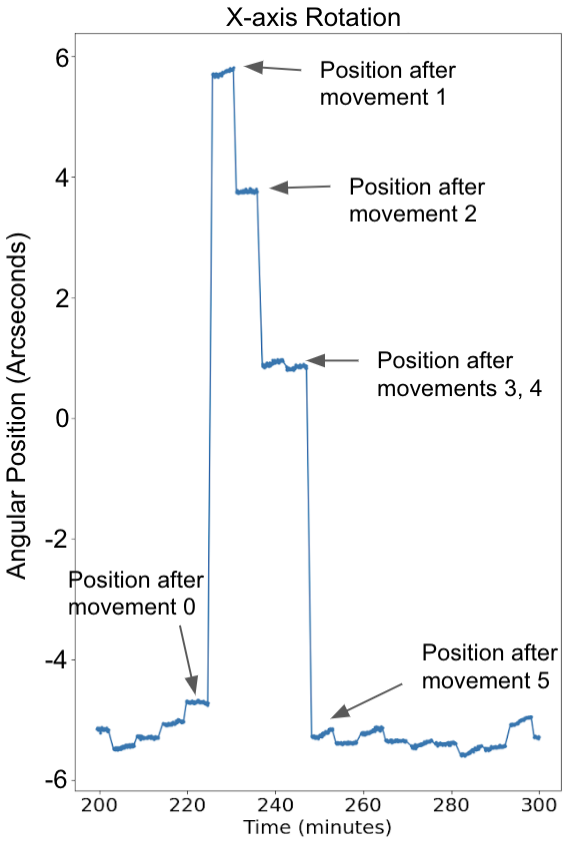


Figure 4.15: This plot is a slice from 200 to 300 minutes of Figure 4.14. The 'quantized' nature of the missed steps can be seen. Each line corresponds to the angular position of the FM1 after a movement.

Turning off motor in between movements

Another cause for skipped steps was whether or not the motor was turned off in between movements. While this had consequences for motor temperature (as keeping the motor idling in between movements added significant heat), a more significant issue was that the motor would relax to the nearest step when turned off. As such, the motor was always driven to a full step (as stated above), including while the mechanism was at its 'away' position. Therefore, the motor would turn off two to three times in between exposures, depending on the test. This was in agreement with HARMONI requirements that motors be turned off when not in use.

Acceleration

The Beckhoff software was edited to define acceleration and deceleration parameters of $25°/s^2$. This number was chosen as it was well within the torque limits of the motor. With a slower

acceleration, the torque would improve minimally (<1%), and the mechanism would take too long to move between positions.

Maximum velocity

A maximum velocity of $500°/s$ was defined, which is fast enough to meet HARMONI requirements, but slow enough to ensure not too much stress is put on the motor, causing missed steps. This also corresponded to ~300steps/second, where the motor provided maximum torque.

Tightness of flex pivots

When initially setting up the system, the flex pivots were incorrectly relaxed at the top mirror position. As the mechanism drove further and further away from this position, tension built up in the springs, adding a slight return force. At small distances, this wasn't an issue, but over distances longer than 7200° - the distance between two positions - the force was high enough to put too much torque on the motor, causing it to miss steps. This explains why good results were achieved with tests of shorter movements, but as larger distances were tested the repeatability went down significantly.

To solve this issue, the mechanism was taken apart, and the flex pivots were relaxed and had their 'home' rest position defined as the central mirror position (P2). This significantly reduced the error due to distance, as the maximum distance away from P2 was limited to $\pm$one mirror position.

The issue of missing steps was compensated for through a mixture of dealing more effectively with temperature, introducing gradual acceleration and deceleration, always driving to a full step, and relaxing the flex pivots to the central mirror position. Together, these removed the missed steps, improving repeatability by up to 10".

2.3.4 Mechanical wear due to constant operation

After the optimization testing had concluded, the mechanism was dismantled. As seen in Figure 4.16, the flex coupling had sheared. It is not known when this happened. However, this clearly

was causing large amounts of error, as the driveshaft would have been spinning without translating to actual motion. Over three lifetimes of movements had been conducted before this was noticed.



Figure 4.16: The sheared flex coupling. One of the unit's spiral veins broke after constant use.

The flex coupling sheared because it was undersized. Both sides required being bored out to accept the larger motor shaft and the large lead screw. The size to which it was bored out was larger than the flex coupling's specifications allowed, ultimately causing it to shear.

Subsequent testing used a larger flex coupling so that the hole diameter required for the shafts was smaller than the maximum allowed for the coupling. On reassembly particular care was taken not to compress the coupling spiral vanes and to reduce axial misalignment.

2.3.5 Conclusions from the optimization tests

A summary of all the errors found and solutions is presented in Table 4.2.

2.4 Warm repeatability tests

The final repeatability testing involved using the mitigations for all of the sources of error that were discovered in the optimization testing. The measurements while the mirror was in position during each movement were averaged, such that each movement corresponded to one data point.

All combinations of movements between the three positions were tested. Active backlash compensation was not used.

Problem	Mitigation	Improvement (arcseconds)
Motor heating up	Tests were conducted with a rest time between movements of 5-8 minutes.	Up to 10
Backlash	The preloads both on the lead screw and within the nut was increased, limiting play.	> 30
Motor missing steps	1) The motor was always rotated in increments of 180°. 2) The motor was turned off in between movements. 3) A gradual acceleration and deceleration was applied for each movement. 4) The maximum velocity was limited to 500°/s. 5) The flex pivots were relaxed around P2.	Up to 10
Shearing of flex coupling	A larger and stronger flex coupling was installed.	N/A

Table 4.2: This table shows all of the main problems encountered with the optimization testing of the FM1, along with corresponding solutions for each. The validation testing was conducted while incorporating all of these solutions.

2.4.1 Repeatability about the X-axis

A plot of a representative test can be seen in Figure 4.17. This test, from P2→P1→P3→P2, produced repeatability about the X-axis of $0.30"$ ($0.52"$ absolute, and $0.27"$ with a 2nd order polynomial fit) which was well within tolerance. This confirmed that mitigating the sources of error significantly improved repeatability. While there appears to be some regular structure in the errors, with some movements consistently off by $\pm\ 0.5"$, this is likely systematic and likely from low-level vibrations or noise in the mechanism. This structure is not seen in the histogram of all the tests (Figure 4.19). As in the repeatability tests of the detent mechanism, temperature recordings were not made during the testing. However, as discussed in Chapter 2, the overall drift can be removed as it is due to temperature, and the absolute drift during this test on timescales of 1hr was negligible ($<<\ 0.1"$).

2.4.2 Repeatability about the Y-axis

Angular repeatability about the Y-axis, seen in Figure 4.18, was also well within tolerance (0.5") at 0.013"(0.16" absolute, and 0.010" with a 2nd order polynomial fit). It is clear drift about the Y-axis is on a similar scale as with the long-term stability tests (Figure 2.8 - stability at 0.013"), meaning that the flex pivots are not subject to any significant runout while moving. Again, the absolute drift during this test on timescales of 1hr was negligible ($<< 0.1$").

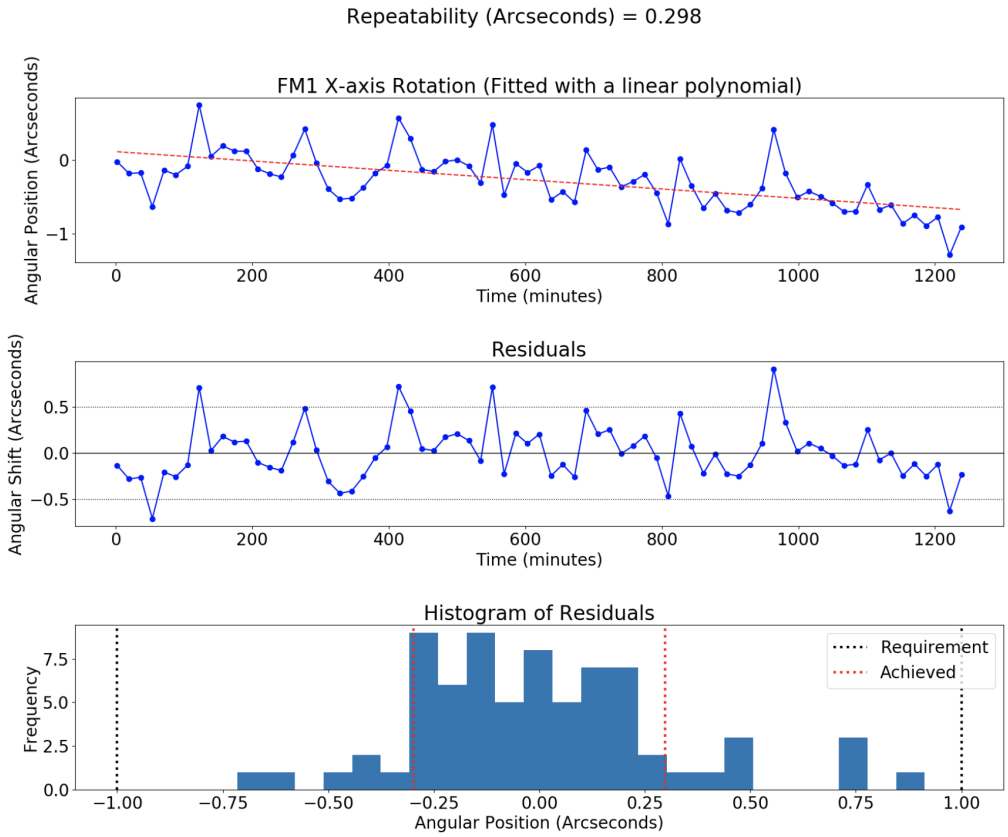


Figure 4.17: (Top) Angular rotation about the X-axis vs time for P2→P1→P3→P2, with a polynomial fit to the trend. (Middle) The residuals of the fit, plotted against time. (Bottom) A histogram of the residuals.

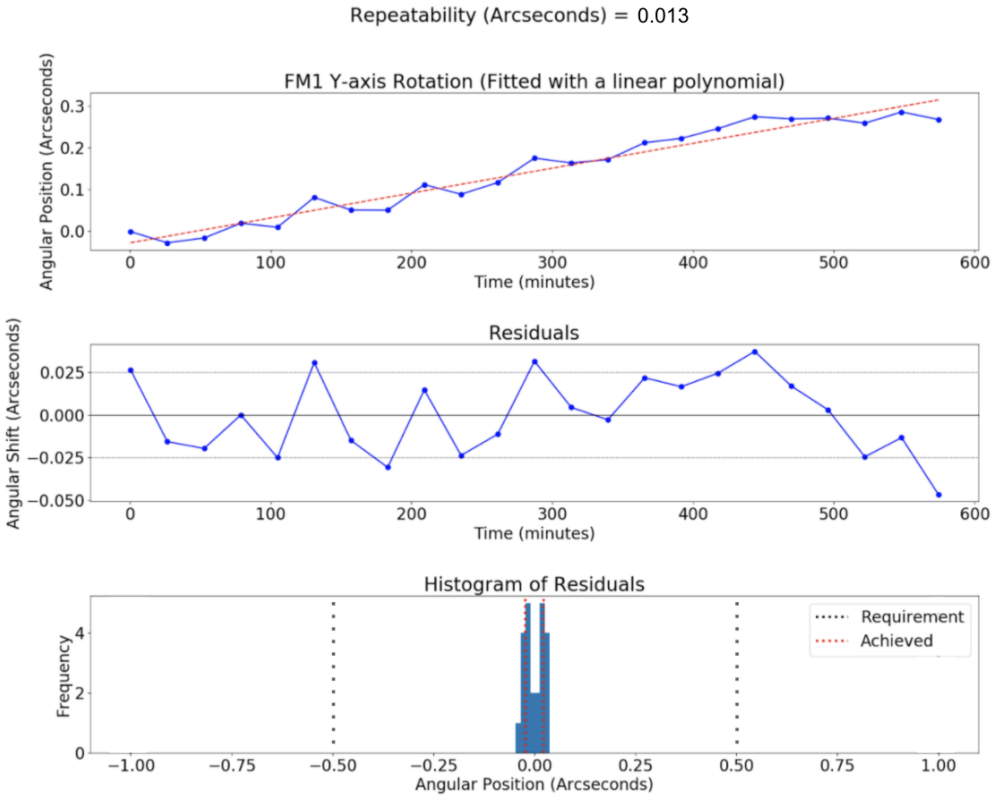


Figure 4.18: (Top) Angular rotation about the Y-axis vs time, with a polynomial fit to the trend. (Middle) The residuals of the fit, plotted against time. (Bottom) A histogram of the residuals.

2.4.3 Accelerated lifetime performance

Over the course of the verification testing, over 15,000 movements were accumulated. There was no noticeable wear to the system or degradation of the measured repeatability. The flex coupling also did not shear during the verification testing as it did in the optimization testing. It was therefore concluded that the system is repeatable in warm environments over the HARMONI system lifetime.

2.5 Final warm repeatability performance

Testing the FM1 in its optimal configuration while implementing the mitigations for sources of error achieved consistent repeatability well within the goal tolerance of $1.0"$. Results were in the $0.3"$ range irrespective of the position tested ($0.57"$ absolute repeatability, and $0.27"$ with a 2nd order polynomial fit). Out to ~3σ, repeatability is $< 1.0"$, indicating that 99.7% of movements

will be within tolerance. Figure 4.19 shows a histogram of the residuals for rotation about the X-axis for all of the validation tests. Stability and repeatability about the Y-axis were well within tolerance and trivial, and accelerated lifetime tests also passed. Thus, the FM1 passed its warm test, and progressed to cold testing at 130K. The remaining errors are likely due to small amounts of residual play and vibrations, as well as micro inaccuracies in the step sizes of the motor. A summary of the warm repeatability can be found in Table 4.3.

X-axis Repeatability Tolerance (RMS)	**1.0"**
Y-axis Repeatability Tolerance (RMS)	**0.5"**
Test Type	**Repeatability (RMS)**
X-axis	0.32"
Y-axis	~0.02"

Table 4.3: A table showing the repeatability tolerances in both axes, as well as the results for six representative tests from the warm testing. The repeatabilities are well within tolerance.

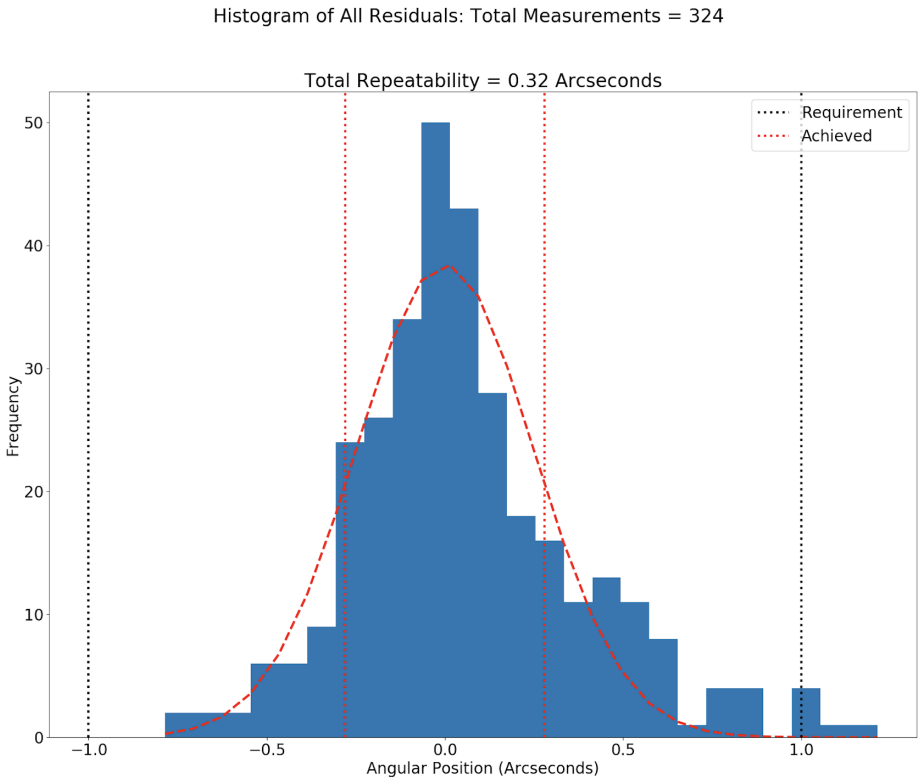


Figure 4.19: Histogram of the warm repeatability test results about the X-axis. The combined repeatability is 0.32" RMS, well within tolerance. A Gaussian is fitted to the distribution, shown in red.

3. Initial Cold Testing

Initial cold tests were conducted with the Fold Mirror 1 mechanism in the HIRDLS Chamber (Dials, 1997) in the Department of Atmospheric, Oceanic, and Planetary Physics. This section will discuss the experimental setup, as well as the results from the initial cold tests.

3.1 Cold test setup

Ahead of testing the FM1 at the cryogenic temperature of 130K $\pm$2K, multiple modifications had to be made to the mechanism in preparation. First, the entire mechanism was disassembled following the warm testing with each part individually cleaned of grease, with special attention paid to all bearings, as any grease would freeze at cold temperatures, locking the mechanism in place.

The mechanism was then rebuilt (with a Phytron VSS 42.200.2.5 cryogenic stepper motor in place of the McLennan 23HSX-206 stepper motor used with the warm testing), and mounted inside the cryostat on top of a base plate, which was bolted to a cold plate via G10 thermal standoffs, as seen in Figure 4.20. The LN_2 lines were directly below the cold plate. The three-sided mirror was aligned to the autocollimator through a viewing port mounted on one of the chamber's side flanges. Specific care was taken to ensure the beam was as close to the center of the window as possible, as the beam hitting the metal edges of the flange would cause aberrations. All three positions of the mirror were simultaneously within the field of view of the autocollimator, allowing all positions to be tested without any external adjustments.

The mechanism was then quickly re-tested in the warm by cycling through all three positions multiple times over the course of 6 hours. The purpose of this was to verify and ensure that the cleaned and prepped mechanism with the Phytron motor still provided the same levels of repeatability in the warm as found in Section 2 of this chapter. All results were $\pm$5% of those found in Section 2, thus verifying the mechanism was working as intended ahead of cold testing.

8 thermometers and 5 heaters were placed on the mechanism, as shown in Figure 4.21. These were connected to two external Lakeshore units for temperature monitoring and control. Copper straps were used to connect the cold plate directly to the mounting legs of the FM1 to

ensure proper and even cooling. The mechanism was then mounted inside a large custom-built radiation shield, as seen in Figure 4.22, with a side port to allow the beam of the autocollimator to be unobstructed.

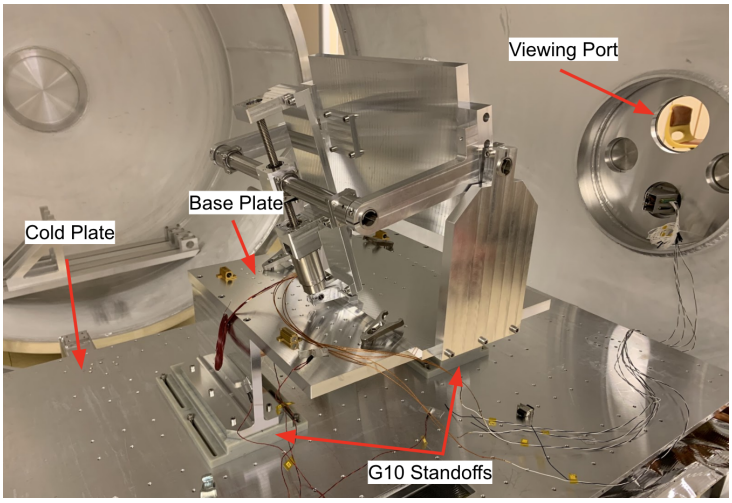


Figure 4.20: An image of the FM1 mounted in the HIRDLS chamber ahead of cryogenic testing.

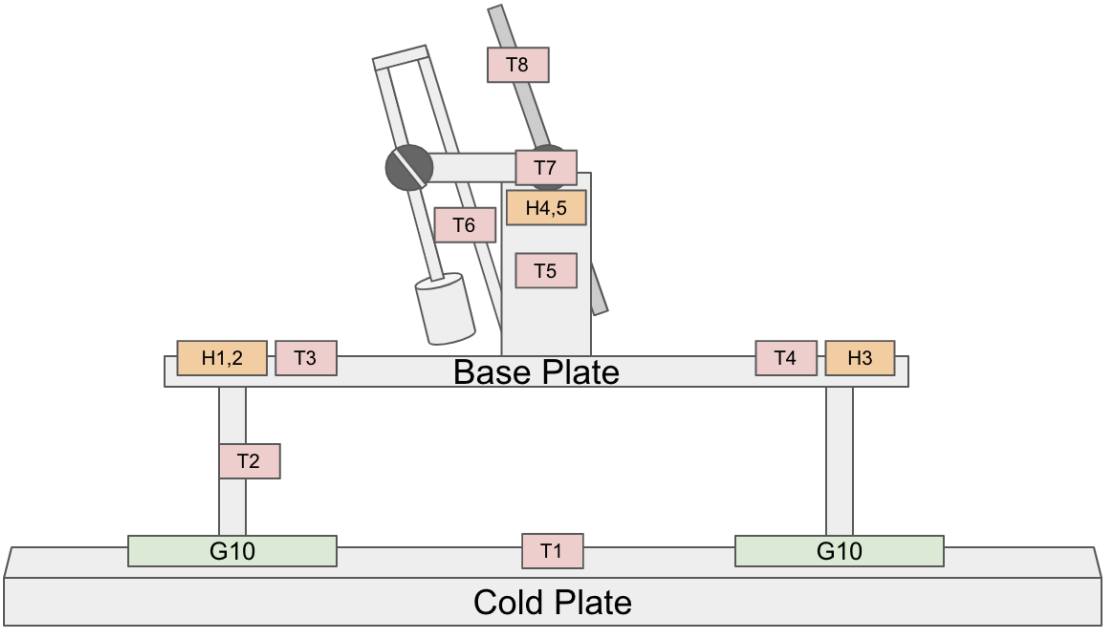


Figure 4.21: A diagram showing the locations of the thermometers and heaters for the FM1 cold test, indicated by red and orange boxes, respectively. Heaters 1 and 2 were on opposite ends of the left side of the base plate ('into' the page in the figure), with Heater 3 at the center of the right side. Heaters 4 and 5 were mounted on each of the two mounting legs of the FM1.



Figure 4.22: (L) An image of the FM1 inside the chamber with the radiation shield mounted. (R) The FM1 within the radiation shield, as seen through the side port. This is equivalent to the viewpoint of the autocollimator.

The chamber was then closed, pumped down, and cooled via a forced-flow LN_2 system from an external 180L dewar. The temperatures of the FM1 were monitored every 30 minutes, with cooling beginning at 8:00AM each morning, and ceasing at 8:00PM each night (as the dewar was empty), with the chamber warming by ~20K overnight. The initial cooldown to 130K was slow, taking almost 48 hours, due to suboptimal thermal coupling.

3.2 Initial cryogenic testing results

The mechanism was not tested as it cooled down, so as to prevent any parts breaking if the temperature (and therefore thermal contraction) across the mechanism was not uniform. Once the entire mechanism was uniformly at 130K$\pm$2K, simple movements were attempted. Unfortunately, the mechanism did not operate properly, even as the speed and torque of the motor were varied.

However, the angular position of the mirror oscillated periodically between $\pm$ 5" $-$ 10" as movements were attempted and the motor was running. This indicated that movement of the

motor did translate to rotation of the mirror - which was a good sign, and meant that the moving parts in the mechanism, and specifically the flex pivots, were not frozen and still free to move while at 130K. The small movements of the motor were successfully translated through the flex coupling to the lead screw, then to the nut, actuator arms, flex pivots, and ultimately to rotation of the main mirror.

It is likely that the periodic oscillation came from the motor being over torqued, and it was attempting to move, but was being prevented by too high of a return force. It was noted that the amplitude of the oscillation in arcseconds was smaller as the ΔT across the mechanism was larger. At $\pm$2K, the oscillation was ~10", or roughly one step. At $\pm$5K, the amplitude was at most 5". This indicated that the motor was unable to move because of different thermal expansion of the parts in the mechanism - most likely between the plastic nut and the steel lead screw, with the nut getting smaller and constricting the lead screw when at low temperatures. It is noted that a resolver was not used here to confirm the position of the motor, as it required additional Beckhoff wiring which was not available.

The mechanism was then brought to warm temperature over two days and dismantled. As the temperature rose, the mechanism was tested at every increase of 10K. At 240K, the mechanism worked as intended, providing the same levels of repeatability as found in Section 2 of this chapter.

Once the mechanism had been disassembled, it was found that the nut was made from Acetal, a non-cryo rated plastic. This confirmed that the issue was thermal contraction of the nut onto lead screw at cryogenic temperatures, causing the motor to be over torqued and preventing motion. As the motor attempted to rotate, it would be pushed back by the lead screw which was locked in place from the constriction of the nut, and would 'fail' to complete a step, and relax back to its initial position. This would then repeat until the motor was stopped. This explains the observed 'oscillation' of movement. Thermal models confirmed that 240K was the lowest temperature at which the mechanism would work with Acetal, and even at 240K the mechanism was very sensitive to a non-uniform ΔT, with $\Delta T_{max,\,240K} = \pm 1$K.

In future testing, the mechanism will feature a nut made out of Torlon, a cryo-rated plastic that will not contract significantly at cryogenic temperatures, and which thermal models predict will work with the FM1 at 130K. As the other parts of the mechanism were proven to function at a basic level at 130K, such as the flex pivots (as the small motions of the motor

translated to rotation of the mirror over a very limited range), once the Torlon nut is used the mechanism may operate as intended. However, exhaustive tests over the full range may expose new issues.

4. FM1 Testing Conclusions

4.1 Warm

The FM1 operated well within tolerance (1.0") in warm temperatures. Results were in the 0.3" range irrespective of the position tested, with the overall RMS repeatability at 0.32". Out to ~3σ, repeatability about the X-axis was $< 1.0"$, indicating that over 99.7% of movements will be within tolerance. Stability and repeatability about the Y-axis were within tolerance, and accelerated lifetime tests also passed. Furthermore, even when there was no linear fit to remove the drifts due to temperature, tests about both axes still achieved absolute repeatabilities that were still within tolerance.

The remaining errors were likely due to small amounts of residual play and vibrations, as well as micro inaccuracies in the step sizes of the motor. These are very high levels of repeatability, especially for a mechanism of this size, and indicate that this type of lead screw mechanism could be used elsewhere within HARMONI, such as with the Fold Mirror 2.

4.2 Cold

Initial testing at the cryogenic temperature of 130K±2K demonstrated that many of the moving parts of the FM1 mechanism worked, as movements of the motor translated to rotation of the mirror. However, a non-cryo rated plastic used in the nut, Acetal, prevented rotation of the lead screw. This caused the motor to be over torqued, and it was unable to move past one step.

5. Future Work

To complete the cold testing of the FM1 and verify its performance at cryogenic temperatures, a Torlon nut will need to be made for the mechanism. Once this part is available, cryogenic testing will be initially conducted for only the lead screw and drive mechanism of the FM1. This small unit will be easier to cool down, and if it works, will provide proof of concept in the cold for the FM1 mechanism as a whole. The full mechanism will then be assembled and tested following the same test plan as with the warm testing.

Despite the movements of the motor translating to rotation of the mirror, indicating there were no issues with any bearings at cryogenic temperatures, the angular bearings for the lead screw will also be dry lubricated with Molybdenum Disulphide to ensure proper operation.

As the repeatabilities from the warm testing were well within tolerance, it is unlikely that further fundamental changes and modifications to the mechanism will be needed.

Chapter 5

Testing of the Infrared Grating Module

The purpose of the Infrared Grating Module (IGM) is to accurately position 1 of 10 gratings in the path of the folded, collimated beam. The IGM must rotate to each of the 10 positions with high repeatability to ensure the dispersed beam enters the camera at the appropriate angle. In all tests, repeatability was defined as the RMS error of the movements (1σ, assuming a Gaussian distribution). Rotation of the IGM translates to a shift of the beam about the spatial axis of the detector. A working design utilizing a stepper motor driven worm gear has been fully developed by James Lynn to meet these mechanical requirements, and a prototype has been built by the Oxford Physics mechanical workshop.

The design features a large rotating wheel with fixed positions for up to 10 gratings, and the module must meet strict tolerances on repeatability. The axes of repeatability of the gratings are defined in Figure 5.1, and the goal repeatabilities for the position of the gratings of the IGM are shown in Table 5.1. Tolerances on the impact of translation of the grating and the corresponding light lost are outside of the scope of this thesis.

Many other astronomical systems and instruments use worm-driven grating exchange mechanisms that achieve similar levels of repeatability, such as KMOS (Sharples et al. 2013), EMIR (Garzon et al. 2016), and CRIRES (Kaufl et al., 2004). The achieved repeatabilities are in the range of tens of arcseconds. Furthermore, none are as large as the HARMONI IGM, which has a diameter of over 1100mm with the gratings mounted. Worm gears are more generally used in ESO instruments for positioning mechanisms than lead screws. While they may not provide as high levels of repeatability, they are mechanically less complex, allow for full 360° rotation, and

are easier to incorporate into rotating designs. The HARMONI IGM design incorporates a larger gear ratio than the aforementioned units, which will theoretically translate to higher achieved repeatabilities. The main challenge, however, is achieving even comparable repeatabilities with a mechanism of this size.

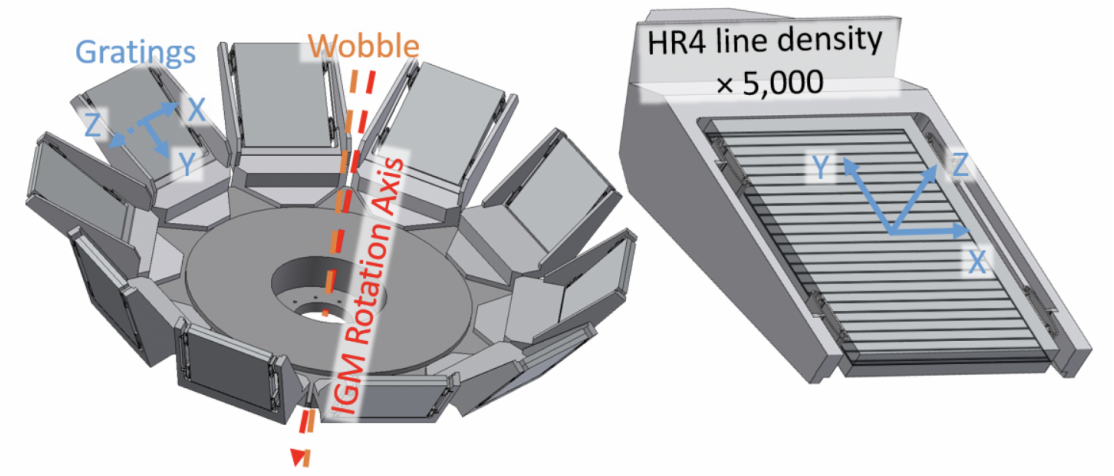


Figure 5.1: A CAD model of the Infrared Grating Module (L), and of a grating (R). The repeatability axes of IGM are highlighted in blue. The tolerances for each axis are shown in Table 5.1. Credit: John Capone.

	X	*Y*	*Z*
Repeatability (RMS)	5. 0"	5. 0"	1. 0"

Table 5.1: A table showing the RMS repeatability tolerances for the IGM about the grating axes defined in Figure 5.1.

Achieving arcsecond-level repeatability on a mechanism of this size at 130K is a significant challenge, but the system does not need to operate to tolerances as strict as the FM1 or detent. The rest of this chapter will discuss the design of the IGM and of the IGM prototype. The prototype was then tested at warm temperatures, with all preparations made for forthcoming tests at cryogenic temperatures.

1. Design

1.1 HARMONI IGM design

The IGM (Figure 5.2) consists of a rotating wheel mounted on a bearing housing that is attached to a worm gear. The worm gear is driven by a McLennan 23HSX-206 stepper motor in the warm (for cold testing, a Phytron VSS UHVC 57.200.2.5 will be used) with a 210:1 worm drive reduction. The rotating wheel has positions for 10 grating mounts (fixed and unable to change angle) on the side opposite to the spur gear, with flexures used to hold the gratings in their mounts. The effect of the grating mounts and flexures on the performance of the grating while operating has not been investigated. With the gratings attached, the total diameter of the mechanism is ~1100mm and it weighs ~80kg.

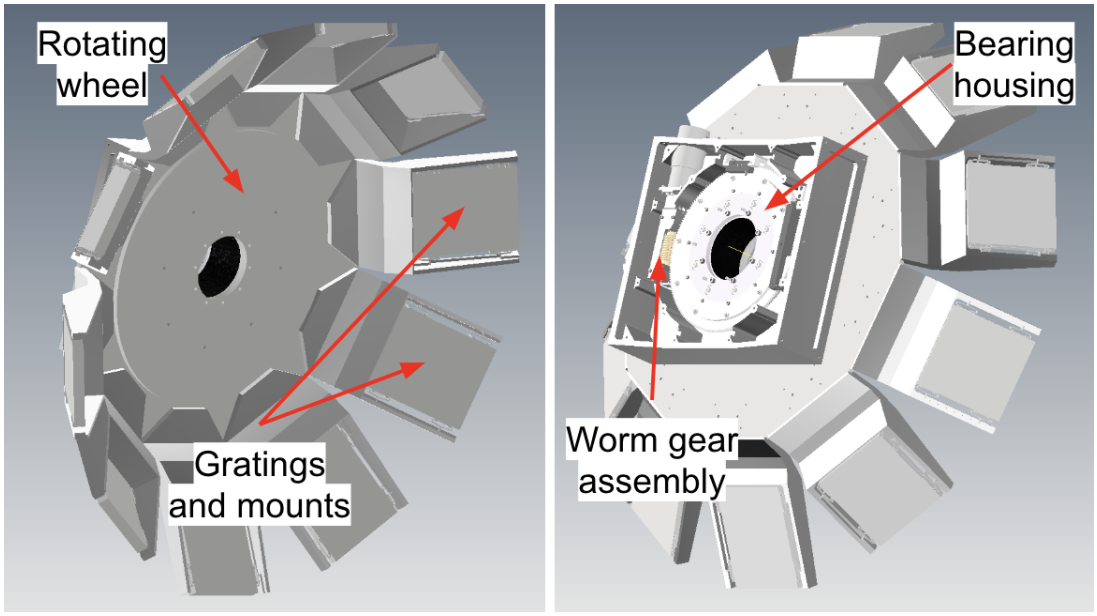


Figure 5.2: (L) CAD model of the IGM showing the rotating wheel as well as the gratings and mounts. The total diameter of the module is ~1100mm and weighs nearly 80kg. (R) CAD model of the IGM showing the worm gear assembly, as well as the bearing housing. A stepper motor drives the system via the worm gear assembly.

The stepper motor is connected to the worm gear via a flex coupling, with a larger diameter than the one used with FM1. The flex coupling is secured to both the motor drive shaft and the worm with spring pins to ensure it does not slip during operation. The worm is housed in a steel mount, which is bolted to the aluminium frame (Figure 5.3), and pushed towards the worm gear with a metal shim to minimize play (this is discussed further in Section 2.3.2).

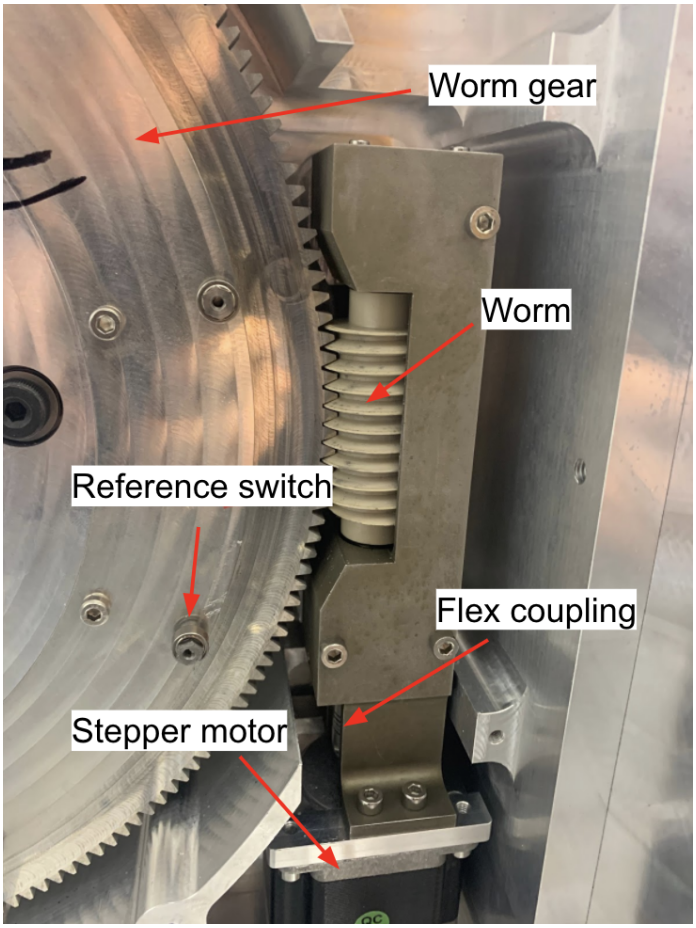


Figure 5.3: An image of the worm gear assembly on the IGM prototype (discussed in Section 1.2). The stepper motor drives the worm gear, which rotates the spur gear. The stepper motor is connected to the worm gear with a flex coupling.

The spur gear has mounting points for reference switches (with sensors at each grating position) to electronically record the position of the IGM; the switch is located at the base of the mechanism. The worm gear and the wheel, both aluminium, are connected by a large bearing housing. This holds two steel angular contact bearings, positioned in opposing directions so the force applied removes play perpendicular to the axis of rotation. Two flexures are used to center the bearings within the bearing housing, and ensure they stay central when the housing contracts in cryogenic temperatures (Figure 5.4).

A friction brake is used to hold the position of the wheel along the axis of rotation when the stepper motor is not in use to mitigate backlash. Both the friction brake and worm gear are made out of Vespel SP-3 MoS2 - a cryo-rated plastic.

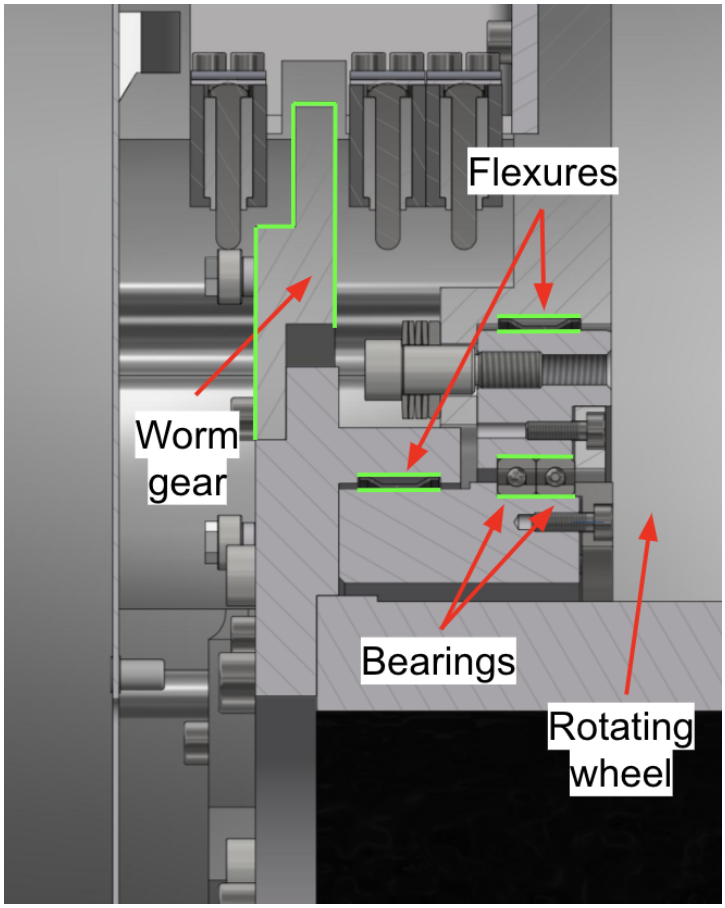


Figure 5.4: A CAD drawing of the bearing housing, with the wheel oriented vertically and extending out of the page. The two bearings can be seen, as well as the flexures that were used to maintain the clearance relative to the driveshaft. The worm gear is seen on the opposite side to the rotating wheel.

As with the FM1, the repeatability of the IGM is entirely dependent on the movement of the stepper motor. No detents or locks are used. The radius of the wheel and gear ratio of the worm define the angular rotation of the wheel per step of the motor. The total gear ratio between the stepper motor (200 steps/revolution) and the IGM is 1:210, with each step corresponding to a 30.86"rotation of the IGM. Assuming a 10% error within a step (as with the FM1, the stepper motors used had a quoted inherent positioning accuracy within a step of 5%, or 0.27°, which is doubled to be safe. This value is also in-line with stepper motor error assumptions used in industry with similar stepper motors) (credit: LTN Engineering, 2020), this gives a theoretical 3.09" repeatability. Increasing the radius of the wheel is not possible due to size constraints within the spectrograph, and a larger gear ratio could cause increased errors due to smaller cogs (such as increased wear).

1.2 IGM test mechanism design

The IGM test mechanism is a 1:1 model of the IGM (Figure 5.5). The unit is made primarily from aluminium and is very large, weighing over 50kg and almost 1 metre in diameter. With the gratings and grating mounts in place, this weight exceeds 80kg, and the diameter is over 1.3 metres. As the HARMONI 1-metre chamber will not be large enough to accommodate this large of a mechanism, and because the gratings and grating mounts are not yet available, the gratings and grating mounts were replaced with ‘dummy masses’ at each grating position. The dummy masses are steel blocks that weigh exactly as much as a grating and its mount. While they will not impact the movement of the IGM exactly as the gratings and grating mounts will, they are a close enough replacement for the prototype testing.

The IGM prototype is mounted on two large aluminium brackets, and inclined at the HARMONI operational orientation of 17°. This ensures the torque applied by gravity is exactly the same as it will be in the real instrument, which may significantly impact performance. The stepper motor is intended to have a resolver attached to help confirm the position of the IGM.

2. Warm Testing

As with the detent mechanism and the FM1, warm testing would first characterize the stability of the setup, followed by operational tests to identify sources of error. Formal repeatability tests would then be conducted while mitigating the sources of error.

The mechanical concepts of the detent mechanism and IGM were relatively similar, and some of what was learned with the detent, such as the impact of backlash, was directly applied to the testing of the IGM.

2.1 Warm test setup

To conduct the warm test of the IGM, the mechanism was placed on an optical table and the test mirror aligned to an autocollimator, which would take constant exposures of the angular position

of the test mirror in both the X and Y axes. The mirror was mounted tangential to the rotation of the grating wheel, to ensure that the system replicated the grating location. A diagram of the test setup can be seen in Figure 5.6. The detector of the autocollimator was also oriented at 17°, so that measurements would be purely in the axis of rotation of the IGM and perpendicular to that axis.

As with the detent mechanism, rotation about the X-axis of the IGM was equated to rotation about its Z-axis, as a shift about the X-axis for one grating would be the same as a shift about the Z-axis for a perpendicular grating. These concepts are outlined in Figure 5.7.

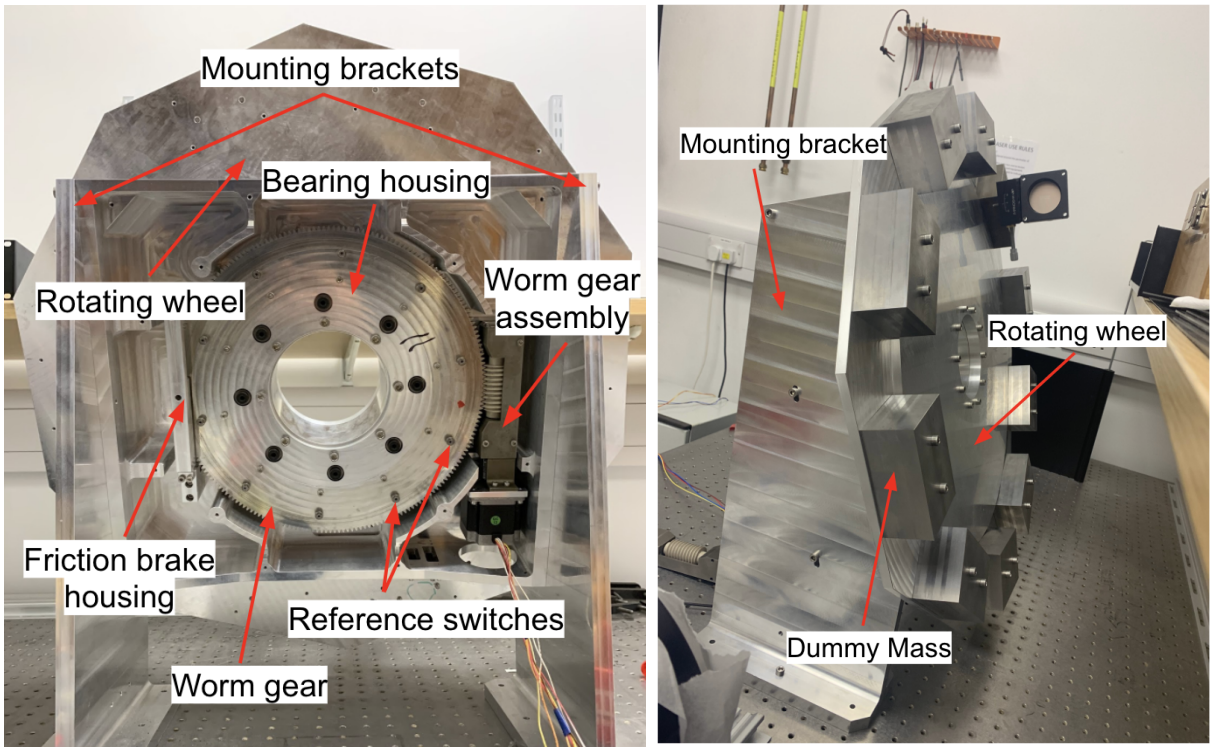


Figure 5.5: (L) Image of the back of the IGM prototype. The rotating wheel, as well as the spur gear and worm gear assembly can be seen. (R) View of the front of the IGM prototype. The 10 dummy masses can be seen, which weighed the same as a grating in a mount. The mounting brackets inclined the IGM at 17°, the HARMONI operational orientation.

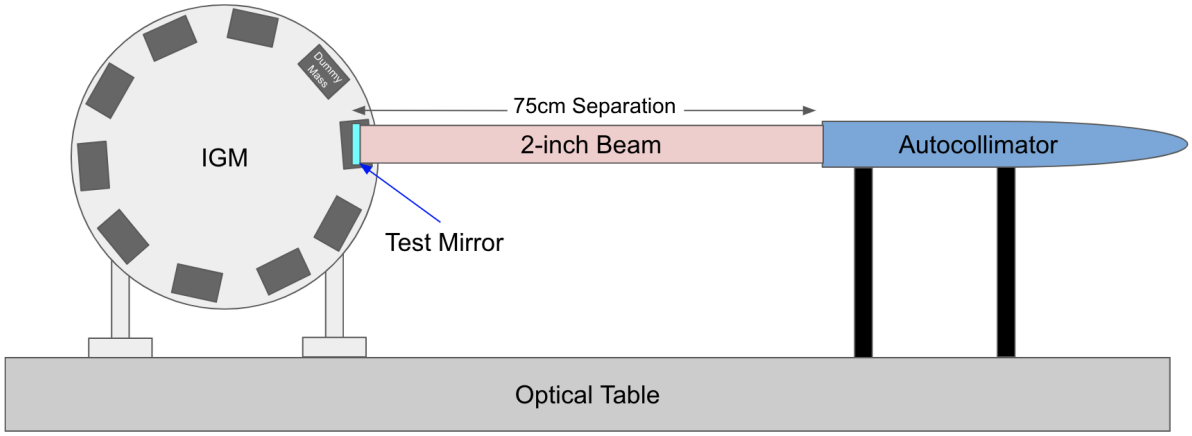


Figure 5.6: A diagram showing the test setup in the warm. The autocollimator was aligned to a test mirror that was mounted on one of the dummy masses.

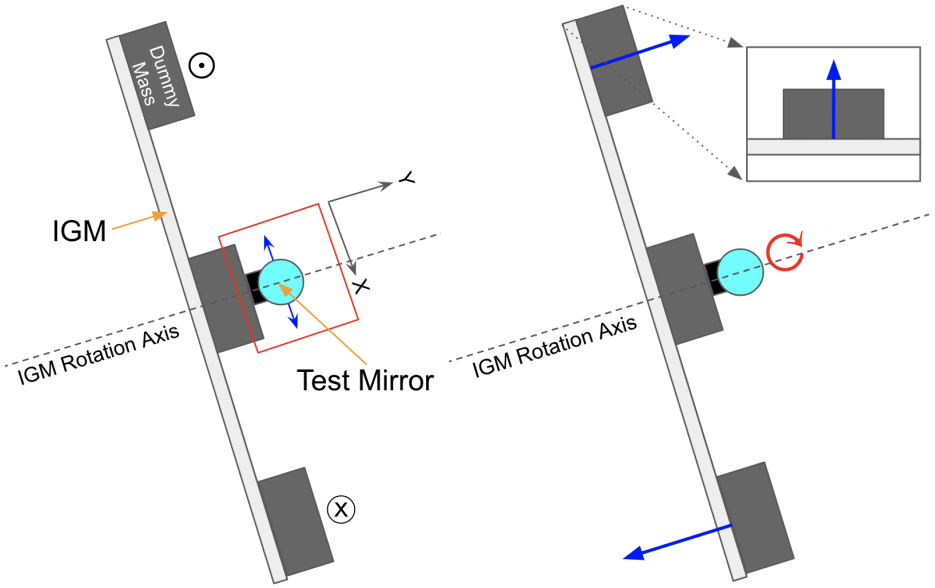


Figure 5.7: (L) A diagram showing the test mirror from the viewpoint of the autocollimator's detector, outlined in red (not to scale). The detector was rotated 17° to match the inclination of the IGM. (R) A diagram showing how rotation about the Z-axis of one grating (represented by the test mirror and the red arc) would be equivalent to rotation about the X-axis for a perpendicular grating (represented by the two dummy masses on the edges).

However, the tolerances in Table 5.1 are for the real gratings, which are at different (and fixed) angles relative to the wheel depending on their resolution (9.12°, 18.75°, and 39.19°). The

test mirror was perpendicular to the wheel, and so the repeatabilities are converted into corresponding repeatabilities for the test mirror, assuming the worst-case grating was used for each axis (9.12° for rotation about the X/Z-axis and 39.19° for rotation about the Y-axis, with degrees defined from normal relative to the wheel). If the test mirror were inclined at 90°, the repeatabilities would effectively be 'flipped', as rotation about the Y-axis of the IGM would translate to a rotation of the grating about its Z-axis (i.e. the tolerance for rotation of the IGM about its Y-axis would now be 1. 0"). This concept is outlined in Figure 5.8.

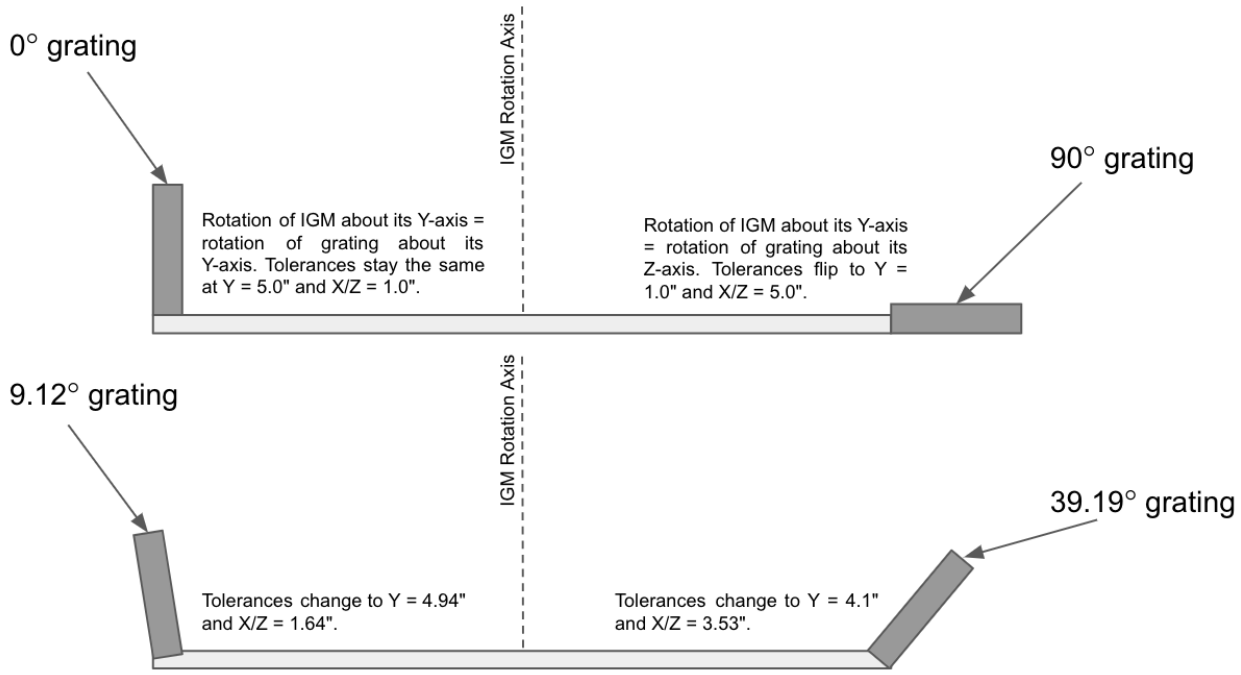


Figure 5.8: Diagram demonstrating how the grating angles change the IGM repeatability tolerances.

To calculate the updated repeatability tolerances, equations 5.1 and 5.2 are used.

$$\theta'_{X/Z} = (\theta_{X/Z,\,90} - \theta_{X/Z,\,0})cos(90 - \varphi) + \theta_{X/Z,\,0} \tag{5.1}$$

$$\theta'_{Y} = (\theta_{Y,\,0} - \theta_{Y,\,90})cos(\phi) + \theta_{Y,\,90} \tag{5.2}$$

where $\theta_{X/Z,\,90}$ is the initial angular repeatability tolerance about the X/Z-axis with a flat grating $(5.0")$, $\theta_{X/Z,\,0}$ is the initial angular repeatability tolerance about the X/Z-axis with a vertical grating $(1.0")$, $\theta'_{X/Z}$ is the final angular repeatability tolerance about the X/Z-axis, φ is the worst-case X/Z-axis angular inclination of the grating (9.12°), $\theta_{Y,\,0}$ is the initial angular repeatability tolerance about the Y-axis with a flat grating $(1.0")$, $\theta_{Y,\,0}$ is the initial angular repeatability tolerance about the Y-axis with a vertical grating $(5.0")$,θ'_{Y} is the final angular repeatability tolerance about the Y-axis, and ϕ is the worse-case Y-axis angular inclination of the grating (39.19°).

As a result, the target repeatabilities were updated to reflect the new definition of rotation about the X/Z and Y axes for the test mirror (not the grating). The updated repeatability goals can be seen in Table 5.2.

	X/Z	Y
Repeatability (RMS)	$1.64"$	$4.1"$

Table 5.2: A table showing the updated RMS repeatability tolerances for the IGM defined in Figure 5.8.

The test mirror was a 2-inch circular mirror bolted directly on the front of one of the dummy masses. Images of the IGM warm test setup in the lab can be seen in Figure 5.9.

The test consisted of the autocollimator taking constant exposures of the angular position of the test mirror. These exposures happened roughly once per second. Simultaneously, the stepper motor (a McLennan 23HSX-206 controlled by a Beckhoff PLC) drove the IGM one full rotation (always in the same direction, and based on step count) and then stopped. The motor was always driven to full steps, as it had to be turned off in between movements to reduce heat load. If the motor was driven to microsteps, it could relax to the nearest step when turned off, negatively impacting repeatability (though the friction brake was designed to mitigate this. However, one full rotation of the IGM corresponds to a movement of full steps, so driving by

microsteps was not needed regardless). The angular shift of the mirror before and after a full rotation could then be compared.

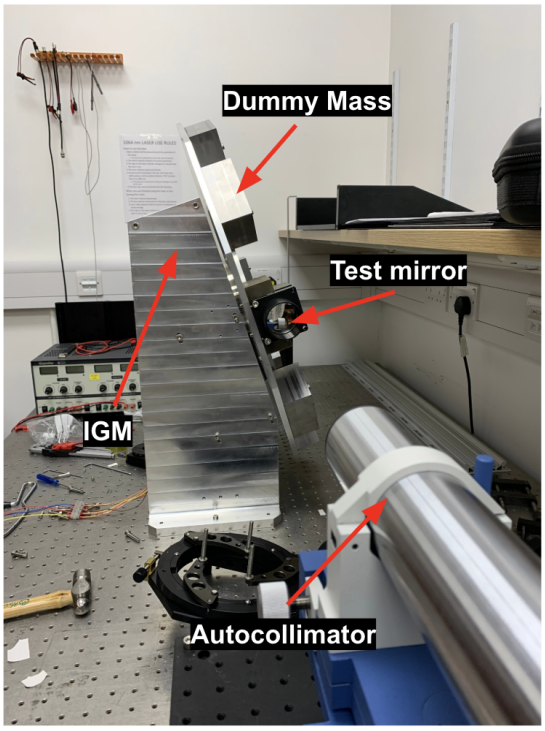


Figure 5.9: An image of the IGM test setup in the laboratory. The test mirror can be seen mounted directly on the side of one of the dummy masses.

2.2 Warm repeatability test plan

As with the testing of the detent mechanism and FM1, warm testing began with characterization of the stability and measurement of background noise, and defining methods of mitigation. Formal repeatability tests were then conducted with the motor moving the IGM complete rotations in both the clockwise and counterclockwise directions while implementing the mitigations for the sources of error using the previously identified methods of mitigation. Despite the movement of a full rotation being within 2 minutes (HARMONI system requirement R-INS-920), both directions were tested in separate tests. This ensured that the IGM would be within tolerance regardless of the direction of rotation. Once each of these tests had passed, the system underwent an accelerated lifetime test of 15,000 movements. A summary of the warm test plan is shown in Figure 5.10.

2.3 Optimizing the operation of the IGM

As with the FM1, optimization tests were run over 10-72 hours each, with movements every 5 minutes. Many parameters of the mechanism were varied so that sources of error could be identified. Optimization testing was broken down into two main sections: re-optimization of test parameters from the FM1 testing, and identification of sources of error inherent to the design of the IGM.

2.3.1 Re-optimization of the FM1 test parameters for the IGM

As a significant amount had been learned from the FM1 testing, many of the lessons were directly applied to the testing of the IGM. It was believed that the same principles of proper operation would hold between the two mechanisms. The main areas where the knowledge from the FM1 testing was directly applied are outlined below. All of the parameters are shown in Table 5.3.

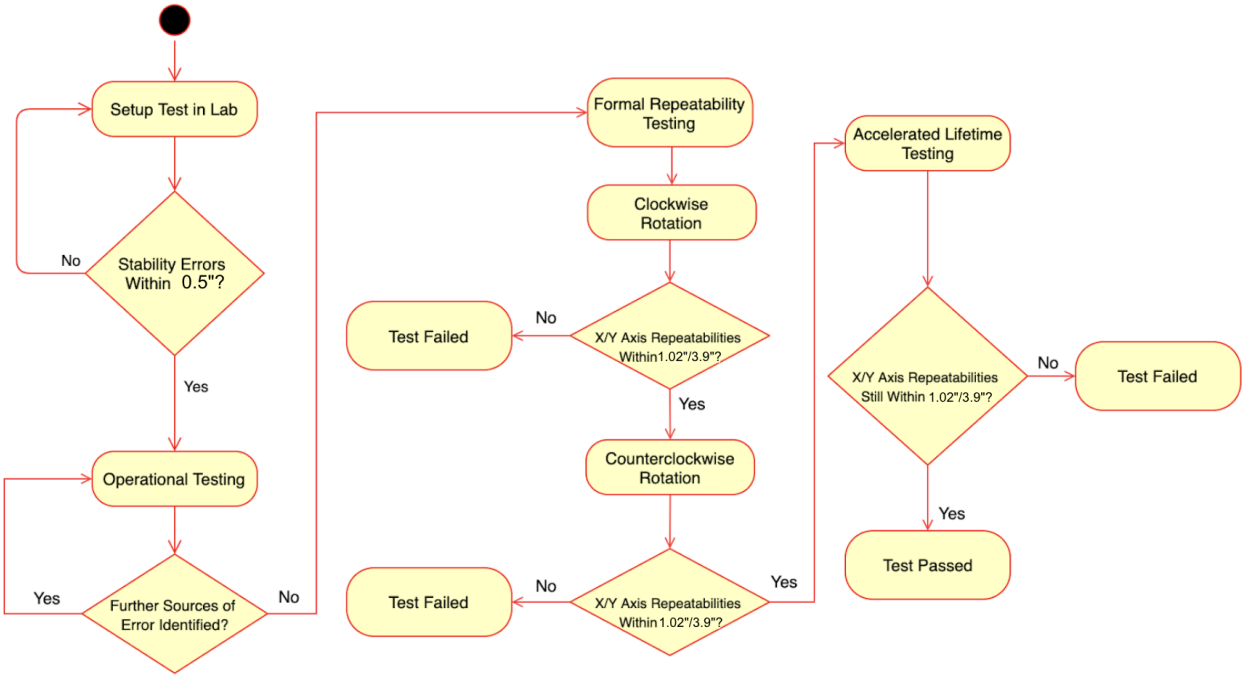


Figure 5.10: The test plan for the warm testing of the IGM.

IGM Test Parameters	
Motor rest time	10 minutes
Active compensation for backlash	Off
Acceleration/Deceleration	$25^{\circ}/s^2$
Maximum Velocity	500°/s
Driving distance	75,600°

Table 5.3: Parameters used for all testing of the IGM. These were drawn from what was learned during the testing of the FM1.

Temperature

By this point, a thorough understanding of the effects of temperature (background temperature and excess heat due to the operation of the motor) had been established through the testing of the detent mechanism and the FM1. The lessons learned from those tests were incorporated into all tests of the IGM. The motor was turned off between all movements, and initially allowed to rest for at least 10 minutes in between movements. This time was longer than the 5 minute rest time for the detent mechanism and FM1, as it was hypothesized that the longer operation time and higher torque required to move the IGM one full rotation would generate more heat than the operation of the detent mechanism and FM1. However, the top level tolerance only allowed for a maximum of 6 minutes between movements, and so this rest time was later reduced to 5 minutes to be in line with the detent mechanism and FM1. Both turning the motor off and allowing for 5 minutes of rest time mitigated errors due to drift from temperature from the operation of the IGM.

Backlash

The profile of backlash with the IGM was similar to the backlash with the detent mechanism (defined in Chapter 3, Section 2.1) and is due to play between the worm and the worm gear. However, there was minimal play in the IGM in the direction of rotation (the worm was pushed into the worm gear with a metal shim to remove play, discussed further in Section 2.3.2).

As with the FM1, using the Beckhoff to provide active compensation for backlash (see Figure 5.11 for the movement profile) was not possible as there was no way to confirm the absolute position of the IGM in the warm testing (no reference switches were in use).

Acceleration

A significant amount of initial error with the FM1 testing came from missed steps due to instant acceleration and deceleration of the stepper motor. This would be even more significant with the IGM, as the inertia of the rotating system was considerably larger, which would increase the potential for missed steps due to the high amount of required torque.

It was established through various tests that a gradual acceleration and deceleration of $25^{\circ}/s^{2}$ was optimal for the FM1 in connection with the warm motor's torque curve. This value was used as a starting point for the warm testing of the IGM, and no missed steps were detected at any point in the testing thereafter. The low deceleration value decreased the time required for the mechanism to 'settle' into position after moving, and measurements were taken five seconds after the movement was completed (as with the FM1). A value has not been set for the cold motor acceleration, but its torque rating is within 10% of the warm motor.

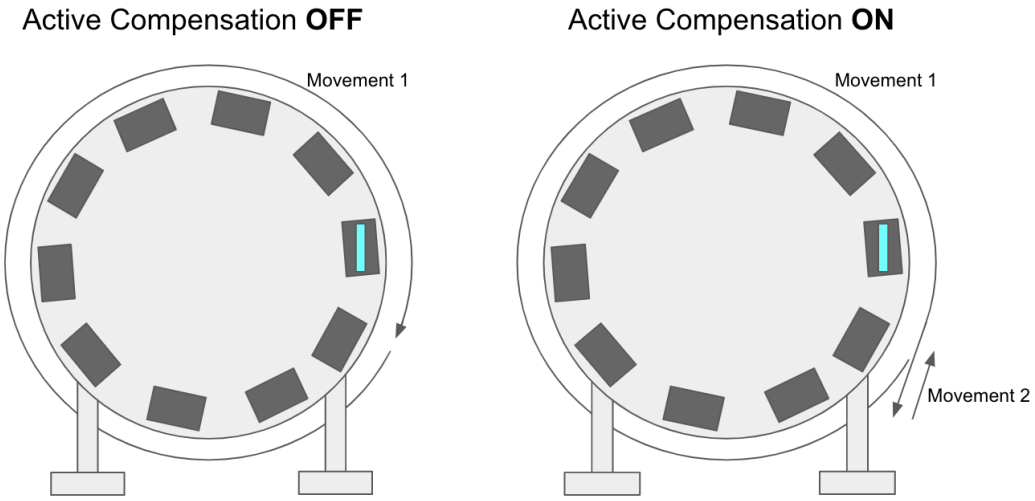


Figure 5.11: (L) A diagram showing the movement of the IGM when active backlash compensation was turned off. The motor drove the wheel one complete rotation. (R) A diagram showing the movement profile when the compensation was turned on. The motor would drive the IGM past the 'home' point (recorded by a reference switch), and then return in the opposite direction.

Velocity

According to HARMONI system requirement R-INS-920 (and as discussed in Chapter 1, Section 2.1) (Clarke et al., 2020), the maximum time allowed for a change in observational setups is two minutes. This set an upper limit on the time required for one full rotation of the IGM.

As the FM1 testing had demonstrated some errors due to increased velocity, an upper limit of the warm motor velocity was set at $500^{\circ}/s$. This was in line with the maximum torque of the motor. This velocity was used for the testing with the IGM, and did not cause any noticeable forms of error. With this velocity, one full rotation took 90 seconds, and the potential negative impact of higher velocities was not investigated. A value has not yet been set for the cold motor velocity.

With a settle time of five seconds as noted above, the full operation of the IGM is still well within the two minute limit (95 seconds). If the IGM were to be used with detents, a 30 second settle time would be required, leaving the maximum possible time required to operate the mechanism at exactly the two minute tolerance. However, the IGM would never actually have to do one full rotation as this wouldn't actually result in a change of configuration, so in reality the longest total operational time would be less than two minutes, as the IGM would rotate for less than 90 seconds. Furthermore, the IGM can rotate both clockwise and counterclockwise, reducing the actual maximum rotation time again to at most 45 seconds, leading to a maximum possible total operational time of 75 seconds (assuming the use of detents), which is well within the two minute tolerance.

Missed Steps

There was significant error with the FM1 when driving to fractions of a step. As such, the movements were always made in increments of 180° at the motor. This meant the motor would always finish a movement at a full step. With the grating wheel, however, movements always had to be made to one complete revolution. This directly translated to 75,600° at the motor, which was to a full step. As such, driving to fractions of a step was not an issue with the IGM. However, if the mechanism were to drive to a fraction of a step, the friction brake would theoretically hold the system in place and prevent relaxation to the nearest full step.

2.3.2 Sources of errors native to the IGM

Eight main sources of error were identified during the optimization testing: friction brake wear, the direction of rotation, flex coupling wear, reference switches preventing rotation, the balance of the rotating wheel, mounting of the test mirror, Y-axis mechanical play, and X/Z-axis mechanical play. Some of these errors were also identified in the FM1 testing, such as the impact of direction of rotation, as well as errors from overuse (such as the flex coupling shearing in both the IGM and FM1). New sources of error were also found that were specific to the IGM.

Friction brake wear

Over the course of the optimization testing, the friction brake showed signs of significant wear. This was seen even after tens of rotations, with a buildup of debris below the mechanism. However, after a few hundred rotations the friction brake was fully worn in, and there was no further debris. While this didn't pose a problem in the warm, and did not impact repeatability, the excess debris could be an issue in a cold environment.

Flex coupling wear

During initial testing, significant 'jumps' were noticed in the repeatability about the axis of rotation (Figure 5.12). They caused large amounts of error, but did not occur often. It was theorized that the jumps were due to the flex coupling slipping on the driveshaft of the motor due to the high levels of torque applied. The flex coupling was tightened significantly with additional grub screws, which removed this error from further tests. The relatively large drift seen over the course of this 20hr test (~20") was due to the flex coupling not being tightened and slowly sliding before a larger 'jump' towards the original 'home' position of the IGM at the start of the test.

However, soon after the flex coupling was tightened (~50 rotations), it sheared. This was most likely due to improper use of the IGM without damped acceleration/deceleration ahead of the start of formal testing. The instant acceleration/deceleration of such a large mass caused the flex coupling to wear at an increased rate. The flex coupling was replaced, with no further errors detected after, improving repeatability by up to10".

Reference switches

The reference switches were removed for all testing as they would occasionally catch and stop the wheel during rotation. The wheel was run by counting steps. To remedy the design flaw, the reference switches could be lowered slightly to ensure they would not catch and prevent rotation (this updated design is being done by James Kariuki). As with the detent and FM1 repeatability tests, temperature measurements were not taken during the tests. However, the overall linear drift could be removed as it was due to temperature, as discussed in Chapter 2.

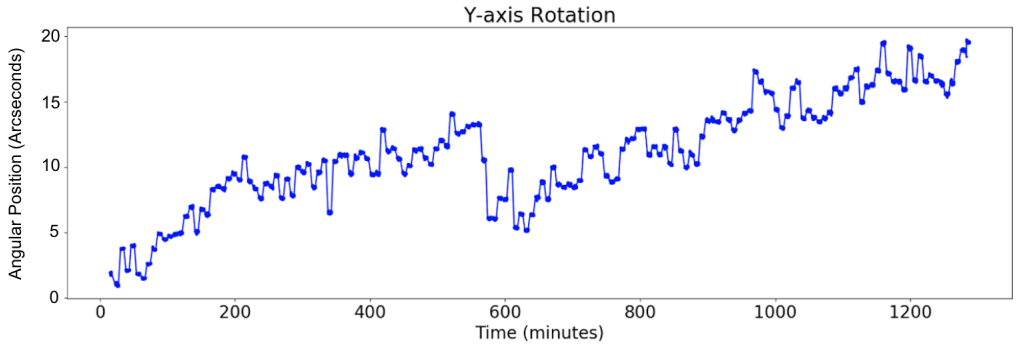


Figure 5.12: Angular rotation about the Y-axis vs time. The IGM was rotating in the clockwise direction for this test.

Wheel balance

The balance of the wheel had a significant impact on the repeatability and smooth operation of the IGM. If one dummy mass was heavier than the others, for example, the wheel would shake and wobble as the motor tried to compensate for the inconsistent axial load while driving the heavy dummy mass upwards. This would cause significant error on repeatability ($> 10''$). This was an issue at first, as the test mirror and mount were attached directly on top of one of the dummy masses, adding an extra 0.25kg. Even this was enough excess weight (at a 550mm radius) to significantly impact the balance. The dummy mass was reduced in weight to compensate, such that the reduced dummy mass, mirror, and mount weighed the same (to within 0.01kg, which was the precision of the scale used) as one original dummy mass. This improved repeatability by over 10".

The wheel balance tolerance will be within 10% when the Phytron cold motor is used, as its torque rating is within 10% of the warm motor. Within HARMONI, the balance of the IGM can be measured by weighing the gratings on opposite sides of the wheel within their mounts

ahead of assembly of the module. As the gratings are at different angles, they will provide different levels of torque. This can be mitigated by having small counterweights on opposing gratings with shallower angles.

Y-axis mechanical play

Upon initial assembly, significant play was found in the direction of rotation of the IGM. It was found to be due to excess space between the gears on the worm gear and the threads on the worm. The interface between the worm and the worm gear allowed for adjustments to be made to reduce or increase the play in the system. For all testing, a 0.6mm shim was used to move the worm towards the worm gear, reducing the spacing and removing the play about the Y-axis in the system. 0.6mm was chosen as it was the minimum required to remove the play, and not put axial load on the worm gear. This value will likely be less for cold testing, but has not yet been determined. The use of a shim to remove play improved the repeatability by ~2".

X/Z-axis mechanical play

However, the most significant error noticed was found in the repeatability about the axis *perpendicular* to the rotation (X/Z axis). Often, this would be at the same level of repeatability as in the direction of rotation, but sometimes it would be even worse. The profile of the movement would be the same, but with worse noise.

Theoretically this made no sense, as repeatability in the direction of rotation couldn't be better than that in a fixed axis, which should have only been limited by the axial runout of the bearing. However, the large trends in the movement (such as the 'jumps' in the first few tests) were also measured about the X/Z axis.

As such, it was determined that the error had to be coming from something common to both axes. After inspecting the mechanism, it was discovered that there was significant play in the system between the wheel and the spur gear - exactly perpendicular to the direction of rotation. Clearly, the wheel was free to move significantly in this direction during rotation, which explained why such poor repeatability was measured about the X/Z axis.

The mechanism was dismantled, and it was discovered that radial bearings had been mistakenly used instead of angular contact bearings. There was no preload being applied about the X/Z axis by the radial bearings, which allowed for significant play in those axes due to axial

runout. These bearings were replaced with angular contact bearings, which removed the play about the X/Z axis, improving repeatability in that axis by ~0. 6".

2.3.3 Conclusions from the optimization tests

All of the errors and corresponding methods of mitigation are shown below in Table 5.4.

2.4 Warm repeatability tests

The final repeatability testing involved implementing the mitigations for each source of error identified in the previous testing. Representative tests that demonstrate the high repeatability achieved in both axes are highlighted below.

Problem	Mitigation	Improvement (arcseconds)
Friction brake wear leaving debris	The friction brake naturally wore in after a few hundred movements, and no more debris was found.	N/A
Jumps due to loose flex coupling/flex coupling shearing	A new flex coupling was used, and tightened on the driveshaft to prevent jumps.	Up to 10
Limit switches preventing rotation	The limit switches were all removed.	N/A
Wheel out of balance	A lighter dummy mass was made. With the mirror mounted, the total weight was equal to one normal dummy mass, balancing the wheel.	> 10"
Y-axis mechanical play	A 0.6mm shim was used to move the motor towards the worm gear.	~2"
X/Z-axis mechanical play	The radial bearings were replaced with angular contact bearings.	~0.6" (X/Z-axis)

Table 5.4: A table showing the various errors identified during the optimization testing of the IGM, along with how they were mitigated.

2.4.1 Repeatability about the Y-axis

The tests were conducted with the wheel rotating initially in the clockwise direction with a 5 minute rest time for four days. The velocity was set at $500°/s$, with a dampened acceleration

and deceleration of $25°/s^2$. As seen in Figure 5.13, the repeatability about the Y-axis was within tolerance at $1.08"(1.86"$ absolute, and $1.02"$ with a 2nd order polynomial fit), which was roughly the same as seen during the optimization tests. This was expected, as the addition of angular bearings should have had no impact on rotation about the Y-axis. As in the repeatability tests of the detent mechanism and FM1, temperature recordings were not made during the testing. However, as discussed in Chapter 2, the overall drift can be removed as it is due to temperature, and the absolute drift during this test on timescales of 1hr was negligible ($< 0.2"$).

2.4.2 Repeatability about the X/Z-axis

However, as can be seen in Figure 5.14, the angular contact bearings, which applied an internal pre-load on the wheel, did have a significant impact on the repeatability of rotation about the X/Z-axis. The repeatability was $0.78"$ (which was better by ~$0.5"$ than when they were not used) and within the tolerance of $1.64"$ (the absolute repeatability in this test was $0.87"$, and $0.74"$ with a 2nd order polynomial fit). The level of repeatability is still not as low as seen the stability measurements of $0.013"$, which implies runout is still seen within the bearings, most likely due to the large weight of the wheel being applied at a non-normal angle. Furthermore, a flexure was not being used at this stage as one was not available, which caused the system to sag due to gravity, creating friction in the lower part of the bearing housing. The absolute drift during this test on timescales of 1hr was negligible ($<< 0.1"$).

Similar results and profiles were seen about both axes when rotating the wheel in the counterclockwise direction. The test was conducted with the same parameters as with clockwise rotation. This implies that direction has no noticeable impact on the repeatability of the system, which is a HARMONI system requirement for the IGM.

2.4.3 Accelerated lifetime performance

As with the FM1 testing, over 15,000 movements were accumulated. There was little noticeable wear to the system or degradation of the measured repeatability over the course of the warm testing. The flex coupling also did not shear during the verification testing as it had in the

optimization testing. It was therefore concluded that the system is repeatable in warm environments over the HARMONI system lifetime.

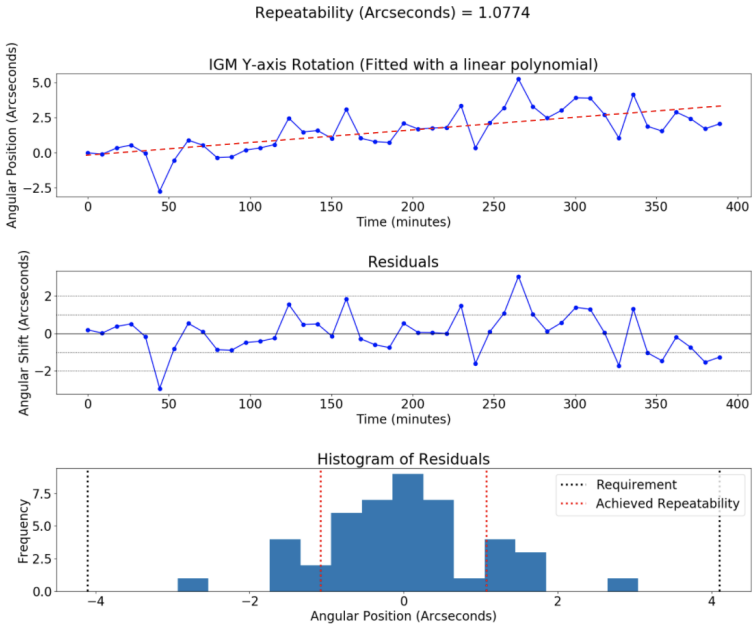


Figure 5.13: (Top) Angular rotation about the Y-axis vs time, with a polynomial fit to the trend. (Middle) The residuals of the fit, plotted against time. (Bottom) A histogram of the residuals. This test was of clockwise rotation about the Y-axis.

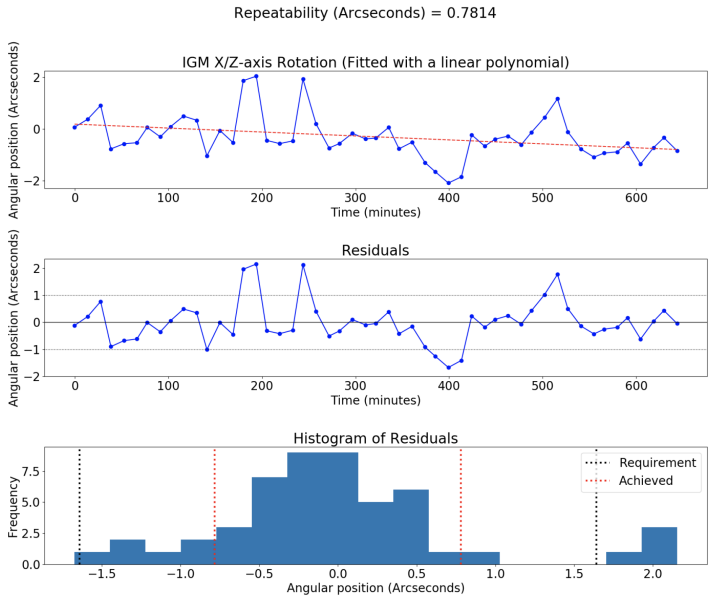


Figure 5.14: (Top) Angular rotation about the X/Z-axis vs time, with a polynomial fit to the trend. (Middle) The residuals of the fit, plotted against time. (Bottom) A histogram of the residuals. This plot shows clockwise rotation about the X/Z-axis in the warm.

2.5 Final warm repeatability performance

As with the FM1, testing the IGM in its operational configurations while correcting for potential sources of error achieved consistent repeatability in both directions of rotation within the goal tolerances of $4.1''$ about the Y-axis and $1.64''$ about the X/Z-axis. Results about the Y-axis had an RMS error of $1.33''$ (~3σ is $< 4.1''$, indicating that over 99% of measurements will be within tolerance) ($1.66''$ absolute, and $1.25''$ with a 2nd order polynomial fit). Results about the X/Z-axis had an RMS error of $0.93''$ (~1.8σ is still within tolerance, indicating ~90% of movements will be within tolerance) ($1.18''$ absolute, and $0.87''$ with a 2nd order polynomial fit). These results were seen during both directions of movement. Figures 5.15 and 5.16 show histograms of the final warm tests about both the Y-axis and X/Z-axis, respectively. Stability was within tolerance and trivial, and accelerated lifetime tests also passed. Thus, the IGM passed its warm test, and progressed to cold testing at 130K.

The remaining errors are likely due to minimal amounts of play between the worm and worm gear, as well as micro inaccuracies in the step sizes of the motor. It is believed that the repeatability about the X/Z-axis would be improved with the use of a flexure to remove sag in the system due to gravity.

A summary of the warm repeatability can be found in Table 5.5. These results are encouraging for a mechanism of this size, and provide mechanical proof of concept ahead of the cryogenic testing. Even without the removal of drift due to temperature, the IGM still provides repeatabilities within tolerance.

Y-axis Repeatability Tolerance (RMS)	**4.1"**
X/Z-axis Repeatability Tolerance (RMS)	**1.64"**
Test Type	**Repeatability (RMS)**
Y-axis	1.33"
X/Z-axis	0.93"

Table 5.5: A table showing the repeatability and stability tolerances in both axes, as well as the results for six representative tests from the warm testing. The repeatabilities and stabilities are well within tolerance.

3. Combined HARMONI Spectrograph Repeatability

Taking the achieved warm repeatability of the IGM together with the warm repeatability results from the FM1, the total shift of the beam about the spectral and spatial axes of the detector between the FM1 and IGM is well within their combined tolerance (absolute repeatabilities were also within tolerance for both the FM1 and IGM). However, as the top-level repeatability budget is for all 3 mechanisms operating together, including the FM2, the FM2 still has to provide repeatability about both axes of the detector to within its tolerance. This should be achievable as the FM2 traces out an ellipse about a focal point a distance of 315mm from its mirror (opposed to the FM1). The FM2 is therefore far less sensitive than the FM1 in terms of shifting the beam about the detector, and as such should achieve repeatabilities that shift the beam about both axes of the detector at least comparably to the FM1. As of the writing of this thesis, the design for the FM2 has not been finalized and testing has not yet been conducted, but it will likely share the same drive mechanism as the FM1. As such, it is likely the final shift of the beam about both axes of the detector due to the simultaneous operation of all three mechanisms (FM1, FM2, and IGM) will be within 0.15 pixels RMS in the warm.

4. Cold Testing Preparations and Future Work

Having passed the warm testing, the IGM will now progress to being tested at cryogenic temperatures. Significant preparation has already been done, with the entire mechanism having been disassembled and cleaned ahead of testing. The cleaned and prepped mechanism was tested in the warm (to verify successful operation while clean) with the McLennan 23HSX-206 stepper motor, and provided repeatabilities within 5% of those achieved in Section 2 of this chapter.

As with the upcoming cold testing of the FM1, the cold testing of the IGM will begin with a cold verification test of only the Phytron motor and worm drive mechanism. This will confirm whether the drive mechanism can operate at 130K$\pm$2K, and save time as the entire mechanism will not need to be cooled down at first, which could take over two days due to its size. However, it is unlikely that there will be preventative issues due to thermal contraction of the materials of the drive mechanism at cryogenic temperatures, as the plastic worm will only get smaller, which won't prevent rotation (unlike with the nut constricting the lead screw in the

FM1, preventing rotation). However, calculations will need to be done to determine the optimal shim size to ensure there is no increased play in the system while it is cold and the worm is properly aligned to the worm gear. The bearings within the worm drive mechanism will also be dry lubricated with Molybdenum Disulphide.

The angular contact bearings within the IGM bearing housing are currently not cryo-rated, as ones of this size were not commercially available. Testing can be attempted with these bearings dry lubricated, otherwise dedicated cryo-rated bearings will need to be made specifically for this mechanism. Beyond that, it is unlikely further major modifications will be needed, as the mechanism provided repeatabilities within tolerance at warm temperatures. However, if better repeatabilities are needed, modifications of the IGM to allow for the use of the detents could be made. Theoretically, as described in Chapter 3, these would provide significantly better repeatabilities, but would make the IGM a more mechanically complex system.

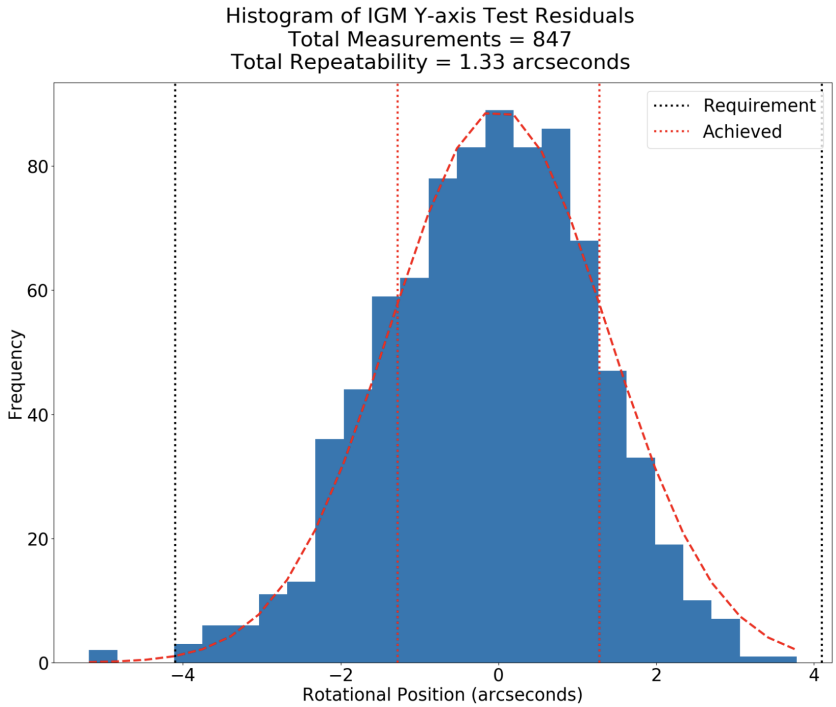


Figure 5.15: Histogram of all tests for the IGM about the Y-axis. The repeatability is 1.33": well within the tolerance of 4.1". A Gaussian is fitted to the distribution, shown in red.

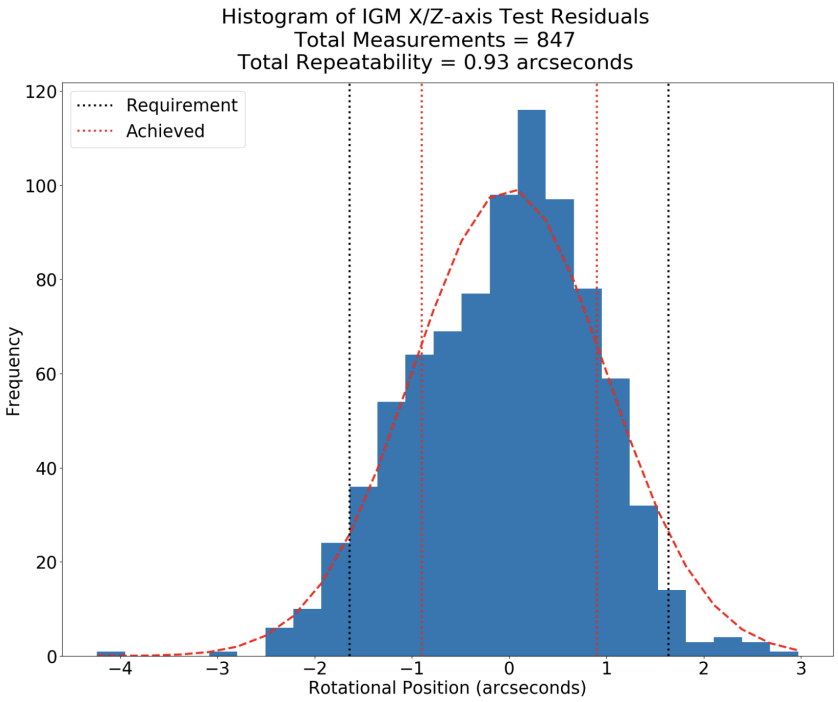


Figure 5.16: Histogram of all tests for the IGM about the X/Z-axis. The repeatability is 0.93": well within the tolerance of 1.64". A Gaussian is fitted to the distribution, shown in red.

Part II

The Drivers of the Main Sequence Positions of 5MUSES Galaxies

Chapter 6

Introduction

This part of the thesis focuses on SWIFT observations of a statistically significant subset of the 24μm flux-limited 5 Milli-Jansky Unbiased *Spitzer* Extragalactic Survey (5MUSES) sample. To determine whether high multiplicative offsets from the expected main sequence of star formation (MSM_{IR} −or the 'main sequence multiple' − and defined in Elbaz et al., 2011 as 'starburstiness') are due to star formation triggered by galactic interactions, or from contributions to L_{IR} from active galactic nuclei (AGN), a relation between the main sequence of star formation and the dynamical ratio (indicative of whether a galaxy is interacting) is plotted. This is then re-plotted using the main sequence multiple corrected for AGN contributions to L_{IR} ($MSM_{IR,\,AGN\ corrected}$) for each galaxy to see if interactions were the true drivers of the high star formation rates.

1. A Brief Introduction to Galaxies

The generally accepted cosmological model states that the universe is expanding and composed of dark energy (Λ), cold dark matter (CDM), and baryonic matter - all of which originated from the Big Bang 13.78 billion years ago. Dark energy and dark matter compromise 68% and 27% of the energy density of the universe, respectively, with baryonic matter (stars, galaxies, and gas) only contributing 5% (Planck Collaboration, 2014). This ΛCDM framework has explained how

the universe evolved to be as it is today - through discoveries such as the cosmic microwave background, accelerating expansion of the universe, and the cosmic web of filaments.

In the ΛCDM paradigm, dark matter started to condense after inflation into the large-scale structure of the universe, with dark matter halos of small sizes coalescing and forming larger dark matter halos. This process is known as the hierarchical assembly of dark matter halos (e.g. Navarro et al., 1997). Baryonic matter then condensed into the potential wells from the dark matter large structure, coalescing into complex structures like stars and galaxies with their own dark matter halos (e.g. Peebles, 2013). Over time, galaxies then evolved through non-linear mechanisms such as mergers, AGN, gas cooling and accretion, star formation feedback, and outflows.

In its most basic definition, a galaxy is a gravitationally bound system of stars, gas, dust, and dark matter, supported by rotation or dispersion. Edwin Hubble morphologically classified the various types of galaxies with the Hubble tuning fork diagram, with the two main types being spiral (rotationally supported) and elliptical (dispersionally supported) (Hubble, 1926). However, the observational reality is far more complicated, with a diversity of shapes, sizes, colors, and morphologies.

Tracing how gas is converted into stars with the global star formation rate (SFR) density and history can give an initial idea of when the baryonic mass started to assemble into stars and galaxies. This metric helps to determine how the baryonic matter assembled over the history of the universe, as well as helping to explain the variety of galaxy shapes and properties seen in the universe (e.g. Buta, 2011).

2. The Evolution of the Global Star Formation Rate Density and the Star Formation Main Sequence

Luminosity can be directly traced in the UV, which probes the direct stellar light emerging from the galaxy. However, UV light is very sensitive to dust extinction (e.g. Calzetti et al., 2004; Hong et al., 2011). In galaxies with a high dust content, a significant fraction (approximately half) (Kennicutt, 2012) of the bolometric luminosity of a galaxy is absorbed by interstellar dust and re-emitted in the thermal IR (as L_{IR}) as the dust heats.

In actively star-forming galaxies (including young spiral and disk galaxies), most of their luminosity is dominated by light from young and massive type O/B stars which have short life spans (~6Myr for type O stars, and ~350Myr for type B stars), the IR emission of dusty galaxies can be a sensitive tracer of the young stellar population and thereby the SFR. Old stars (type M/K) also contribute to the IR emission, but significantly less so per star as their luminosity is multiple orders of magnitude lower than type O/B stars. While they are more numerous than type O/B stars by multiple orders of magnitude, it is argued that young stars dominate the 40-120μm emission in both early and late-type star forming galaxies (e.g. Devereux & Young, 1990) and therefore L_{IR} can be a direct tracer of the SFR on timescales of 100Myr. However, the contribution of the old stellar populations in the heating of the dust (and therefore some of the output IR luminosity of the galaxies) could lead to an overestimate of the SFR based on this relation. This will likely only be an issue for old, high mass galaxies with low values for SFR (i.e. quiescent), which comprise only ~10% of the sample later used in this study.

As an alternative, emission from gas ionized by young (10Myr) and hot stars (such as $[H\alpha]6563$Å) can also be used to trace the SFR in galaxies. However, $SFR_{H\alpha}$ does have drawbacks as a calibrator, as $H\alpha$ emission is subject to significant light loss due to interstellar extinction and obscuration (e.g. Kewley & Dopita, 2002), and can underestimate the true SFR unless the extinction can be corrected for. SFRs calculated from $[H\alpha]6563$Å can be lower than those derived from IR tracers by orders of magnitude (e.g. Pereira-Santaella et al., 2019). One method to correct for dust attenuation is by using the Balmer decrement, and comparing the observed ratio of $H\alpha/H\beta$ to its physically-defined ratio (e.g. Hammer et al., 2017). Furthermore, at redshifts higher than z ~ 0.5, $[H\alpha]6563$Å is redshifted outside of the visible spectrum, making it possible to observe only at local redshifts with many ground-based instruments.

Polycyclic aromatic hydrocarbon (PAH) emission can be used as a diagnostic for SFR, and is far less affected by dust extinction when compared to the SFR traced by $[H\alpha]6563$Å. PAHs are strong nuclear features (found in the photodissociation regions of galaxies) that excite as they absorb photons from the photospheres of stars (typically UV light from bright, young stars) (Rigopoulou et al., 2021). The electronic excitation causes the molecules to vibrate, and then relax by radiating energy in the infrared at various wavelengths (such as 3.3μm, 6.2μm, 7.7μm, 8.6μm, 11.3μm, 12.4μm, and 17μm). This radiation can account for up to 10% of the total

infrared luminosity of galaxies (Shipley et al., 2016). As such, PAH features can be used as robust calibrators for star formation rates in the infrared, and are less sensitive to extinction than other SFR calibrators, (such as $H\alpha$). The equivalent width of the PAH features can also measure the compactness of the SFR regions (e.g. Shipley et al., 2016). In bright local galaxies, there is substantial evidence for lower PAH luminosity with higher IR luminosity (e.g. Shipley et al., 2016; Papovich et al., 2009).

As $H\alpha$ is redshifted outside of the visible spectrum at redshifts greater than z ~ 0.5, there is also the need for a tracer that is at a shorter wavelength in the blue. $H\beta$ and the higher order Balmer lines are too weak to be reliably used to trace SFR, and are heavily impacted by stellar emission. The $[OII]3727$Å doublet is the strongest feature in the short wavelengths, and its luminosity is not intrinsically linked to the ionizing flux, but rather the ionization state of the gas (e.g. Kennicutt et al., 2009; Kennicutt et al., 1992). Most importantly, it can be observed with ground-based instruments out to z ~ 1.7, making it viable for use with a large number of galaxies. However, the $[OII]3727$Å doublet is highly impacted by dust extinction, and can be difficult to approximate.

While SFRs traced by emission from UV, IR, $H\alpha$, PAHs, and OII are some of the most frequently used, there are many other diagnostics available such as emission from the radio continuum, as well as $24\mu m$flux, Paα, and Lyα emission (e.g. Hammer et al., 2017). However, for the galaxies studied in this work, the SFR was calculated using L_{IR} and $L_{H\alpha}$ (see Chapter 7, Sections 2 and 3.5).

The gas-phase metallicity can be used as a tracer of the star formation history (SFH) of a galaxy, as galaxies having undergone periods of enhanced star formation will have a higher metal content due to the enrichment of the ISM (e.g. Maiolini et al., 2010; Pettini et al., 2004; Hogan et al., 2021). As oxygen accounts for ~50% of the metal content in the ISM, metallicity can be traced using the relative amount of oxygen relative to hydrogen, as expressed in equation 6.1:

$$A(O) = 12 + log(O/H) \tag{6.1}$$

where $A(O)$ is the metallicity, O/H is the ratio of oxygen to hydrogen, with 12 being the value for hydrogen.

While metallicity can be measured directly using the temperature, abundance, and density of electrons in gas, this is often difficult as the auroral lines required to make these measurements are often too weak or redshifted and difficult to observe (e.g. Hammer et al., 2017). As a proxy, ratios of strong emission lines can be used as a calibrator of metallicity. One of the most commonly used ratios is the N_2 ratio, defined as $[NII]6584\text{Å} / [H\alpha]6563\text{Å}$, (e.g. Storchi-Bergmann et al., 1994; Pettini et al., 2004). This ratio has the benefit of using two emission lines with very similar wavelengths, which implies that any extinction would be uniform to the two, which would not significantly impact the ratio (Hammer et al., 2017). However, this ratio can become saturated at high metallicities and can become uncertain.

Observations show that the global star formation density of the universe increased from the Big Bang through to $z \sim 1.5$-3, where it peaked (Figure 6.1, Madau & Dickinson 2014). Since then it has constantly decreased, implying that the universe is slowing in the creation of new stars, with more galaxies becoming quiescent. During this early period of the universe, most massive galaxies were in a heightened period of star formation, forming most of their stellar mass (Madau & Dickinson, 2014) with a heightened rate of galactic mergers. This significant discovery allowed for the entire history of cosmic star formation to be plotted in a single figure. Given a redshift, the star formation density can be inferred - and with high accuracy. Furthermore, at $z > 1$, luminous and ultra-luminous galaxies ($L/L_\odot > 10^{11}, 10^{12}$) are responsible for about half of the total SFR density. Yet, these galaxies are very rare locally (e.g. Le Floc'h et al., 2005; Magnelli 2011; Rigopoulou et al., 1996), and the present-day SFR density is much lower (~5%) due to this lower number density. This figure also demonstrates that between $0.5 < z < 2.5$, galaxies formed 75% of their present-day stellar mass.

Most star-forming galaxies exhibit a strong correlation between their SFRs and stellar masses (M_*) (e.g. Noeske et al., 2007; Elbaz et al., 2007) as seen in Figure 6.2 (from Whitaker et al., 2012). This is now known as the 'main sequence' (MS) of star-forming galaxies, and the positive relationship between SFR and M_* is regulated by quasi-static feedback processes (Lee et al., 2015). The main sequence also exhibits a strong evolution with redshift (Pearson, 2018) and can be found at $z \sim 0$ (Brinchmann et al., 2004), $z \sim 1$ (Noeske et al., 2007), $z \sim 2$ (Daddi et al., 2007), $z \sim 3$-4 (e.g. Daddi et al., 2009; Magdis et al., 2010), and even up to $z \sim 7$ (e.g. Stark et al., 2009; Bouwens et al., 2012).

While mergers were thought to be the primary cause of star formation in galaxies along the MS, cold inflows from the IGM are now thought to be the main driver (e.g. Dekel et al., 2009). Galaxies move above the MS as this gas migrates inward and collapses into clumps, which causes instabilities in the galaxy and episodes of star formation. The SFR then lowers as the gas depletes (either from being used up in periods of star formation, or due to negative feedback mechanisms such as supernovae), moving the galaxy below the MS. At this point, the galaxy either becomes quiescent, or new gas inflows from the IGM cause the cycle to repeat. Ultimately, once all the gas is depleted, or when the replenishment time becomes longer than the depletion time, the galaxy becomes quiescent (Tacchella et al., 2016). This process is referred to as secular evolution (e.g. Sellwood, 2014).

While there is some debate, it is generally accepted that the MS follows a simple power law of the form

$$log(SFR/M_{\odot}yr^{-1}) = \alpha log(M_{*}/M_{\odot}) + \beta \quad (6.2)$$

where α is the slope (usually between 0.6 and 1) and β is the normalisation (Speagle et al., 2014). There is a remarkably low amount of scatter (0.3 dex) around the main sequence up to $z \sim 3$ (e.g. Schreiber et al., 2015) - which demonstrates the efficiency and sustainability of this process, and makes the MS an even more significant relation. This implies that given only a galaxy's redshift and stellar mass (at redshifts up to $z \sim 3$, which is over 80% of the history of the universe), 68% of galaxies have the same SFR to within a factor of 2, which is remarkably precise given the broad range of redshifts, and is indicative of a stable star formation history and a continuous and steady supply of cold inflows from the IGM that consistently replenish the disk (as opposed to frequent powerful bursts of star formation, which would cause large offsets from the main sequence, increasing the scatter) (e.g. Dekel et al., 2009). 66% of stars currently in existence were formed in main sequence galaxies (Schreiber et al., 2015).

Stellar mass is one such variable that has been found to have a significant inverse relationship with the scatter of the MS, as shown by Hopkins et al., 2014. They found a scatter of 0.1 dex with $log(M_{*}/M_{\odot})$> 11, but a much larger scatter of 0.4 dex as stellar mass approached $log(M_{*}/M_{\odot})$~ 8. This makes intuitive sense, as the smaller the galaxy (and lower amount of

stellar mass), the more sensitive it would be to negative feedback mechanisms such as winds caused by AGN and supernovae.

However, some recent studies have shown a sub-linear relation between SFR and M_* in the low redshift end at high stellar mass, causing a bending of the main sequence (e.g. Schreiber et al., 2015; Popesso et al., 2019; Leslie et al., 2020). This bending disappears at high redshift and low stellar mass, and is likely due to the hot halo preventing gas inflow onto the disk, as well as the red bulge created by increased merger activity (and not only stellar mass) (Popesso et al., 2019). However, not all studies find evidence for the bending theory, such as Elbaz et al., 2011, Speagle et al., 2014, and Pearson et al., 2018.

Furthermore, as shown in Figure 6.2, the higher the $log(L_{IR}/L_{UV})$ (an indicator of obscuration and dust content, as L_{IR} is luminosity emitted from dust heated by UV light), the higher the galaxy sits on the expected main sequence with higher stellar masses (Whitaker et al., 2012). The slope of the main sequence is also found by Whitaker et al., 2012 to decrease with increased dust and obscuration (as well as higher stellar mass and lower SFRs). However, some more recent studies (such as Popesso et al., 2019) have shown that the redder color of galaxies at the high end of the main sequence is due to older stellar populations, rather than reddening due to dust content. This was demonstrated by a constant Balmer decrement at greater than $log(M_*/M_\odot)$ > ~11, implying reduced star formation in disks of galaxies and complete quenching of the bulge with increased stellar mass (as the gas for star formation has been completely used up, in line with the theory of secular evolution). In addition, the higher a galaxy sits above the expected main sequence, the more obscured its star formation is expected to be (Hogan et al., 2021).

It has also been found that the population of starbursting galaxies does not evolve with redshift, and these galaxies consistently make up 2% to 4% of the total galaxy population between $0.5 < z < 4$ (e.g. Rodighiero et al., 2011; Schreiber et al., 2015). This is especially interesting given that the merger rate should increase with redshift (proportional to $(1 + z)^m$, where m is the slope of the evolution of the merger rate) (e.g. Hopkins et al., 2010a), thereby increasing the proportion of starbursting galaxies. However, some studies (such as Perret et al., 2014) have shown that at earlier epochs (z ~ 2), isolated galaxies have already become saturated in their SFRs due to large amounts of feedback processes (such as stellar winds and supernovae)

and already heightened levels of star formation, with the majority of star formation being in a compact region near the mass center of the galaxy (Elbaz et al., 2018). This implies that even if a merger were to occur, it wouldn't necessarily increase the amount of star formation in the galaxy, which is consistent with a constant fraction of starbursting galaxies over time.

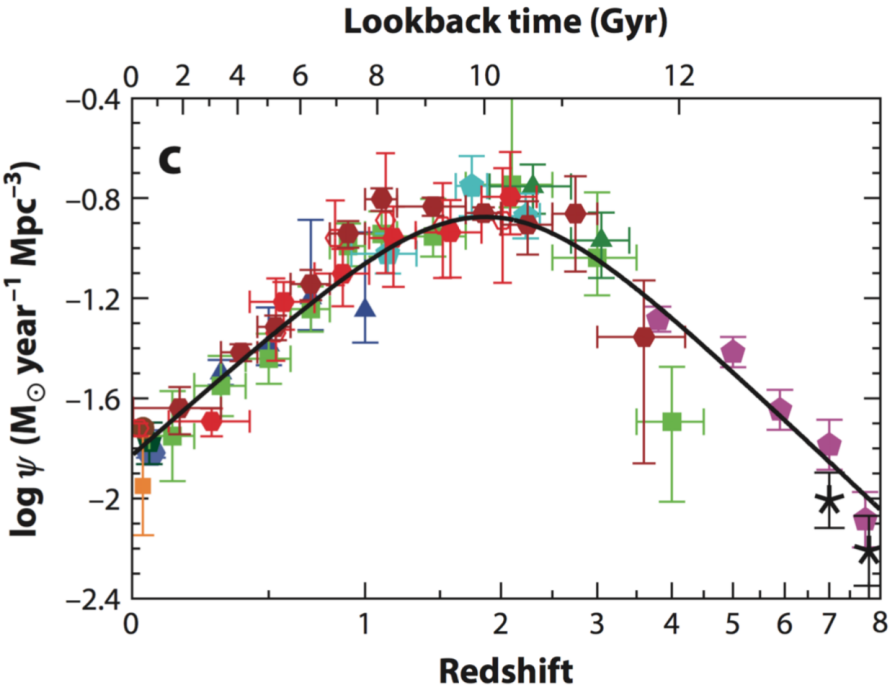


Figure 6.1: A plot of the global SFR density vs redshift, demonstrating how the global SFR density peaked at around z = 2, and has been decreasing to the present. Credit: Madau & Dickinson.

3. Triggers of Star Formation

While star formation in most galaxies usually happens as a result of secular evolution, there are phenomena which can trigger periods of increased star formation - known as starbursts. One of the main triggers of starbursts are galactic interactions, where the gravitational fields (from the dark matter halos) of two (or more) galaxies disturb each other, and gas from both galaxies combines, compresses, and collapses to form new stars at an increased rate. The most violent type of interaction is a merger, where the galaxies collide and ultimately form one single heterogeneous galaxy.

Large-scale galactic mergers are one of the most important drivers of dynamic and kinematic evolution, along with triggering large bursts of star formation. The most extreme episodes of starbursts in galaxies are almost always associated with recent mergers (e.g. Sanders and Mirabel, 1996; Puglisi et al., 2017), as tidal torques drive rapid inflows of gas to the centers of galaxies, causing periods of massive star formation (Barnes & Hernquist 1996). The molecular gas is then quickly consumed or blown away by winds caused by supernovae, causing the star formation to quickly subside - with the galaxy evolving from being dominated by young, blue stars to old, red stars.

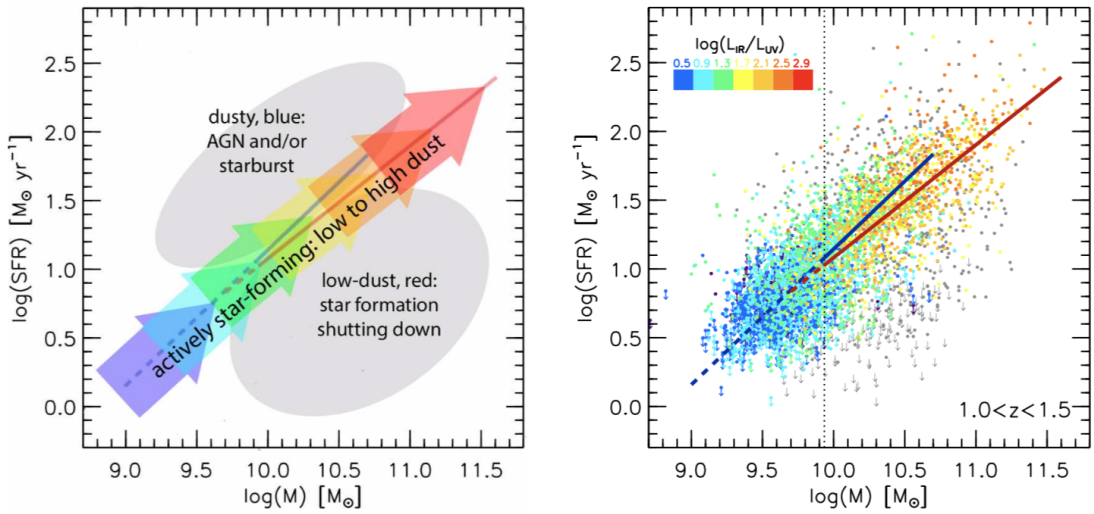


Figure 6.2: The $SFR - M_*$ (star formation main sequence) relation, shown as a cartoon (L) and from observed data with a linear fit for $log(L_{IR}/L_{UV}) \geq 1.5$ (red, implying a higher dust content and obscuration, or older stellar populations) and $log(L_{IR}/L_{UV}) < 1.5$ (blue, implying a lower dust content and obscuration, or younger stellar populations) (R). As galaxies form stars through secular evolution, they move upwards and along the main sequence. At this point, the galaxy either becomes quiescent, or new gas inflows from the IGM cause the cycle to repeat. These plots do not contain the SWIFT data. Credit: Whitaker et al., 2012.

While stars almost never collide in mergers, their orbits are greatly altered by the changing gravitational potential, and post-merger do not resemble their prior orbit (e.g. Van Albada, 1982). This process is known as violent relaxation, and results in a galaxy dominated by the random and complicated new orbits of stars (i.e. dispersionally dominated/ellipticals) and slower rotation. Galaxies which are not interacting (i.e. isolated disks/spirals) have lower

dispersions and more ordered orbits of stars and gas, and are rotationally dominated. However, the picture is more complicated than this, as gas-rich mergers are likely to reform a disk after the violent relaxation (e.g. Athanassoula et al., 2016; Athanassoula & Bosma, 2019; Peschken et al., 2020).

The ratio of the rotational velocity 'V_{max}' to the intrinsic disk dispersion 'σ_0', known as the 'dynamical ratio', traces how rotationally supported the galaxy is (e.g. Epinat et al., 2010; Bellocchi et al., 2013, Wisnioski et al., 2015, Stott et al., 2016). V_{max} is the maximum rotational velocity of the galaxy, and σ_0 is the spatially constant disk dispersion (assumed to always be spatially constant, and separate from the dispersion due to a galactic bulge or AGN). Rotationally supported objects (stable disks) have high V_{max}/σ_0 ratios, as the motion of the stars and gas is relatively ordered with strong rotation. Interacting systems (ellipticals and reformed disks) will have much higher disorderly motion, leading to higher dispersion, and a lower dynamical ratio (e.g. Epinat et al., 2010; Bellocchi et al., 2011). For context, the Milky Way is rotationally dominated and has a dynamical ratio of around 4.0 (e.g. Sofue et al., 2017), whereas elliptical galaxies will have dynamical ratios less than 0.5 (e.g. Bellocchi et al., 2013; Pereira-Santaella et al., 2019). Recent studies have shown that galaxies are typically rotationally dominated, with ~80% of galaxies on the MS having dynamical ratios greater than 1.83 (Wisnioski et al., 2015; Wisnioski et al., 2019).

This ratio effectively traces whether the galaxy is dominated by rotation or dispersion, and as such is a tracer of dynamical evolution and kinematic history. If a galaxy has a low ratio of V_{max}/σ_0 and is dominated by dispersion, it may have been previously involved in a merger, or had significant periods of strong outflows or inflows (Wisnioski et al., 2019). If the ratio is high, the galaxy may be a stable disk and not have had a significant interaction with another galaxy. However, as noted above, this may not always be the case, as gas-rich mergers may reform a disk after the violent relaxation (e.g. Athanassoula et al., 2016). The dynamical ratio may also evolve with redshift, luminosity, SFR, gas fractions, and stellar mass (e.g. Stott et al., 2016; Wisnioski et al., 2015; Wisnioski et al., 2019; Beifiori et al., 2014; Hogan et al., 2021), and velocity dispersion is expected to increase with redshift due to increased gas fractions at higher redshift. Further discussion and comparison of the results of recent kinematical studies at various redshifts is presented in Chapter 8.

It is important to note that the kinematic parameters (rotational velocity and the intrinsic disk dispersion) were later measured in this study using $H\alpha$ emission which is very sensitive to the effects of dust obscuration and extinction (e.g. Hogan et al., 2021; Pereira-Santaella et. al., 2019). This could cause incorrect morphological and kinematic classifications, as both the velocity and dispersion could be improperly measured. However, it is often the case that the majority of the dust is located at the center of the galaxy, which would not cause a significant impact on the measurement of the rotational velocity and intrinsic disk dispersion (as both are measured at the edges of galaxies).

However, star formation triggers from both gas inflows and interactions are subject to negative feedback mechanisms from AGN - supermassive black holes at the centers of galaxies that re-radiate accreted matter as energy. This is an efficient process that provides massive amounts of energy to galaxies, and can quench star formation by causing outflows of molecular gas (e.g. Magorrian et al., 1998).

In some highly luminous galaxies, a significant fraction of the observed luminosity is due to a luminous AGN rather than strong episodes of star formation (e.g. Tran et al., 2001). This is an issue in the infrared, as it is difficult to determine whether the high L_{IR} (from thermal radiation of dust) is due to the luminosity from young O/B stars, or the energy radiated from an AGN which also heats dust. AGN therefore can cause significant over estimation of the integrated SFR_{IR} in some galaxies (and therefore incorrect positions relative to the star formation main sequence. Spatially resolved $SFR_{H\alpha}$could be used as a proxy, but is subject to significant underestimation due to dust extinction, and an integrated value would still be affected by the AGN ionizing nearby gas. However, Mullaney et al., 2012 found that the strength of the AGN source has minimal actual impact on the position of the host galaxy on the main sequence, as there is no detected correlation between the X-ray and IR luminosities at any redshift (indicating that star formation is not related to nuclear activity). This could potentially be due to increased scatter from the variability of the AGN, as X-ray observations will only provide instantaneous luminosities (e.g. Hopkins & Hernquist, 2006). Furthermore, other studies have shown that SFRs in the galaxy nucleus are highly correlated with the strength of the AGN (e.g. Diamond-Stanic & Rieke, 2012).

On the other hand, M_* is a strong indicator of whether the galaxy has a moderate luminosity AGN due to increased accretion on the AGN, and 79% of local high mass ($M_\star > 10^{11} M_\odot$) main sequence galaxies contain moderate luminosity AGN (Mullaney et al., 2012). It has also found that there is a relationship between AGN activity and the compactness of the star formation (Elbaz et al., 2018).

The equivalent widths of PAH features can help indicate whether a source is powered by AGN or star formation (e.g. Rigopoulou et al., 1999; Laurent et al., 2000; Brandl et al., 2006; Spoon et al., 2007; Magdis et al., 2013). In galaxies with an AGN, it is believed that the radiated energy from the AGN in the UV (and thereby heat from dust) destroys PAH molecules, causing less intense PAH features (e.g. Tielens et al., 2005; O'Dowd et al., 2009). As such, the equivalent width of the PAH feature scales inversely with the AGN contribution to overall luminosity, and can then be accounted for (e.g. Magdis et al., 2013). However, the theory that AGN destroy PAHs has been recently challenged (e.g. Jensen et al., 2017).

There are, however, various other AGN selection techniques that could have been used to detect and remove AGN luminosity (such as the radio excess and X-rays). The radio excess was the original way to detect AGN (due to AGN emitting very strongly in radio wavelengths due to comptonization from the accretion disk in the hot corona) (e.g. Crummy et al., 2006; Wilkins et al., 2015), however only ~10% of AGN emit strongly in those wavelengths (White et al., 2000) and the SWIFT subset did not have readily available radio data. Strong X-ray emission is, however, ubiquitous in AGN, and also produces a power law (e.g. Ishibashi et al., 2010). The X-rays are produced by both the continuum of the AGN and accretion disks, and are very resistant to extinction and absorption (unlike in the IR). However, X-ray detection of AGN would not help to determine the contribution of the AGN to the total IR luminosity.

To correct L_{IR} for AGN contribution, the spectral energy distribution (SED) of the galaxy can be fitted using a combination of components that model the multi-band luminosity of the host-galaxy and the AGN (e.g. Mullaney et al., 2011; Magdis et al., 2013). The fractional contribution of the AGN component to the overall SED (f_{AGN}) can then be calculated, which is detected from an excess in the near-IR luminosity that can be modelled by a power law

(dominant in shorter wavelengths). This near-IR power law can then be removed to calculate the true L_{IR} due purely to star formation.

4. Relating Increased Star Formation with Interactions or AGN

As the star formation main sequence and dynamical ratio are both important diagnostics used to learn more about the evolution of galaxies, it would be valuable to have a relation between the two to see how changes in the dynamical ratio (and whether the galaxies are isolated or interacting) impact a galaxy's offset from the star formation main sequence. Some galaxies, as shown in Figure 6.2, have higher rates of star formation than would be expected given their stellar mass, which could be due to starbursts caused by interactions, or AGN leading to falsely high values for SFR_{IR}. The objective of Part II of this thesis is to determine whether the high multiplicative offsets from the expected main sequence of star formation are due to star formation due to interactions, or due to luminosity from an AGN.

Chapter 7 discusses data reduction, ancillary data used, and kinematic analysis. Chapter 8 presents the results of the study, along with a discussion of the main conclusions.

Similar studies have been done with other samples, i.e. the KROSS survey (e.g. Magdis et al., 2016; Stott et al., 2016; Johnson et al., 2018; Harrison et al., 2017), but none have incorporated the star formation main sequence, kinematics, and AGN contribution simultaneously. However, some studies have shown a positive correlation between merger state and position relative to the main sequence (e.g. Stott et al., 2013; Hung et al., 2013).

The rest of Part II will be structured as follows:

- Chapter 7 will discuss the 5MUSES sample and the SWIFT subset, along with observations, data reduction, kinematic analysis, extinction correction, and estimates of metallicity .

- Chapter 8 will present and discuss results, along with conclusions and suggested areas for future work.

- Appendix A: SDSS images and kinematic fits for the SWIFT-5MUSES galaxies.

- Appendix B: SED template fits for the SWIFT-5MUSES galaxies.

Chapter 7

Sample and Data Analysis

For this study, spatially resolved data of a statistically significant subset of the 5MUSES sample (Wu et al., 2010. Hereafter W10) was acquired with the Oxford SWIFT integral field spectrograph (Thatte et al., 2006). This is the first spatially resolved optical study of a subset of the 5MUSES sample.

For this work, a flat ΛCDM cosmology is used with $H_0 = 70\, kms^{-1}MPc^{-1}$, $\Omega_\Lambda = 0.73$, and $\Omega_m = 0.27$. This is consistent with the 5MUSES data from W10. A Kroupa IMF is used for the entirety of this work, except for the calculation of stellar mass (Shi et al., 2011) where a Chabrier IMF was used. However, the conversion to a Kroupa IMF from a Chabrier IMF is very small and we do not attempt to correct for the differences (e.g. Zahid et al., 2012; Kirkpatrick et al., 2014).

1. Sample Selection - 5MUSES and the SWIFT Subset

The 5 Milli-Jansky Unbiased *Spitzer* Extragalactic Survey (5MUSES) is a sample of 330 galaxies with $f_\nu(24\mu\text{m} > 5mJy)$from the *Spitzer* Wide-area Infrared Extragalactic Survey (SWIRE) (Lonsdale et al., 2003) and the Extragalactic First Look Survey (XFLS) (Fadda et al., 2006) fields. This relatively bright infrared flux cut allows for detailed infrared properties to be studied as the infrared features are strong. The luminosities range from $10^9 L_\odot$ to $10^{13.5} L_\odot$,with

83% in the range $10^{10}L_{\odot} < L_{IR} < 10^{12}L_{\odot}$. Redshifts range from 0.008 to 4.27, with a median of 0.144. A broad range of $PAH_{6.2\mu m}$ equivalent widths are also covered in the survey, as the mid-IR is home to many PAH features, which were detected with low-resolution spectra from the *Spitzer Space Telescope's* Infrared Spectrograph (IRS). Based on the $PAH_{6.2\mu m}$ equivalent widths, galaxies are classified as starburst-dominated (43% of the overall sample), starburst-AGN composites (23%), and AGN-dominated (34%). (W10)

The SWIFT subset consists of 34 (~10% of the 5MUSES sample) randomly selected galaxies from 5MUSES up to $z \sim 0.3$. The redshift limit is applied to ensure that the galaxies are sufficiently bright for SWIFT observations. Infrared luminosities range from $9.15 < log(L_{IR}/L_{\odot}) < 11.72$, with a median of 10.93. Redshifts range from $0.032 < z < 0.305$ with a median of 0.114. Starburst-dominated galaxies represent 40% of the overall sample, with starburst-AGN composites 33%, and AGN-dominated 27%.

Plots of the evolution of luminosity with increasing redshift and the main sequence for 5MUSES galaxies with the SWIFT subset highlighted can be seen in Figures 7.1 and 7.2.

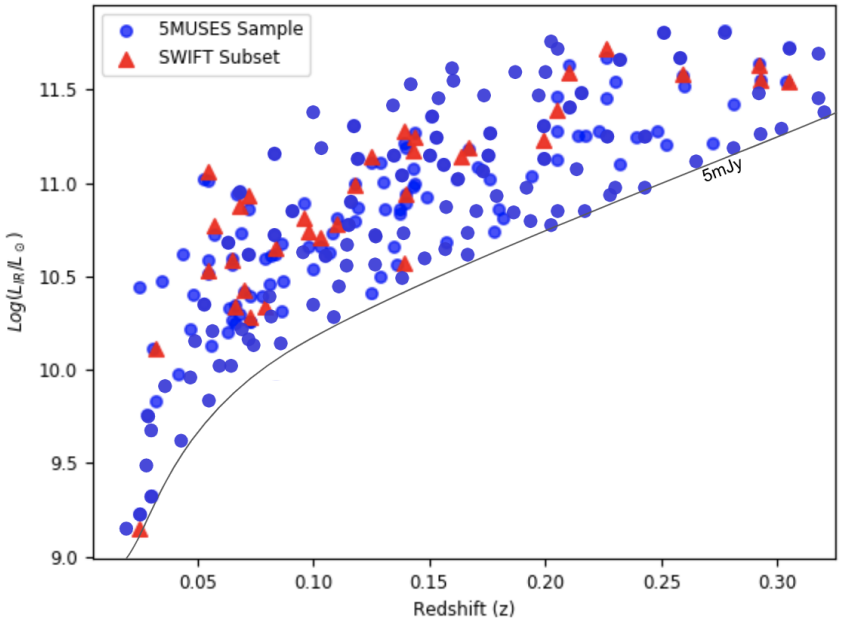


Figure 7.1: A plot showing L_{IR} vs redshift for the entire 5MUSES sample up to $z \sim 0.3$ (blue) with the 5MUSES galaxies observed by SWIFT in red. The 5mJy cutoff for the 5MUSES sample is shown by the black line.

To determine if the subset was representative of the full 5MUSES sample, Kolmogorov-Smirnov (K-S) tests were conducted between both populations in L_{IR}, z, SFR_{IR}, and M_*. All had p-values greater than 0.05, meaning the null hypothesis that the data is from the same sample cannot be rejected. These plots, along with the similar proportions of starburst and AGN dominated galaxies, demonstrate that the SWIFT subset is statistically significant and can be used to make inferences about the 5MUSES sample as a whole.

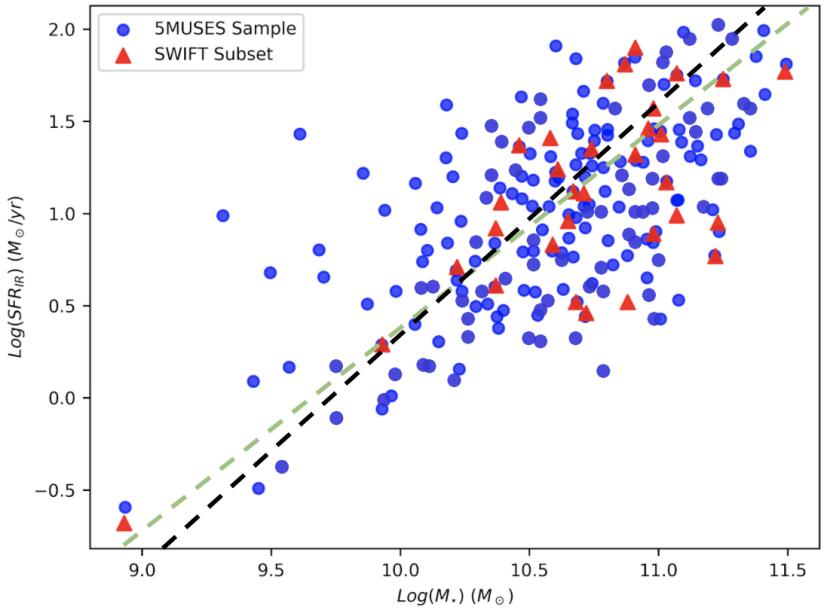


Figure 7.2: A plot showing the main sequence of star formation $Log(SFR_{IR})$ vs $Log(M_*)$ for the entire 5MUSES sample (blue) with the 5MUSES galaxies observed by SWIFT in red. The Elbaz et al., 2011 MS track is shown by the dashed black line, with a fit to the SWIFT data in the green dashed line (which is influenced by the bottom left-most SWIFT galaxy. Without this galaxy included, the fit would be a near direct overlap with the MS track). The SWIFT subset does not include some galaxies with a high SFR_{IR} and a low M_* due to the implicit selection biases based on SWIFT's detection limit.

However, as seen in Figure 7.2, the SWIFT subset does not include some galaxies with a high SFR_{IR} and a low M_* that are in the 5MUSES sample. This is likely due to the fact that the SWIFT subset was inherently biased by SWIFT's detection limit, and so did not feature compact galaxies with a high SFR_{IR} and a low M_* (as they may have been unresolvable). Furthermore, any optical facility will have unconscious biases, and it is noted that this SWIFT subset was

originally selected for CO observations (e.g. Garrett, 2018), and the objective in this observing run was to focus observing time on galaxies with good detections. However, this was not investigated any further as the K-S tests demonstrated the subset was a statistically significant representation of the 5MUSES sample.

The SWIFT subset was a prime target for IFS observations as the 5MUSES sample did not have any spatially resolved optical data. However, the distinguishing feature about the subset is that it is generic. The galaxies are relatively standard and don't exhibit any extreme behavior - this is partially due to the simple selection criteria of 5MUSES. While there are some LIRGs, there are no ULIRGs, and the galaxies represent the bulk of star-forming, main sequence galaxies.

2. Ancillary Data

Integrated IR and $EW_{PAH6.2\mu m}$ data was retrieved from W10. The IR data was acquired with the Infrared Array Camera (IRAC - 3.6μm, 4.5μm, 5.8μm, 8.0μm) on the *Spitzer Space Telescope* and with the Multiband Imaging Photometer (MIPS) at 24μm, 70μm, and 160μm, with low resolution spectra from 5.5μm - 14μm and 14μm - 35μm taken with the IRS. All IRAC and MIPS photometry, as well as IRS spectra, are publicly available online. L_{IR} was estimated by W10 by fitting a spectral energy density model to the mid-IR spectra and photometry from the IRS, IRAC, and MIPS. SFR_{IR} was then calculated using the following equation (Kennicutt et al., 2009) assuming a Kroupa IMF:

$$SFR_{IR}\,(M_{\odot}yr^{-1}) = (1.509 \times 10^{-10}) \times L_{IR}({L_{\odot}}^{-1}) \tag{7.1}$$

$PAH_{6.2\mu m}$ emission properties were also measured by W10 by fitting a spline to the areas between the PAH emission to isolate the main feature, and also by using the PAHFIT software package (Smith et al., 2007). $EW_{PAH6.2\mu m}$ was then determined from the PAH emission strength.

Stellar masses were calculated by Shi et al., 2011 by fitting a Bruzual & Charlot (2003) stellar population synthesis (SPS) model to the multiband spectral energy densities from IRAC

and MIPS, and were calculated for 32 out of 34 galaxies. Assuming a fixed IMF (which defines the distribution of stars formed in an initial burst of star formation), and an assumed star formation history, an SPS model can be generated to fit the broadband SED. The best-fit SPS model will define various galaxy parameters such as the age, metallicity, and dust - as well as the proportion of young and old stars, which defines the stellar mass of the galaxy.

Optical images were taken from the Sloan Digital Sky Survey (SDSS) DR14 data available online. SDSS images can be found in Appendix A. 13 of the 34 galaxies also had 1D spectra available from SDSS, which automatically classified the galaxies as AGN, star forming, or starbursting by fitting a template to the spectrum.

A full table of all the ancillary data used for this work can be seen in Table 7.1.

3. SWIFT Data

The Oxford Short Wavelength Integral Field specTrograph (SWIFT) (Thatte et al., 2006) is an image slicer-based IFS built for the Hale 200 inch telescope at Palomar Observatory, covering the wavelength range 0.63 - 1.04μm. It has multiple spaxel scales, from 16 mas/spaxel, 80 mas/spaxel, to seeing limited at 235 mas/spaxel, all at a resolution of ~2Å. Cryogenically cooled 250μm Silicon CCD detectors, along with the PALM 3K single conjugate adaptive optics system (Bouchez et al., 2008) allow high-quality data to be taken across the spectral range. A table listing the full system specifications is shown in Table 7.2 (adapted from Zieleniewski, 2016).

3.1 Observations

SWIFT data was taken over 10 nights on a series of four observing runs from October, 2014 to October 2016. Flat, arc, and vertical line frames were taken for each run, along with observations of telluric and flux standard stars for each galaxy. 5 galaxies had sky frames simultaneously taken. Seeing was around ~1” full width half maximum (FWHM) for most of the runs, as measured from the telluric standards. Observations were taken at the 235 mas spaxel scale, which covers a field of 10" × 21", with an observing time of 900 seconds per object. A table of the coordinates, observation date, seeing PSF FWHM, and redshift of the galaxies observed can be found in Table 7.3.

ID #	$Log(L_{IR}/L_{\odot})^{(1)}$	$SFR_{IR}\ (M_{\odot}/yr)^{(2)}$	$EW_{PAH6.2\mu m}{}^{(3)}$	$Log(M_{\star}/M_{\odot})^{(4)}$
5	11.54 ± 0.02	52.32 ± 2.41	<0.09	10.8 ± 0.20
12	10.11 ± 0.03	1.94 ± 0.13	0.65 ± 0.08	9.93 ± 0.15
13	11.72 ± 0.04	79.2 ± 7.30	0.53 ± 0.04	10.91 ± 0.12
18	11.63 ± 0.03	64.37 ± 4.45	0.57 ± 0.06	10.87 ± 0.05
19	11.23 ± 0.06	25.62 ± 3.55	<0.16	10.58 ± 0.03
20	10.74 ± 0.02	8.29 ± 0.38	<0.19	10.37 ± 0.12
22	10.71 ± 0.05	7.74 ± 0.89	0.20 ± 0.03	10.98 ± 0.20
28	10.93 ± 0.03	12.84 ± 0.89	0.78 ± 0.02	10.71 ± 0.16
35	10.88 ± 0.04	11.44 ± 1.06	0.71 ± 0.04	10.39 ± 0.02
36	9.15 ± 0.02	0.21 ± 0.01	0.81 ± 0.04	8.93 ± 0.11
37	11.14 ± 0.03	20.83 ± 1.44	0.75 ± 0.10	-
39	10.28 ± 0.03	2.88 ± 0.20	0.36 ± 0.02	10.72 ± 0.10
41	10.57 ± 0.08	5.61 ± 1.04	0.31 ± 0.01	-
50	11.17 ± 0.02	22.32 ± 1.03	0.69 ± 0.003	10.74 ± 0.10
55	11.58 ± 0.02	57.37 ± 2.64	0.58 ± 0.02	11.07 ± 0.08
57	10.81 ± 0.01	9.74 ± 0.22	0.46 ± 0.01	11.07 ± 0.20
61	11.55 ± 0.05	53.54 ± 6.18	0.03 ± 0.002	11.25 ± 0.10
62	11.25 ± 0.02	26.83 ± 1.24	0.72 ± 0.01	11.01 ± 0.30
66	11.39 ± 0.04	37.04 ± 3.42	0.92 ± 0.03	10.98 ± 0.09
69	10.77 ± 0.04	8.89 ± 0.82	0.17 ± 0.01	11.23 ± 0.20
70	10.43 ± 0.04	4.06 ± 0.38	0.38 ± 0.02	10.37 ± 0.20
73	11.06 ± 0.04	17.32 ± 1.60	0.63 ± 0.03	10.61 ± 0.20
75	10.53 ± 0.03	5.11 ± 0.35	0.63 ± 0.004	10.22 ± 0.20
86	10.94 ± 0.03	13.14 ± 0.91	0.55 ± 0.02	10.67 ± 0.09
107	10.99 ± 0.02	14.75 ± 0.68	0.59 ± 0.10	11.03 ± 0.07
185	10.34 ± 0.02	3.3 ± 0.15	0.59 ± 0.10	10.68 ± 0.08
188	10.65 ± 0.02	6.74 ± 0.31	0.824 ± 0.06	10.59 ± 0.08
202	10.59 ± 0.01	5.87 ± 0.14	0.62 ± 0.02	11.22 ± 0.10
294	11.59 ± 0.04	58.71 ± 5.41	0.51 ± 0.01	11.49 ± 0.10
297	10.34 ± 0.04	3.3 ± 0.30	0.78 ± 0.02	10.88 ± 0.08
299	11.19 ± 0.03	23.37 ± 1.62	0.78 ± 0.01	10.46 ± 0.09
310	10.78 ± 0.06	9.09 ± 1.26	0.49 ± 0.05	10.65 ± 0.13
315	11.28 ± 0.07	28.75 ± 4.65	0.50 ± 0.01	10.96 ± 0.14
317	11.14 ± 0.03	20.83 ± 1.44	0.50 ± 0.01	10.91 ± 0.06

Table 7.1: Ancillary data used for this work. (1) IR data from W10. (2) SFR_{IR} calculated from Equation 7.1. (3) $EW_{PAH6.2\mu m}$ from W10. (4) Stellar mass from Shi et al., 2011.

3.2 Data reduction

To reduce the raw SWIFT science frames, the `IRAF` routine `swiftredMS` (written by Ryan Houghton) was used. This pipeline does bias subtraction, flat fielding, wavelength calibration, and error propagation on the input science frames. It also corrects for illumination and

reconstructs the cube at the end of the process (written by Azin Khan). Cosmic ray detection and removal was done with the `LACOSMIC` routine (Van Dokkum, 2001).

Wavelength range	0.63 - 1.04 μm
Spatial scales (FoV)	16 mas ($1.42'' \times 0.7''$), 80 mas ($7.1'' \times 3.5''$) 235×235 mas ($20.9'' \times 10.3''$)
Resolving Power	3250 at 0.65 μm 4400 at 1.0 μm
Temperature	155 K detectors
Detector	2$\times$ LBNL 250 μm, fully depleted, 4k $\times$ 2k CCDs
Throughput	23% (avg. inc. tel. & det.)
AO modes	SCAO, seeing-limited

Table 7.2: The SWIFT system parameters. Credit: Simon Zieleniewski.

First order sky subtraction was completed using the `doABBA` routine within the SWIFT pipeline. The sky frames were observed adjacent in time to each science frame, but were only taken for 5 out of the 34 galaxies. These fields were far enough away to avoid contamination from the target galaxy. For the galaxies without sky frames, the 'A' frame was subtracted from the 'B' frame, and vice-versa, producing an A-B frame and a B-A frame, which were then combined. The `doABBA` routine also propagates bad pixels and estimates the variance of each pixel assuming Poisson statistics. Telluric features were also removed at this stage using the `IRAF Telluric` routine, and the cubes were flux calibrated. To check the accuracy of the calibration, the integrated flux values were taken for a specific band (such as the I band from Johnson UBVRI) and then converted to magnitude. This magnitude was then compared to the literature value for that specific standard star in that wavelength band (available publicly online for the standard stars used). An error of 20% on the computed flux calibrations of the SWIFT cubes is assumed. However, integrated flux values were ultimately not used in this work.

ID #	*RA*	*DEC*	*Observation Date*	*Seeing FWHM (arcsec)*	*Redshift*
5	34.1593	-4.3808	1/10/2014	2.5	0.305
12	34.4326	-5.2977	3/10/2014	1.8	0.032
13	34.4787	-3.9740	1/10/2014	2.5	0.226
18	34.7074	-5.3662	2/10/2014	1.3	0.292
19	34.7490	-4.0437	3/10/2014	1.3	0.199
20	34.7901	-5.4202	11/10/2016	0.8	0.098
22	34.8170	-5.9575	11/10/2016	0.8	0.103
28	34.9710	-5.3067	11/10/2016	0.8	0.072
35	35.4493	-2.9585	14/10/2016	1.1	0.068
36	35.4495	-4.7705	11/10/2016	1.1	0.025
37	35.4648	-3.4866	14/10/2016	1.1	0.164
39	35.5970	-4.7221	13/10/2016	0.9	0.073
41	35.6723	-4.9478	1/10/2014	1.3	0.139
50	35.9377	-5.7096	21/10/2015	1.1	0.143
55	36.1430	-4.2587	13/10/2016	0.9	0.259
57	36.1959	-4.1475	12/10/2016	1.1	0.096
61	36.2848	-5.6549	13/10/2016	0.7	0.293
62	36.3443	-4.9144	12/10/2016	1.2	0.144
66	36.5000	-5.0293	12/10/2016	1.2	0.205
69	36.5727	-5.0788	13/10/2016	0.9	0.057
70	36.6575	-3.9783	12/10/2016	1.0	0.070
73	36.8363	-4.7604	14/10/2016	0.7	0.055
75	36.9236	-4.9473	13/10/2016	0.9	0.055
86	159.1935	58.7252	11/10/2016	1.0	0.140
107	161.2254	57.7405	14/10/2016	1.2	0.118
185	242.2433	55.5029	12/10/2016	0.8	0.066
188	242.2846	55.3782	14/10/2016	0.9	0.084
202	243.2257	54.9238	7/7/2015	1.3	0.065
294	258.1348	59.3572	8/7/2015	1.3	0.210
297	258.3189	58.5431	7/7/2015	1.0	0.079
299	258.5618	58.8727	13/10/2016	1.0	0.167
310	259.2964	60.4528	11/10/2016	0.8	0.110
315	259.8890	59.4619	8/7/2015	1.3	0.139
317	260.1804	58.6741	13/10/2016	0.8	0.125

Table 7.3: Galactic locations, observation dates, seeing PSF FWHM, and redshift of target galaxies.

3.3 Initial kinematic analysis

To perform initial kinematic analysis on the reduced cubes, an end-to-end python routine was used (written by the author). The routine starts by cutting the cube in *x, y,* and λ space around the galaxy and wavelength regions of interest, as specified by the user. The spatial size would vary for each galaxy, but the wavelength range was typically restricted to 300 channels centered around the *H*α emission. A continuum is then fit to the central spaxel of the galaxy, using either a linear or polynomial equation. A Gaussian is simultaneously fit (with no background level

allowed) using the Python package `LMFIT` (Newville et al., 2014) to the observed $H\alpha$ emission. The Gaussian is fit using several iterations of χ^2 minimization to best optimize the fit. The resulting value for the observed $H\alpha$ emission center is then compared to the rest wavelength of 6563Å and the redshift (z) is calculated. The entire cube is then shifted to rest frame using the systemic velocity (later reduction required rest-frame cubes as inputs).

With the new cut rest frame cube, the program then iterates through each spaxel, subtracts the continuum, and fits three emission lines - $[NII]6548\text{Å}$, $[H\alpha]6563\text{Å}$,and $[NII]6584\text{Å}$. Some parameters of these fits (such as the physically-defined flux ratio and separation of $[NII]6548\text{Å}$ and $[NII]6584\text{Å}$) are fixed to ensure the model is physical. Each fit for each spaxel is only considered if the signal-to-noise ratio of the emission line is above 3, and other galaxy-specific cuts are met (such as appropriate values for the amplitude, center, and width of the Gaussian). However, this was an issue when fitting the $[NII]6548/6584\text{Å}$ doublet - as some of the Nitrogen dispersion could broaden the $H\alpha$ line - causing errant calculations that produced false emission centers and integrated fluxes. To solve this, the $[NII]6548/6584\text{Å}$ doublet was fit simultaneously and then subtracted from the spectrum, leaving only the $H\alpha$ emission which then could be individually fit. Errors on the fits were calculated automatically by `LMFIT` using the variance cubes created by the `doABBA` routine as an input. $[H\alpha]6563\text{Å}$ was able to be successfully fit for 30 out of 34 galaxies, and $[NII]6584\text{Å}$ was able to be fit for 26 out of 34 galaxies.

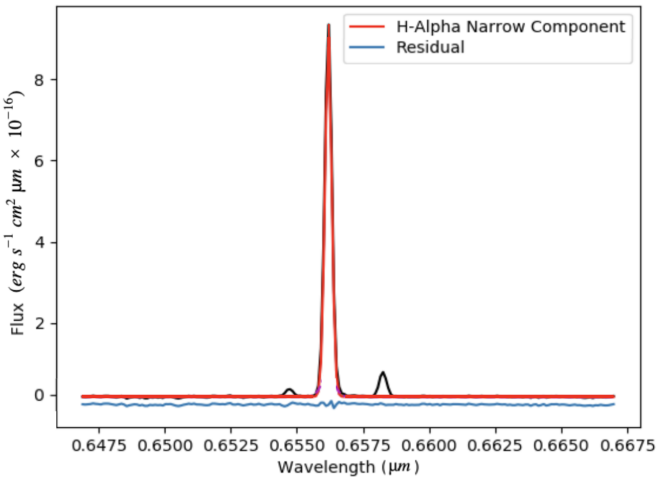


Figure 7.3: The fitted $[H\alpha]6563\text{Å}$ emission line for M036, shown in red. The residuals of this fit are shown in blue.

The spaxels that have successful $H\alpha$ fits are added to a new array that acts as a mock aperture. Their spectra are summed together to create what is effectively the entire galaxy without bad spaxels (due to high noise, detector issues, leftover cosmic rays, etc). This integrated spectrum is then fit with the same three emission lines as above. Examples of spectral fits on the 'integrated' galaxy (for only $[H\alpha]6563$Å)can be seen in Figure 7.3.

The spaxel-by-spaxel fits are used to create rotational line-of-sight velocity maps from the small shifts of the $[H\alpha]6563$Å central wavelengths. Maps of the $[H\alpha]6563$Å velocity dispersion (σ) are also produced. Figure 7.4 shows examples of output 2D integrated flux, rotational velocity, and velocity dispersion maps for M202.

3.4 GalPak analysis

To model the true dispersion and de-projected rotation curves to find V_{max}, as well as the intrinsic isotropic velocity dispersion σ_0, the GalPak (Bouché et al., 2015) Python package was used. The GalPak routine required different input cubes to those used above for the initial kinematic analysis: observed frame SWIFT cubes centered around the observed $[H\alpha]6563$Å emission, cut to 100 wavelength channels, and cut spatially as in Section 3.3. Furthermore, the Nitrogen doublet and continuum were subtracted and removed (leaving only the $[H\alpha]6563$Å emission). Each of these new cubes is taken as an input, and GalPak creates a model galaxy using an exponential flux profile and arctangent rotation profile, and convolves the model with the instrumental point spread function and line spread function of SWIFT from the observation and based on the observed $[H\alpha]6563$Å emission central wavelength. An exponential flux profile is used because the galaxies are assumed to be disks. The model is then rotated about the kinematic position angle (PA) and inclination until the best fits are found, and creates 2D line-of-sight flux, velocity, and dispersion maps. The velocity of the model is then de-projected according to the equation below to find the maximum velocity:

$$V_{max} = V_{obs}/sin(i) \tag{7.2}$$

where V_{max} is the de-projected maximum rotational velocity, V_{obs} is the line-of-sight velocity, and i is the inclination. The intrinsic disk dispersion σ_0 is also measured at this point, and does not need to be de-projected as the model is assumed to be symmetric. M_{dyn} is also calculated using V_{max} and the radius, R (see Chapter 8, Section 2). However, GalPak can only fit a single model. Therefore, interacting galaxies where two nuclei were present or were perturbed (with evidence of tidal features) were unable to be fit.

Errors are calculated by GalPak from the residuals of the fit of the model to the observed data. These errors are then convolved with the scaled variance cubes containing the individual spaxel variance values to come up with a true error parameter for the kinematic data. GalPak takes these variances into account when calculating the errors on V_{max}, as the estimates of V_{max} are very sensitive to the galaxy inclination. GalPak can recover inclination without degeneracy with V_{max} as it uses a variable ratio of the elliptical axes *b* and *a*. Also, as the model GalPak fits is 3-dimensional, GalPak is able to recover errors on both morphological parameters (such as *R* and *i*) and kinematic parameters (V_{max} and σ_0) irrespectively of redshift and seeing (Bouché et al., 2015).

It is noted that the SWIFT resolving power (~3300) at the $H\alpha$ line corresponds to ~90km/s of resolution at that wavelength. However, this can be interpreted being a Gaussian distribution centered at 90km/s, and as GalPak fits a model to recreate the observed data (for every spaxel in the field of view), the error can be significantly lower than 90km/s, especially with data that has a high signal-to-noise ratio (as in the SWIFT subset). Furthermore, since the PSF and LSF are well known and applied to both the model and observed data, the returned parameters are intrinsic and deconvolved. Other studies using similar fitting methods have returned errors of ~30% of the intrinsic resolution error (which is then added in quadrature to the statistical errors) (e.g. Wisnioski et al., 2015). Errors on the kinematical parameters for the SWIFT subset are between 5%-15%. As noted in Wisnioski et al., 2015, in face-on galaxies (with $\sin i < 0.8$) dispersion can be underestimated due to a less mixing of the radial and vertical components of dispersion. As such, for highly inclined systems ($\sin i > 0.9$), dispersion could be inflated due to the effects of enhanced mixing as well as beam smearing, but <10% of the SWIFT subset had inclinations larger than this, and so this effect is not considered significant in

this study. It is also noted that GalPak does not fit extinction, which could lead to incorrect estimations of V_{max}, R, and σ_0, as described in Chapter 6. Inclination would not be affected assuming spatially constant extinction over the spatial extent of the galaxy.

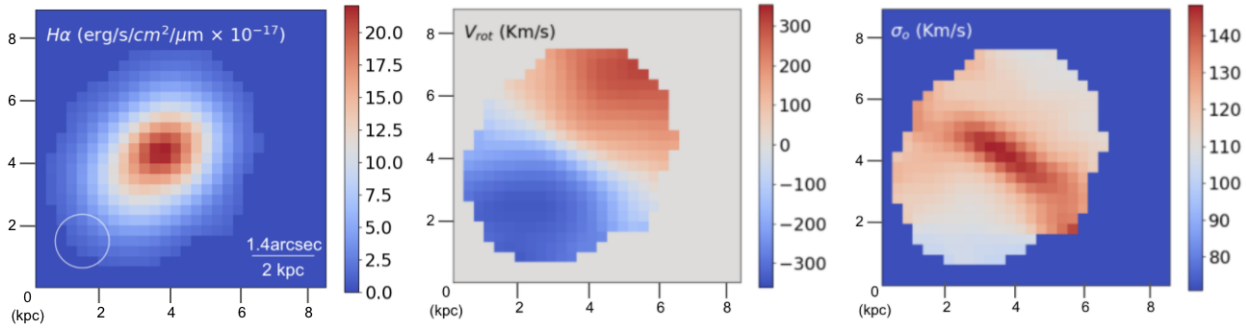


Figure 7.4: Integrated flux (left), line-of-sight velocity (middle), and velocity dispersion (right) maps for M202 modeled from the $[H\alpha]6563$Å emission line.

Increased σ_0 due to AGN, a galactic bulge, or beam smearing was not an issue as all of the galaxies were spatially resolved past the AGN/bulge (and the PSF was narrower than the radius of each galaxy). This was confirmed as all galaxies had resolved velocity fields and the observed dispersions approached an asymptote, indicating good sampling of the rotation field and disk dispersion. If the disk was not resolved, beam smearing would cause the recovered disk dispersions to be artificially high (due to the excess dispersion from the bulge/AGN), preventing accurate measurements. The effects of beam smearing were further mitigated by narrow PSFs, with seeing of at or below 1" for most of the SWIFT subset, further helping to resolve the disk relative to the bulge. Galaxies that were classified as AGN are identified, but as the galaxies were resolved past the AGN/bulge, the AGN did not impact the measurement of the disk dispersion (measured at the outer spaxels). Furthermore, as both of the kinematic metrics were measured at the maximum resolved spatial extent of the galaxy, beam smearing would be less significant, as it is least impactful in these outer areas. However, the beam smeared local velocity gradient ($\Delta V/\Delta r$) over the radius of the PSF (at the spatial extent of the galaxy in the model velocity field) was still removed from the observed dispersion. This helped to account for any minimal effects of beam smearing at the spatial extent of the galaxy (this is in line with the method used in Stott et al., 2016, and $\Delta V/\Delta r$ was close to zero for all galaxies at their spatial extent as the outer disk was resolved).

Each of the parameters fit were restricted to a range of values and then cut based on initial guesses from the initial fits. To check the quality of the model and the fits, the convolved model was then subtracted from the observed data to create a map of the residuals. This was completed for flux, velocity, and dispersion. Maps of the observed, convolved model, and residual flux, velocity, and dispersion for M202 can be seen in Figure 7.5. To make curves of the rotation and dispersion, data points from the velocity/dispersion maps were taken radially outwards from the center of the galaxy along its PA, using apertures with a diameter equal to the size of the PSF FWHM. The 'stopping' criteria for retrieving the data points was when the signal-to-noise ratio within the aperture fell below 3. Typically, at least five to six data points are required before the rotation and dispersion curves can be considered to be statistically significant and actually detected.

An example of the output de-projected observed and modelled velocity and dispersion maps and curves for M202 can be seen in Figure 7.6. All observed, model, and residuals maps, along with velocity and dispersion curves can be found in Appendix A.

GalPak was able to successfully fit 22 out of 34 galaxies. Out of these 22, 20 had at least 6 resolved data points for rotation and dispersion, with the remaining 2 galaxies having 5 resolved data points. Of the 12 galaxies that were not able to be fit, two of the galaxies - M012 and M013 - had SWIFT datacubes that had poor wavelength calibration between the master and slave spectrographs, preventing any kinematic fits. M005, M039, M041, M057, M061, M070, M075 and M294 had a low S/N ratio from the SWIFT datacube which prevented accurate fitting and convolving of the kinematic model. M020 had evidence of tidal features, and M062 had two resolved nuclei, and as such neither could not be fit by a single model. M073 was visually interacting with two nuclei, and had a slight perturbation in the velocity field. However, GalPak produced a good fit which is included in the following discussion. None of the galaxies later classified as interacting had two resolved nuclei in the SWIFT datacubes, and only one model was fit to each galaxy. Many of the galaxies unable to be fit with GalPak were able to be later classified visually as isolated or interacting.

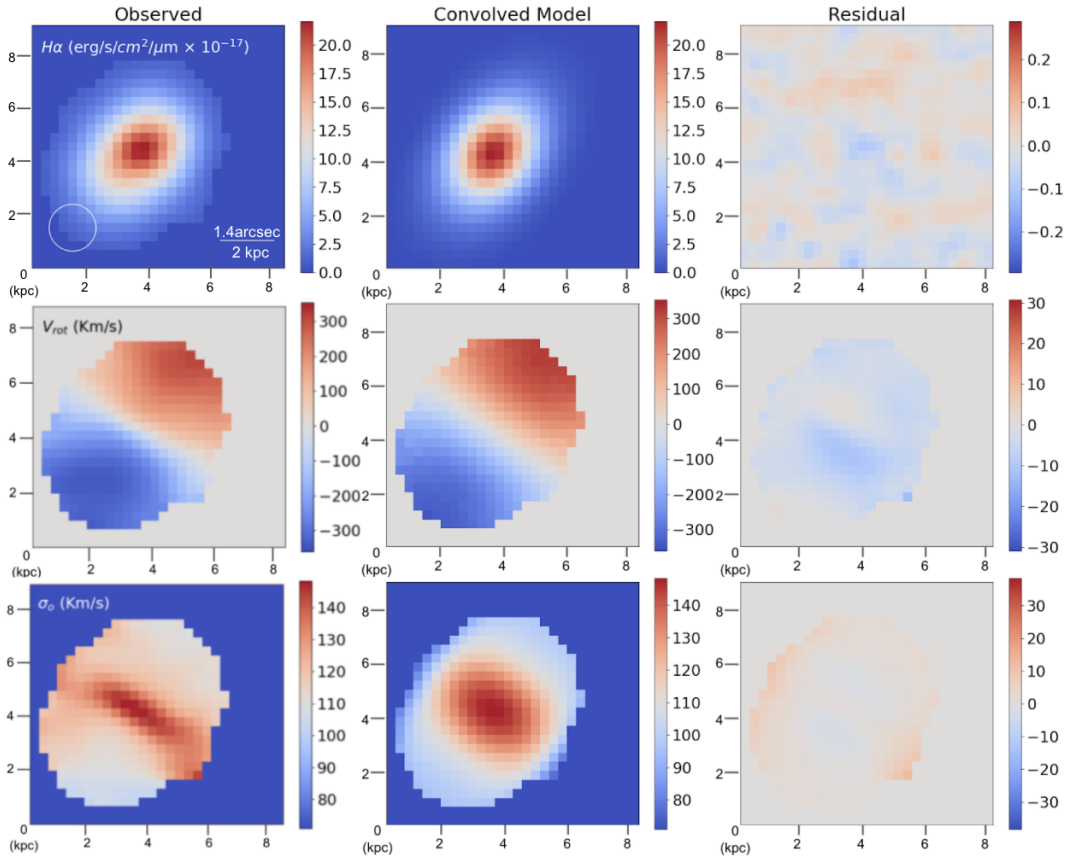


Figure 7.5: Output maps from M202 for [$H\alpha$]6563Å integrated flux (top row), rotational velocity (middle row), and velocity dispersion (bottom row). The observed maps are shown in the left column, with the maps of the convolved model in the central column, and the residuals of the fit in the right column.

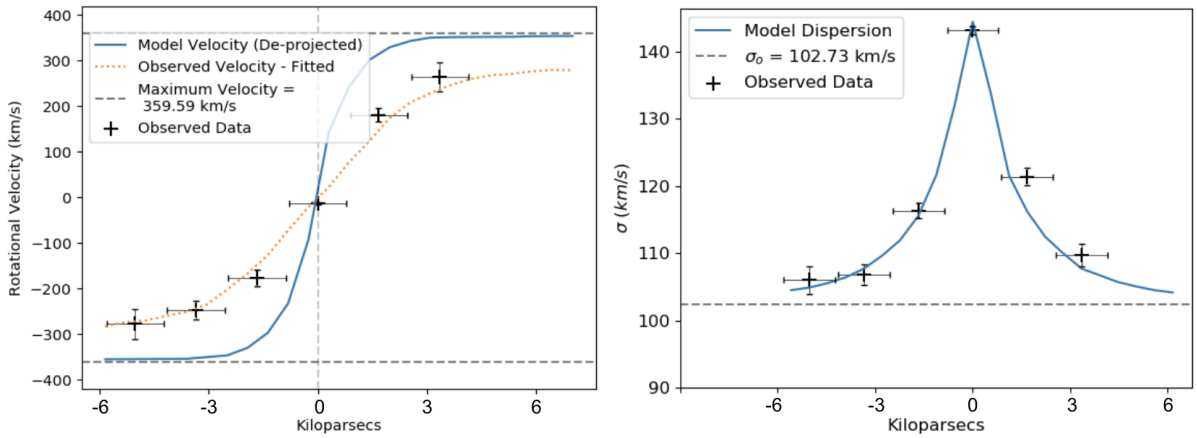


Figure 7.6: Observed and de-projected model rotation and dispersion curves for M202. The models were fitted by GalPak, compared to the observed curves output by the initial fits, and then de-projected to calculate V_{max}. Data points were taken radially outwards starting at the rotation center, with each subsequent point taken one PSF FWHM away.

3.5 Extinction correction

As described in Chapter 6, the $H\alpha$ emission can be underestimated due to dust extinction which could negatively impact the kinematic measurements. As the 5MUSES sample and the SWIFT subset emit strongly in the IR, it is likely that there is a component of dust that will lead to some degree of attenuation. To estimate the obscured star formation, or the degree to which $SFR_{H\alpha}$ is underestimated due to dust extinction, the ratio of $log(SFR_{H\alpha}/SFR_{IR})$ can be taken (e.g. Pereira-Santaella et al., 2019; Hogan et al., 2021), as SFR_{IR} will not be strongly impacted by dust extinction. It is noted that the $SFR_{H\alpha}$ used in this equation is not corrected for extinction. As described in Chapter 6, SFR_{IR} is measured from stars with ages of ~100Myr, whereas $SFR_{H\alpha}$ is measured from stars with ages of ~10Myr. This ratio therefore assumes a constant SFH for the past 100Myr.

$SFR_{H\alpha}$ was calculated using equation 7.2 below from Kennicutt et al., 2009 assuming a Kroupa IMF:

$$SFR_{H\alpha}\,(M_{\odot}yr^{-1}) = (5.5 \times 10^{-42}) \times L_{H\alpha}(L_{\odot}{}^{-1}) \tag{7.3}$$

The values for $SFR_{H\alpha}$ are shown in Table 7.4, along with the ratio $log(SFR_{H\alpha}/SFR_{IR})$.The average ratio for the SWIFT subset is -1.49$\pm$ 0.4, which is compared to the -2.2$\pm$0.4 for intermediate redshift U/LIRGs in Pereira-Santaella et al., 2019, and -1.6$\pm$0.5 for local LIRGs in Rodriguez-Zaurin et al., 2011. This demonstrates that the SWIFT sample is similarly obscured to local LIRGs but less obscured compared to intermediate redshift U/LIRGs.

However, 13 galaxies had SDSS spectra available which contained integrated fluxes for both $H\alpha$ and $H\beta$. These spectra were fit and integrated fluxes calculated using the same routine used for the initial SWIFT kinematic analysis. As noted in Chapter 6, the Balmer decrement can be used to estimate extinction by calculating the ratio of $H\alpha/H\beta$ and comparing it to the physically expected value of 2.86 (assuming case B recombination and electron temperatures of ~10,000K for the SWIFT subset) (Osterbrock et al., 2019; Hammer et al., 2017). The Calzetti et

al., 2000 extinction curve for $H\alpha$ was used when calculating extinction as it is applicable to starburst galaxies similar to those in the SWIFT subset.

Of the 13 galaxies with available SDSS spectra, only 8 had resolved $H\alpha$ and $H\beta$ emission, and only 5 of these 8 were successfully fit by GalPak. The dust extinction, or A_V, for these galaxies can be seen in Table 7.4, and these 8 galaxies had an average $A_V = 1.81 \pm 0.41$. M013 had the highest extinction with $A_V = 2.28 \pm 0.27$. These values are in-line with extinctions for local LIRGs (e.g. Liang et al., 2004; Flores et al., 2003) (which implies agreement with the obscuration as estimated by $log(SFR_{H\alpha}/SFR_{IR})$, as discussed above) and higher than extinctions for normal spiral galaxies (e.g. Greener et al., 2020; Kennicutt et al., 1992). This makes sense as LIRGs should have higher extinctions when compared to normal spiral galaxies as they will have higher dust content and IR luminosity.

As the extinctions for the SWIFT subset were relatively low, and as the SDSS emission lines were integrated over the whole galaxy and not spatially resolved, it was therefore decided to not correct $SFR_{H\alpha}$ for dust extinction, and use the kinematic measurements from GalPak as-is (described above in Section 3.4) for the rest of this thesis. However, it is noted that there will in reality be some additional errors on both V_{max} and σ_0 due to extinction, even if the dust is located mainly in the center of the galaxy.

3.6 Metallicity

As described in Chapter 6, the gas-phase metallicity can be used as a tracer of the star formation history (SFH) of a galaxy, which could help explain the ratio between $SFR_{H\alpha}$ and SFR_{IR} as these trace star formation on different timescales. As the SWIFT subset had both data for both $[NII]6584$Å and $[H\alpha]6563$Å, the N_2 ratio was taken to estimate metallicity using the relation from Pettini et al., 2004:

$$12 + log(O/H) = 8.90 + 0.57 \times N_2 \tag{7.4}$$

where N2 is the ratio of $[NII]6584$Å to $[H\alpha]6563$Å. The metallicities for the SWIFT subset can be seen in Table 7.4, and the average of the subset is 8.69 ± 0.14. This is in-line with metallicities for local LIRGs presented in Rupke et al., 2008, Alonso-Herrero et al., 2009, and Monreal-Ibero et al., 2010, but slightly lower than those for intermediate redshift U/LIRGs presented in Pereira-Santaella et al., 2019, and higher than the higher-redshift U/LIRGs from Hogan et al., 2021.

To give further context to the metallicities calculated above, these values are then compared to the expected metallicity of a galaxy given a redshift and stellar mass (the mass-metallicity relation, or MZR) as prescribed by Tacconi et al., 2018:

$$12 + log(O/H) = a - 0.087 \times (logM_* - b)^2 \quad (7.5)$$

where $a = 8.74 \pm 0.06$ and $b = 10.4 \pm 0.05 + 4.46 \pm 0.3 \times log(1+z) - 1.78 \pm 0.4 \times log(1+z)^2$. These values are also shown in Table 7.4, and the average for the subset is 8.71 ± 0.15, which demonstrates that in general the galaxies have similar metallicities to what would be expected given their redshifts and stellar masses.

ID #	$SFR_{H\alpha}(M_{\odot}/yr)$	$log(SFR_{H\alpha}/SFR_{IR})$	A_V	$12+log(O/H)^1$	$12+log(O/H)^2$
5	-	-	-	-	8.67 ± 0.11
12	-	-	1.47 ± 0.35	-	8.71 ± 0.12
13	1.52 ± 0.23	-1.72 ± 0.05	2.28 ± 0.27	8.71 ± 0.10	8.69 ± 0.12
18	1.24 ± 0.12	-1.71 ± 0.04	-	8.68 ± 0.16	8.67 ± 0.12
19	0.78 ± 0.10	-1.51 ± 0.06	-	8.82 ± 0.14	8.69 ± 0.16
20	0.47 ± 0.08	-1.24 ± 0.05	1.85 ± 0.46	-	8.71 ± 0.15
22	0.28 ± 0.04	-1.44 ± 0.03	1.68 ± 0.38	8.68 ± 0.15	8.71 ± 0.15
28	0.14 ± 0.01	-1.93 ± 0.04	1.58 ± 0.54	8.72 ± 0.13	8.72 ± 0.15
35	0.31 ± 0.04	-1.55 ± 0.04	-	8.64 ± 0.18	8.72 ± 0.17
36	0.02 ± 0.00	-1.12 ± 0.03	-	8.45 ± 0.18	8.53 ± 0.16
37	0.46 ± 0.05	-1.64 ± 0.06	-	8.51 ± 0.11	-
39	0.12 ± 0.01	-1.37 ± 0.03	-	8.65 ± 0.10	8.72 ± 0.16
41	0.25 ± 0.03	-1.35 ± 0.04	-	-	-
50	0.78 ± 0.11	-1.45 ± 0.05	-	8.69 ± 0.12	8.70 ± 0.17
55	1.83 ± 0.27	-1.49 ± 0.07	-	8.69 ± 0.15	8.74 ± 0.14
57	0.54 ± 0.07	-1.25 ± 0.05	-	-	8.72 ± 0.13
61	-	-	-	-	8.74 ± 0.14
62	0.34 ± 0.02	-1.88 ± 0.04	-	8.79 ± 0.13	8.73 ± 0.10
66	0.57 ± 0.04	-1.81 ± 0.05	-	8.73 ± 0.16	8.69 ± 0.14
69	0.77 ± 0.09	-1.06 ± 0.05	-	8.72 ± 0.17	8.72 ± 0.15
70	0.43 ± 0.05	-0.97 ± 0.03	-	8.70 ± 0.16	8.72 ± 0.18
73	0.39 ± 0.05	-1.64 ± 0.07	1.94 ± 0.41	8.73 ± 0.15	8.72 ± 0.17
75	0.50 ± 0.03	-1.01 ± 0.05	-	-	8.72 ± 0.18
86	0.41 ± 0.04	-1.50 ± 0.06	-	8.72 ± 0.14	8.70 ± 0.10
107	0.27 ± 0.02	-1.71 ± 0.02	-	8.61 ± 0.10	8.73 ± 0.17
185	0.21 ± 0.03	-1.20 ± 0.03	-	8.72 ± 0.18	8.72 ± 0.17
188	0.18 ± 0.01	-1.57 ± 0.01	1.79 ± 0.39	8.66 ± 0.17	8.71 ± 0.14
202	0.09 ± 0.00	-1.79 ± 0.02	-	8.71 ± 0.14	8.72 ± 0.16
294	-	-	-	-	8.73 ± 0.17
297	0.07 ± 0.00	-1.67 ± 0.03	-	8.75 ± 0.13	8.71 ± 0.16
299	0.69 ± 0.09	-1.52 ± 0.04	-	8.71 ± 0.14	8.70 ± 0.11
310	0.47 ± 0.06	-1.28 ± 0.06	-	8.75 ± 0.17	8.71 ± 0.13
315	0.43 ± 0.05	-1.81 ± 0.05	-	8.76 ± 0.10	8.70 ± 0.13
317	0.47 ± 0.05	-1.63 ± 0.04	1.93 ± 0.55	8.72 ± 0.12	8.71 ± 0.16

Table 7.4: From left to right: (1) $SFR_{H\alpha}$ as calculated from equation 7.3 from Kennicutt et al., 2009, uncorrected for dust extinction. (2) The ratio of $log(SFR_{H\alpha}/SFR_{IR})$ which is a tracer of star formation obscuration. (3) Dust attenuation as calculated from the Balmer decrement, with $H\alpha$ and $H\beta$ integrated fluxes taken from SDSS spectra. (4) Metallicity calculated using the relation from Pettini et al., 2004 (method 1). (5) The expected metallicity given the MZR prescribed by Tacconi et al., 2018 (method 2).

Chapter 8

Results and Discussion

This chapter will be organized into three sections. The first will discuss the main sequence of star formation, along with the calculated multiplicative offsets from the main sequence of star formation (defined in this work as the main sequence multiple or MSM_{IR} – and defined as 'starburstiness' in Elbaz et al., 2011) and classifications of galaxies as AGN/starforming/starbursting. The SEDs are also fit with host-galaxy and AGN templates to determine f_{AGN}, allowing for the calculation of $MSM_{IR,\,AGN\,Corrected}$. The second section will discuss galactic kinematics and kinematic classification of galaxies as isolated or interacting. The third section will offer a relation between the MSM_{IR} and kinematics, offering a comparison between star forming properties and kinematic evolution. To determine if the MSM_{IR} is dependent on galaxy kinematics or AGN content, this relation will be investigated with MSM_{IR} values calculated from the total L_{IR} as well as the AGN-corrected L_{IR}.

1. The Main Sequence of Star Formation

1.1 Calculation of MSM_{IR}, and the AGN/star forming classification

The infra-red 'main sequence multiple' (MSM_{IR}), or the multiplicative offset each galaxy has from the expected main sequence given a certain redshift (i.e., a galaxy exactly on the expected

main sequence would have an $MSM_{IR} = 1$), is calculated from Elbaz et al., 2011 as (and defined therein as 'starburstiness' or R_{SB}) :

$$MSM_{IR} = sSFR/sSFR_{MS} \tag{8.1}$$

Where , also according to Elbaz et al., 2011, and assuming a Kroupa IMF:

$$sSFR = SFR_{IR}/M_{*} \tag{8.2}$$

$$sSFR_{MS}(Gyr^{-1}) = 38 \times t_{cosmic}^{-2.2} \tag{8.3}$$

where $sSFR$ is the specific star formation rate, $sSFR_{MS}$is the specific star formation rate that would be expected if the galaxy were exactly on the MS, and t_{cosmic} is the time in Gyr since the Big Bang for the galaxy. $sSFR$ can be thought of as the fractional 'growth rate' of the galaxy, as it is the ratio of current star formation (represented by SFR_{IR}) to past star formation (represented by M_{*}). The inverse of the $sSFR$ can also be thought of as the stellar mass doubling time of the galaxy (e.g. Madau & Dickinson, 2014). $sSFR_{MS}$ only depends on t_{cosmic} as it is based on the evolution of expected SFR over increasing redshifts without including stellar mass, and therefore $sSFR$ only increases with higher redshifts (as seen in Figure 8.1 from Elbaz et al., 2011). Equation 8.3 is the best fit for the trend shown in Figure 8.1 from Elbaz et al., 2011, and is converted to a Kroupa IMF (Kirkpatrick et al., 2014). SFR_{IR} and M_{*} are shown in Table 7.1. The trend in Figure 8.1 is in line with Figure 6.1, as $sSFR > 1$ at $z \geq 2$, implying that the global SFR was increasing until $z \approx 2$.

It is noted that the prescription of the main sequence by Elbaz et al., 2011 does not take into account the 'bending' of the MS that disappears at higher redshifts and lower stellar masses (e.g. Schreiber et al., 2015; Popesso et al., 2019), and there are more recent studies that map the main sequence. However, the definitions of the main sequence, as well as MSM_{IR}(referred to as 'starburstiness' in other studies), and the $sSFR$ are consistent across multiple studies, with only $sSFR_{MS}$ changing between studies to account for the bending. These differences are minimal,

and as the stellar masses are not significantly large (the SWIFT subset has an average $log(M_\star/M_\odot) = 10.60$, and bending starts to appear above $log(M_\star/M_\odot) \sim 11$) (Schreiber et al., 2015) the bending would not impact the galaxies in this subset substantially. However, to test the validity of the Elbaz et al., 2011 main sequence versus other studies, the values for MSM_{IR} were also calculated using the methods prescribed by Speagle et al., 2014 and Schreiber et al., 2015. It was found that the values for and classifications based on MSM_{IR} (presented later in this chapter) deviated less than 15% between the three methods. The Elbaz et al., 2011 method is used for the remainder of this thesis.

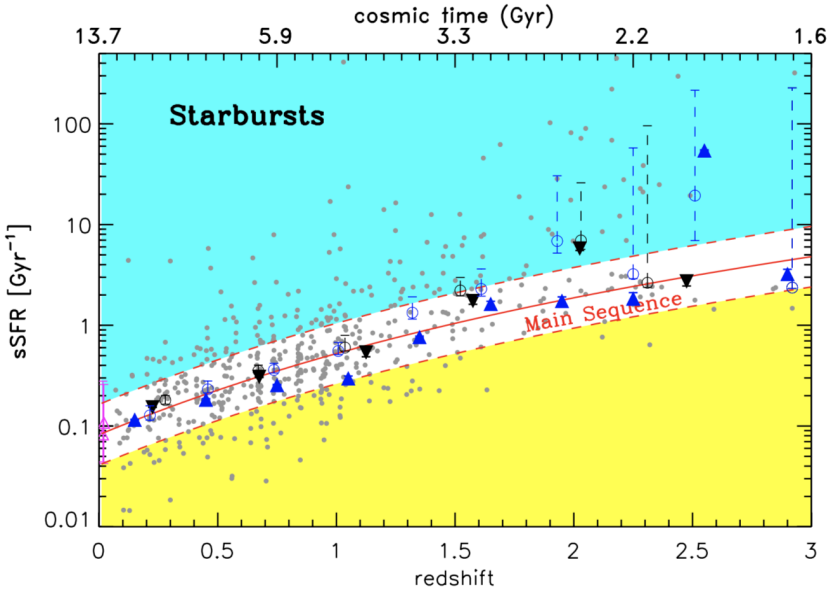


Figure 8.1: The evolution of $sSFR$ with redshift. The red dashed lines correspond to the expected main sequence multiple range of $0.5 < MSM_{IR} \leq 2.0$. Credit: Elbaz et al., 2011.

The main sequence has a width, and is not just a straight line. This width is defined in Elbaz et al., 2011 as being a factor of 2 above and below the expected main sequence ($MSM_{IR,\,Min} = 0.5$, $MSM_{IR,\,Max} = 2$) given a certain stellar mass and redshift, due to the evolution of the main sequence with cosmic time. This width encompasses 68% of galaxies with $z < 3$ (Elbaz et al., 2011). MSM_{IR} values above 2 correspond to significantly higher than expected rates of star formation given a certain stellar mass and redshift, indicating a starbursting galaxy. MSM_{IR} values below 0.5 correspond to significantly lower than expected rates of star

formation for a certain stellar mass and redshift, and correspond to galaxies that have used up their gas reserves and can no longer form new stars, and are passively evolving.

To classify whether the observed luminosity in the galaxies is dominated by an AGN or star-formation, multiple methods were used. AGN-dominated sources were identified based on their $EW_{PAH6.2\mu m}$, with $EW_{PAH6.2\mu m} \leq 0.4\mu m$ sources classified as AGN-dominated. Magdis et al., 2013 set this classification at $EW_{PAH6.2\mu m} \leq 0.2\mu m$, as sources below this cutoff were dominated by luminosity from an AGN. For sources with $EW_{PAH6.2\mu m} > 0.2\mu m$, star formation contributed to at least 50% of the total L_{IR} (Magdis et al., 2013). However, this cutoff is increased to give a conservative identification of AGN. This is in line with the study presented in Garrett, 2018.

SDSS classifications based on the optical spectra, which were available for 13 out of 34 galaxies, were then used to classify the non-AGN galaxies as starforming or starbursting. If $log(OIII/H\beta) < 0.7 - 1.2 \times [log(NII/H\alpha) + 0.4]$, the galaxy was classified as starforming. Then if $EW_{H\alpha} > 50\text{Å}$, the classification was changed to starbursting (Brescia et al., 2015). These cutoffs were taken from the publicly available SDSS optical spectra catalogs.

Finally, the remaining non-AGN sources without SDSS spectra were classified as quiescent, starforming, or starbursting based on the MSM_{IR}. Objects with $0 < MSM_{IR} < 0.5$ were classified as quiescent, $0.5 \leq MSM_{IR} < 2.0$ as star-forming, and $MSM_{IR} \geq 2.0$ as starbursting. These are in line with the cutoffs defined by Elbaz et al., 2011 and described above.

In general, the classifications based on $EW_{PAH6.2\mu m}$ and MSM_{IR} agree well with the SDSS classifications. However, some of the SDSS classifications did not agree with the classifications based on the MSM_{IR}. In each case the differences in classifications were small (i.e. there were no galaxies classified as quiescent by the MSM_{IR} but SDSS classified as starbursting), and so the SDSS classifications were used before the MSM_{IR} classifications. M037 did not have a value for MSM_{IR} (due to no value for stellar mass), an SDSS classification, or $EW_{PAH6.2\mu m} \leq 0.4\mu m$, and as such could not be classified beyond 'non-AGN'. A plot of MSM_{IR} vs $EW_{PAH6.2\mu m}$ is shown in Figure 8.2 to demonstrate the classifications and cutoffs, and the classifications are shown in

Table 8.1. The classifications are in good agreement with the cutoffs, with only some disagreements with SDSS classifications (i.e. M012 and M028).

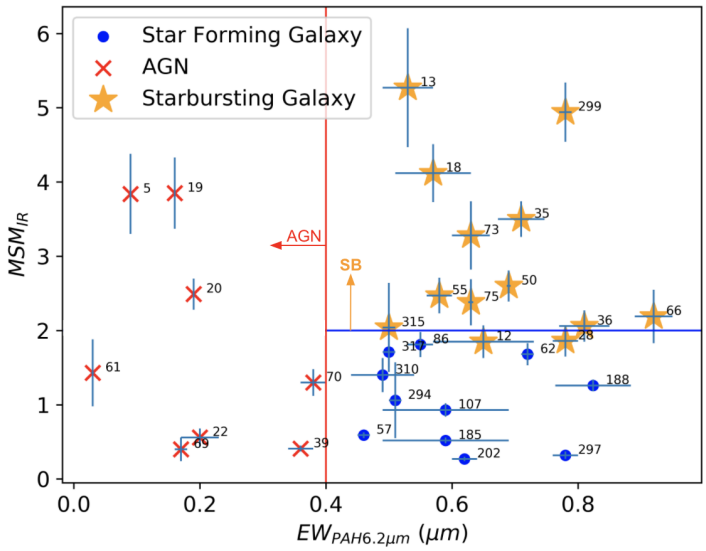


Figure 8.2: A plot of the MSM_{IR} vs $EW_{PAH6.2\mu m}$. Galaxies that had $EW_{PAH6.2\mu m} \leq 0.4\mu m$ were labelled as AGN. The remaining galaxies were then classified by SDSS, where data was available, and then by their MSM_{IR}, where galaxies with $MSM_{IR} \geq 2.0$ classified as starbursting.

1.2 Calculation of f_{AGN} and $MSM_{IR,\,AGN\ Corrected}$

The AGN contribution to L_{IR} (AGN fraction, or f_{AGN}) was first calculated by Magdis et al., 2013, who combined the existing *Spitzer* data with submm (250μm, 350μm, 500μm) *Herschel*-SPIRE observations drawn from the HerMES project. The fractional contribution of the AGN to the total luminosity was measured by fitting a host-galaxy and an intrinsic AGN template SED to the infrared data (synthetic photometry from four bands of the IRS spectra, as well as observed photometry from *Spitzer* and *Herschel*-SPIRE) by the method prescribed by Mullaney et al., 2011 (DECOMPIR). The best fit is found through a χ^2 minimisation of the model SED and by varying six parameters: 1) the host-galaxy SED 2) the spectral break wavelength in the mid-IR AGN SED 3) two spectral indices above and below the break wavelength 4) the peak AGN SED wavelength 5) the dust extinction of the galaxy and AGN and 6) the normalisations of both the galaxy and AGN components. The infrared luminosity due to

the modelled AGN is then divided by the total infrared luminosity to retrieve f_{AGN}. AGN fractions were available for 31 out of 34 galaxies, and errors on all values are $\leq 10\%$, as quantified by a Monte Carlo simulation of the fits to the photometry (within the observed photometric errors) with 1000 iterations (Magdis et al., 2013).

However, as seen in Figure 8.3, some of these values for f_{AGN} are inconsistent with what would be expected physically (larger AGN destroy PAH features) given the classifications and values for $EW_{PAH6.2\mu m}$ shown in Figure 8.2. Specifically, half of the galaxies classified as AGN (M019, M039, and M070) have lower values for f_{AGN} than many of the star forming galaxies, with $f_{AGN} \lesssim 0.1$ or even $f_{AGN} = 0.0$ for M039. Furthermore, some of the star forming galaxies with values for $EW_{PAH6.2\mu m} \geq 0.5\mu$m have high values for f_{AGN}, such as M013 and M036.

There are two main potential causes of the inconsistencies in the f_{AGN} values presented in Magdis et al., 2013. First, the fits in Magdis et al., 2013 are to spectrophotometric data, and the IRS spectra used exhibit significant noise and errors from 5.2μm - 6.2μm and 35μm - 38μm, which would negatively impact the accuracy of the fit, specifically for the AGN component which dominates in this wavelength range ($\lesssim$40μm, as the thermal emission from the dust surrounding the AGN is too hot to impact the far-infrared) (e.g. Rosario et al., 2012). Despite the IRS spectra containing more information than just photometry, these errors could lead to potential over/underestimation of the AGN contributions to the total L_{IR} for many of the galaxies in the sample, which is exactly what is seen in Figure 8.3.

The second potential cause of error in the values for f_{AGN} presented in Magdis et al., 2013 can be found in the empirical templates presented in Mullaney et al., 2011. These templates were created from a sample of standard X-ray AGN which had *Spitzer*-IRS spectra as well as *IRAS* photometry. The excess flux in each of the infrared SEDs (after the host galaxy component was removed) was used to create an average AGN template (Mullaney et al., 2011). However, there were three problems with the construction of these templates. First, far-infrared photometry (such as from *Herschel*) for all sources was not yet available in 2011, which prevented access to photometry above 100μm - these long wavelengths being critical in the accurate measurement of luminosity from dust heated by star formation in the host-galaxy (e.g. Ciesla et al., 2015). Instead, these wavelengths were extrapolated using a modified blackbody (and checked with

AKARI photometry at 65μm, 140μm, and 160μm - however *AKARI* photometry was only available for 13 of the host-galaxy SEDs) (Mullaney et al., 2011), which leads to clear uncertainties when modelling the host-galaxy contribution to the total L_{IR}.

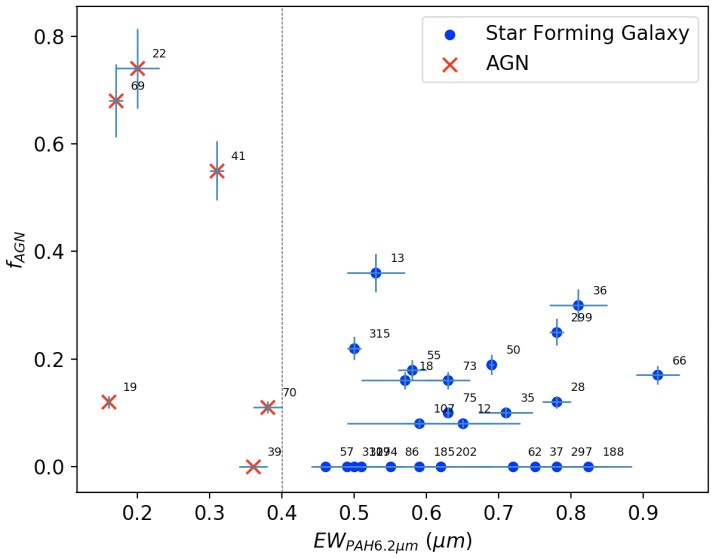


Figure 8.3: $EW_{PAH6.2\mu m}$ vs f_{AGN} from Magdis et al., 2013. Errors are $\leq$ 10% for f_{AGN}, and come from errors in the estimation of the fractions from the fitting program used (DECOMPIR). The vertical dashed grey line at 0.4μm represents the cutoff for AGN classification with $EW_{PAH6.2\mu m}$.

Second, differences in the aperture sizes used to measure the IRAS photometry and IRS spectra had to be accounted for when collecting the data, as the IRAS apertures were 2 and 9 arcminutes in diameter, compared to 3.6 and 10.5 arcseconds for the *Spitzer*-IRS instrument. This would lead to significantly more host galaxy flux being captured by the IRAS instrument when compared to the *Spitzer*-IRS, leading to poor calibration between the spectra and photometry. These aperture effects were mitigated by Mullaney et al., 2011 by only using sources with at least a 30% agreement between the 12μm and 25μm IRAS flux and the integrated flux density of the IRS spectrum over those two IRAS bandpasses. However, a 30% minimum threshold of agreement is high, leading to further significant sources of error and uncertainties. Third, there is potential for further errors from high levels of contamination from light from nearby sources in the IRAS photometry.

While these two main sources of error (IRS spectra errors and construction of the empirical templates) were significant, it is noted that the values for f_{AGN} presented in Magdis et

al., 2013 were only used to generally confirm the $EW_{PAH6.2\mu m}$ AGN classification method, rather than for detailed analysis, and therefore did not need to be highly accurate. In this work, however, it was necessary to have correct values for f_{AGN} to allow for the proper calculation of the L_{IR} due purely to star formation, with the AGN contribution removed.

To check and confirm the values for f_{AGN} calculated by Magdis et al., 2013, f_{AGN} was recalculated for each galaxy in the SWIFT subset by fitting only the observed IRAC (3.6μm, 4.5μm, 5.8μm, 8.0μm) and MIPS (24μm) photometry to the galaxy and AGN SED templates presented in Brown et al., 2014 and Brown et al., 2019, respectively. IRS spectra were not used for fitting for the reasons described above (large errors in the IRS spectra in the regions where AGN dominate L_{IR}, and up to 30% errors in equating the IRS aperture sizes with the photometry).

The galaxy SED templates presented in Brown et al., 2014 were created directly from a sample of 129 nearby galaxies ($z < 0.05$) with a wide range of morphologies, magnitudes, and colors. The SEDs extend from 0.1μm - 34μm, and were constructed using optical spectra from *Spitzer* and *Akari*, with the gaps in between these spectra filled in by using a spectral energy distribution model (MAGPHYS, da Cunha et al., 2008). The SEDs were then confirmed with matched aperture photometry from *Swift*, GALEX, SDSS, 2MASS, *Spitzer,* and WISE, and were shown to have minimal systematic errors (Brown et al., 2014). Similarly, the AGN SED templates presented in Brown et al., 2019 were created directly from a sample of 41 AGN, using a combination of available spectra and photometry, with the gaps filled in by polynomial interpolation. These AGN SEDs also extend from 0.1μm - 34μm.

To increase the utility of these galaxy and AGN templates, Brown et al., 2019 also presented a series of composite templates. These were created by normalising the SEDs of both a host galaxy SED (taken from Brown et al., 2014) and an AGN SED (taken from Brown et al., 2019), and then adding the two together with various ratios to represent different AGN:galaxy contributions to luminosity (the ratios used were 2:1, 1:1, 1:2, 1:4, 1:8, 1:16, 1:32 and 1:64). In total, 72 composite SED templates were created by Brown et al., 2019 from nine different AGN and galaxy SEDs to ensure multiple shapes and types of SEDs were used.

To check the values for f_{AGN} presented in Magdis et al., 2013, these composite templates (redshifted to the target galaxy) were then used to directly fit the observed IRAC (3.6μm, 4.5μm, 5.8μm, 8.0μm) and MIPS (24μm) photometry of the SWIFT subset. Each of the composite templates was convolved with the appropriate IRAC and MIPS filters, with the resulting 'synthetic' photometry from the template fit directly to the photometry of each galaxy using χ^2 minimisation. The only free parameters were the normalisation and the slope of the continuum. Varying the slope of the continuum allowed for a broader range of SED shapes to be theoretically modelled, as this was one main difference between the 0.1μm - 34μm shape of many of the SEDs found in Brown et al., 2014 (and SEDs in general). Physically, this represents varying the star formation rate by altering the contribution of the young stellar population (e.g. Popescu et al., 2011). For some galaxy SEDs there were multiple templates that provided good fits to the photometry, but they were always templates with the same AGN:galaxy luminosity ratio. The 'new' value for f_{AGN} was then taken as the AGN:galaxy luminosity ratio of the best-fit composite template. An example of SED fits for both an AGN and a non-AGN galaxy can be seen in Figure 8.4. In the far-infrared, the SEDs slope downwards longward of 100μm, as can be seen in Figure 8.5 (Credit: Wu et al., 2010, Figure 3). It is important to note that the Magdis values for f_{AGN} were calculated from the total L_{IR}, whereas the Brown templates only allowed for fitting up to 34μm. This may lead to overestimation of f_{AGN} vs the Magdis values, but agreement between the two values for f_{AGN} is demonstrated in Figure 8.7.

This method of template fitting offers an advantage over the Mullaney et al., 2011 fitting method and templates used in Magdis et al., 2013, as it involves the use of composite templates made directly from the observed spectra and photometry from a real AGN and a real galaxy. However, the composite templates used only allowed for a rough calculation of the AGN strength and f_{AGN}, as the luminosity ratios were fixed and imprecise within certain ranges. Therefore, these new values are used only to check and confirm those presented in Magdis et al., 2013, and demonstrate that the errors in that work were likely minimal.

It would have been possible to create a further series of composite templates with a more exhaustive range of AGN:galaxy luminosity ratios, but this was not needed as all fits of the 34 SWIFT galaxies were good (the lowest χ^2 was 1.03 for M036, the highest χ^2 at 2.44 for M035,

and a sample average χ^2 of 1.46). This implies reduced χ^2 values (assuming 3 degrees of freedom for 5 data points with 2 free parameters) ranging from 0.34 to 0.81, with an average of 0.49. This indicates that on average, ~70% of tests would not expect to find fits better than those provided in this work (Bevington et al., 1969).

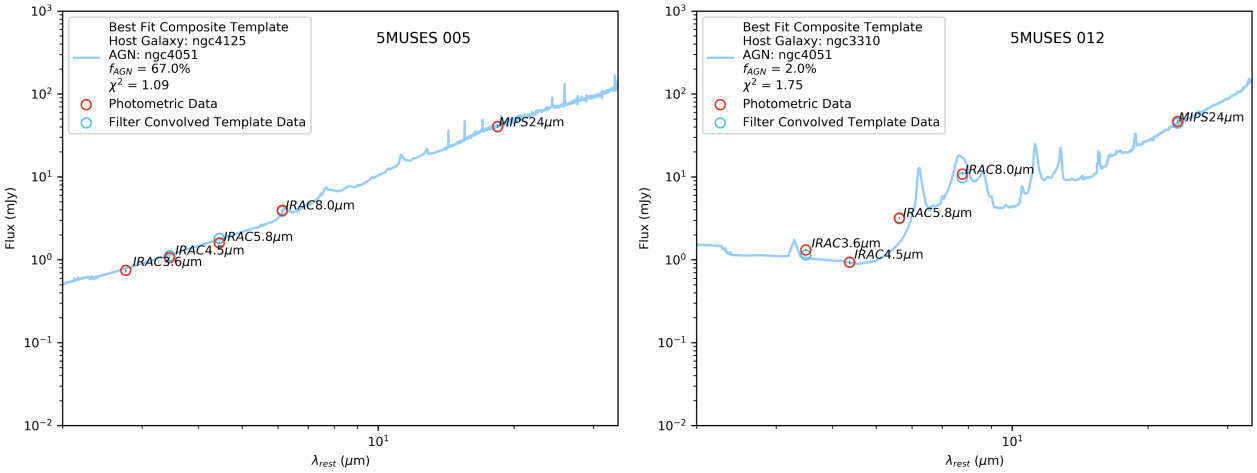


Figure 8.4: (L) SED fit for M005, a typical AGN. (R) SED fit for M012, a typical starforming galaxy with a minimal AGN component. Errors on the fits are shown by black lines within the data circles. The photometry of both galaxies was fit using one of the composite templates from Brown et al., 2019, with the best fit model shown in blue.

The residuals from the fit were used to estimate errors on the fits for the entire sample, and were then convolved with the systematic calibration error of IRAC and MIPS (3% and 4%, respectively) (Carey, 2010). The output errors were on the order of ≤15%. A Monte Carlo simulation was then run to check these errors. For each galaxy SED, artificial random photometric fluxes were simultaneously generated for each of the 5 synthetic photometric fluxes (within their stated measurement errors). These 5 'random' synthetic photometric data points were then re-fit in the exact same way as above, and this was done 750 times for each galaxy. The standard deviation of all 750 of these fits was treated as the error in the original synthetic data. These errors ultimately have an impact on the final IR luminosity after the AGN component has been removed, and all further values in this thesis that involve $L_{IR,\,AGN\ corrected}$ have errors that are convolved with the errors of f_{AGN}.

To again check the quality of the fits for each galaxy, these Monte Carlo simulations were then re-run for the two templates nearest in AGN:galaxy contributions to the original best fit

template of the same galaxy SED (i.e., if the original best fit was 1:8, the simulations were then run for 1:4 and 1:16 for the same galaxy SED). In over 90% of cases the original best fit template produced errors from the Monte Carlo simulations that were lower than both of the adjacent templates.

However, as all the templates that were fit were relatively fixed with minimal free parameters (as they were directly observed) the errors were only used to demonstrate the quality of the fit and accuracy of the template, rather than directly quote a measured error on f_{AGN}. Further free parameters within the template itself would have had to have been introduced to come up with more meaningful errors on f_{AGN}, but would inherently reduce the efficacy of the template, as the defining feature of the Brown templates is that they are from real and directly observed galaxies.

To determine whether these fits made physical sense, they are shown plotted against $EW_{PAH6.2\mu m}$ in Figure 8.6. As expected, as $EW_{PAH6.2\mu m}$ decreases, f_{AGN} increases. The profile is similar to that shown in Figure 8.3 with the values from Magdis et al., 2013. However, there is less degeneracy in the galaxies with $f_{AGN,\,Magdis} < 0.10$, as many galaxies shown in Figure 8.6 have values for f_{AGN}~ 0.02- 0.10. Most importantly, the luminous AGN with the smallest values for $EW_{PAH6.2\mu m}$ all have the highest values for f_{AGN}, which is in agreement with the theory that strong AGN destroy PAH features.

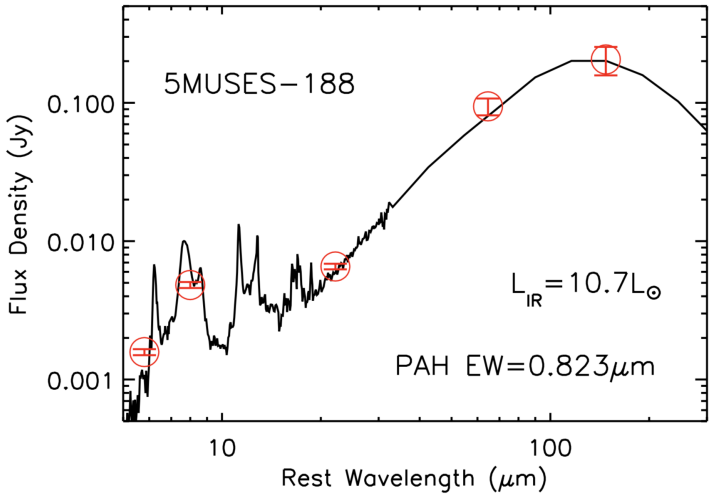


Figure 8.5: The far-infrared SED for 5MUSES 188. The red circles are the fitted photometric data points. Credit: Wu et al., 2010, Figure 3.

To check the agreement between $f_{AGN,\,Foster}$ and $f_{AGN,\,Magdis}$, the two are plotted against each other in Figure 8.7. In general, there is very good agreement between the two values for both AGN and non-AGN. Specifically, the powerful AGN (M022, M041, and M069) have agreement between the two values to within ± 0.05. It is important to have the values for the powerful AGN in agreement, as these galaxies are the most affected by the removal of the AGN contribution to L_{IR}. The three powerful AGN ($EW_{PAH6.2\mu m} < 0.19$) M005, M020, and M061 had no values for $f_{AGN,\,Magdis}$ due to lack of *Herschel* data, and are not shown in Figure 8.7. As such, and as discussed in Section 3 of this chapter, further calculations are done for these three galaxies using $f_{AGN,\,Foster}$.

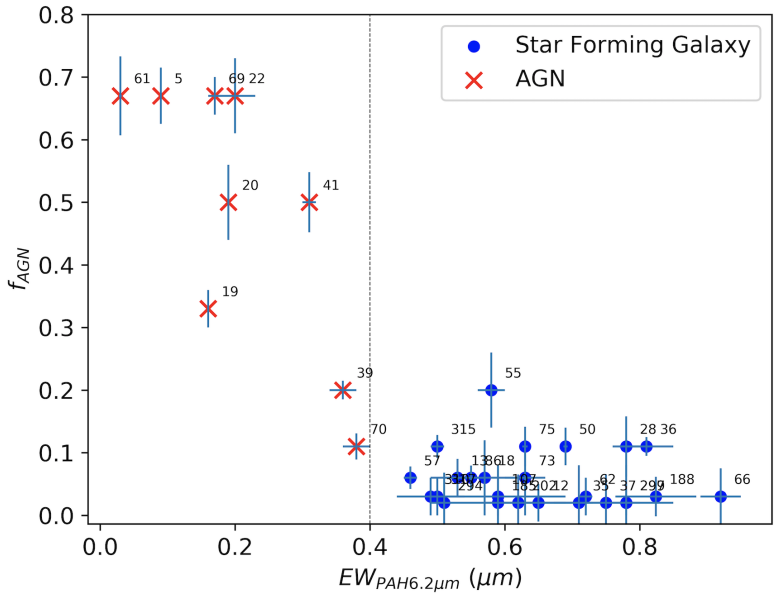


Figure 8.6: $EW_{PAH6.2\mu m}$ vs $f_{AGN,\,Foster}$ for all 34 galaxies in the SWIFT subset. The vertical dashed line at 0.4μm represents the cutoff for classification as AGN.

Two AGN (M019 and M039) have values for $f_{AGN,\,Foster}$ that are greater than $f_{AGN,\,Magdis}$ by ~0.20. As these two are AGN that have relatively low values for $f_{AGN,\,Magdis}$, it is possible that these values were underestimated. As a check, in Section 3 of this chapter these galaxies are discussed and classified as starforming/bursting using both values for f_{AGN}. However, the classifications for each galaxy do not change regardless of which value for f_{AGN} is used, and so the differences for these two galaxies are overlooked and have minimal impact on the final outcome of the study.

Two non-AGN galaxies (M013 and M299) have values for $f_{AGN,\,Foster}$ that are lower than those for $f_{AGN,\,Magdis}$ by more than 0.20. However, as these two galaxies had large values for $EW_{PAH6.2\mu m}$ (at $0.53\pm\ 0.04$ and $0.78\ \pm\ 0.01$ respectively), it is possible that these values were overestimated, and the true values for f_{AGN} are lower than calculated by Magdis et al., 2013. Both galaxies are discussed in Section 3 of this chapter using both values for $f_{AGN,}$ Again, neither of their classifications changed regardless of the value for f_{AGN} used, and the discrepancies between the values for f_{AGN} are not considered significant.

However, for the vast majority of the SWIFT subset galaxies, the two values for f_{AGN} are in great agreement, serving to confirm the calculations from Magdis et al., 2013. As such, for the rest of this work, $f_{AGN,\,Magdis}$ will be used for further calculations as it is a more precise measurement than $f_{AGN,\,Foster}$. Furthermore, as seen in Figure 8.3, Magdis et al., 2013 set discrete values for low f_{AGN} at 0% and 10% to avoid degeneracy. The re-calculated values do not have this same level of degeneracy, as the composite templates used allowed for f_{AGN} values of 2%, 3%, and 5%. It is important to note that some of the galaxies with low values for f_{AGN} have errors of $\pm$ 5%, indicating that degeneracy is possible. However, as $f_{AGN,\,Magdis}$ will be used for the remainder of this work, the raw values for $f_{AGN,\,Foster}$ are shown in Figure 8.6.

Using the values for f_{AGN} calculated by Magdis et al., 2013, $L_{IR,\,AGN\ corrected}$ was then calculated by removing the AGN contribution to L_{IR} with f_{AGN}, as shown below in equation 8.4:

$$L_{IR,\,AGN\ corrected} = L_{IR}\ \times\ (1\ -\ f_{AGN}) \tag{8.4}$$

$SFR_{IR,\,AGN\ corrected}$ was then calculated with $L_{IR,\,AGN\ corrected}$ using the equation below:

$$SFR_{IR,\,AGN\ corrected}\,(M_{\odot}yr^{-1}) = (1.509\ \times 10^{-10}) \times L_{IR,\,AGN\ corrected}({L_{\odot}}^{-1}) \tag{8.5}$$

Finally, to calculate $MSM_{IR,\,AGN\ corrected}$, or the 'main sequence multiple' due purely to star formation, equations 8.1, 8.2, and 8.3 can then be used as described in Section 1.1 of this chapter, but with $SFR_{IR,\,AGN\ corrected}$ used in place of SFR_{IR}. The errors for $MSM_{IR,\,AGN\ corrected}$ are calculated by convolving the errors of MSM_{IR} and f_{AGN}. Higher errors on f_{AGN} would negatively impact the estimates of $MSM_{IR,\,AGN\ corrected}$. However, galaxies with the highest value for f_{AGN} (which would have the largest impact on $MSM_{IR,\,AGN\ corrected}$) were in great agreement and would need to be <10% of their current value of f_{AGN} for their final classification to be impacted.

A table showing values for MSM_{IR}, f_{AGN}, and $MSM_{IR,\,AGN\ corrected}$ for each galaxy, along with classifications as AGN, starforming, starbursting, or quiescent, can be found in Table 8.1.

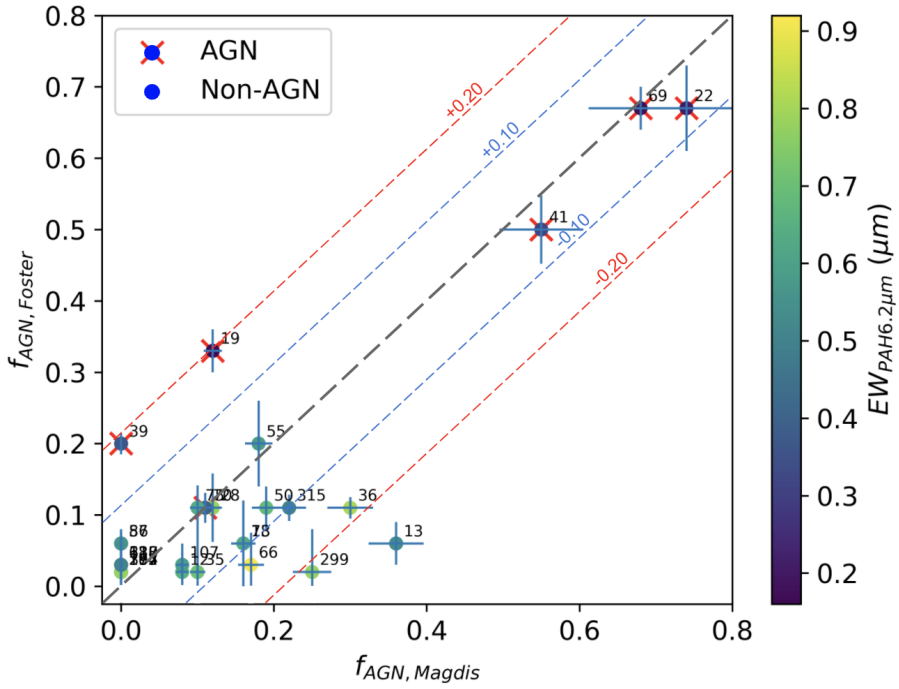


Figure 8.7: $f_{AGN,\,Magdis}$ vs $f_{AGN,\,Foster}$, with red crosses representing AGN, and dots representing non-AGN galaxies. All data points are colored according to their $EW_{PAH6.2\mu m}$. The gray dashed line represents a 1:1 relation between the values for f_{AGN}, with values between the blue dashed lines corresponding to differences within $\pm$0.10, and values between the red dashed lines corresponding to differences within $\pm$0.20.

2. Galactic Kinematics and Kinematic Classification

To investigate whether the enhanced star formation of the galaxies with an $MSM_{IR} \geq 2$ was due to interactions, galaxies were further classified kinematically as interacting or isolated. Two methods of classification will be discussed here - the first using the ratio of rotational velocity to velocity dispersion as a tracer of rotational support, and the second by visual inspection.

As explained in Chapter 6, the dynamical ratio (V_{max}/σ_0) can trace the rotational support of a galaxy. Rotationally supported objects (stable, isolated disks) have high V_{max}/σ_0 ratios, with ordered stellar orbits and strong rotation. Interacting systems have higher amounts of disorderly motion, with higher dispersion and lower dynamical ratios. As noted in Chapter 6, dispersion is expected to increase with increasing redshift at significance levels $> 2\sigma$ due to increased gas fractions at higher redshift (e.g. Wisnioski et al., 2015; Wisnioski et al., 2019; Beifiori et al., 2014). Errors on the GalPak fits were calculated by GalPak directly as explained in Chapter 7, Section 3.4.

The average dynamical ratio for the SWIFT subset is 3.16 ± 0.36, which is higher than the KROSS survey (which had an average dynamical ratio of 2.2 ± 1.4 at $z \sim 1$ and median $log(M_\star/M_\odot) = 10.0$)(Stott et al., 2016), but lower than the KMOS 3D sample measured by Wisnioski et al., 2015, which had an average dynamical ratio of ~5.5 at $z \sim 1$ and more similar stellar masses to the SWIFT subset with an average $log(M_\star/M_\odot) = 10.65$. The average of $3.16 \pm 0.36$for the SWIFT subset is, however, in line with the 3.2 ± 0.3 average from the slightly lower redshift ($0.01 < z < 0.1$) sample from Bellochi et al., 2013. The sample from Bellochi et al., 2013 is the most comparable to the SWIFT subset presented here, as 31 of the 38 galaxies studied were of similar luminosity ($log(L_{IR}/L_\odot) = 11.3$) with an average redshift of 0.024.

ID #	MSM_{IR}	f_{AGN}	MSM_{IR} (AGN Corrected)	AGN/Star Forming Classification			
				$EW_{PAH6.2\mu m}$	SDSS	MSM_{IR}	Final
5	3.84 ± 0.54	-	-	AGN	→	→	AGN
12	1.85 ± 0.22	0.08 ± 0.01	1.70 ± 0.20	-	SB	(SF)	SB*
13	5.27 ± 0.80	0.36 ± 0.04	3.37 ± 0.51	-	SB	→	SB
18	4.12 ± 0.39	0.16 ± 0.02	3.46 ± 0.33	-	-	SB	SB
19	3.85 ± 0.48	0.12 ± 0.02	3.39 ± 0.42	AGN	→	→	AGN
20	2.49 ± 0.21	-	-	AGN	(SB)	→	AGN*
22	0.56 ± 0.12	0.74 ± 0.07	0.15 ± 0.03	AGN	→	→	AGN
28	1.86 ± 0.21	0.12 ± 0.02	1.64 ± 0.18	-	SB	(SF)	SB*
35	3.50 ± 0.24	0.10 ± 0.01	3.15 ± 0.22	-	-	SB	SB
36	2.06 ± 0.21	0.30 ± 0.03	1.44 ± 0.04	-	-	SB	SB
37	-	0.00	-	-	-	-	Non-AGN
39	0.41 ± 0.04	0.00	0.41 ± 0.04	AGN	→	→	AGN
41	-	0.55 ± 0.06	-	AGN	→	→	AGN
50	2.60 ± 0.21	0.19 ± 0.02	2.11 ± 0.17	-	-	SB	SB
55	2.47 ± 0.24	0.18 ± 0.02	2.03 ± 0.20	-	-	SB	SB
57	0.59 ± 0.04	0.00	0.59 ± 0.04	-	-	SF	SF
61	1.43 ± 0.45	-	-	AGN	→	→	AGN
62	1.68 ± 0.15	0.00	1.68 ± 0.15	-	-	SF	SF
66	2.19 ± 0.36	0.17 ± 0.02	1.82 ± 0.30	-	-	SB	SB
69	0.40 ± 0.16	0.68 ± 0.07	0.13 ± 0.05	AGN	→	→	AGN
70	1.30 ± 0.18	0.11 ± 0.01	1.15 ± 0.16	AGN	→	→	AGN
73	3.28 ± 0.46	0.16 ± 0.02	2.76 ± 0.39	-	SB	→	SB
75	2.38 ± 0.31	0.10 ± 0.01	2.14 ± 0.28	-	-	SB	SB
86	1.81 ± 0.17	0.00	1.81 ± 0.17	-	-	SF	SF
107	0.93 ± 0.09	0.08 ± 0.01	0.85 ± 0.08	-	SF	→	SF
185	0.52 ± 0.04	0.00	0.52 ± 0.04	-	-	SF	SF
188	1.26 ± 0.08	0.00	1.26 ± 0.08	-	SF	→	SF
202	0.27 ± 0.03	0.00	0.27 ± 0.03	-	SF	(Q)	SF*
294	1.06 ± 0.51	0.00	1.06 ± 0.51	-	-	SF	SF
297	0.32 ± 0.05	0.00	0.32 ± 0.05	-	SF	(Q)	SF*
299	4.94 ± 0.40	0.25 ± 0.03	3.71 ± 0.30	-	-	SB	SB
310	1.40 ± 0.23	0.00	1.40 ± 0.23	-	-	SF	SF
315	2.04 ± 0.60	0.22 ± 0.02	1.59 ± 0.47	-	-	SB	SB
317	1.71 ± 0.20	0.00	1.71 ± 0.20	-	SF	→	SF

Table 8.1: The above table shows MSM_{IR}, f_{AGN} (calculated by Magdis et al., 2013), and AGN-corrected MSM_{IR}, along with AGN/Star Forming classifications. Errors on f_{AGN} are $\leq$ 10%. Galaxies where the classifications based on MSM_{IR}, $EW_{PAH6.2\mu m}$ and SDSS do not agree are labelled in parentheses, with final classifications labelled with a *, with both classifications shown. The $EW_{PAH6.2\mu m}$ and SDSS classifications take priority over the MSM_{IR} classifications, which is indicated by the right arrows. SB = starbursting, SF = starforming, and Q = quiescent.

From isolated systems in Bellocchi et al., 2013, threshold values are defined to separate isolated and interacting galaxies, with interacting galaxies having $\sigma_0 \geq 60\, kms^{-1}$ and $V_{max}/\sigma_0 \leq 2.7$. These were taken from the mean value of isolated systems plus (for σ_0) or minus (for V_{max}/σ_0) four times the measured standard deviation, as shown by Bellocchi et al., 2013. This allows for a conservative identification of interacting galaxies. Of the 22 galaxies that were fit, 5 exhibited kinematics indicative of interaction, with 17 isolated. Figure 8.8 shows a plot of dynamical ratio vs dispersion for the 22 fit galaxies, along with cutoffs for interacting vs isolated.

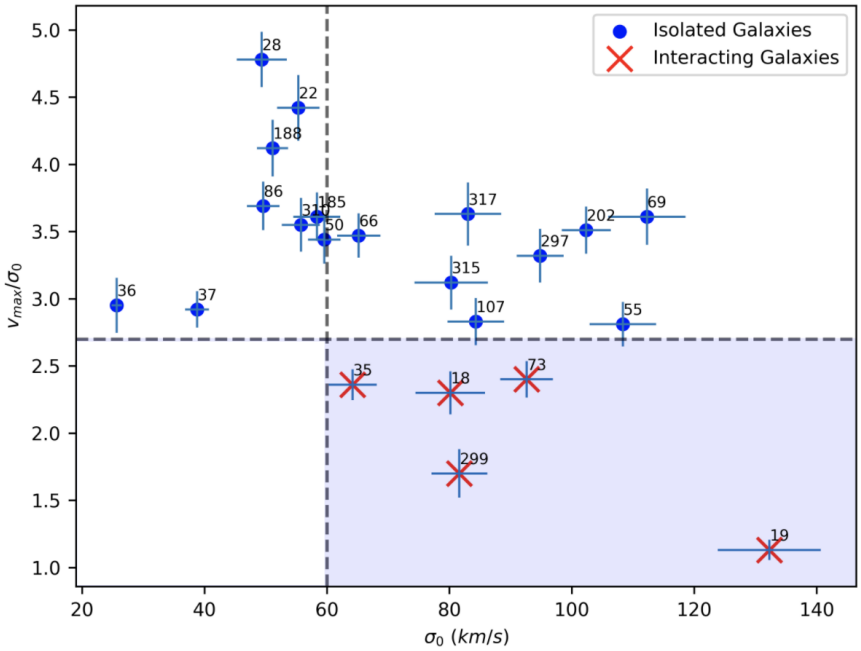


Figure 8.8: A plot of the dynamical ratio vs dispersion. Galaxies with a dispersion greater than 60km/s (shown by the vertical dotted line) and a dynamical ratio lower than 2.7 (shown by the horizontal dotted line) were classified as interacting, and labeled with a red cross.

However, it is important to note that the kinematic parameters (velocity and dispersion) were measured using $H\alpha$ emission which, as mentioned in Chapter 6, is very sensitive to the effects of dust obscuration and extinction. This could be accounted for using the Balmer decrement (by mapping the observed ratio of $H\alpha/H\beta$ vs. the physically-defined and expected ratio) as described in Chapter 7 for the 13 galaxies that had available SDSS spectra.

However, as $H\beta$ was only from SDSS for 8 out of the 34 galaxies (and only 5 of the 22 fitted by GalPak), the entire sample could not be appropriately corrected for extinction, but only compared relatively between the 8 individual galaxies. Furthermore, the SDSS spectra were not spatially resolved, which would limit the extinction corrections to be integrated over the whole galaxy, and making it not possible to determine exactly where the dust was located (though dust is typically located in at the center of galaxies, and the kinematic measurements in this study were taken from $H\alpha$ measured at the edges of the galaxies). However, the integrated extinction values for the 8 galaxies measured had an average $A_v = 1.81 \pm 0.41$, implying that extinction would not add significant additional errors on the kinematic measurements.

The second method was visual classification. Galaxies in advanced mergers will typically show evidence via tidal tails or binary nuclei. However, depending on the resolution of the instrument used for the observations, the redshift, or the stage at which the merger is in, a visual identification may not be possible. While there are other methods to identify galaxies as interacting, such as measuring the misalignment between the kinematic and morphological position angles (e.g. Rodrigues et al., 2017), these were not investigated. Including various other methods in this work would potentially give a higher proportion of interacting galaxies.

For the twelve galaxies with no kinematic data, visual classification as interacting or isolated based on the SDSS optical images was attempted. Galaxies that had clear evidence of spiral arms and a disk-like shape were classified as isolated. Galaxies with two identifiable nuclei and signs of interaction were classified as interacting. M039, M041, M057, M061, M070, M075, and M294 have evidence of a spiral structure, and were classified as isolated. M012 is involved in an active merger and tidal features can be seen, and was classified as interacting. M020 has evidence of tidal features, and M062 is in an active merger with two resolved nuclei. Both were also classified as interacting. M005 and M013 were not able to be visually classified by the SDSS images, as the resolution of the images was too low.

As a check, visual inspection of the SDSS and integrated flux images was then done for the 5 galaxies classified as interacting by the dynamical ratio to see if a companion could be seen. M035 and M073 exhibited clear signs of interaction with tidal features or companion galaxies, which confirmed their classification. However, the SDSS images for M019 suggest it is isolated. This could be due to the merger being at an advanced stage where the separation

between the two nuclei is not resolved. M018 and M299 had too low resolution for a visual classification to be made.

ID #	$V_{max}\ (km/s)$	$\sigma_0\ (km/s)$	$V_{max}/\ \sigma_0$	***Kinematic Classification***
5	-	-	-	-
12	-	-	-	Interacting (Visual)
13	-	-	-	-
18	184.21 ± 20.01	80.31 ± 7.11	2.29 ± 0.32	Interacting
19	149.75 ± 12.27	132.06 ± 14.51	1.13 ± 0.15	Interacting
20	-	-	-	Interacting (Visual)
22	244.73 ± 19.42	55.42 ± 4.33	4.40 ± 0.49	Isolated
28	235.55 ± 18.34	49.56 ± 5.10	4.74 ± 0.61	Isolated
35	144.43 ± 7.92	61.26 ± 4.89	2.35 ± 0.23	Interacting
36	75.96 ± 10.23	25.67 ± 2.06	2.96 ± 0.48	Isolated
37	113.69 ± 8.47	38.50 ± 2.45	2.94 ± 0.29	Isolated
39	-	-	-	Isolated (Visual)
41	-	-	-	Isolated (Visual)
50	205.73 ± 18.71	59.44 ± 3.33	3.45 ± 0.36	Isolated
55	304.87 ± 30.77	108.09 ± 6.79	2.81 ± 0.33	Isolated
57	-	-	-	Isolated (Visual)
61	-	-	-	Isolated (Visual)
62	-	-	-	Interacting (Visual)
66	225.91 ± 14.58	65.43 ± 4.44	3.44 ± 0.33	Isolated
69	405.36 ± 37.23	112.41 ± 7.91	3.60 ± 0.42	Isolated
70	-	-	-	Isolated (Visual)
73	222.61 ± 21.65	92.90 ± 5.39	2.39 ± 0.27	Interacting
75	-	-	-	Isolated (Visual)
86	182.71 ± 19.31	49.39 ± 3.30	3.68 ± 0.46	Isolated
107	237.83 ± 24.09	83.91 ± 5.78	2.82 ± 0.35	Isolated
185	210.75 ± 12.31	58.35 ± 4.80	3.60 ± 0.36	Isolated
188	210.33 ± 17.45	51.26 ± 3.22	4.10 ± 0.42	Isolated
202	359.59 ± 31.03	102.73 ± 5.00	3.50 ± 0.35	Isolated
294	-	-	-	Isolated (Visual)
297	315.50 ± 27.40	94.47 ± 4.77	3.33 ± 0.33	Isolated
299	138.80 ± 12.90	81.43 ± 5.66	1.69 ± 0.20	Interacting
310	197.96 ± 14.31	55.47 ± 3.91	3.55 ± 0.36	Isolated
315	250.66 ± 22.32	80.71 ± 7.47	3.10 ± 0.40	Isolated
317	301.69 ± 29.87	82.87 ± 6.82	3.63 ± 0.47	Isolated

Table 8.2: A table of the fitted kinematic parameters for the SWIFT subset. 22 out of 34 galaxies were able to be fit and then classified based on their kinematics. For the remaining twelve galaxies, SDSS optical images and $H\alpha$ integrated flux maps were used for visual kinematic classification. M005 and M013 had too low SDSS resolution to be visually classified.

ID #	*Position Angle (°)*	*Inclination (°)*	Radius (kpc)	$Log(M_{dyn}/M_{\odot})$
5	-	-	-	-
12	-	-	-	-
13	-	-	-	-
18	73.10 ± 0.76	33.87 ± 2.31	12.44 ± 0.42	11.00 ± 0.04
19	67.01 ± 1.63	12.89 ± 1.61	11.63 ± 0.61	10.78 ± 0.01
20	-	-	-	-
22	30.65 ± 0.24	60.11 ± 1.87	7.40 ± 0.31	11.01 ± 0.02
28	219.49 ± 0.08	59.22 ± 2.03	4.11 ± 0.21	10.72 ± 0.03
35	69.63 ± 0.21	60.45 ± 1.71	5.34 ± 0.14	10.42 ± 0.02
36	168.92 ± 0.24	43.34 ± 2.22	1.44 ± 0.08	9.28 ± 0.02
37	146.57 ± 0.20	58.67 ± 1.44	7.52 ± 0.36	10.36 ± 0.03
39	-	-	-	-
41	-	-	-	-
50	209.86 ± 0.51	11.52 ± 1.99	5.97 ± 0.18	10.77 ± 0.02
55	338.50 ± 0.26	68.92 ± 1.70	11.42 ± 0.59	11.39 ± 0.01
57	-	-	-	-
61	-	-	-	-
62	-	-	-	-
66	244.87 ± 0.48	53.17 ± 2.39	9.77 ± 0.72	11.07 ± 0.03
69	194.96 ± 0.24	56.52 ± 1.84	4.67 ± 0.11	11.25 ± 0.01
70	-	-	-	-
73	225.39 ± 0.14	54.40 ± 1.99	3.90 ± 0.30	10.66 ± 0.03
75	-	-	-	-
86	126.09 ± 0.13	89.47 ± 2.89	11.16 ± 0.54	10.94 ± 0.02
107	286.36 ± 0.47	73.83 ± 1.52	15.40 ± 0.45	11.31 ± 0.02
185	134.29 ± 0.23	26.64 ± 1.59	4.97 ± 0.10	10.71 ± 0.04
188	233.01 ± 0.33	55.77 ± 2.76	5.54 ± 0.20	10.76 ± 0.02
202	325.35 ± 0.15	59.60 ± 2.01	5.76 ± 0.29	11.24 ± 0.02
294	-	-	-	-
297	1.18 ± 0.48	33.06 ± 1.50	4.54 ± 0.12	11.02 ± 0.01
299	181.49 ± 0.14	12.34 ± 1.96	7.04 ± 0.40	10.50 ± 0.08
310	92.50 ± 0.46	49.81 ± 1.74	6.85 ± 0.33	10.79 ± 0.04
315	344.63 ± 0.19	41.17 ± 2.22	13.38 ± 0.67	11.29 ± 0.03
317	14.53 ± 0.42	53.09 ± 1.81	9.61 ± 0.41	11.31 ± 0.02

Table 8.3: A table of further fitted kinematic parameters for the SWIFT subset. Position angle was defined as a counter-clockwise offset relative to normal. Inclination was defined with 0° being face-on. Dynamic mass was calculated using equation 8.6.

In summary, 8 out of 34 galaxies (~24%) were classified as interacting and 24 out of 34 (~71%) were classified as isolated. 2 galaxies out of 34 (~5%) were unable to be classified. The

final list of classifications can be seen in Table 8.2. These values are in-line with the 70% of galaxies identified as isolated in the KMOS 3D sample at z ~ 2 (Wisnioski et al., 2015), but slightly lower than the 83% found in the KROSS survey at z ~ 0.9 (Johnson et al., 2018) and the 76% from Bellocchi et al., 2013, and higher than the ~35% at z ~ 3.5 from Turner et al., 2017 and z ~ 2.3 from Hogan et al., 2021. However, it is possible that at least some of the variation is due to differences in the methodology used for classification (e.g. Rodrigues et al., 2017). Local U/LIRGs have been found to be primarily dispersion dominated, with ~5% classified as isolated (Bellocchi et al., 2013), with intermediate redshift U/LIRGs being 10-25% isolated (Pereira-Santaella et al., 2019).

Furthermore, dynamic masses of each galaxy (treated as a rotating body within a given radius) were then calculated using basic principles, as shown in equation 8.6 below:

$$M_{dyn} = V_{max}^{2} R G^{-1} \tag{8.6}$$

where M_{dyn} is the dynamic mass in $M_{\odot}$, V_{max} is the maximum rotational velocity in km/s, R is the radius in kpc, and G is the gravitational constant in kpc$\cdot M_{\odot}^{-1} \cdot (\mathrm{km}/s)^{2}$. Dynamic masses, which trace the complete rotational mass of a galaxy (stars, as well as gas (molecular and atomic), dust, stellar remnants, and non-baryonic matter: dark matter in the dark matter halo) were calculated to serve as a check of the stellar masses calculated by Shi et al., 2011 (as the dynamic mass of a galaxy must be larger than its stellar mass) as well as allow for an estimation of the gas mass and halo mass. For all galaxies in the SWIFT subset, $M_{dyn} > M_{\star}$, in agreement with physical principles.

The SWIFT subset has an average $log(M_{\star}/M_{\odot}) = 10.60$ and $log(M_{dyn}/M_{\odot}) = 10.82$, which is slightly lower than other studies at redshifts of $z \sim 1$ (such as KMOS 3D which has an average $log(M_{\star}/M_{\odot}) = 10.65$ and $log(M_{dyn}/M_{\odot}) = 10.86$) (Wisnioski et al., 2015). This is in line with physical expectations, as stellar mass is expected to increase with redshift (e.g. Beifiori et al., 2014). This is also confirmed by Beifiori et al., 2014, who find an anticorrelation between redshift and the ratio $log(M_{dyn}/M_{*})$ for $0.1 \leq z \leq 0.6$ with $> 2\sigma$ confidence. The dynamical masses of the rotation dominated galaxies in Bellocchi et

al., 2013 (which, as described above, is the most similar sample to the SWIFT subset in terms of luminosity and redshift) are on average slightly lower, with $log(M_{dyn}/M_{\odot}) = 10.76$.This could be partly explained by the Bellocchi sample having a slightly lower average redshift than the SWIFT subset, but Bellocchi et al., 2013 do not show stellar masses for their sample.

These numbers infer that, on average, galaxies in the SWIFT subset are composed of 60% non-stellar material. This is again lower than the ~70% from the KROSS study mentioned earlier (Stott et al., 2016), which is as expected given the higher redshift (z ~ 1) of the galaxies in that study (at higher redshift, galaxies will have higher proportions of gas relative to stars, as the star formation rates are higher). Table 8.3 shows values for the dynamic mass for each galaxy, as well as its position angle, inclination, and radius.

3. The Main Sequence Multiple-Dynamical Ratio Relation

To relate the star formation with the kinematics of the sample, the MSM_{IR} (not AGN corrected) is plotted against the dynamical ratio, with the color of each galaxy set relative to its $EW_{PAH6.2\mu m}$ to indicate relative AGN content (Figure 8.9). Galaxies that were not fit by `GalPak` but had values for MSM_{IR} and were classified as interacting or isolated (M012, M020, M039, M057, M061, M062, M070, M075, M294) are not included in the plot, but are noted in the final conclusions and statistics based on their visual classification.

It can be seen that the interacting galaxies have substantially higher MSM_{IR} than the rest of the sample, with the exception of M012 and M062. This is in line with findings from other studies, (e.g. Stott 2013; Hung 2013). In general, a lower dynamical ratio (indicative of interaction) corresponds to a higher MSM_{IR}, which is what is expected given that interactions will cause bursts of star formation. Some AGN powered galaxies, such as M022 and M069, have low values for MSM_{IR}, while M019 is much higher.

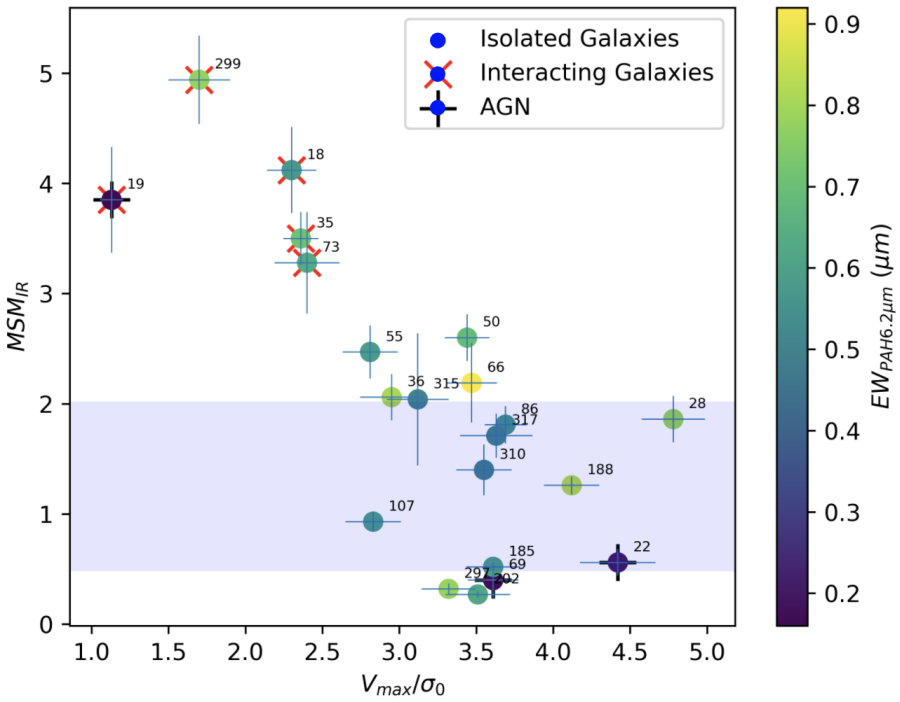


Figure 8.9: A plot of the MSM_{IR} vs the dynamical ratio (V_{max}/σ_0), with all galaxies colored according to their $EW_{PAH6.2\mu m}$, with lower values corresponding to higher AGN contributions. The main sequence of star formation from $0.5 < MSM_{IR} \leq 2.0$ is shaded in blue, with quiescent galaxies below, and starbursting galaxies above. Interacting galaxies are labeled with red crosses, and AGN are labelled with rotated black crosses. Interacting AGN are labelled with both a red and black cross. Galaxies that were not fit by `GalPak` but were classified as interacting or isolated are not included in the plot.

However, 6 of the 12 starbursting galaxies ($MSM_{IR} \geq 2$) are isolated (M036, M050, M055, M066, M075, and M315). This raises the question of whether or not the high main sequence multiples of starbursting galaxies are explained by interactions and the corresponding star formation, or if they are 'fake' multiples caused by a significant contribution from a powerful AGN. To investigate this, the AGN-corrected MSM_{IR} is plotted against the dynamical ratio in Figure 8.10. As in Figure 8.9, galaxies that were not fit by `GalPak` but were kinematically classified are not included in the plot.

Once the MSM_{IR} is corrected for AGN content, it is clear that interactions are the main driver of the high main sequence multiples observed in the SWIFT subset. The interacting galaxies are not significantly affected by the removal of AGN content, and still exhibit high main sequence multiples (M018, M019, M020, M035, M073, M299). Only 2 interacting galaxies are

not starbursting (M012 and M062), but are still high on the main sequence, with $MSM_{IR} \geq 1.50$. On the other hand, only 3 out of the 6 isolated galaxies previously with an $MSM_{IR} \geq 2$ are still above the main sequence (M050, M055, and M075). Furthermore, they have multiples marginally above the main sequence (2.11 ± 0.17, 2.03 ± 0.20, and 2.14 ± 0.28 respectively), and all have errors that could place them back in the main sequence with an $MSM_{IR} < 2$.

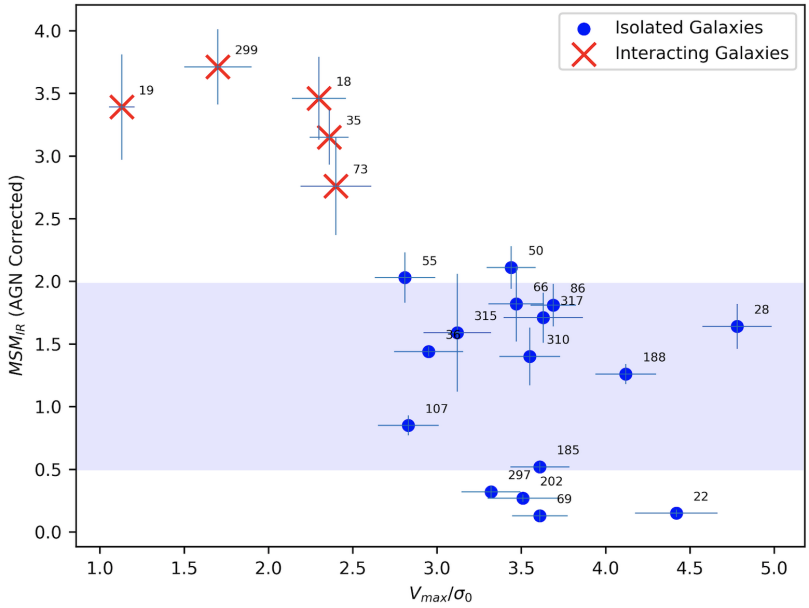


Figure 8.10: A plot of the AGN-corrected MSM_{IR} vs the dynamical ratio (V_{max}/σ_0). The main sequence of star formation from $0.5 < MSM_{IR} \leq 2.0$ is highlighted in blue. Interacting galaxies are represented by red crosses, and isolated galaxies are represented by blue circles. Galaxies that were not fit by `GalPak` but were classified as interacting or isolated are not included in the plot.

However, a few caveats and outliers must be discussed. In addition to the visually classified galaxies, four galaxies are not shown in either plot due to lack of data (M005, M013, M037, M041). M005 and M013 are not shown on either plot as they had neither kinematic data nor a classification, and M037 and M041 had no values for MSM_{IR}. Furthermore, M005, M020, and M061 had no values for $f_{AGN,\,Magdis}$. However, all three of these galaxies were classified as

AGN with values for $EW_{PAH6.2\mu m}$ <0.19, and as shown in Figure 8.7, powerful AGN had similar values for $f_{AGN,\,Magdis}$ and $f_{AGN,\,Foster}$.

M005 has a high MSM_{IR} at 3.84 ± 0.54, but does not have an AGN-corrected MSM_{IR}. It was classified as an AGN by its $EW_{PAH6.2\mu m}$ <0.09μm, the second lowest of the SWIFT subset, and lower than the third lowest by nearly a factor of 2. As AGN fraction increases with decreasing $EW_{PAH6.2\mu m}$, its f_{AGN} would likely be high (Figure 8.6) with its AGN-corrected MSM_{IR} significantly decreased.

M012 was visually categorized as interacting. However, it was not able to be modelled due to a bad datacube, and kinematic data could not be retrieved. Despite it being an interacting galaxy, it exhibits a slightly lower MSM_{IR} than would be expected, with $MSM_{IR,\,M012} = 1.85 \pm 0.22$. However, the two nuclei are separated by at least 3.5kpc, indicating an early stage of interaction which may not yet have caused significant episodes of star formation. This explains the relatively lower MSM_{IR} than expected. This same argument holds for M062, which can visually be seen to be interacting, but has an even larger separation of ~10kpc of the two nuclei. It also has no AGN contribution, with its corrected and uncorrected $MSM_{IR} = 1.68 \pm 0.15$. M012 and M062 are not plotted in either figure.

M013 has an uncorrected $MSM_{IR} = 5.27 \pm 0.80$, the highest of the SWIFT subset. Once corrected for AGN, it has an $MSM_{IR} = 3.37 \pm 0.51$, the fourth highest of the subset. This does not change regardless of whether $f_{AGN,\,Magdis}$ or $f_{AGN,\,Foster}$ is used to calculate $MSM_{IR,\,AGN\ Corrected.}$ A similar argument holds for M299, an interacting galaxy with the highest value for MSM_{IR} of the subset.

M019 is a powerful interacting AGN ($EW_{PAH6.2\mu m,\,M019}$ <0.16μm) that was specifically mentioned in Section 1.2 of this chapter as its value for $f_{AGN,\,Foster}$ was higher than that for $f_{AGN,\,Magdis}$ by ~0.20 ($f_{AGN,\,Foster,\,M019} = 0.33$, $f_{AGN,\,Magdis,\,M019} = 0.12$). As a check, its $MSM_{IR,\,AGN\ Corrected}$ was recalculated using $f_{AGN,\,Foster}$, with its MSM_{IR} decreasing from 3.85 to

2.58 (as opposed to 3.39). As such, it is still classified as a starbursting interacting galaxy, regardless of which value for f_{AGN} is used.

M020 did not have data for f_{AGN}, but has a low value for $EW_{PAH6.2\mu m}$: the fourth lowest with $EW_{PAH6.2\mu m,\,M020}$ <0.19μm. The uncorrected value for its main sequence multiple is $MSM_{IR,\,M020} = 2.49 \pm 0.21$. M020 is interacting, classified visually. As it has a strong tidal tail but only one resolved nucleus, it is believed that M020 is in an advanced state of merging, and some of the star formation may have subsided, and it is moving down to the expected MS before becoming quiescent (this could also be possible for M012 and M062). However, it could also be a projection effect, with the two nuclei appearing close as they are along the line of sight.

M037 and M041 had no values for MSM_{IR}. However, both were visually classified as isolated.

M039 is a weak AGN ($EW_{PAH6.2\mu m} = 0.36$) that had a value for $f_{AGN,\,Foster}$ that was greater than $f_{AGN,\,Magdis}$ by 0.20. However, as M039 was a quiescent galaxy even before correcting for f_{AGN}, its classification does not change regardless of which value is used.

M061 was the third galaxy with no data for f_{AGN}, and had the lowest value for $EW_{PAH6.2\mu m}$ at 0.03μm. Thus, its f_{AGN} is likely high (Figure 8.6), with a low value for MSM_{IR}.

The remaining galaxies that had no `GalPak` fits but were classified visually and not included in the plots are M039, M057, M061, M070, M075 and M294. All of these galaxies were classified as isolated, and with the exception of M075 have values for MSM_{IR} less than 2.0, which is in line with the hypotheses that isolated galaxies are generally not starbursting.

4. Conclusions

In this part of the thesis, a subset of 34 galaxies from the 5MUSES sample was observed with the SWIFT integral field spectrograph. The kinematic data from SWIFT was combined with existing infrared data from literature to probe the whether the high values for MSM_{IR} observed in some galaxies were due to bursts of star formation from interactions (traced by the dynamical ratio), or from AGN (traced by $EW_{PAH6.2\mu m}$).

Two main conclusions have been presented in this part of the thesis. First, a lower dynamical ratio corresponds, in general, to a higher MSM_{IR}, even before correcting for AGN content. 6 out of 8 galaxies classified as interacting lie above the main sequence (defined as $0.5 \leq MSM_{IR} \leq 2.0$) with values for $MSM_{IR} \geq 2.0$. Only 6 out of 24 galaxies classified as isolated have values for $MSM_{IR} \geq 2.0,$ with only 1 out of 24 having an $MSM_{IR} \geq 2.5$.

Second, once the AGN contribution to L_{IR} is removed, the galaxies still exhibit this trend, meaning that high values for MSM_{IR} are due to star formation from interactions rather than from AGN contributions to L_{IR}. 6 out of 8 interacting galaxies still lie above the main sequence, with all having corrected values for MSM_{IR} at or above 2.50. Furthermore, once the AGN content is removed, there is a significantly better agreement with the isolated galaxies. Only 3 out of 24 isolated galaxies remain above the main sequence, and all have values for MSM_{IR} marginally above the main sequence ($2.11 \pm 0.17, 2.03 \pm 0.20,$ and 2.14 ± 0.28).

As such, the data is in agreement with the hypothesis that it is star formation caused by interactions that is driving the increased values for MSM_{IR}, rather than contribution to the L_{IR} from an AGN. This leads to a final total of 8 out of 34 interacting galaxies (~24%) and 24 out of 34 isolated galaxies (~71%), with 2 unable to be classified. Of these 8 interacting galaxies, after correcting for AGN contribution, 75% are starbursting, with the remaining 25% in the upper star forming region with $1.5 \leq MSM_{IR} < 2.0$. Of the 24 isolated galaxies, after correcting for AGN contribution, at most 12% (3) are starbursting. Of the isolated galaxies, roughly 20% are quiescent, and 68% star forming. This value is in agreement with the value of 68% of galaxies being star forming as presented in Elbaz et al., 2011.

As the SWIFT subset is representative of the 5MUSES sample, these percentages can be extrapolated to the full sample. The 5MUSES sample is representative of the bulk of generic, star forming galaxies, and so these ratios can be further applied to most samples out to intermediate redshifts.

5. Future Work

As this is the first spatially resolved optical study of the 5MUSES sample, it will serve as a good comparison to spatially resolved PAH data with JWST. However, there is still significant work that can be done with unused SWIFT data. Star formation rates for $H\alpha$ and $PAH_{6.2\mu m}$ have been calculated (with $SFR_{H\alpha}$ extinction corrected with $H\beta$ data from the 13 available SDSS spectra), and could be used to compare the MSM_{IR} with a theoretical $MSM_{H\alpha}$ and $MSM_{PAH6.2\mu m}$. These could then all be re-calculated with the dynamical mass, to see how the values compare vs when using stellar mass.

$NII/H\alpha$ metallicities have also been calculated, along with metallicity gradient maps. These could be investigated alongside evidence of outflows, traced by the broad component of the $H\alpha$ emission lines in each galaxy. This could help constrain metallicity content of the overall 5MUSES sample, as well as the percentage of galaxies containing outflows, which could help to explain the low star formation rates seen in some galaxies.

Appendix A

SDSS Images and Kinematic Fits for the SWIFT-5MUSES Galaxies

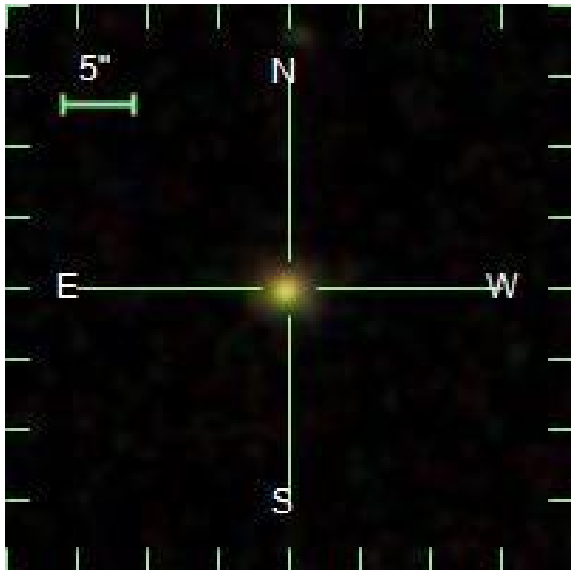


Figure A.1: SDSS continuum image for M005.

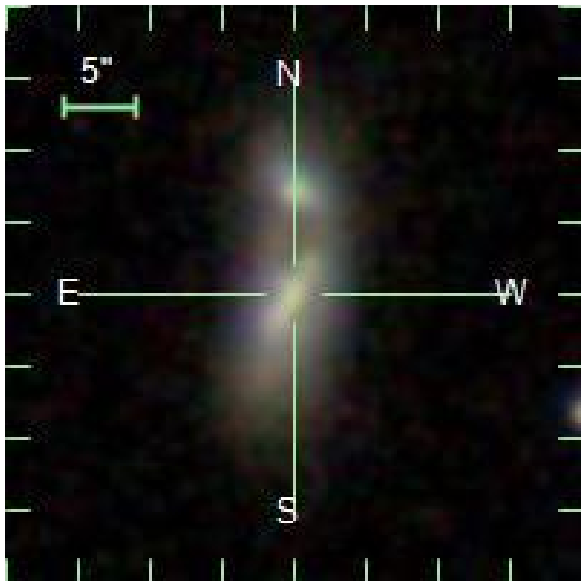


Figure A.2: SDSS continuum image for M012.

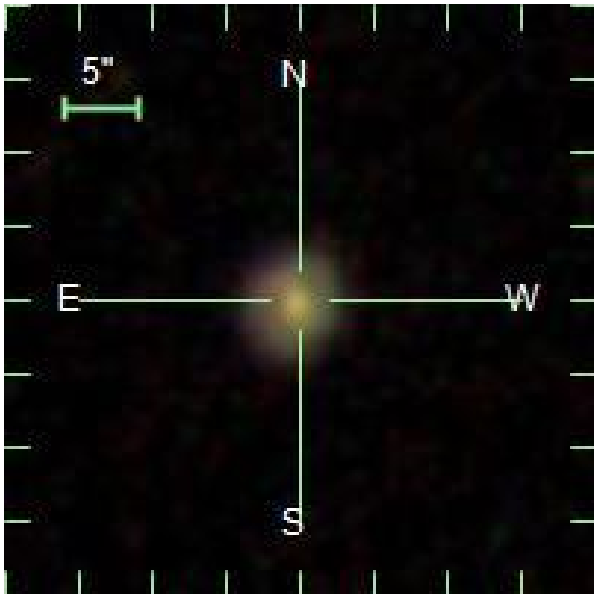


Figure A.3: SDSS continuum image for M013.

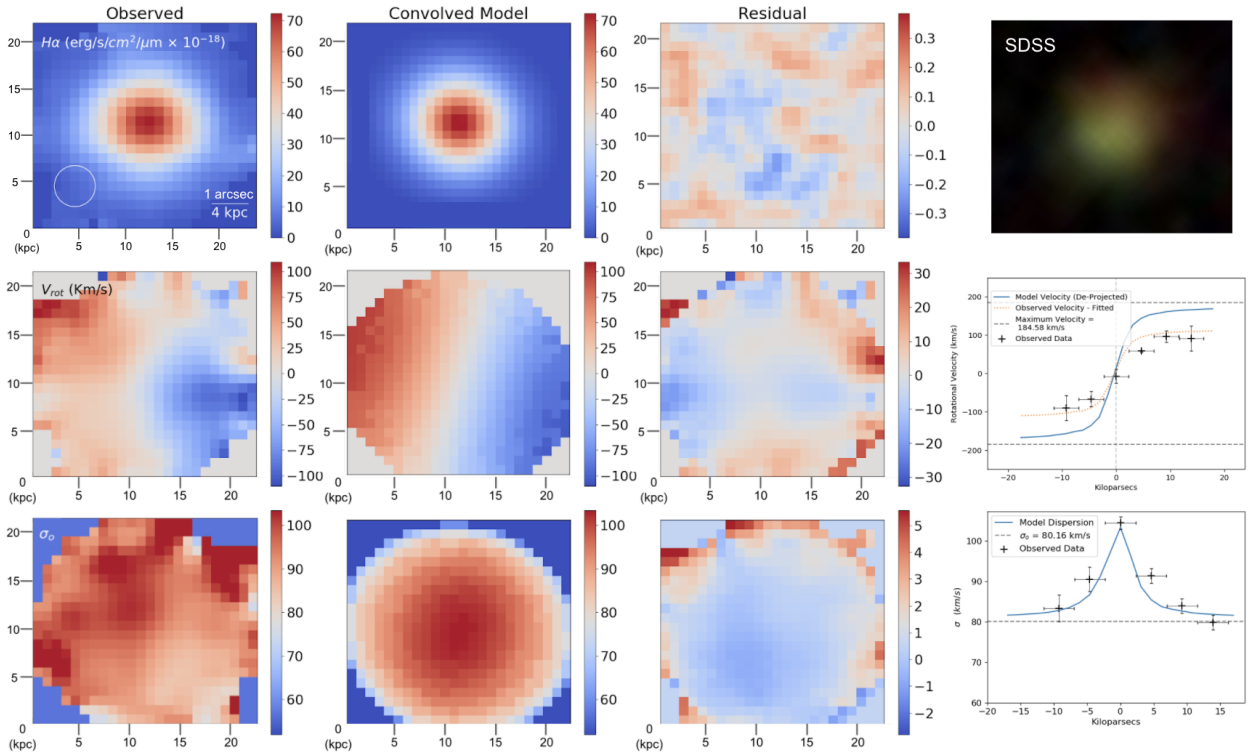


Figure A.4: Images and curves for M018. (Top row, left to right) (1) Observed [$H\alpha$]6563Å flux. (2) Convolved model [$H\alpha$]6563Å flux. (3) Residual [$H\alpha$]6563Å flux. (4) SDSS continuum image. (Middle row, left to right) (1) Observed [$H\alpha$]6563Å velocity. (2) Convolved model [$H\alpha$]6563Å velocity. (3) Residual [$H\alpha$]6563Å velocity. (4) Observed and model [$H\alpha$]6563Å velocity curves. (Bottom row, left to right) (1) Observed [$H\alpha$]6563Å dispersion. (2) Convolved model [$H\alpha$]6563Å dispersion. (3) Residual [$H\alpha$]6563Å dispersion. (4) Observed and model [$H\alpha$]6563Å dispersion curves.

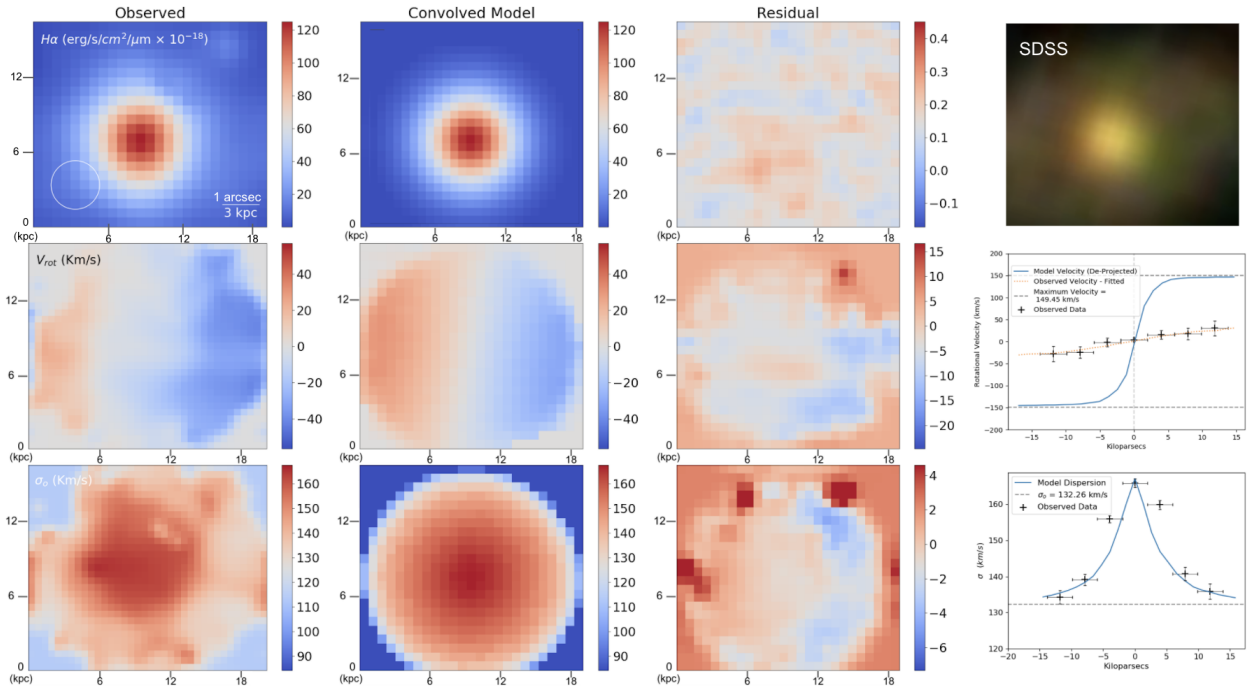


Figure A.5: Same as Figure A.4 but for M019.

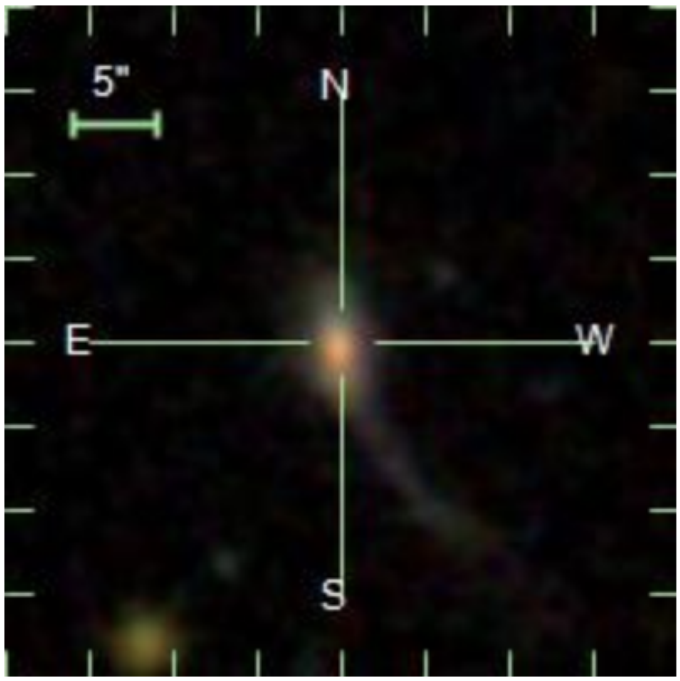


Figure A.6: SDSS continuum image for M020.

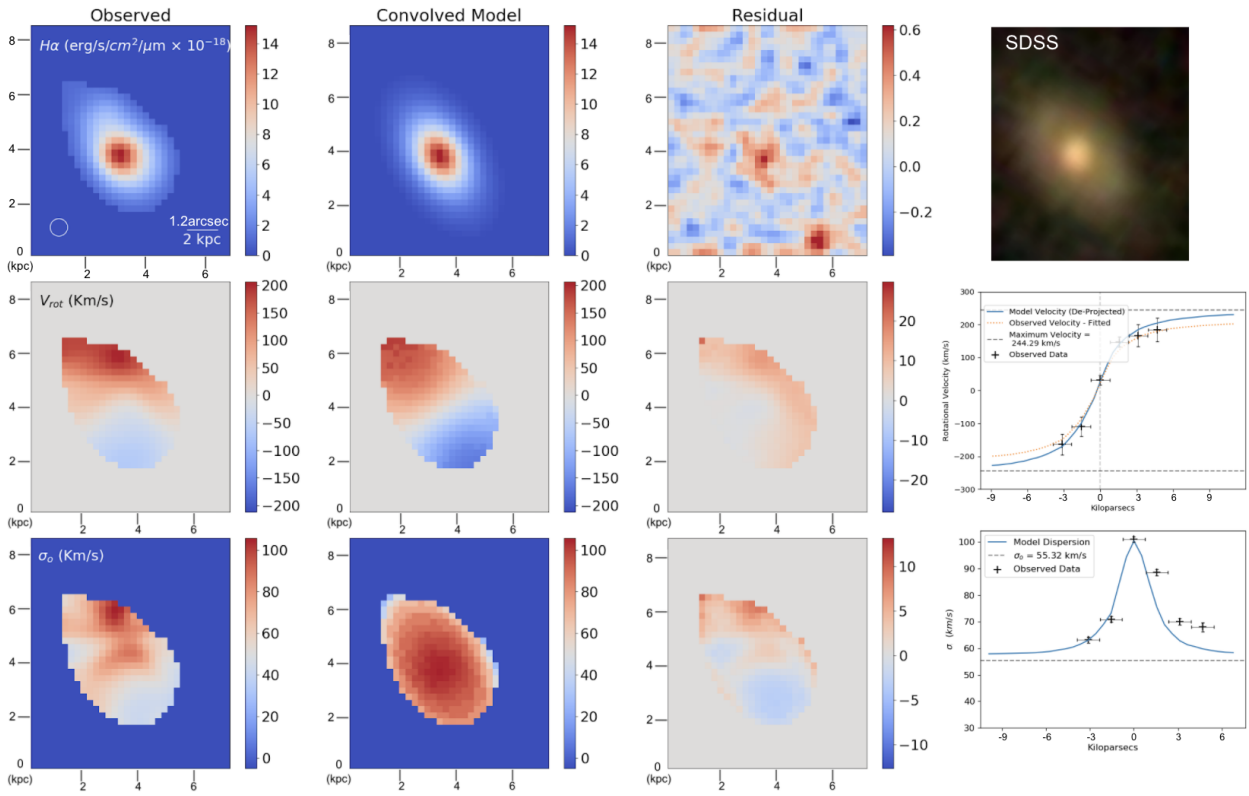


Figure A.7: Same as Figure A.4 but for M022.

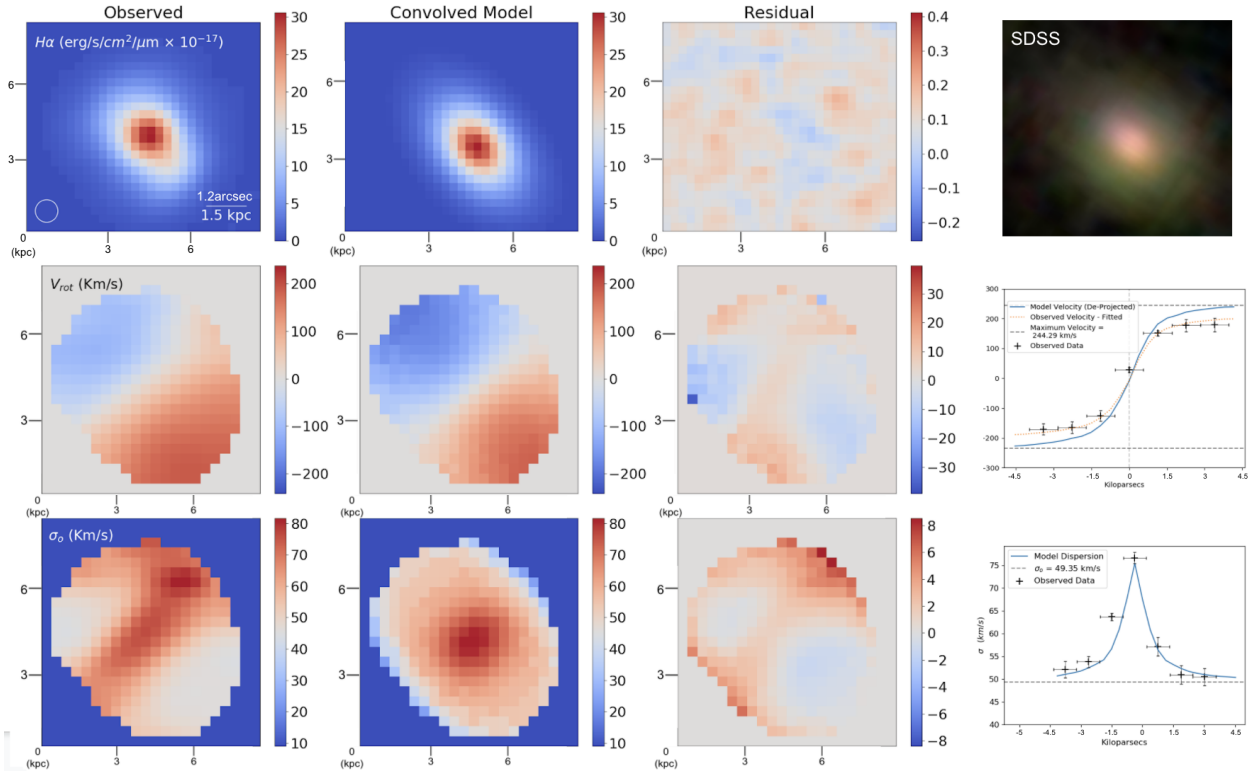


Figure A.8: Same as Figure A.4 but for M028.

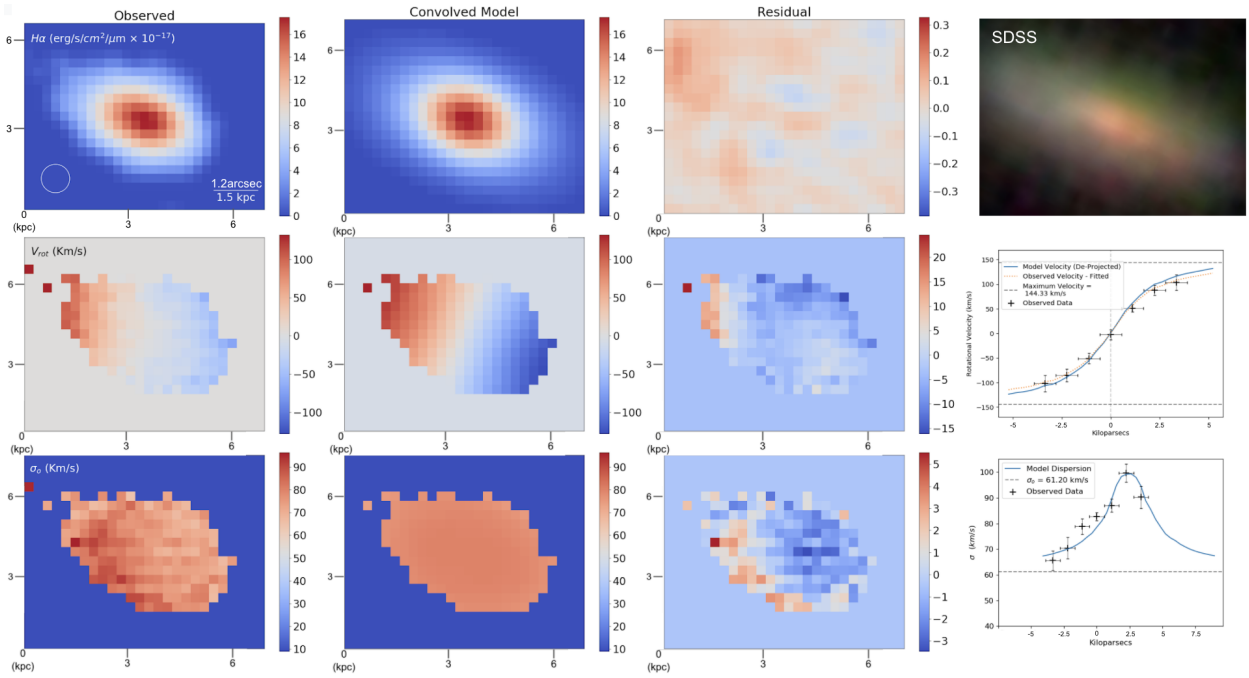


Figure A.9: Same as Figure A.4 but for M035.

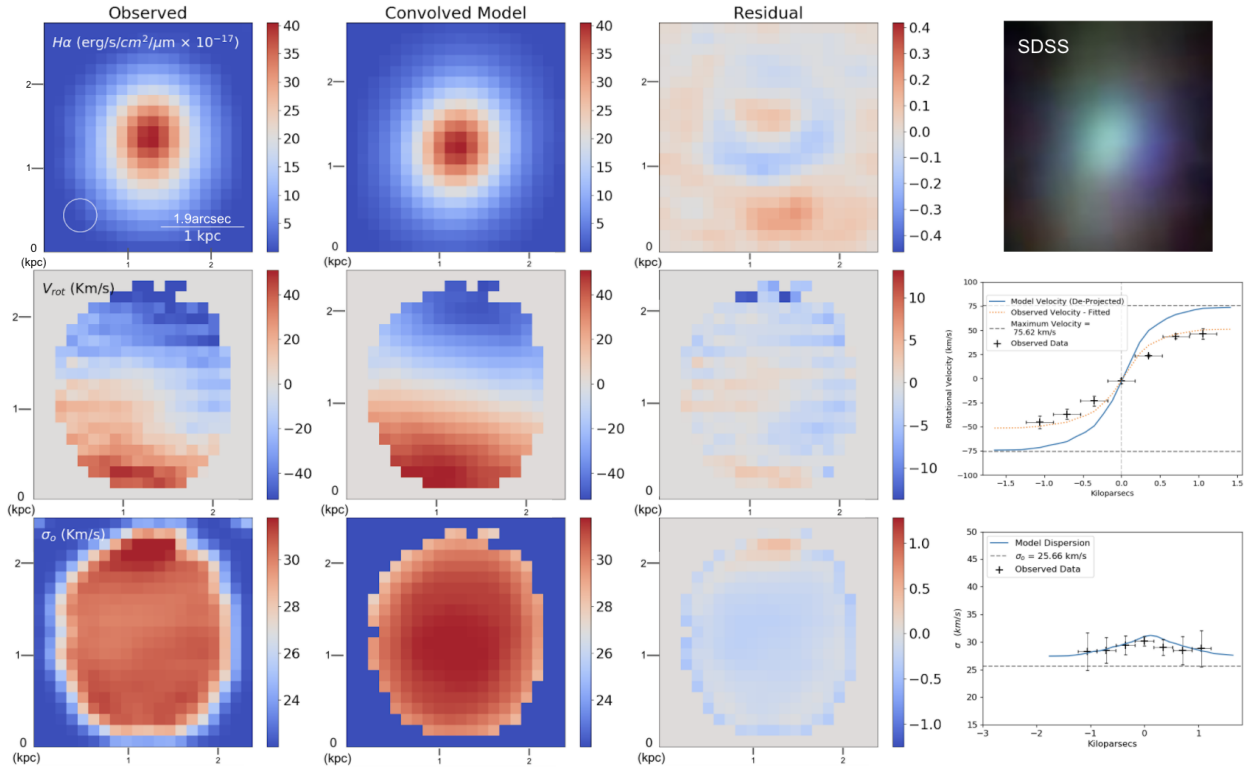


Figure A.10: Same as Figure A.4 but for M036.

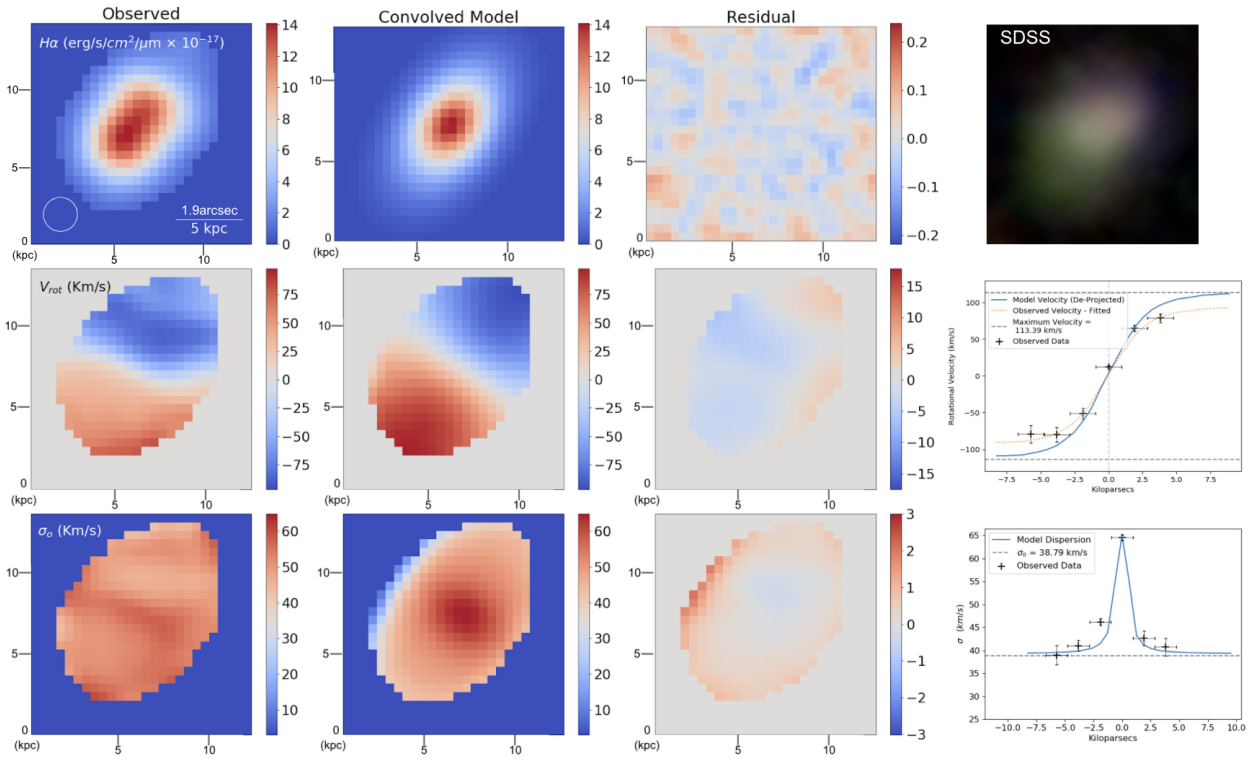


Figure A.11: Same as Figure A.4 but for M037.

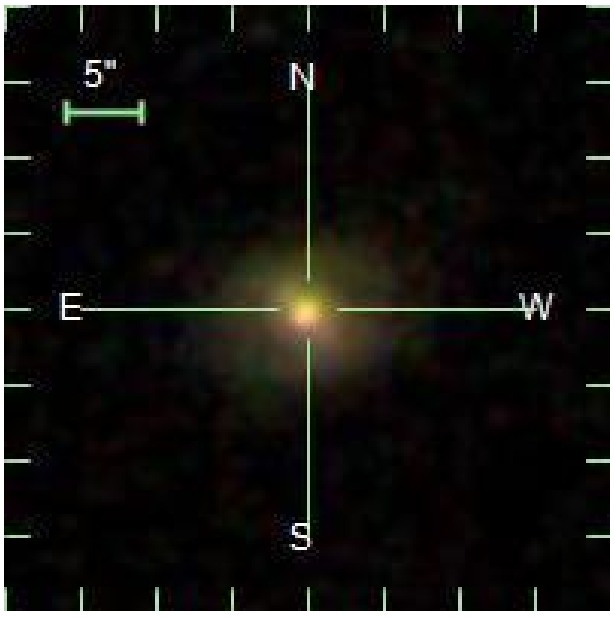


Figure A.12: SDSS continuum image for M039.

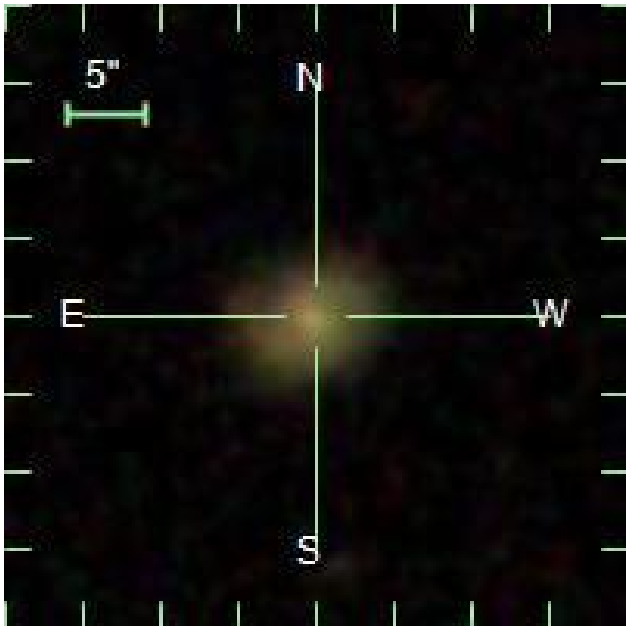


Figure A.13: SDSS continuum image for M041.

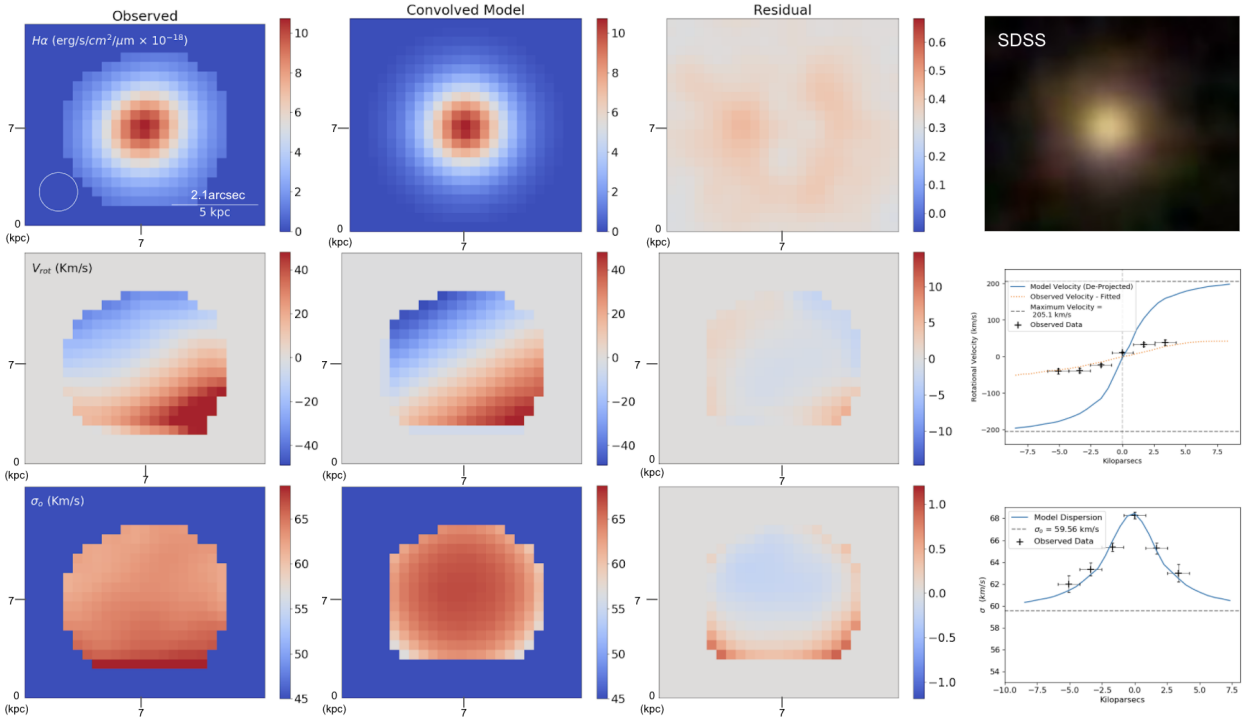


Figure A.14: Same as Figure A.4 but for M050.

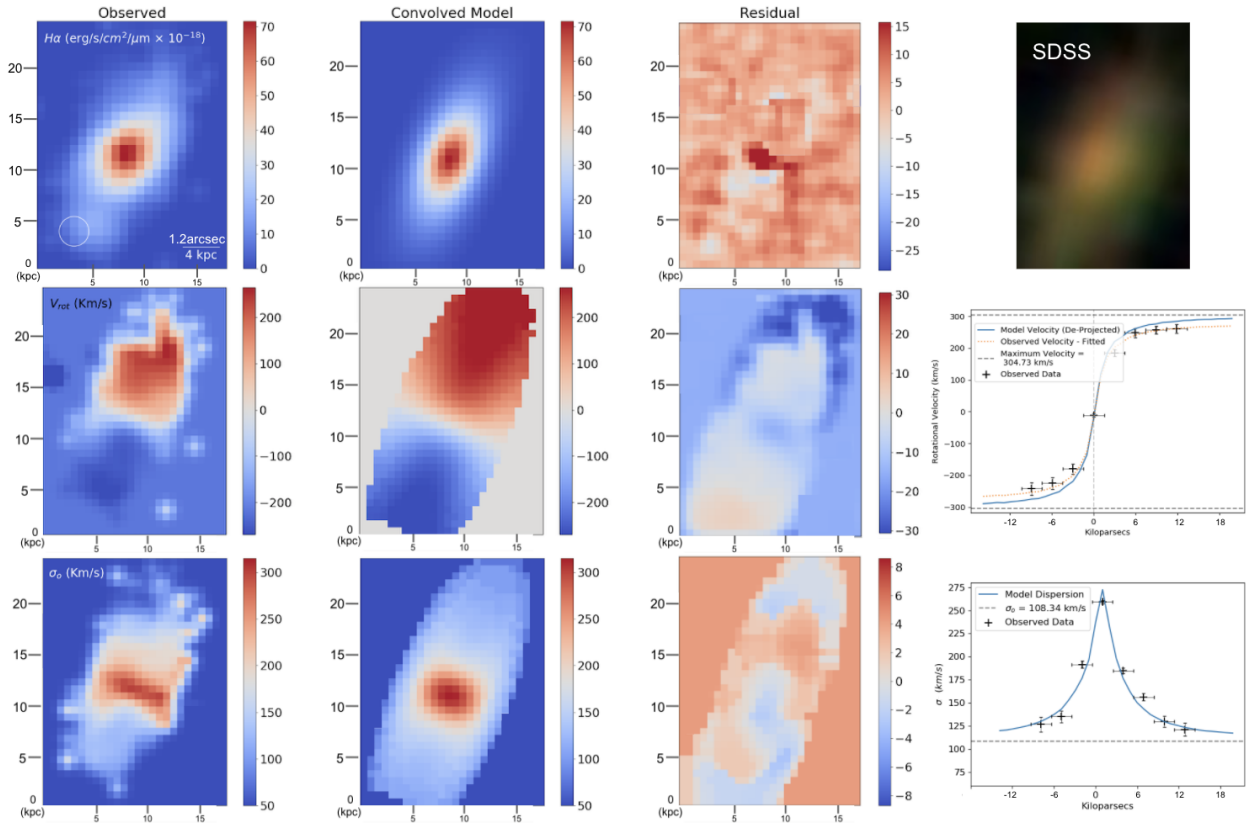


Figure A.15: Same as Figure A.4 but for M055.

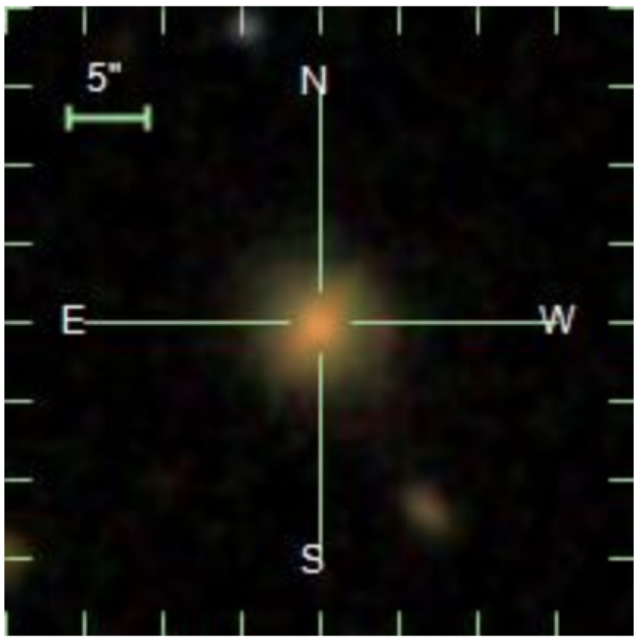


Figure A.16: SDSS continuum image for M057.

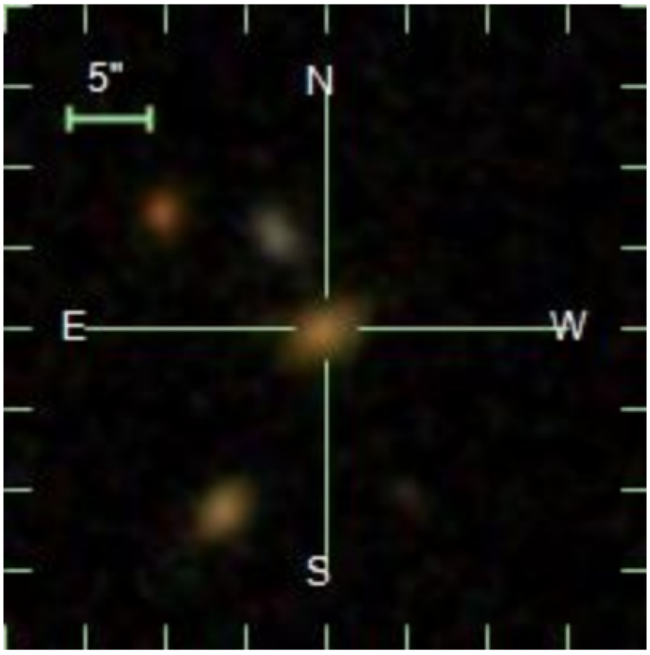


Figure A.17: SDSS continuum image for M061.

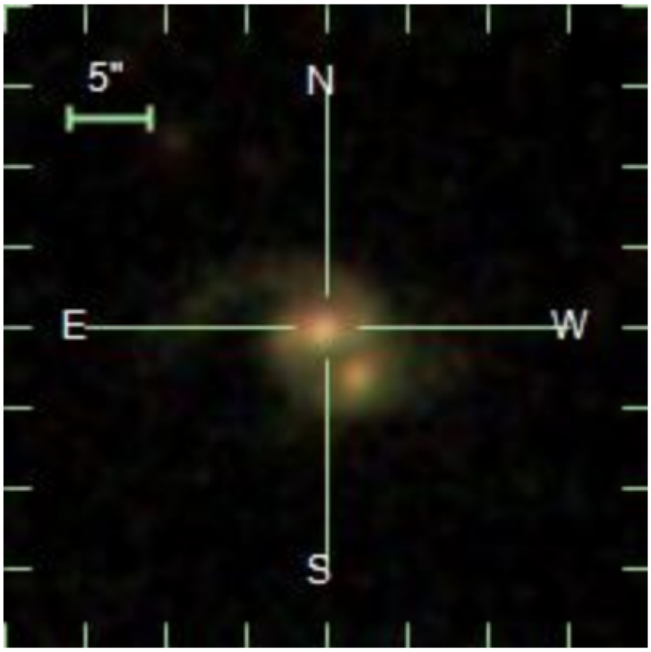


Figure A.18: SDSS continuum image for M062.

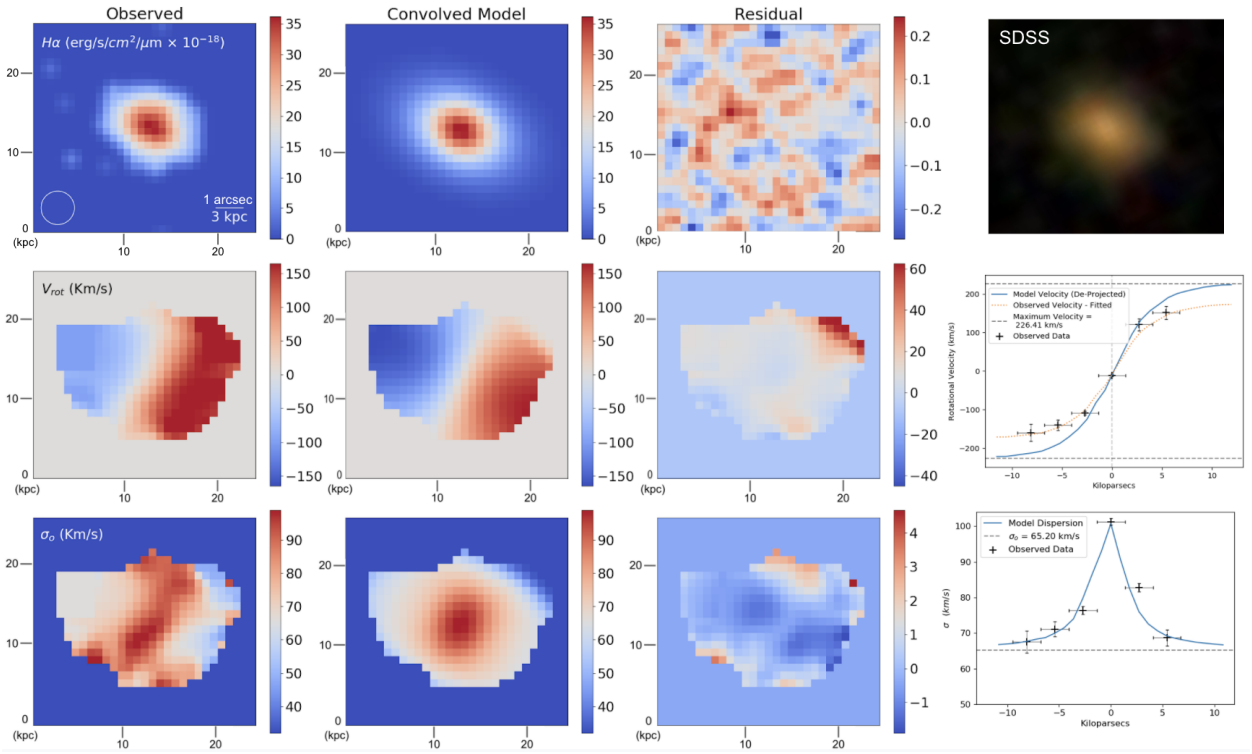


Figure A.19: Same as Figure A.4 but for M066.

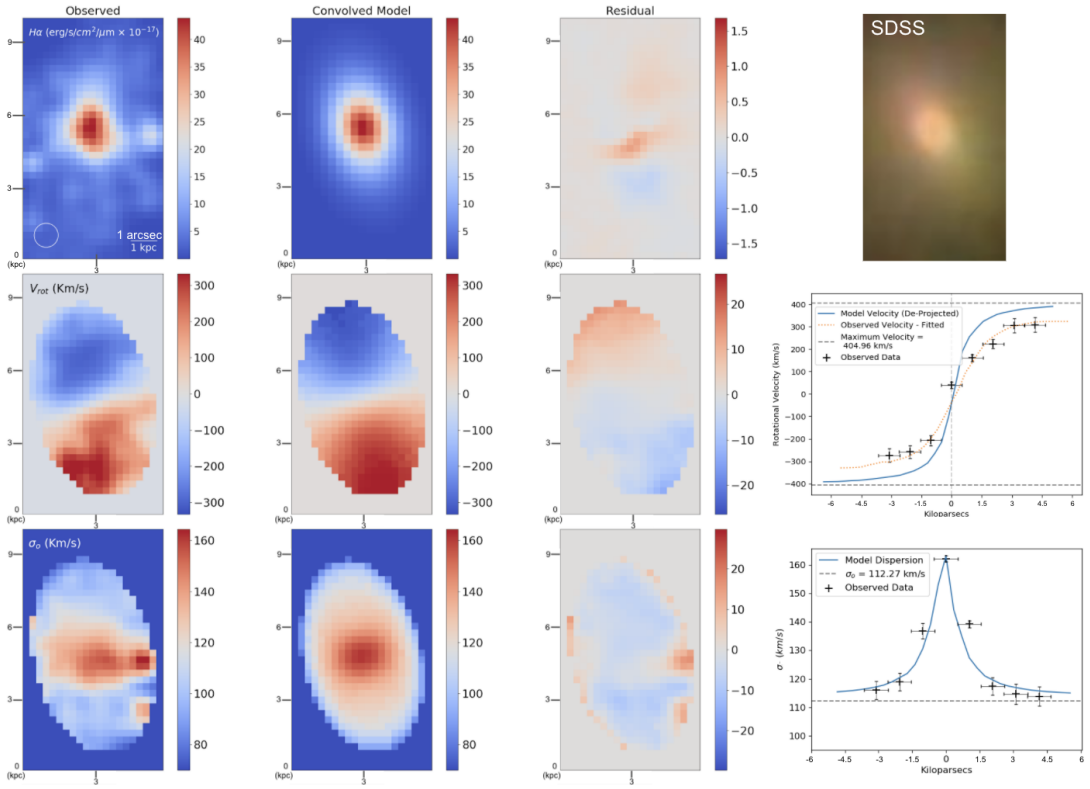


Figure A.20: Same as Figure A.4 but for M069.

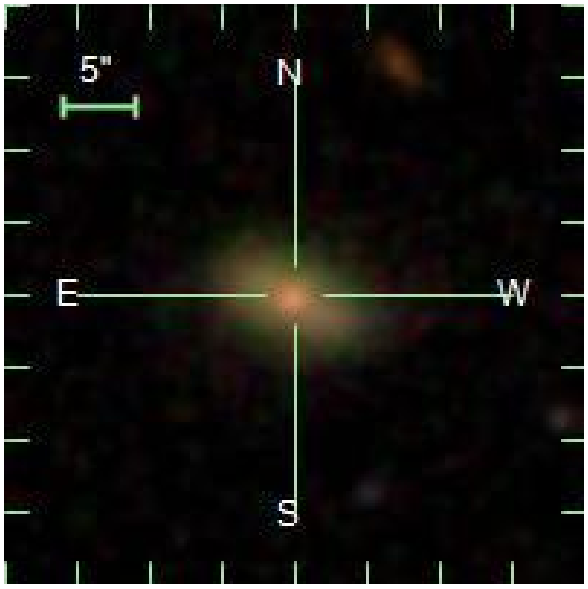


Figure A.21: SDSS continuum image for M070.

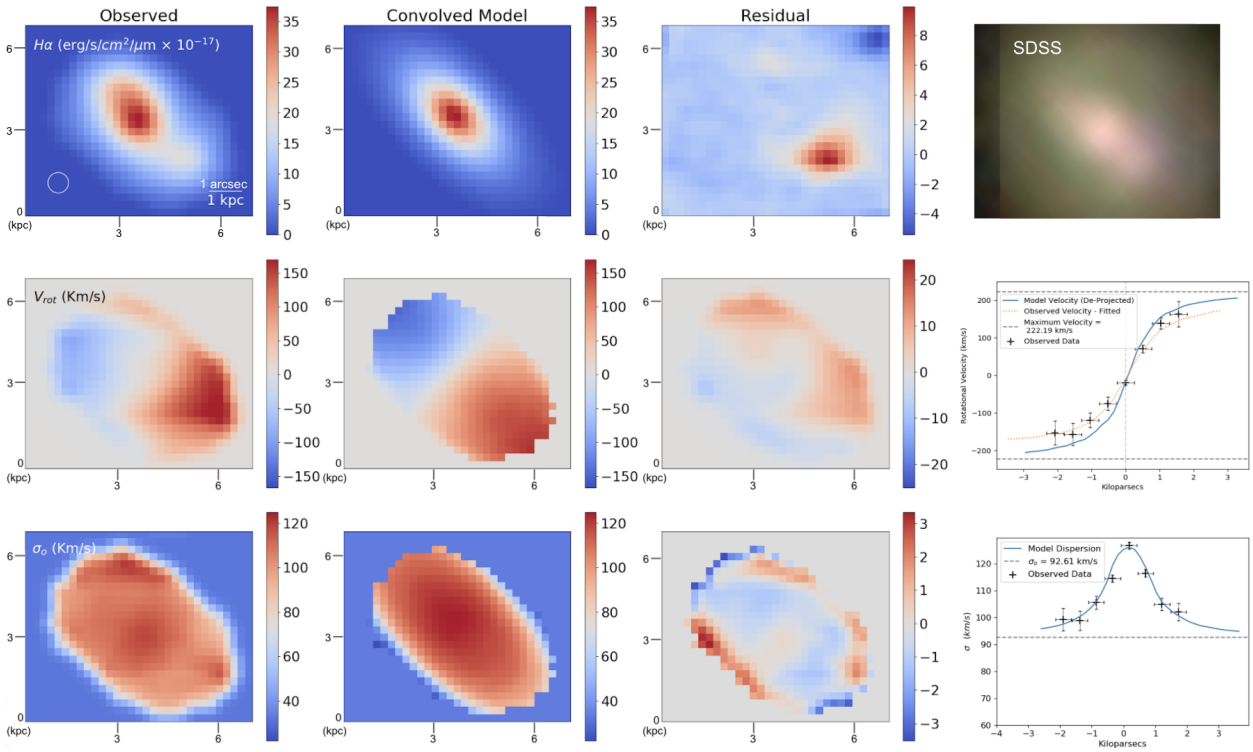


Figure A.22: Same as Figure A.4 but for M073.

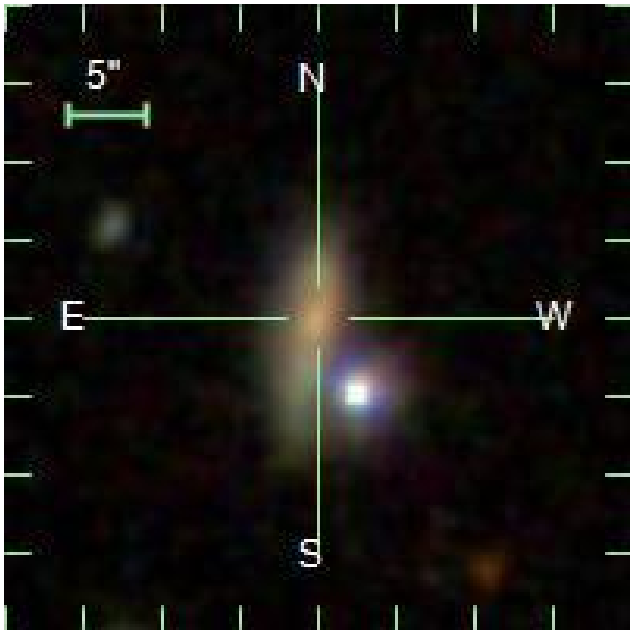


Figure A.23: SDSS continuum image for M075.

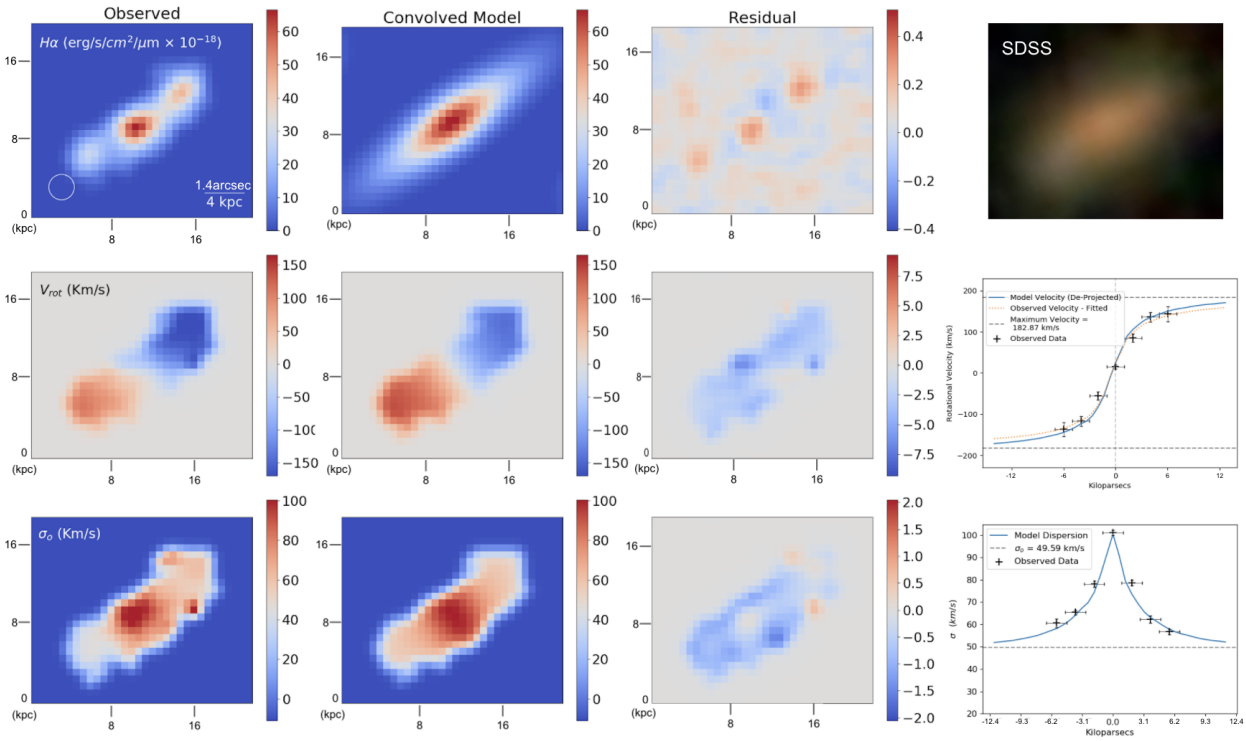


Figure A.24: Same as Figure A.4 but for M086.

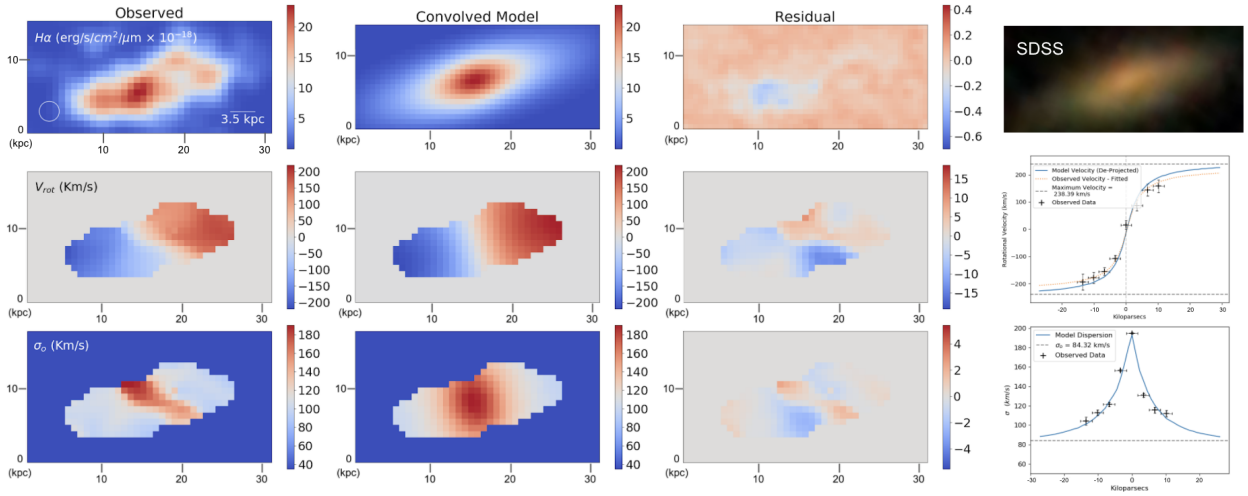


Figure A.25: Same as Figure A.4 but for M107.

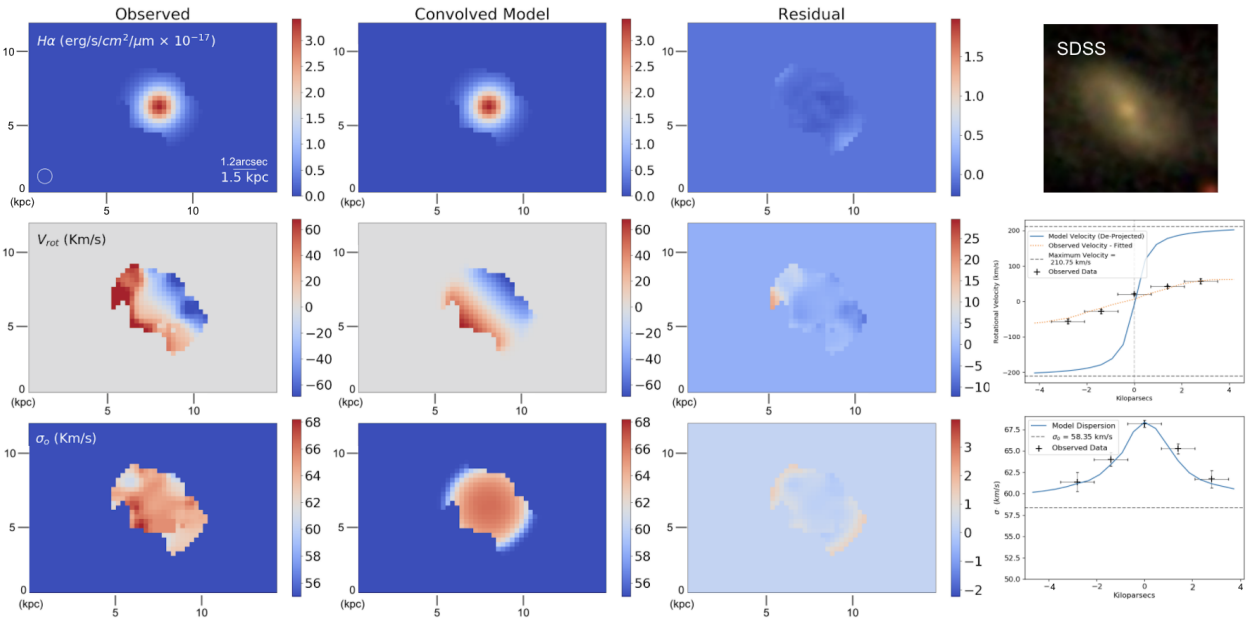


Figure A.26: Same as Figure A.4 but for M185.

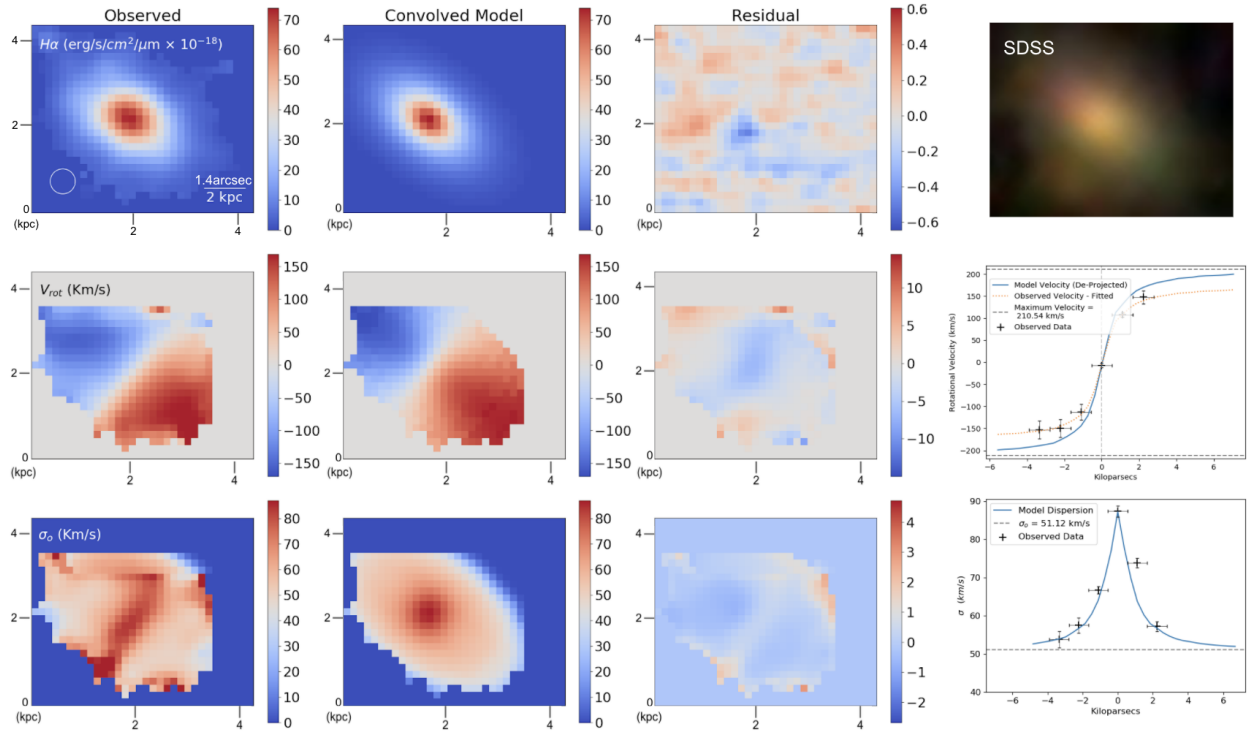


Figure A.27: Same as Figure A.4 but for M188.

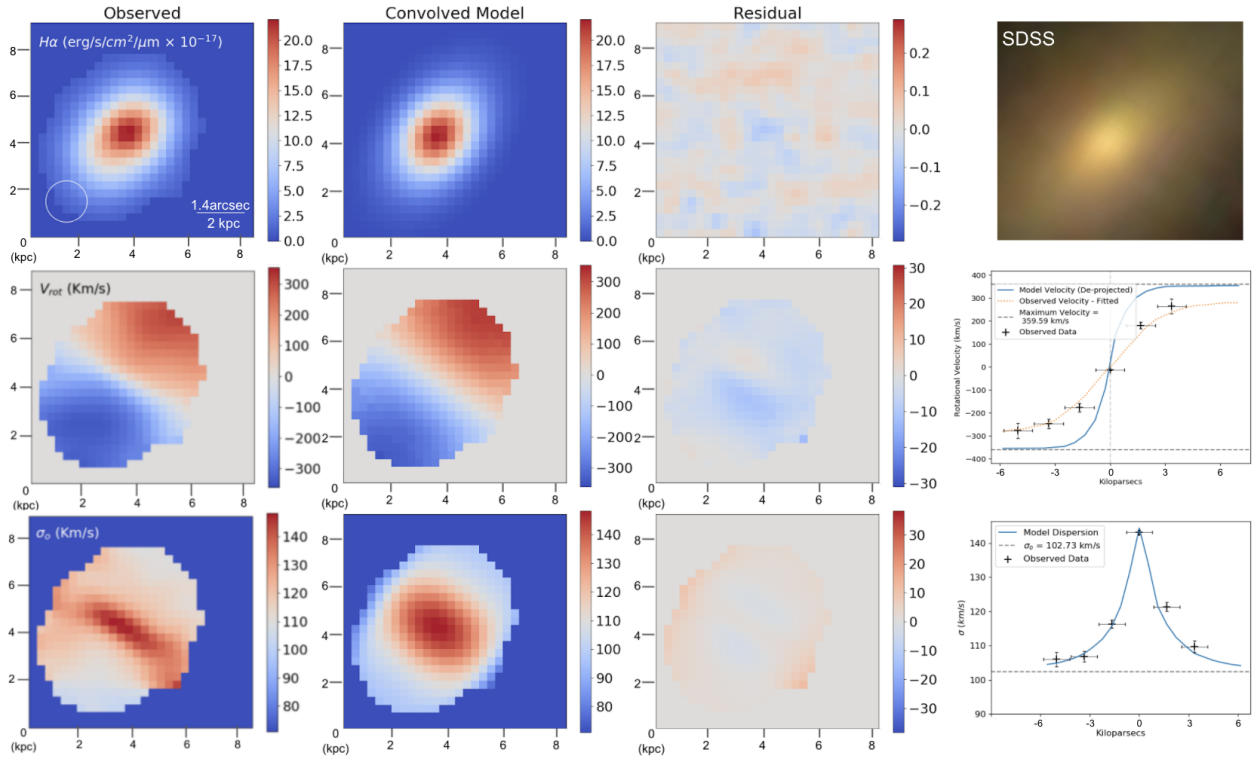


Figure A.28: Same as Figure A.4 but for M202.

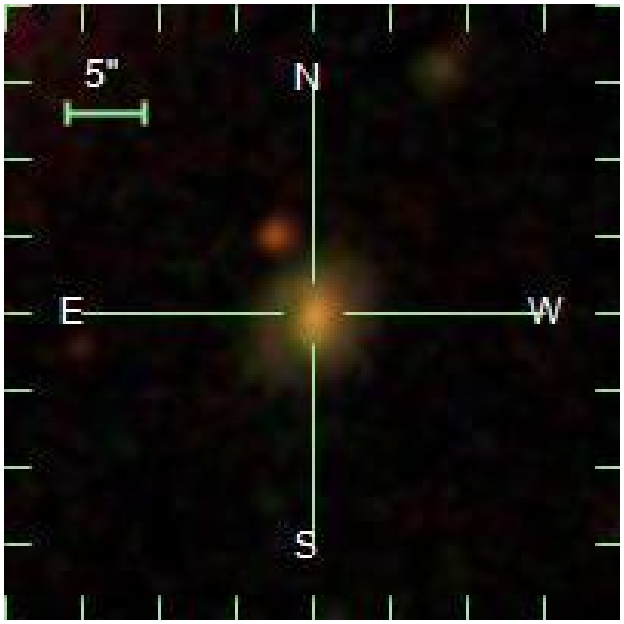


Figure A.29: SDSS continuum image for M294.

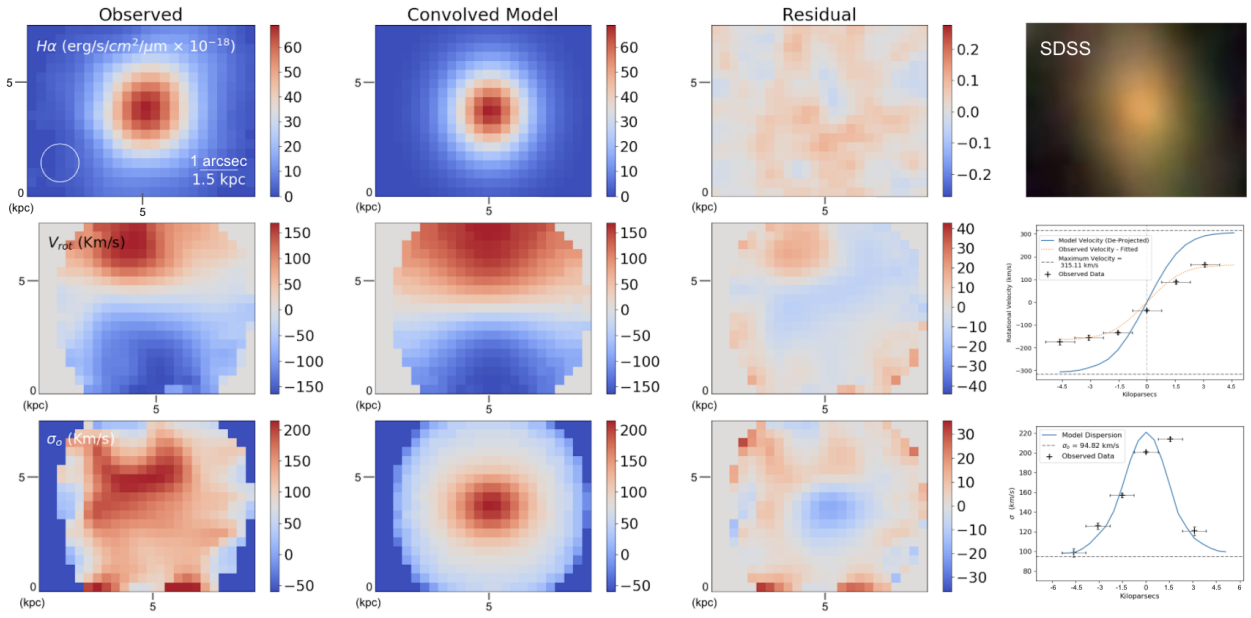


Figure A.30: Same as Figure A.4 but for M297.

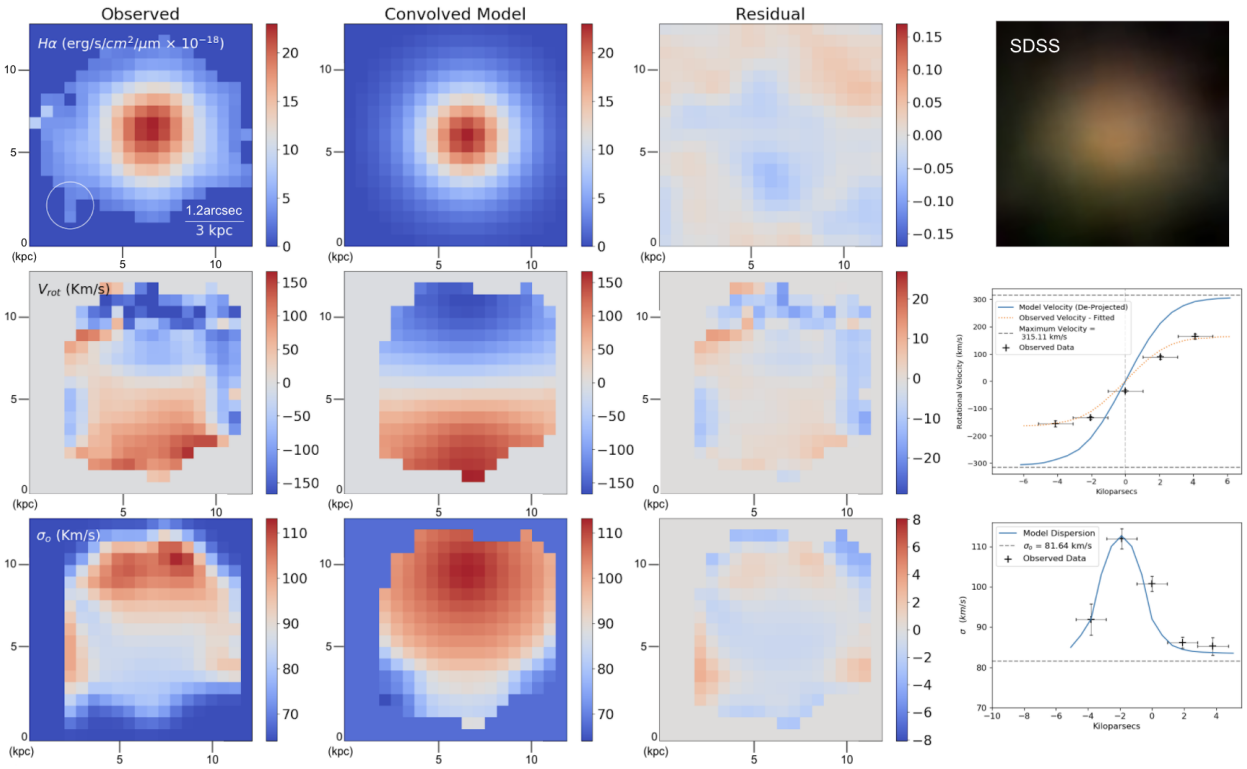


Figure A.31: Same as Figure A.4 but for M299.

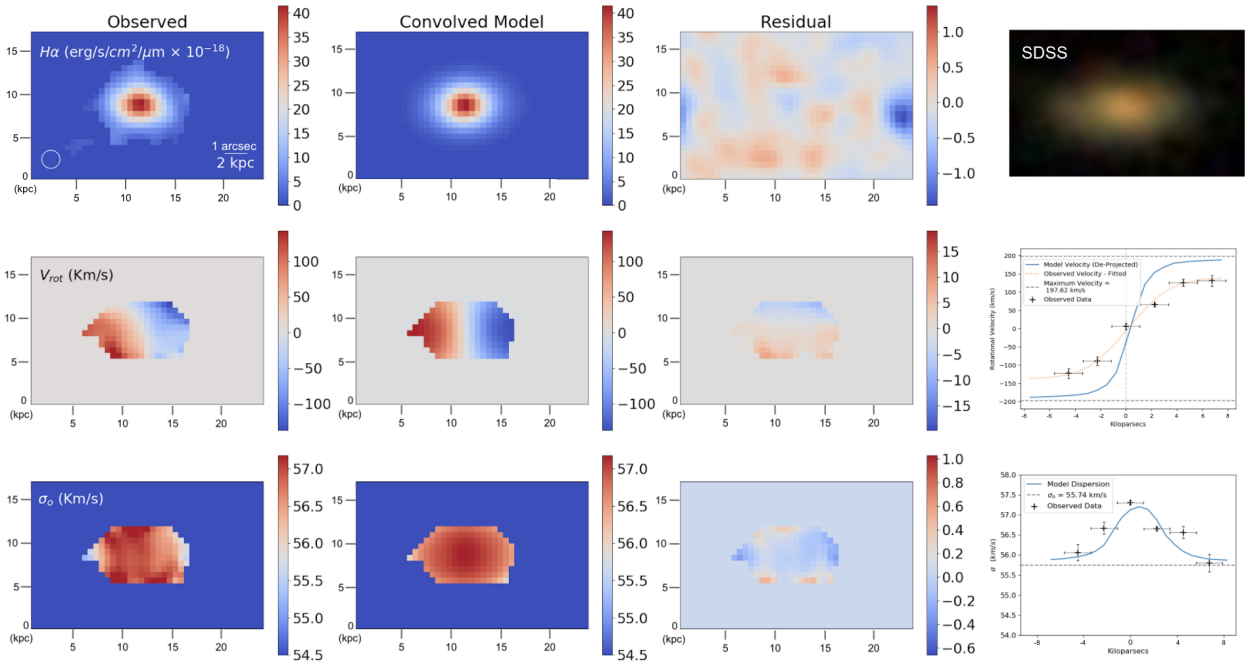


Figure A.32: Same as Figure A.4 but for M310.

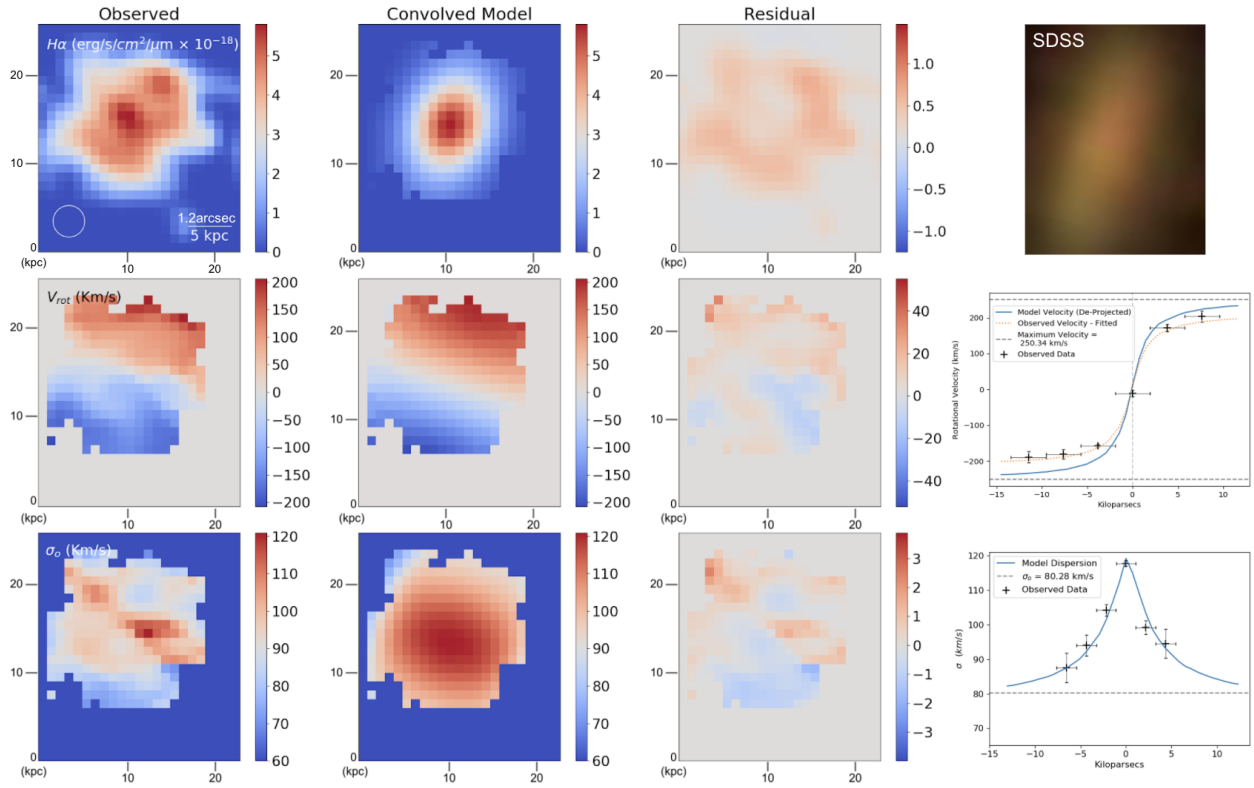


Figure A.33: Same as Figure A.4 but for M315.

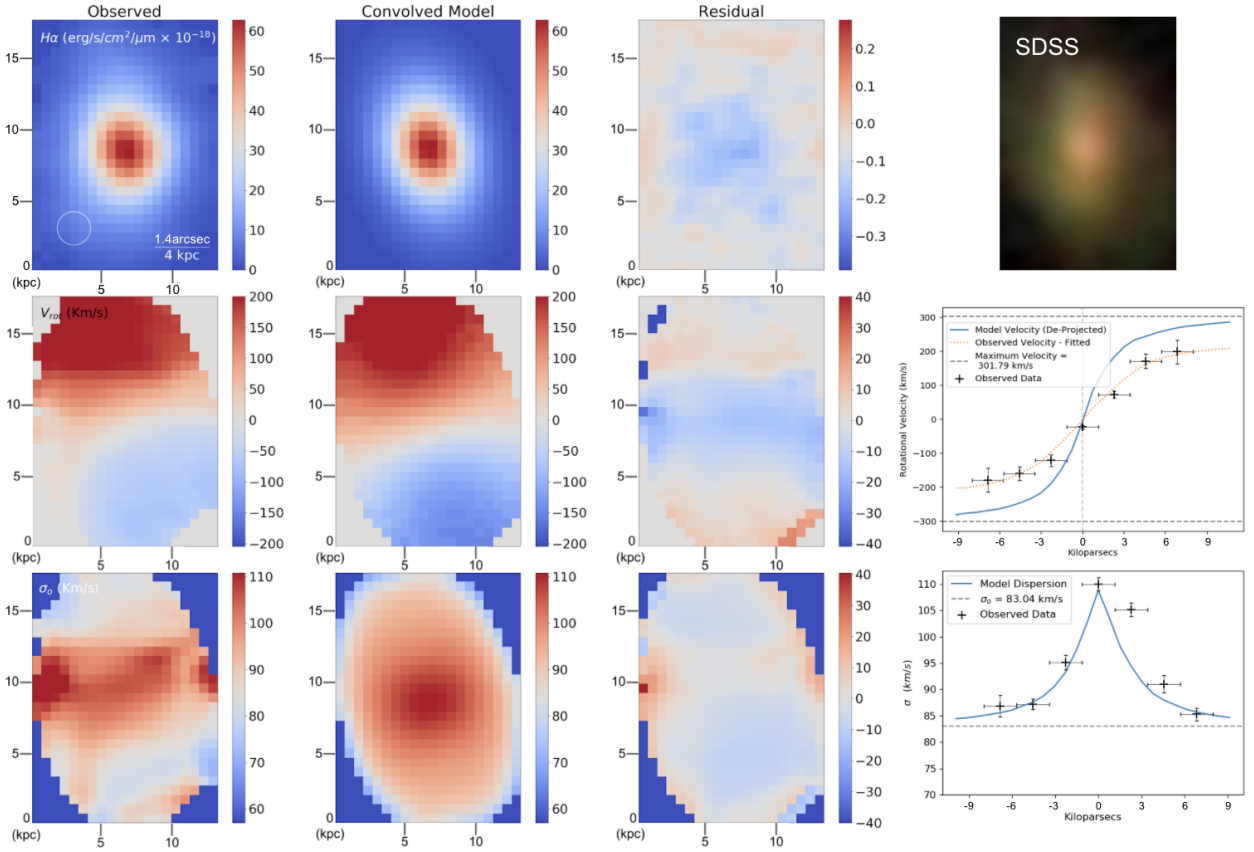


Figure A.34: Same as Figure A.4 but for M317.

Appendix B

SED Template Fits for the SWIFT-5MUSES Galaxies

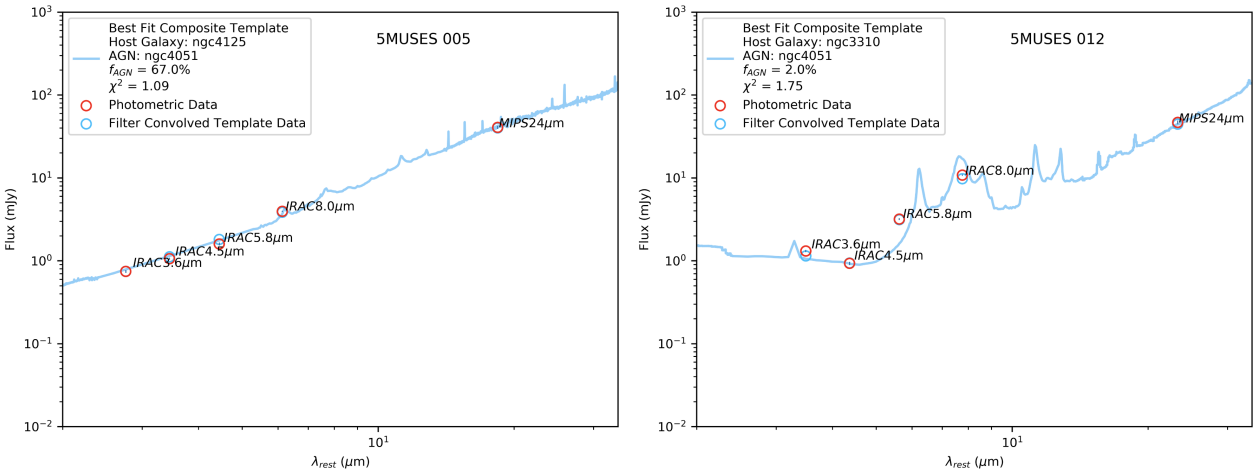


Figure B.1: SED template fits for M005 and M012.

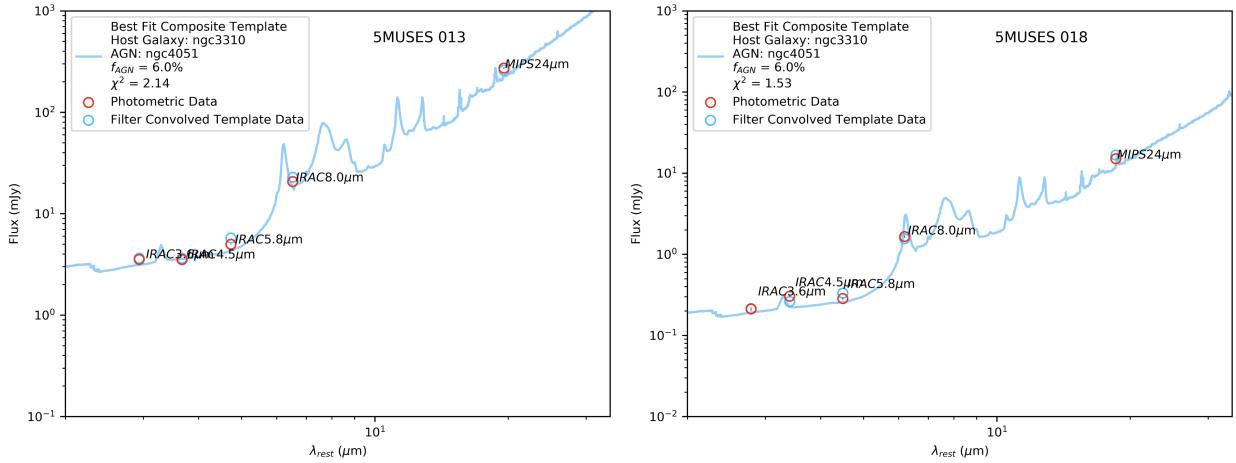


Figure B.2: SED template fits for M013 and M018.

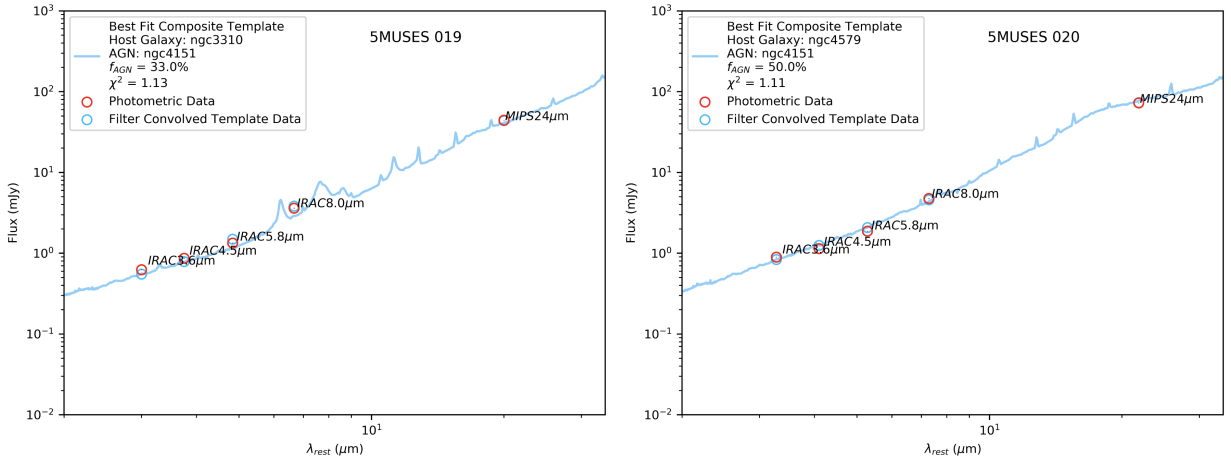


Figure B.3: SED template fits for M019 and M020.

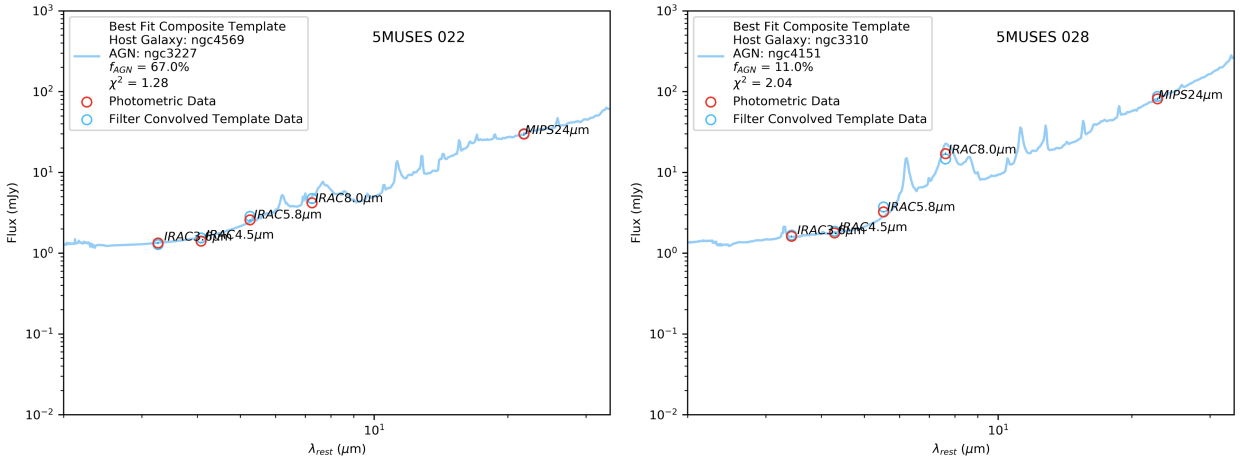


Figure B.4: SED template fits for M022 and M028.

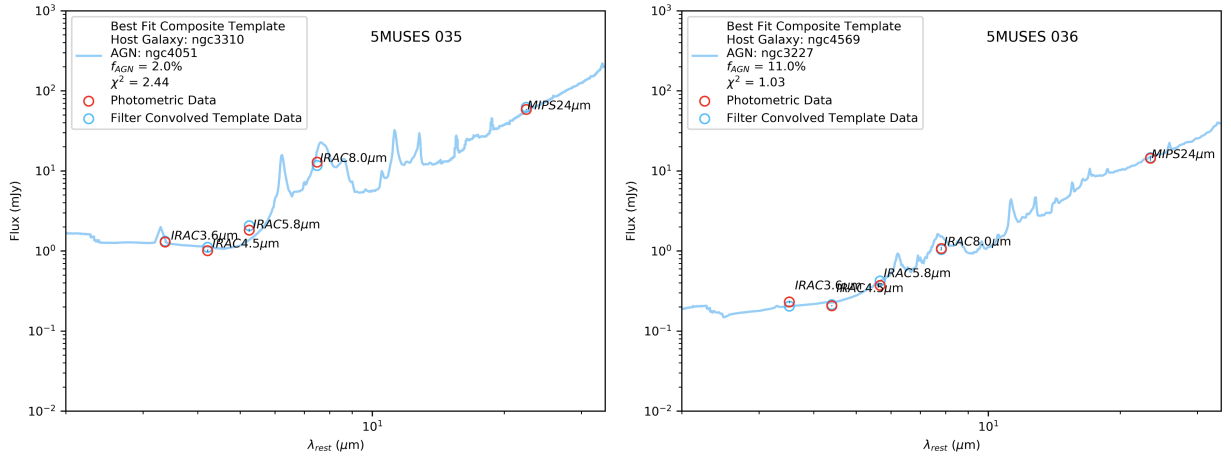


Figure B.5: SED template fits for M035 and M036.

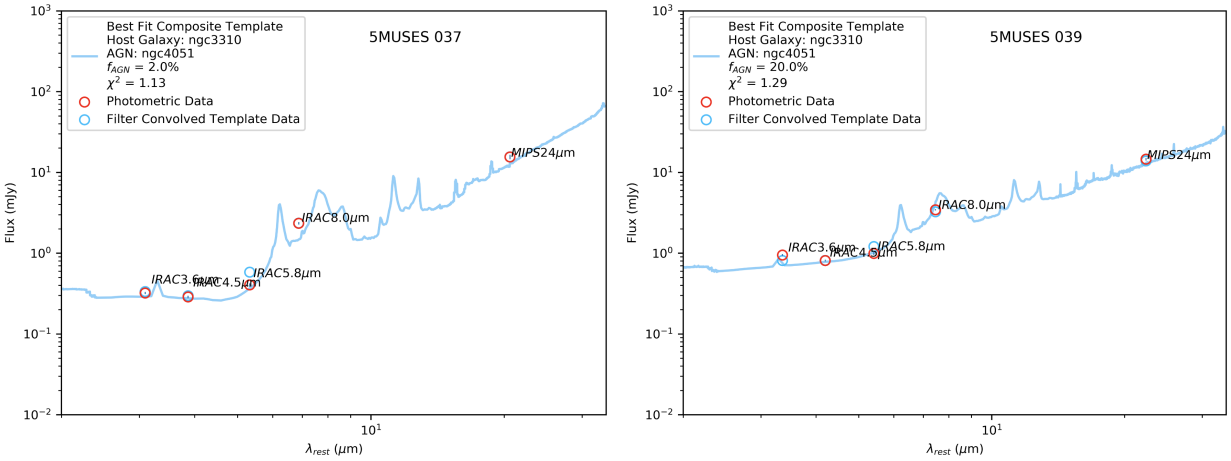


Figure B.6: SED template fits for M037 and M039.

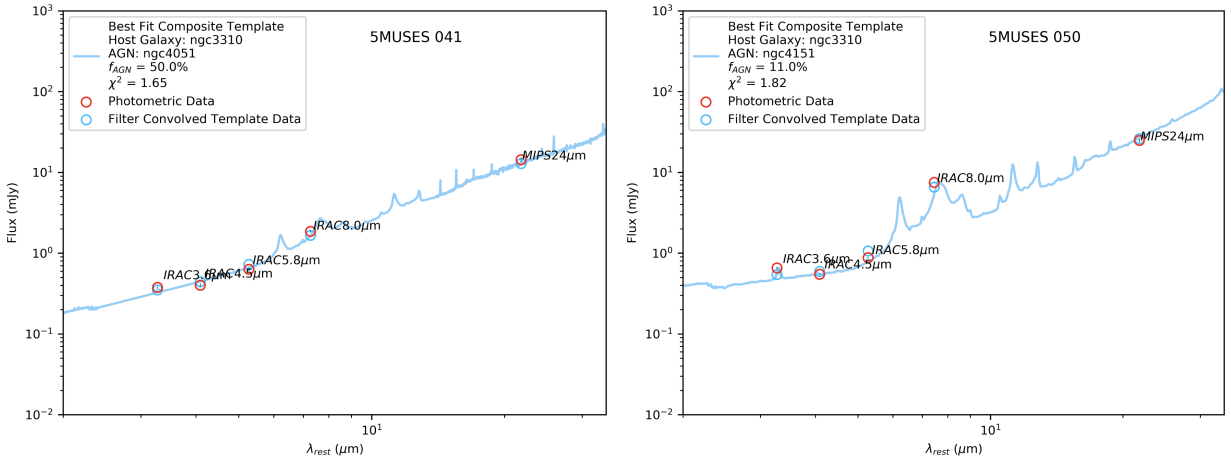


Figure B.7: SED template fits for M041 and M050.

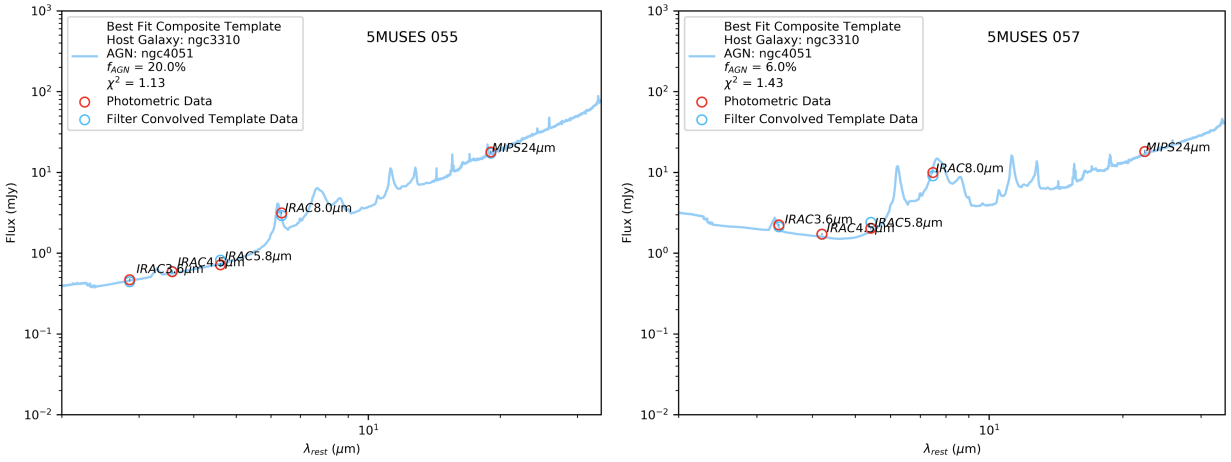


Figure B.8: SED template fits for M055 and M057.

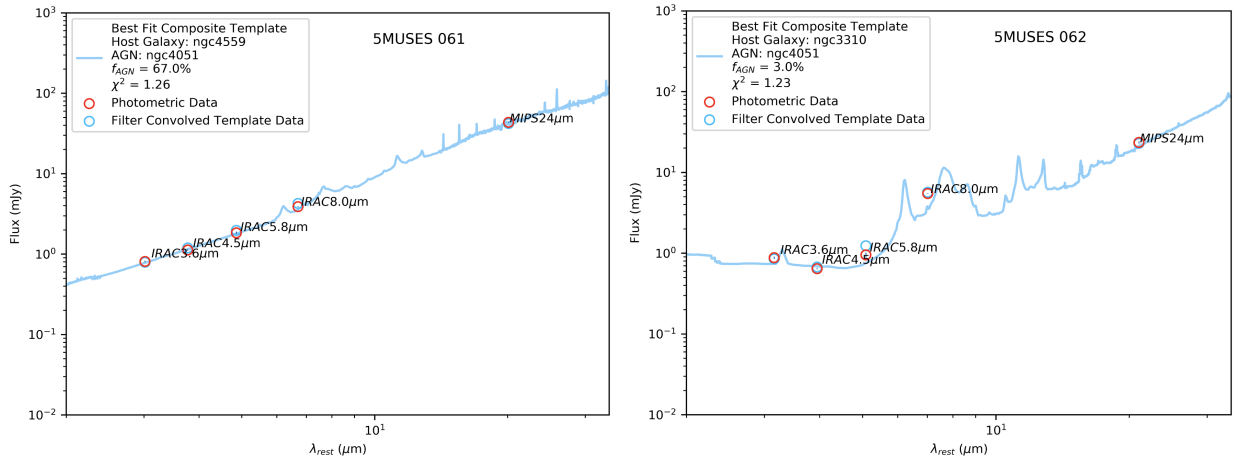


Figure B.9: SED template fits for M061 and M062.

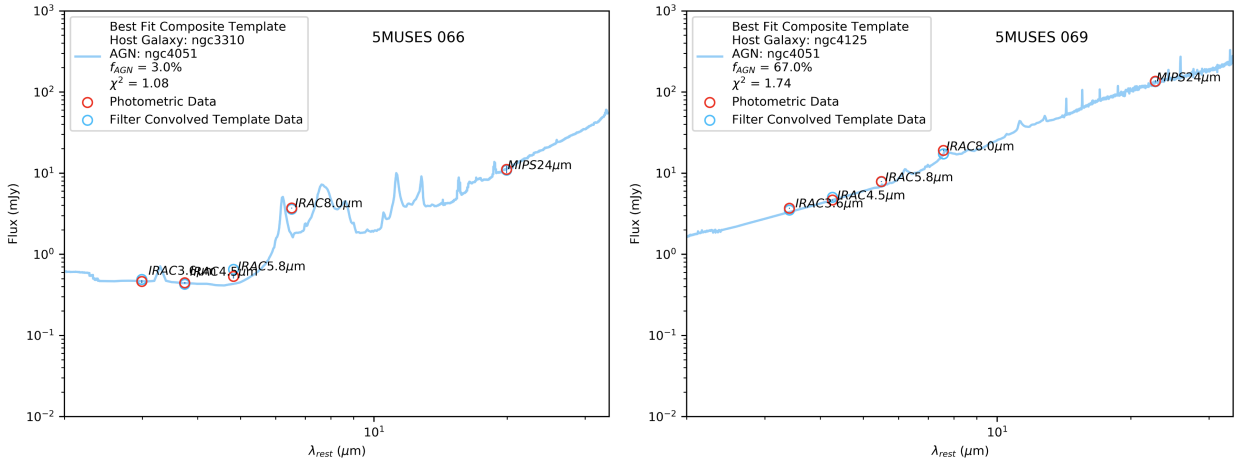


Figure B.10: SED template fits for M066 and M069.

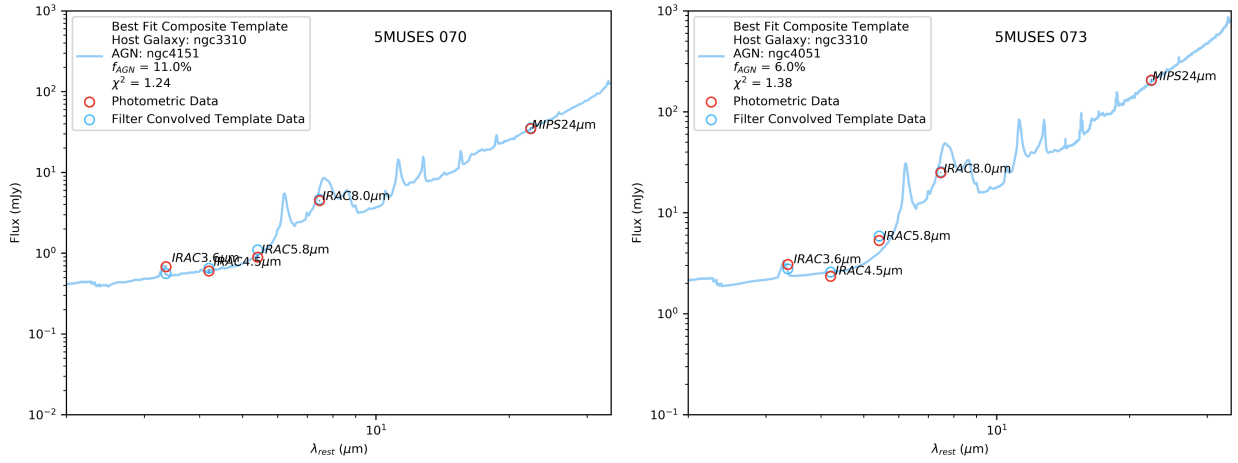


Figure B.11: SED template fits for M070 and M073.

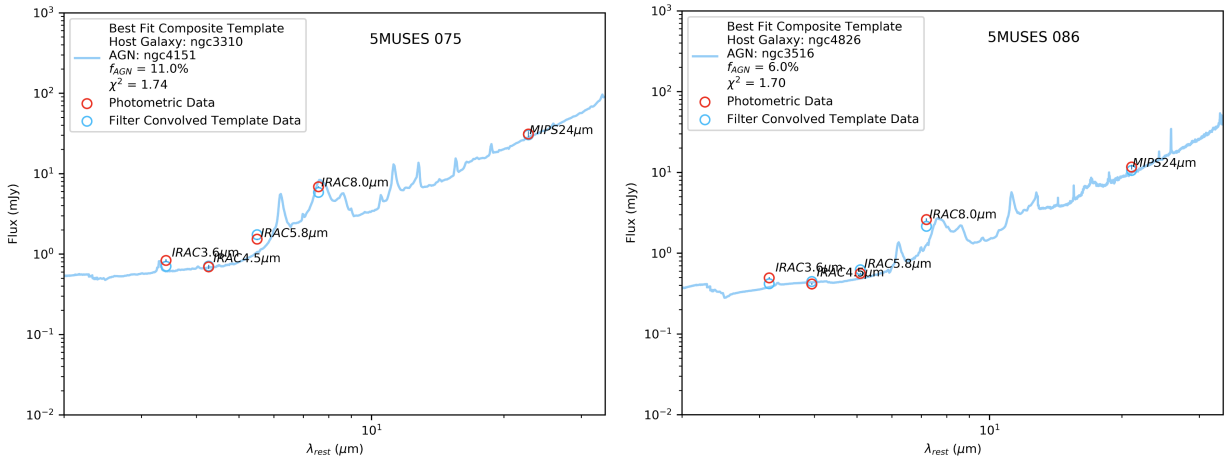


Figure B.12: SED template fits for M075 and M086.

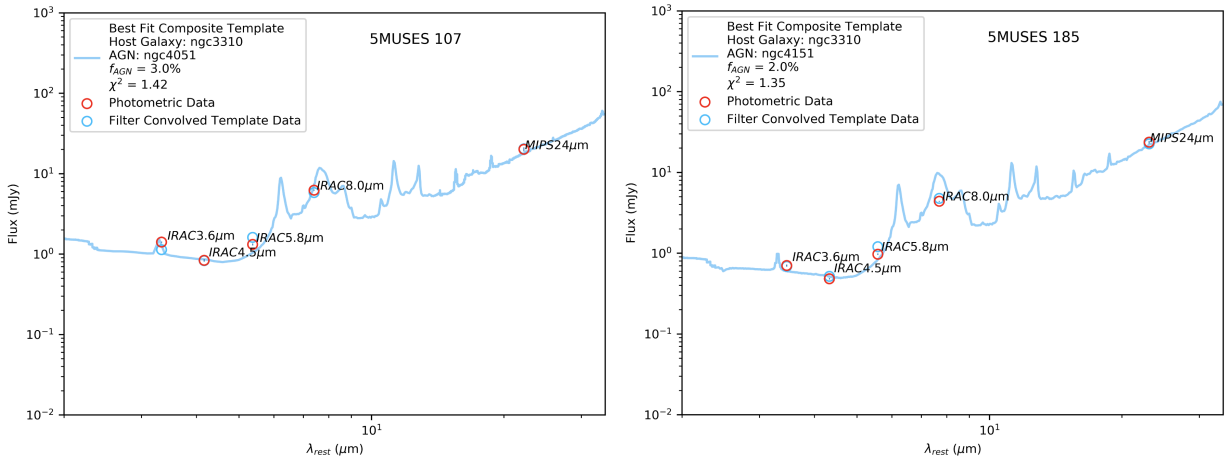


Figure B.13: SED template fits for M107 and M185.

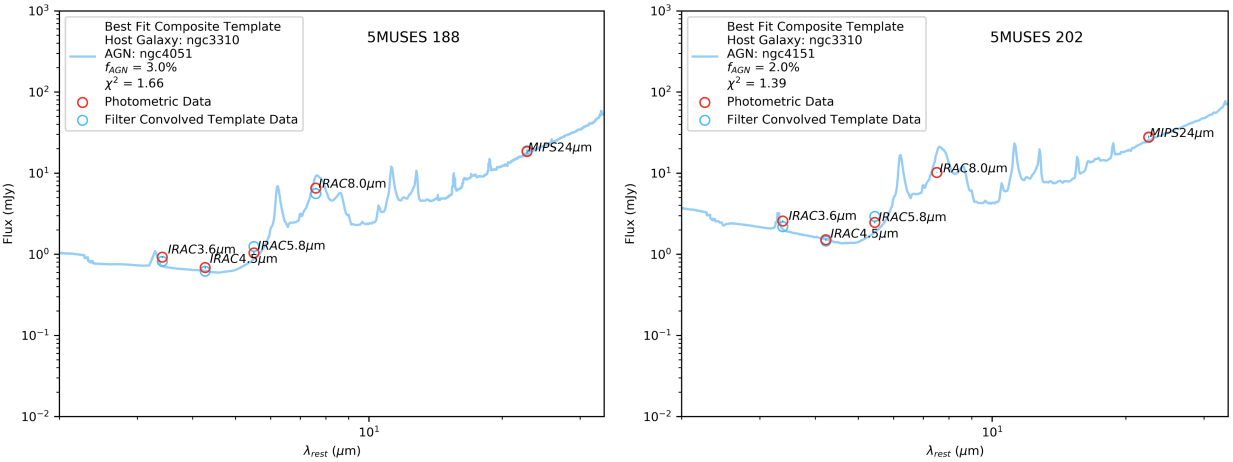


Figure B.14: SED template fits for M188 and M202.

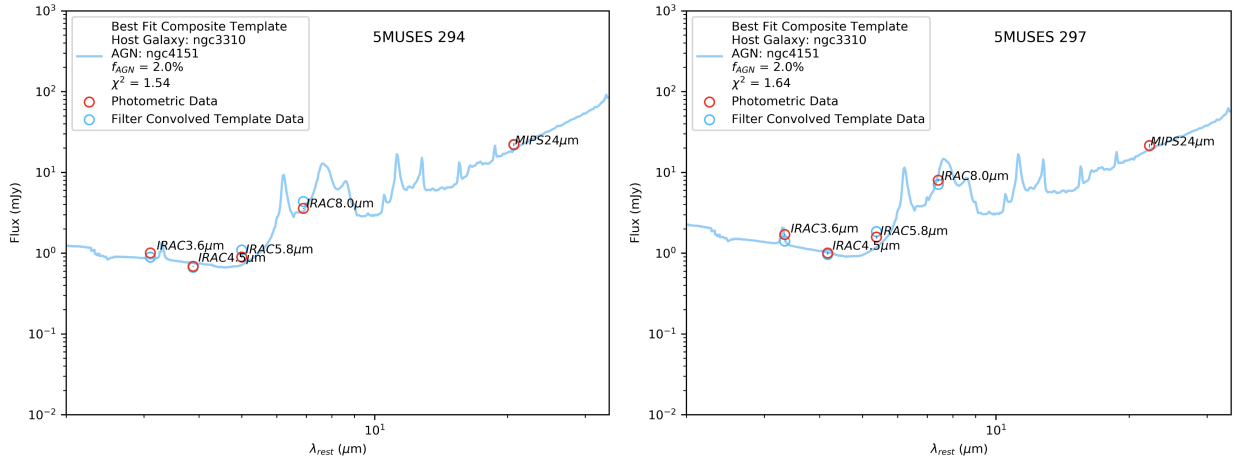


Figure B.15: SED template fits for M294 and M297.

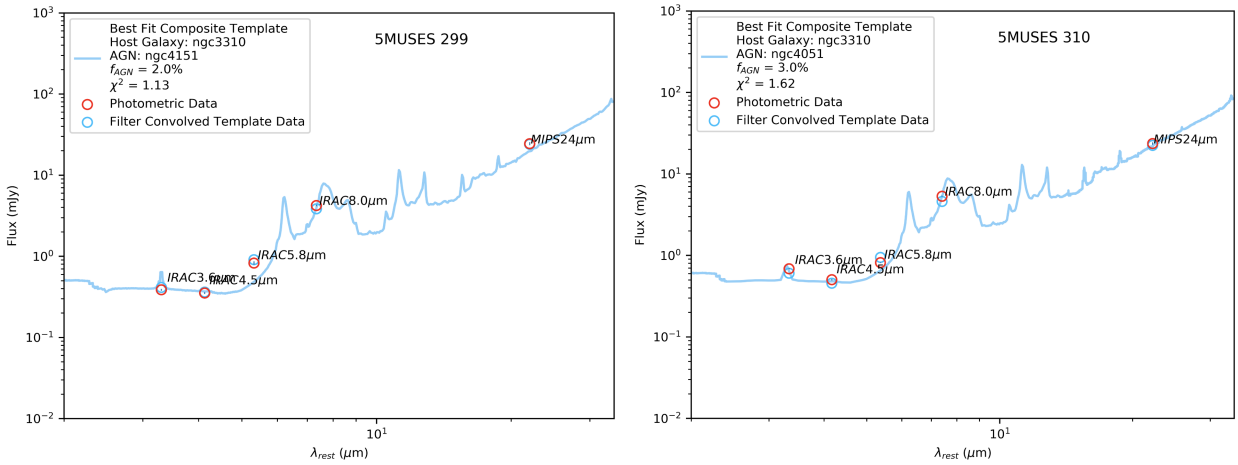


Figure B.16: SED template fits for M299 and M310.

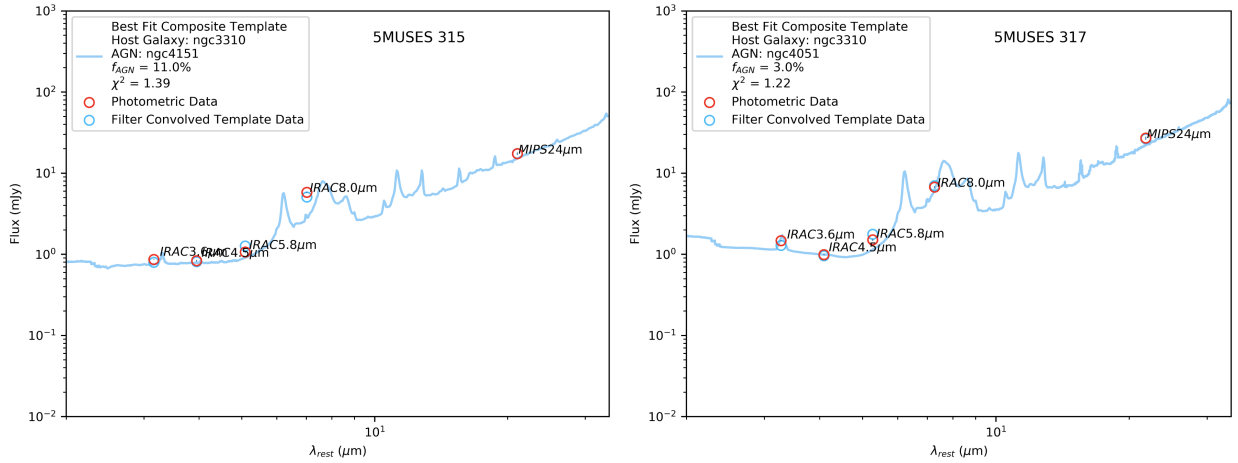


Figure B.17: SED template fits for M315 and M317.

Bibliography

ALONSO-HERRERO, A. et al., “Massive star formation in local luminous infrared galaxies”. In *Astrophysics and Space Science*, vol. 324, no. 2-4, p. 333-336, Dec. 2009.

ATHANASSOULA, E. & BOSMA. A., “Interacting galaxies and mergers”. In *Nature Astronomy*, vol. 3, pp. 588-589, 2019.

ATHANASSOULA, E. et al., “Forming Disk Galaxies in Wet Major Mergers. I. Three Fiducial Examples”. In *The Astrophysical Journal*, vol. 821, no. 2, p. 90, Apr. 2016.

BARNES, J. E. & HERNQUIST, L., “Transformations of Galaxies. II. Gas Dynamics in Merging Disk Galaxies”. In *The Astrophysical Journal*, vol. 471, p. 115, Nov. 1996.

BACON, R. & MONNET, G., “Optical 3D-Spectroscopy for Astronomy”. Published by *Wiley*, ISBN 9783527412020, Mar. 2017.

BACON, R. et al., “The MUSE second-generation VLT instrument”. In *Proceedings of Society of Photo-Optical Instrumentation Engineers* (*SPIE) Conference Series*, vol. 7735, Jul. 2010.

BEIFIORI, A. et al., “Redshift Evolution of the Dynamical Properties of Massive Galaxies from SDSS-III/BOSS”. In *The Astrophysical Journal*, vol. 789, no. 2, p. 92, Jul. 2014.

BELLOCCHI, E. et al., “VLT/VIMOS integral field spectroscopy of luminous and ultraluminous infrared galaxies: 2D kinematic properties”. In *Astronomy & Astrophysics*, vol. 557, no. A59, Aug. 2013.

BEVINGTON, P. R. et al., “Data Reduction and Error Analysis for the Physical Sciences”. The American Institute of Physics, published by McGraw Hill, 1969.

BOUCHÉ, N. et al., “GalPak 3D: A Bayesian Parametric Tool for Extracting Morphokinematics of Galaxies from 3D Data”. In *The Astrophysical Journal*, vol. 150, no. 3, p. 92, Sep. 2015.

BOUCHEZ, A. et al., “The PALM-3000 high-order adaptive optics system for Palomar Observatory”. In *Society of Photo-Optical Instrumentation Engineers* (*SPIE) Conference Series*, vol. 7015 of *Society of Photo-Optical Instrumentation Engineers* (*SPIE) Conference Series*, 0.

BOUWENS, R. J. et al., “UV-continuum Slopes at z ~ 4-7 from the HUDF09+ERS+CANDELS Observations: Discovery of a Well-defined UV Color-Magnitude Relationship for z >= 4

Star-forming Galaxies". In *The Astrophysical Journal*, vol. 754, no. 2, p. 83, Aug. 2012.

BRANDL, B. R. et al., "The Mid-Infrared Properties of Starburst Galaxies from Spitzer-IRS Spectroscopy". In *The Astrophysical Journal*, vol. 653, no. 2, pp. 1129-1144, Dec. 2006.

BRESCIA, M. et al., "Automated Physical Classification in the SDSS DR10. A Catalogue of Candidate Quasars". In *Monthly Notices of the Royal Astronomical Society*, vol. 450, no. 4, pp. 3893-3903.

BRINCHMANN, J. et al., "The physical properties of star-forming galaxies in the low-redshift Universe". In *Monthly Notices of the Royal Astronomical Society*, vol. 351, no. 4, pp. 1151-1179, Jul. 2004.

BROWN, M. J. I. et al., "An Atlas of Galaxy Spectral Energy Distributions from the Ultraviolet to the Mid-infrared". In *The Astrophysical Journal*, vol. 212, no. 2, pp. 18, Jun. 2014.

BROWN, M. J. I. et al., "The spectral energy distributions of active galactic nuclei". In *Monthly Notices of the Royal Astronomical Society*, vol. 489, no. 3, pp. 3351-3367, Nov. 2019.

BRUZUAL, G. and CHARLOT, S., "Stellar Population Synthesis at the Resolution of 2003". In *Monthly Notices of the Royal Astronomical Society*, vol. 344, no. 4, pp. 1000-1028, Oct. 2003.

BUTA, R. J., "Galaxy Morphology". Feb. 2011. ArXiv eprint:1102:0550.

CAGIGAS, M. A. et al., "HARMONI pre-optics design at PDR". In *Society of Photo-Optical Instrumentation Engineers* (*SPIE) Conference Series*, vol. 10702, Jul. 2018.

CALZETTI, D. et al., "The Dust Content and Opacity of Actively Star-forming galaxies". In *The Astrophysical Journal*, vol. 533, no. 2, pp. 682-695, Apr. 2000.

CALZETTI, D. et al., "The Ionized Gas in Local Starburst Galaxies: Global and Small-Scale Feedback from Star Formation". In *The Astrophysical Journal*, vol. 127, no. 3, pp. 1405-1430, Mar. 2004.

CAREY, S., "Cross-Calibration in the Mid-Infrared". In *STScI Calibration Workshop*, 2010.

CIESLA, L. et al., "Constraining the properties of AGN host galaxies with spectral energy distribution modelling". In *Astronomy & Astrophysics*, vol. 576, no. A10, Apr. 2015.

CLARKE, F. et al., "HARMONI Operational Concept Definition Document". *Internal HARMONI Document*, 2020.

CLARKE, F. et al., “Technical Budget Allocations”. *Internal HARMONI Document*, 2020.

CLARKE, F. et al., “HARMONI Spectrograph Design and Analysis Document”. *Internal HARMONI Document*, 2019.

CLARKE, F. et al., “HARMONI System Design and Analysis Report”. *Internal HARMONI Document*, 2017.

CRUMMY, J. et al., “An explanation for the soft X-ray excess in active galactic nuclei”. In *Monthly Notices of the Royal Astronomical Society,* vol. 365, no. 4, p. 1067-1081, Feb. 2006.

DA CUNHA, E., et al., “A simple model to interpret the ultraviolet, optical and infrared emission from galaxies”. In *Monthly Notices of the Royal Astronomical Society*, vol. 388, no. 4, pp. 1595-1617, Aug. 2008.

DADDI, E. et al., “Multiwavelength Study of Massive Galaxies at z ~ 2. I. Star Formation and Galaxy Growth”. In *The Astrophysical Journal*, vol. 670, no. 1, pp. 156-172, Nov. 2007.

DADDI, E. et al., “The Molecular Gas Content of Massive Spirals at z = 1.5”. In *The Astrophysical Journal*, vol. 694, p. 1517, 2009.

DEKEL, A. et al., “Cold streams in early massive hot haloes as the main mode of galaxy formation”. In *Nature*, vol. 457, p. 451-454, Jan. 2009.

DEVEREUX, N. A. & YOUNG, J. S., “The Origin of the Far-Infrared Luminosity from Spiral Galaxies”. In *The Astrophysical Journal*, vol. 350, p. L25, Feb. 1990.

DIALS, M. A. et al., “Description of the High Resolution Dynamics Limb Sounder (HIRDLS) instrument”. In *Proceedings of Society of Photo-Optical Instrumentation Engineers* (*SPIE) Conference Series*, vol. 3437, pp. 84-91, 1998.

DIAMOND-STANIC, A. M. & RIEKE, G. H., “The Relationship between Black Hole Growth and Star Formation in Seyfert Galaxies”. In *The Astrophysical Journal*, vol. 746, no. 2, Feb. 2012.

ELBAZ, D. et al., “The reversal of the star formation-density relation in the distant universe”. In *Astronomy & Astrophysics*, vol. 468, no. 1, pp. 33-48, Jun. 2007.

ELBAZ, D. et al., “GOODS-Herschel: an infrared main sequence for star-forming galaxies”. In *Astronomy & Astrophysics*, vol. 533, p. A119, Sep. 2011.

ELBAZ, D. et al., “Starbursts in and out of the star-formation main sequence”. In *Astronomy & Astrophysics*, vol. 616, Aug. 2018.

EPINAT, B. et al., “Evidence for strong dynamical evolution in disc galaxies through the last 11 Gyr. GHASP VIII - a local reference sample of rotating disc galaxies for high-redshift studies”. In *Monthly Notices of the Royal Astronomical Society*, vol. 401, no. 4, pp. 2113-2147, Feb. 2010.

FADDA, D. et al., “The Spitzer Space Telescope Extragalactic First Look Survey: $24\mu m$ Data Reduction, Catalog, and Source Identification”. In *The Astronomical Journal*, vol. 131, no. 6, pp. 2859-2876, Jun. 2006.

FLORES, H. et al., “Star formation rates of distance luminous infrared galaxies derived from Ha and IR luminosities”. In *Astronomy & Astrophysics*, vol. 415, Oct. 2003.

GARRETT, J., “A 230 GHz Focal Place Array Using a Wide IR Bandwidth SIS Receiver”. D.Phil Thesis, University of Oxford, 2018.

GARZON, F. et al., “EMIR at the GTC: results on the commissioning at the telescope”. In *Proceedings of Society of Photo-Optical Instrumentation Engineers* (*SPIE) Conference Series*, vol. 9908, 2016.

GREENER, M. J. et al., “SDSS-IV MaNGA: spatially resolved dust attenuation in spiral galaxies”. In *Monthly Notices of the Royal Astronomical Society*, vol. 495, no. 2, p 2305-2320, Jun. 2020.

HAMMER, F. et al., “Studying Distant Galaxies”. Published by *World Scientific,* 2017.

HARRISON, C. M. et al., “The KMOS Redshift One Spectroscopic Survey (KROSS): rotational velocities and angular momentum of z ~0.9 galaxies”. In *Monthly Notices of the Royal Astronomical Society*, vol. 467, no. 2, pp. 1965-1983, May 2017.

HOGAN, L. et al., “Integral Field Spectroscopy of Luminous Infrared Main Sequence Galaxies at Cosmic Noon”. Submitted to *Monthly Notices of the Royal Astronomical Society*, 2021.

HOPKINS, P. F. et al., “Mergers and Bulge Formation in LambdaCDM: Which Mergers Matter?”. In *The Astrophysical Journal*, vol. 715, no. 1, pp. 202, May 2010.

HOPKINS, P. F. et al., “Stellar Feedback in Galaxies and the Origin of Galaxy-Scale Winds”. In *Monthly Notices of the Royal Astronomical Society*, vol. 421, no. 4, pp. 3522, Apr. 2012.

HOPKINS, P. F. et al., “Galaxies on FIRE (Feedback In Realistic Environments)”. In *Monthly*

Notices of the Royal Astronomical Society, vol. 445, no. 1, pp. 581, Nov. 2014.

HOPKINS, P. F. & HERNQUIST, L., "Fueling Low-Level AGN Activity through Stochastic Accretion of Cold Gas". In *The Astrophysical Journal*, vol. 166, no. 1, Sep. 2006.

HONG, S. et al., "Large-scale Shock-ionized and Photoionized Gas in M83: The Impact of Star Formation". In *The Astrophysical Journal*, vol. 731, no. 1, p. 45, Apr. 2011.

HOWAT, S. K. et al., "The commissioning of and first results from the UIST imager spectrometer". In *Proceedings of Society of Photo-Optical Instrumentation Engineers* (*SPIE) Conference Series*, vol. 5492, pp. 1160-1171, 2004.

HUBBLE, E., "Extragalactic Nebulae". In *The Astrophysical Journal*, vol. 64, pp. 321-369, Dec. 1926.

HUNG, C. et al., "The role of galaxy interaction in the SFR-M relation: characterizing morphological properties of Herschel-selected galaxies at $0.2<z<1.5$". In *The Astrophysical Journal*, vol. 778, no. 2, p. 129, Dec. 2013.

ISHIBASHI, W. et al., "X-ray power law spectra in active galactic nuclei". In *Astronomy and Astrophysics*. Vol. 512, Mar. 2010.

JENSEN, J. et al., "PAH features within a few hundred parsecs of active galactic nuclei". In *Monthly Notices of the Royal Astronomical Society*, vol. 470, no. 3, pp. 3071-3094, Sep. 2017.

JOHNSON, H. L. et al., "The KMOS Redshift One Spectroscopic Survey (KROSS): the origin of disc turbulence in $z \sim 1$ star-forming galaxies". In *Monthly Notices of the Royal Astronomical Society*, vol. 474, no. 4, pp. 5076-5104, Mar. 2018.

KAUFL, H. et al., "CRIRES: a high-resolution infrared spectrograph for ESO's VLT". In *Proceedings of Society of Photo-Optical Instrumentation Engineers* (*SPIE) Conference Series*, vol. 5492, pp. 1218-1227, 2004.

KENNICUTT, R. C., "The Integrated Spectra of Nearby Galaxies: General Properties and Emission-Line Spectra". In *The Astrophysical Journal*, vol. 388, p. 310, Apr. 1992.

KENNICUTT, R. C., "Star Formation in Galaxies Along the Hubble Sequence". In *Annual Review of Astronomy and Astrophysics*, vol. 36, no. 1, pp. 189-231, Sep. 1998.

KENNICUTT, R. C. and Evans, N. J., "Star Formation in the Milky Way and Nearby Galaxies". In *Annual Review of Astronomy and Astrophysics*, vol. 50, no. 1, pp. 531-608, Sep. 2012.

KENNICUTT, R. et al., “Dust-corrected star formation rates of Galaxies. I. Combinations of H-Alpha and infrared tracers”. In *The Astrophysical Journal*, vol. 703, pp. 1672-1695, Oct. 2009.

KEWLEY, L. J., DOPITA, M. A., “Using Strong Lines to Estimate Abundances in Extragalactic HII Regions and Starburst Galaxies”. In *The Astrophysical Journal*, vol. 142, no. 1, pp. 35-52, Sep. 2002.

KIRKPATRICK, A. et al., “Early Science with the Large Millimeter Telescope: Exploring the Effect of AGN Activity on the Relationships Between Molecular Gas, Dust, and Star Formation”. In *The Astrophysical Journal*, vol. 796, no. 2, p. 135, Nov. 2014.

KOSMALSKI, J. et al., “Preliminary design study of the integral field unit for the E-ELT Harmoni instrument”. In *Proceedings of Society of Photo-Optical Instrumentation Engineers (SPIE) Conference Series*, vol. 9908 of *Ground-based and Airborne Instrumentation for Astronomy VI*, Aug. 2016.

LAURENT, O. et al., “Mid-infrared diagnostics to distinguish AGNs from starbursts”. In *Astronomy & Astrophysics*, vol. 359, pp. 887-899, Jul. 2000.

LEE, E. J. et al., “Time-varying Dynamical Star Formation Rate”. In *The Astrophysical Journal*, vol. 800, no. 1, p. 49, Feb. 2015.

LESLIE, S. K. et al., “The VLA-COSMOS 3 GHz Large Project: Evolution of specific star formation rates out to $z\sim5$”. In *The Astrophysical Journal*, vol. 899, no. 1, Aug. 2020.

LE FLOC’H, E. et al., “Infrared Luminosity Functions from the Chandra Deep Field-South: The Spitzer View on the History of Dusty Star Formation at $0 < z < 1$”. In *The Astrophysical Journal*, vol. 632, no. 1, pp. 169-190, Oct. 2005.

LIANG, Y. C. et al., “The Luminosity-Metallicity Relation of distant luminous galaxies”. In *Astronomy & Astrophysics*, vol. 423, Apr. 2004.

LONSDALE, C. et al., “SWIRE, The SIRTF Wide-Area Infrared Extragalactic Survey”. In *Publications of the Astronomical Society of the Pacific*, vol. 115, no. 810, pp. 897-927, Aug. 2003.

MADAU, P. and DICKINSON, M. “Cosmic Star-Formation History”. In *Annual Review of Astronomy and Astrophysics*, vol. 52, no. 1, pp. 415-486, Aug. 2014.

MAIOLINO, R. et al., “AMAZE. I. The evolution of the mass-metallicity relation at $z > 3$”. In *Astronomy and Astrophysics*, vol. 488, no. 2, p. 463-479, Sep. 2008.

MAGDIS, G. E. et al., “Stellar masses of Lyman break galaxies at z ~ 3”. In *Monthly Notices of the Royal Astronomical Society*, vol. 401, p. 1521, 2010a.

MAGDIS, G. et al., “KROSS: mapping the H-Alpha emission across the star formation sequence at z ~1”. In *Monthly Notices of the Royal Astronomical Society*, vol. 456, no. 4, pp. 4533-4541, Mar. 2016.

MAGDIS, G. et al., “Mid-to-far infrared properties of star-forming galaxies and active galactic nuclei”. In *Astronomy & Astrophysics*, vol. 558, p. A136, Oct. 2013.

MAGNELLI, B. et al., “Evolution of the dusty infrared luminosity function from z = 0 to z = 2.3 using observations from Spitzer”. In *Astronomy & Astrophysics*, vol. 528, p. A35, Apr. 2011.

MAGORRIAN, J. et al., “The Demography of Massive Dark Objects in Galaxy Centers”. In *The Astronomical Journal*, vol. 115, pp. 2285-2305, 1998.

MARTIN, C. L. et al., “Demographics and Physical Properties of Gas Outflows/Inflows at 0.4 < z < 1.4”. In *The Astrophysical Journal*, vol. 760, no. 2, p. 127, Dec. 2012.

MONREAL-IBERO, A. et al., “VLT-VIMOS integral field spectroscopy of luminous and ultraluminous infrared galaxies. II. Evidence for shock ionization caused by tidal forces in the extra-nuclear regions of interacting and merging LIRGs”. In *Astronomy & Astrophysics*, vol. 517, Jul. 2010.

MULLANEY, J. et al., “Defining the intrinsic AGN infrared spectral energy distribution and measuring its contribution to the infrared output of composite galaxies”. In *Monthly Notices of the Royal Astronomical Society*, vol. 414, no. 2, pp. 1082-1110, Jun. 2011.

MULLANEY, J. et al., “GOODS-Herschel: the Far-Infrared View of Star Formation in Active Galactic Nuclei Host Galaxies since z ~ 3”. In *Monthly Notices of the Royal Astronomical Society*, vol. 419, no.12, pp. 95-115, Jan. 2012.

NAVARRO, J. F. et al., “A Universal Density Profile from Hierarchical Clustering”. In *The Astrophysical Journal*, vol. 490, no. 2, pp. 493-508, Dec. 1997.

NEWVILLE, M. et al., “Lmfit: Non-Linear Least-Square Minimization and Curve-Fitting for Python”. 2014, Zenodo, doi: 10.5281/zenodo.11813.

NOESKE, K. G. et al., “Star Formation in AEGIS Field Galaxies since z=1.1: The Dominance of Gradually Declining Star Formation, and the Main Sequence of Star-forming Galaxies”. In *The Astrophysical Journal*, vol. 660, no. 1, pp. L43-L46, May 2007.

O'DOWD, M. J. et al., "Polycyclic Aromatic Hydrocarbons in Galaxies at z ~ 0.1: The Effect of Star Formation and Active Galactic Nuclei". In *The Astrophysical Journal*, vol. 705, no. 1, pp. 885-898, Nov. 2009.

OSTERBROCK, D.E., "Astrophysics of gaseous nebulae and active galactic nuclei". 1989.

PEARSON, W. J. et al., "Main sequence of star forming galaxies beyond the Herschel confusion limit". In *Astronomy & Astrophysics*, vol. 615, p. A146, Jul. 2018.

PEEBLES, P. J. E., "Dark Matter". In *Proceedings of the National Academy of Sciences*, vol. 112, no. 40, May. 2013.

PEREIRA-SANTAELLA, M. et al., "Optical integral field spectroscopy of intermediate redshift infrared bright galaxies". In *Monthly Notices of the Royal Astronomical Society*, vol. 486, no. 4, pp. 5621-5645, Jul. 2019.

PERRET, V. et al., "Evolution of the mass, size, and star formation rate in high redshift merging galaxies". In *Astronomy & Astrophysics*, vol. 562, Feb. 2014.

PESCHKEN, N. et al., "Disc galaxies formed from major mergers in Illustris". In *Monthly Notices of the Royal Astronomical Society*, eprint 1909.01033, Feb. 2020.

PETTINI, M. et al., "[OIII]/[NII] as an abundance indicator at high redshift". In *Monthly Notices of the Royal Astronomical Society*, vol. 348, no. 3, Mar. 2004.

PIRARD, J. et al., "HAWK-I: A new wide-field $1 - 2.5\mu m$ imager for the VLT". In *Proceedings of Society of Photo-Optical Instrumentation Engineers* (*SPIE) Conference Series*, vol. 5492, pp. 1763-1772, 2004.

PLANCK COLLABORATION: Ade, P. A. R. et al., "Planck 2013 results. XVI. Cosmological Parameters". In *Astronomy & Astrophysics*, vol. 571, no. A16, 2014.

POPESCU, C. C. et al., "Modelling the spectral energy distribution of galaxies. V. The dust and PAH emission SEDs of disk galaxies". In *Astronomy & Astrophysics*, vol. 527, pp. A109, Mar. 2011.

POPESSO, P. et al., "The main sequence of star forming galaxies I. The local relation and its bending". In *Monthly Notices of the Royal Astronomical Society*, vol. 483, no. 3, p. 3213, Mar. 2019.

POPESSO, P. et al., "The main sequence of star forming galaxies II. A non-evolving slope at the

high-mass end". In *Monthly Notices of the Royal Astronomical Society*, vol. 490, no. 4, p. 5285, Dec. 2019.

POPESSO, P. et al., "The dust and cold gas content of local star-forming galaxies". In *Monthly Notices of the Royal Astronomical Society*, vol. 496, no. 3, p. 2531, Jun. 2020.

PROCHASKA, J. X. et al., "Detailed Design of a Deployable Tertiary Mirror for the Keck I Telescope". In *Proceedings of Society of Photo-Optical Instrumentation Engineers* (*SPIE) Conference Series*, vol. 9910, p. 22, Jul. 2016.

PUGLISI, A. et al., "The Bright and Dark Sides of High-redshift Starburst Galaxies from *Herschel* and *Subaru* Observations". In *The Astrophysical Journal*, vol. 838, no. 2, Mar. 2017.

RIGOPOULOU, D. et al., "Multiwavelength Energy Distributions of Ultraluminous IRAS Galaxies". In *Monthly Notices of the Royal Astronomical Society*, vol. 273, p. 1049, Feb. 1996.

RIGOPOULOU, D. et al., "A Large Mid-Infrared Spectroscopic and Near-Infrared Imaging Survey of Ultraluminous Infrared Galaxies: Their Nature and Evolution". In *The Astrophysical Journal*, vol. 118, no. 6, p. 2625, Dec. 1999.

RIGOPOULOU, D. et al., "Herschel Observations of Far-infrared Cooling Lines in Intermediate Redshift (Ultra)-luminous Infrared Galaxies". In *The Astrophysical Journal*, vol. 781, no. 1, p. L15, Jan. 2014.

RIGOPOULOU, D. et al., "The properties of Polycyclic Aromatic Hydrocarbons in galaxies: constraints on PAH sizes, charge and radiation fields". Submitted to MNRAS, Nov. 2020..

RODIGHIERO, G. et al., "The Lesser Role of Starbursts in Star Formation at z = 2". In *The Astrophysical Journal*, vol. 739, no. 2, Oct. 2011.

RODRIGUES, M. et al., "Morpho-Kinematics of z~1 galaxies probe the hierarchical scenario". In *Monthly Notices of the Royal Astronomical Society*, vol. 465, no. 1, pp. 1157-1180, Feb. 2017.

RODRIGUES, M. et al., "HARMONI Spectrograph Design Document". *Internal HARMONI Document*, 2019.

RODRIGUEZ-ZAURIN, J. et al., "VLT-VIMOS integral field spectroscopy of luminous and ultraluminous infrared galaxies. III. The atlas of the stellar and ionized gas distribution". In *Astronomy and Astrophysics*. Vol. 527, Mar. 2011.

ROSARIO, D. et al., "The Mean Star Formation Rate of X-ray selected Active Galaxies and its

Evolution from z=2.5: Results from PEP-Herschel". In *Astronomy & Astrophysics*, vol. 545, no. 45, Mar. 2012.

RUPKE, D. S. N. et al., " The Oxygen Abundances of Luminous and Ultraluminous Infrared Galaxies". In *The Astrophysical Journal*, vol. 674, no. 1, p. 172-193, Feb. 2008.

SANDERS, D. B. & MIRABEL, I. F., "Luminous Infrared Galaxies". In *Annual Review of Astronomy and Astrophysics*, vol. 34, p. 749, Jan. 1996.

SCHREIBER, C. et al., "The Herschel view of the dominant mode of galaxy growth from $z = 4$ to the present day". In *Astronomy & Astrophysics*, vol. 575, Mar. 2015.

SELLWOOD, J. A., "Secular evolution in disk galaxies". In *Reviews of Modern Physics*, vol. 86, no. 1, Jan. 2014.

SHARPLES, R. et al., "First Light for the KMOS Multi-Object Integral-Field Spectrometer". In *The Messenger*, vol. 151, pp. 21-23, Mar. 2013.

SHI, Y. et al., "Extended Schmidt Law: Role of Existing Stars in Current Star Formation". In *The Astrophysical Journal*, vol. 733, no. 2, p. 87, Jun. 2011.

SHIPLEY, H. V. et al., "A New Star Formation Rate Calibration from Polycyclic Aromatic Hydrocarbon Emission Features and Application to High-redshift Galaxies". In *The Astrophysical Journal*, vol. 818, no. 1, p. 60, Feb. 2016.

SMITH, J. et al., "The Mid-Infrared Spectrum of Star-Forming Galaxies: Global Properties of Polycyclic Aromatic Hydrocarbon Emission". In *The Astrophysical Journal*, vol. 656, no. 2, pp. 770-791, Feb. 2007.

SOFUE, Y. et al., "Rotation and Mass in the Milky Way and Spiral Galaxies". In *Publications of the Astronomical Society of Japan*, vol. 69, no. 1, Feb. 2017.

SPEAGLE, J. S. et al., "A Highly Consistent Framework for the Evolution of the Star-Forming 'Main Sequence' from $z \sim 0.6$". In *The Astrophysical Journal*, vol. 214, no. 2, p. 15, Oct. 2014.

SPOON, H. W. W. et al., "Mid-Infrared Galaxy Classification Based on Silicate Obscuration and PAH Equivalent Width". In *The Astrophysical Journal*, vol. 654, no. 1, pp. L49-L52, Jan. 2007.

STARK, D. P. et al., "The Evolutionary History of Lyman Break Galaxies Between Redshift 4 and 6: Observing Successive Generations of Massive Galaxies in Formation". In *The Astrophysical Journal*, vol. 697, no. 2, pp. 1493-1511, Jun. 2009.

STORCHI-BERGMANN, T. et al., “Ultraviolet to Near-Infrared Spectral Distributions of Star-forming Galaxies: Metallicity and Age Effects”. In *The Astrophysical Journal*, vol. 429, p. 572, Jul. 1994.

STOTT, J. P. et al., “The merger rates and sizes of galaxies across the peak epoch of star formation from the HiZELS survey”. In *Monthly Notices of the Royal Astronomical Society*, vol. 430, p. 1158, Jan. 2013.

STOTT, J. P. et al., “The KMOS Redshift One Spectroscopic Survey (KROSS): Dynamical properties, gas and dark matter fractions of typical $z \sim 1$ star-forming galaxies”. In *Monthly Notices of the Royal Astronomical Society*, vol. 457, p. 1888, Apr. 2016.

TACCHELLA, S. et al., “The confinement of star-forming galaxies into a main sequence through episodes of gas compaction, depletion and replenishment”. In *Monthly Notices of the Royal Astronomical Society*, vol. 457, no. 3, pp. 2790-2813, Apr. 2016.

TACCONI, L. J. et al., “PHIBSS: Unified Scaling Relations of Gas Depletion Time and Molecular Gas Fractions”. In *The Astrophysical Journal*. Vol. 853, no. 2, p. 179, Feb. 2018.

TAMAI, R. et al., “The ESO’s ELT Construction Status”. In *Society of Photo-Optical Instrumentation Engineers* (*SPIE) Conference Series*, vol. 10700, pp. 1070014, Jul. 2018.

THATTE, N. et al., “The Oxford SWIFT integral field spectrograph”. In *Society of Photo-Optical Instrumentation Engineers* (*SPIE) Conference Series*, vol. 6269 of *Society of Photo-Optical Instrumentation Engineers* (*SPIE) Conference Series*, 3, 2006

THATTE, N. et al., “HARMONI: the first light integral field spectrograph for the E-ELT”. In *Society of Photo-Optical Instrumentation Engineers* (*SPIE) Conference Series*, vol. 9147 of *Society of Photo-Optical Instrumentation Engineers* (*SPIE) Conference Series*, 5, 2014

TIELENS, A., “The Physics and Chemistry of the Interstellar Medium”. Cambridge University Press, 2005.

TIELENS, A. et al., “Interstellar Polycyclic Aromatic Hydrocarbon Molecules”. In *Annual Review of Astronomy and Astrophysics*, vol. 46, no. 1, pp. 289-337, Sep. 2008.

TRAN, Q. et al., “Isocam-Cvf 5-12 Micron Spectroscopy of Ultraluminous Infrared Galaxies”. In *The Astrophysical Journal*, vol. 552, no. 2, pp. 527-543, May 2001.

TURNER, O. J. et al., “The KMOS Deep Survey (KDS) - I. Dynamical measurements of typical star-forming galaxies at $z \simeq 3.5$”. In *Monthly Notices of the Royal Astronomical Society*, vol. 471,

no. 2, Oct. 2017.

VAN ALBADA, T. S., “Dissipationless galaxy formation and the R to the ¼-power law”. In *Monthly Notices of the Royal Astronomical Society*, vol. 201, pp. 939-955, Dec. 1982.

VAN DOKKUM, P. G., “Cosmic-Ray Rejection by Laplacian Edge Detection”. *PASP*, 113, 1420-1427, 2001.

VIVES, S. & PRIETO, E., “Original image slicer designed for integral field spectroscopy with the near-infrared spectrograph for the James Webb Space Telescope”. In *Society of Photo-Optical Instrumentation Engineers* (*SPIE) Optical Engineering*, vol. 45, no. 9, pp. 1-6, Sep. 2006.

WHITAKER, K. E. et al., “The Star Formation Mass Sequence Out to z = 2.5”. In *The Astrophysical Journal*, vol. 754, no. 2, p. L29, Aug. 2012.

WHITE, R. L. et al., “The FIRST Bright Quasar Survey”. In *The Astrophysical Journal*, vol. 126, no. 2, p. 133, Feb. 2000.

WILKINS, D. et al., “The Comptonization of accretion disc X-ray emission: consequences for X-ray reflection and the geometry of AGN coronae”. In *Monthly Notices of the Royal Astronomical Society*, vol. 448, no.1, p. 703, Mar. 2015.

WISNIOSKI, E. et al., “The KMOS 3D Survey: Design, First Results, and the Evolution of Galaxy Kinematics from $0.7 \leq z \leq 2.7$”. In *The Astrophysical Journal*, vol. 799, no. 2, p. 209, Feb. 2015.

WISNIOSKI, E. et al., “The KMOS3D Survey: Data Release and Final Survey Paper”. In *The Astrophysical Journal*, vol. 886, no. 2, p. 124, Dec. 2019.

WU, Y. et al., “Infrared Luminosities and Aromatic Features in the $24\mu m$ Flux-Limited Sample of 5MUSES”. In *The Astrophysical Journal*, vol. 723, no. 1, pp. 895-914, Nov. 2010.

ZAHID, H. J. et al., “A Census of Oxygen in Star-Forming Galaxies: An Empirical Model Linking Metallicities, Star Formation Rates, and Outflows”. In *The Astrophysical Journal*, 2012, vol 757, no. 2, p. 54, Sep. 2012.

ZIELENIEWSKI, S., “Science with Integral Field Spectrographs Present and Future”. D.Phil Thesis, University of Oxford, Apr. 2016.